Bayesian Model Selection with Gravitational Waves from Supernovae

Joshua Logue, MSci

Submitted in fulfilment of the requirements
for the Degree of Doctor of Philosophy

School of Physics & Astronomy
College of Science & Engineering
University of Glasgow

September 2014

Abstract

This thesis concerns inferring core collapse supernova physics using gravitational waves. The mechanism through which the supernova is re-energised is not well understood and there are many theories of the physical processes behind the so called supernova mechanism. Gravitational waves provide an opportunity to see through to the core of a collapsing star. This thesis provides an algorithm that will analyse a detected gravitational waveform from a core collapse supernova and identify the supernova mechanism. This is achieved through the use of Bayesian model selection and a nested sampling algorithm. This Bayesian data analysis algorithm is called the Supernova Model Evidence Extractor (SMEE). SMEE is designed to classify detected gravitational waveforms from core-collapse supernovae and 3 different versions which employ different types of data have been developed. These 3 versions utilise time domain (which has been fast Fourier transformed into the frequency domain), power spectrum domain and spectrogram data and the success of each version is investigated.

Firstly, results for a simplified idealised version of SMEE are discussed. In this scenario only a single gravitational wave detector is considered and the effect of the sky position of the source are ignored. Next, techniques which can be employed to improve SMEE are investigated. Finally, SMEE is tested using 3 gravitational wave detectors and the full effect of the time delay between detectors and the antenna response on each detector is included. As well as this, recoloured detector noise from the Science runs from both LIGO and Virgo are utilised here. This thesis demonstrates that each version of SMEE is successful and are able to infer the supernova mechanism for a galactic supernova. The spectrogram version of SMEE is deemed the most accurate and it is recommended that this technique should be further explored in the future.

Contents

List of Figures

List of Tables

Acknowledgements

When starting my PhD in the Institute for Gravitational Research (IGR) I had no idea what I was letting myself in for. Four years and many, many doughnuts later I have stopped feeling like an imposter but still feel amazed at the intelligence, friendliness and passion of the people that make up the IGR and the rest of the Physics and Astronomy Department. I have studied at the University of Glasgow for 9 years as both an undergraduate and postgraduate and during that time it has become my home. I'm not sure how I will cope without it.

I am extremely grateful to my supervisor Siong Heng for his constant support, patience and understanding. There is no way I would have finished my research without him. Thanks too to the STFC for funding this mad endeavour. There are many others in the IGR that have helped me over the years. Thank you to Matt Pitkin for always being there to answer stupid questions and help me get over my ineptness with a computer. Thank you to Graham Woan and Martin Hendry for your many words of wisdom. I have had many amazing office mates and would like to single out Ignacio Santiago, Craig Lawrie, John MacArthur and Colin Gill as well as Erin MacDonald, Gareth Davies and Jade Powell in the office next door.

As part of the LIGO Scientific Collaboration, I would like to especially thank Christian Ott for his support and help in this research. I would also like to thank Peter Kalmus and Sarah Gossan for the fantastic impact you have had in my research.

In my personal life I would like to thank everyone in my family, especially my mum and dad for always supporting me and especially for giving me the "Tell me Why?" book when I was little which fueled my curiosity and inspired me to study science. To my nieces Islay, Arya and Jura. You are all a constant inspiration and

I can't wait to see the amazing things you will accomplish. And most importantly I wouldn't be here without my amazing wife Sophie. I love you and thank you for your patience and support during this time. This is for you.

"Would it save you a lot of time if I just gave up and went mad now?"

– Arthur Dent

"I don't know, I'm makin' this up as I go."

– Indiana Jones

"Then I will tell you a great secret, Captain. Perhaps the greatest of all time. The molecules of your body are the same molecules that make up this station, and the nebula outside, that burn inside the stars themselves. We are star stuff, we are the universe, made manifest, trying to figure itself out."

– Delenn

Declaration

I, Joshua Logue, confirm that the work presented in this thesis is my own. Where information or figures have been derived from other sources, appropriate references have been given.

Chapter 1 discusses the background of gravitational waves and their sources. Citations have been given where relevant. The discussion of different theories pertaining to supernova in Section 1.7 as well as Figure 1.8 comes from the Logue et al 2012 [70] publication and is shown here with permission from the other authors.

Chapter 2 discusses the Bayesian Inference Techniques and appropriate citations are given where applicable.

Chapter 3 discusses the Supernova Model Evidence Extractor and presents work which is my own.

The results shown in Chapter 4 are entirely my own and uses the computing software MATLAB. It is the result of discussions with my supervisor, Siong Heng, as well as Christian Ott, Peter Kalmus, Sarah Gossan and Jade Powell. The plots and analysis are entirely my own.

The work in Chapter 5 is entirely my own and is the result of discussions with Siong Heng, Christian Ott, Sarah Gossan and Jade Powell. All plots and analysis are entirely my own.

Chapter 6 provides a full analysis of the Supernova Model Evidence Extractor and is entirely my own work and is the result of discussions with Siong Heng, Christian Ott, Sarah Gossan and Jade Powell. All plots and analysis are entirely

my own.

The conclusions given in Chapter 7 is my own analysis of the work and results in this thesis. Where necessary, work has been properly cited.

Chapter 1

Introduction

For most of its history, the field of astrophysics has been limited to observations in the electromagnetic spectrum. While this has led to countless scientific discoveries there are still many mysteries waiting to be solved. The detection of gravitational waves will open up a completely new and complementary way of understanding the universe. Astrophysical source properties which were previously imperceptible in the electromagnetic spectrum will be detectable in the gravitational wave spectrum. One possible source are core collapse supernovae and the motivation of this thesis is to demonstrate how gravitational waves can be used to better understand these events. This Chapter provides a brief introduction to gravitational waves and the instruments which are used to detect them. There is an introduction to the likely sources of gravitational waves, in particular supernovae, which will be the focus of this thesis.

1.1 Introduction to Gravitational Radiation

Gravitational waves (GW) are ripples in the curvature of spacetime that carry information about changing gravitational fields. They were predicted in one of the greatest scientific breakthroughs of the 20th century made by Einstein when he developed his General Theory of Relativity in 1915 [36]. This theory revolutionised the way in which physicists perceived the nature of spacetime. It described gravity in terms of the geometry of spacetime curved by the presence of massive objects.

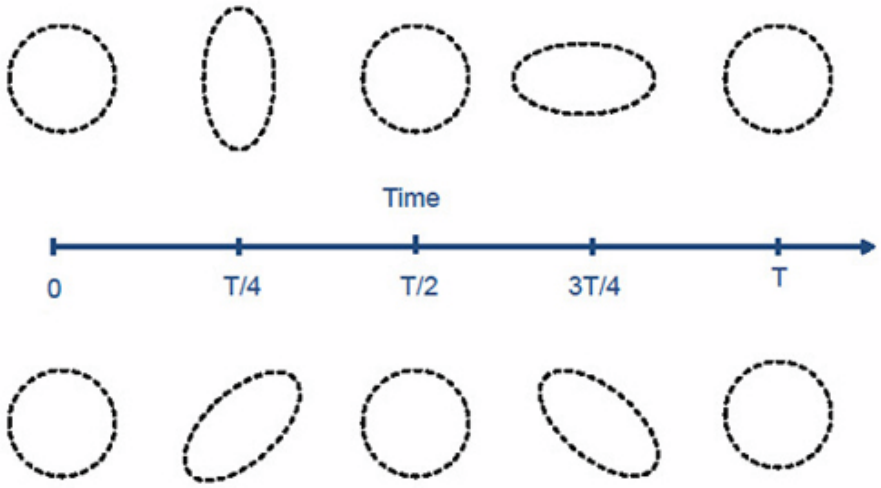

Figure 1.1: A gravitational wave travelling into the page stretches and compresses spacetime along perpendicular axes. Upper diagram: For free masses initially arranged in a circle, a gravitational wave with a period, T, stretches and then compresses space along the vertical axis and vice versa along the horizontal axis. This is called the "+" polarization state of the wave. Lower diagram: The "×" polarisation state stretches and compresses space along axes tilted 45 degrees from vertical [67].

This is often described by the phrase "matter tells spacetime how to curve, and spacetime tells matter how to move" [129]. Many consequences of this theory have since been proved such as the bending of light in a gravitational field, shown by Eddington in 1919 [35] and the precession of the perihelion of Mercury [124].

Gravitational waves are a consequence of small perturbations to the local spacetime metric in the linearised Einstein Equations, a weak-field approximation of a more general relation between the matter and energy distribution and the curvature of spacetime known as the Einstein Equations. The solution is simply expressed as a plane wave with a propagation speed equal to the speed of light.

An illustration of the effects of gravitational waves can be shown in the deformation of a ring of particles in perfectly flat space. When a gravitational wave propagating perpendicular to the plane of the ring passes through this space it causes spacetime to oscillate i.e. it will make the test particles become closer or further apart from each other, as shown in Figure 1.1. As in the case for electromagnetic signals; gravitational radiation has two independent polarisation states. However, the angle between the two states is $\pi/4$ rather than $\pi/2$ [99]. These two polarisations are labelled plus (+) and cross (×). The gravitational strains (a dimensionless measure of the magnitude of the spacetime perturbation in terms of the proper distance between particles) are denoted h_+ and $h_\times$.

1.1.1 Amplitude of Gravitational Waves

The Einstein field equations are often solved numerically with post-Newtonian approximations to infer the amplitude of gravitational waves due to the fact they are too complicated to be solved analytically. The lowest order post-Newtonian approximation for the emitted radiation is the quadropole formula [99]. This depends on the mass density, ρ, and the velocity fields of the Newtonian system. The amplitude at its lowest order is then the tensor,

$$h_{jk} = \frac{2}{r}\frac{d^2 Q_{jk}}{dt^2}, \tag{1.1}$$

where r is the distance from the source and Q_{jk} is the second moment of the mass distribution,

$$Q_{jk} = \int \rho x_j x_k d^3x. \tag{1.2}$$

The internal dynamical motion of the source produces gravitational waves dependent on how spherically asymmetric the system is. For example, a symemetric star pulsating spherically would not produce any gravitational radiation, whereas a non-radial oscillation or a spinning non-asymmetric object would generate gravitational radiation. How much the shape of the system changes can be measured from the non-spherical part of the kinetic energy, E^{ns}_{kin} i.e the energy which is converted into gravitational wave emission. Thus the shape changing dynamical motions of the system provoke gravitational wave to oscillate with an amplitude (for each polarisation) [117],

$$h \sim \frac{G}{c^4}\frac{E^{\rm ns}_{\rm kin}}{r} \sim 10^{-20}\Big(\frac{E^{\rm ns}_{\rm kin}}{M_{\rm s}c^2}\Big)\Big(\frac{10{\rm Mpc}}{r}\Big), \tag{1.3}$$

where M_s is the mass of the Sun and 10 Mpc is the approximate distance scale for the local group of galaxies. This demonstrates the small amplitudes of the gravitational field that needs to be detected on Earth, typically on the order of $10^{-20}{\rm Hz}^{-1/2}$.

1.1.2 Observed Evidence for Gravitational Waves

The first observed evidence of the existence of gravitational radiation came from radio measurements of the binary pulsar PSR B1913+16, a binary consisting of two

neutron stars closely orbiting each other at relativistic speed [126]. For this particular binary, tracking the evolution of their orbital period can be achieved through the analysis of radio pulses emitted from one of the neutron stars. The shrinkage of the orbit was accurately established after eight years of measurements. This data was then compared to that predicted by general relativity as a consequence of energy loss through the emission of gravitational waves. There was only a discrepancy of $< 0.5\%$ between the measurement and prediction thus providing strong evidence to support the existence of gravitational radiation albeit through the use of indirect evidence i.e where the gravitational waves have not been measured through the use of a detector. Since then, this study has been repeated with various binary pulsar systems and the shrinkage of their orbits due to gravitational wave emission has been confirmed [127].

1.2 Gravitational Wave Detectors

It has been nearly a century since gravitational waves (GWs) were first theorised but no direct detections have been made. The first GW detectors typically consisted of a cylinder of aluminium of around 3 metres in length with a mass of 1000 kg. These "bar detectors" [122, 12] had a narrow resonant frequency of 500 Hz - 1.5 kHz, thus a passing GW at this frequency would cause the detector to vibrate. This type of detector is affected by noise that greatly exceeds the amplitude of the vibrations caused by the GW so coincident detections from two or more detectors are required to make reliable claims of detection. Despite a great deal of work to resolve the limitations of bar detectors, no definitive evidence exists of a significant event. While this type of detector is still being used [5], they have fallen out of favour and the use of ground based interferometers has come to be the dominant type of detector. These interferometers are preferred over bar detectors due to the fact they are sensitive over a wide band of frequencies, so they can be used to detect GWs from various sources. These detectors are predominantly made up of two arms of the same length, perpendicular to each other, where laser light is sent down each arm and reflected off test masses (Figure 1.2). As a GW travelling through space passes through the detector it will slightly alter the lengths of the interferometer e.g. making one longer and the other shorter in the same fashion as for the ring of particles described in Figure 1.1. This relative change in lengths can then be measured and the characteristics of the GW, and thus the source that emitted the

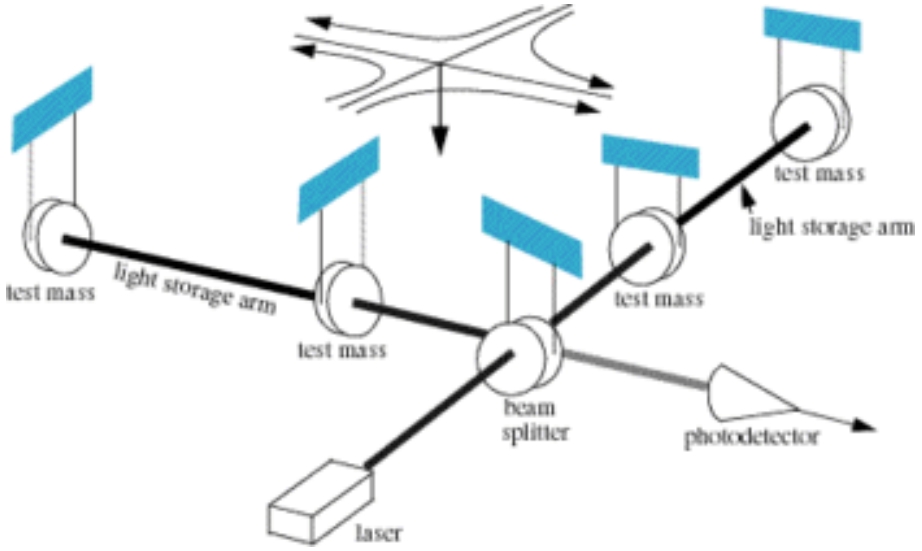

Figure 1.2: Schematic of a laser interferometer [130]

GW, can be determined.

In this case, if two test masses were picked a length L apart a GW will cause a strain

$$\frac{\Delta L}{L} = \frac{h}{2} \tag{1.4}$$

between the masses of approximately 10^{-21} metres, so for a distance of say 1 kilometre a change in length of 10^{-18} metres would need to be measured. This demonstrates the difficulty of gravitational wave detection and why detectors need to be able to perform extremely precise measurements if they are to make a significant detection.

GWs are made of two different polarisation states, plus and cross, denoted by h_+ and $h_\times$. The directional sensitivity of a detector depends on the polarisation of the incoming wave, thus, two antenna patterns (one for each polarisation state) need to be taken into account, see Figure 1.3 for an example of a typical interferometric GW detector antenna pattern. The total gravitational wave strain is then a combination of these two polarisation states, adjusted by the antenna responses to reflect the directional sensitivity,

$$h = F_+ h_+ + F_\times h_\times, \tag{1.5}$$

where h is the GW signal, F_+ and $F_\times$ are the antenna responses.

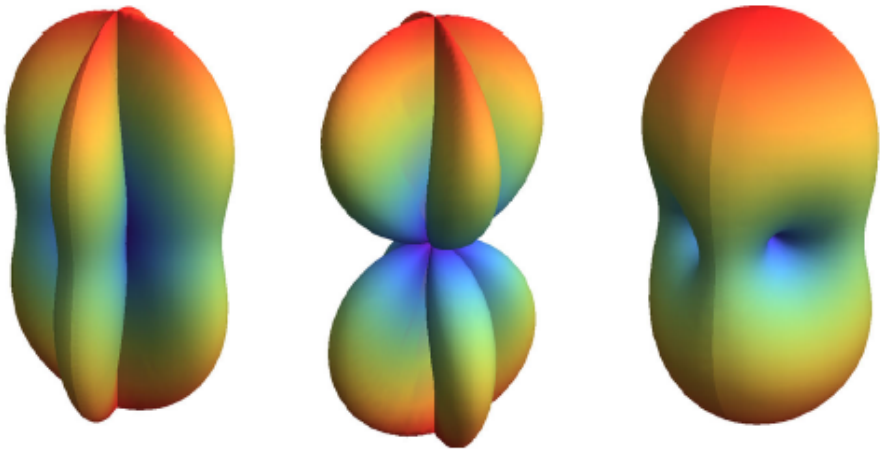

Figure 1.3: Antenna patterns for GW detector [4]. Interferometer antenna response for (+) polarization (left), (×) polarization (middle), and unpolarized waves (right). Here the colours represent the scale of the antenna response with red indicating where it is at the maximum i.e where the source is perpendicular to the plane of the detector. Blue represents where the source is parallel to detector and the antenna response is at its minimum.

The antenna response, F_+ and $F_\times$ are given by:

$$F_+ = \frac{1}{2}(1+\cos^2\theta)\cos 2\phi\cos 2\psi - \cos\theta\sin 2\phi\sin 2\psi \tag{1.6}$$

$$F_\times = \frac{1}{2}(1+\cos^2\theta)\cos 2\phi\sin 2\psi + \cos\theta\sin 2\phi\cos 2\psi \tag{1.7}$$

where θ is the polar angle of the sky position of a source of gravitational waves and ϕ is the azimuthal angle of the sky position of the source. ψ is the local polarisation angle of the source [96].

Figure 1.4 demonstrates this by showing the polar angle, θ, and azimuthal angle, ϕ, at which the waveform arrives at the detector. On the left hand plot the dececter plane represents an interferometer with two arms, x-arm and y-arm with unit vectors $\hat{e}_x$ and $\hat{e}_y$. This plane of the sky, representing the direction a GW is travelling from, is offset by θ and ϕ from the detector plane. In the case of the left plot the two vectors $\hat{e}_x^R$ and $\hat{e}_y^R$ are parallel to $\hat{e}_x$ and $\hat{e}_y$ i.e the plane of the sky has no rotation relative to the detector plane. However in the right hand plot, a rotation angle,ψ, has been applied and $\hat{e}_x^R$ and $\hat{e}_y^R$ are now offset to the directions represented by α and β. This angle is the polarisation angle, ψ, in Equation 1.7.

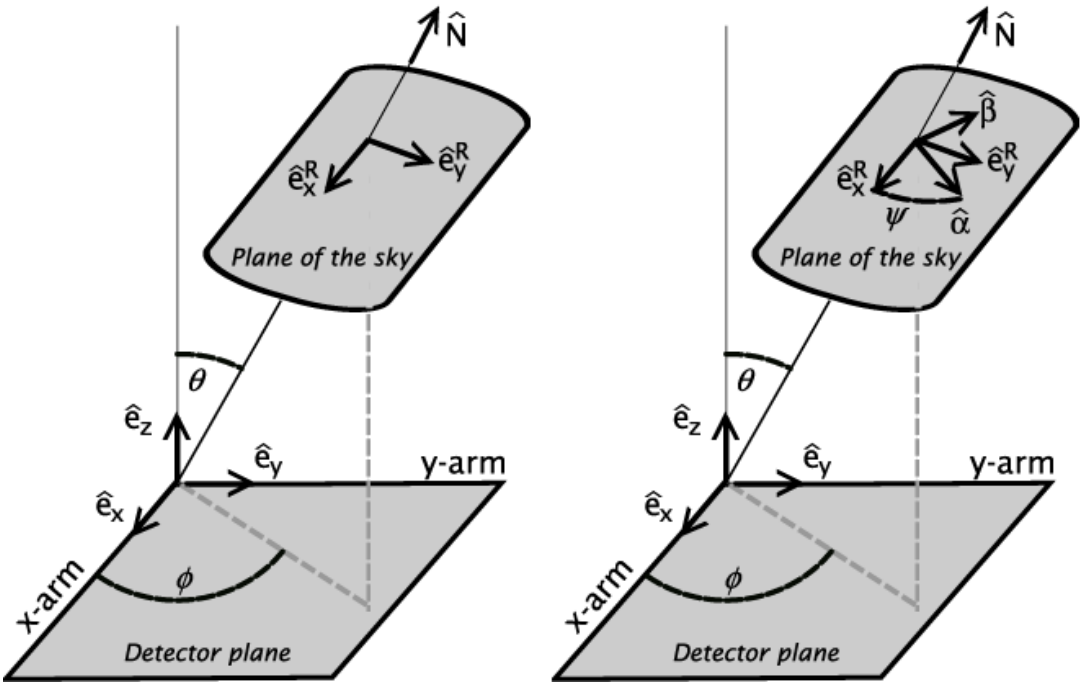

Figure 1.4: **Left** The relative orientation of the sky and detector frames **Right** The effect of a rotation by the angle ψ in the sky frame [99]

1.3 Network of Gravitational Wave Detectors

1.3.1 First Generation of Ground Based Interferometers

Over the last 2 decades a worldwide network of detectors has been established. This network is necessary due to the fact that laser interferometers have a poor directional sensitivity as they only measure a projection of the wave passing through the detector. A network of detectors can then be used to locate the source's sky position by triangulation as well as increasing the potential signal-to-noise ratio.

Detectors of different size and sensitivity are spread all over the world. The largest current detectors are the LIGO detectors in Livingston, Louisiana and Hanford, Washington in the United States of America. Both of these sites house GW detectors with 4km arms with Hanford also having a second detector with 2km arms [92]. In Cascina, Italy, there is the French Italian detector called Virgo which has arm length of 3km [52]. There is also the 600m arm length GEO detector in Ruthe, Germany [29], see Figure 1.5.

The LIGO Scientific Collaboration (LSC), which consists of members from around

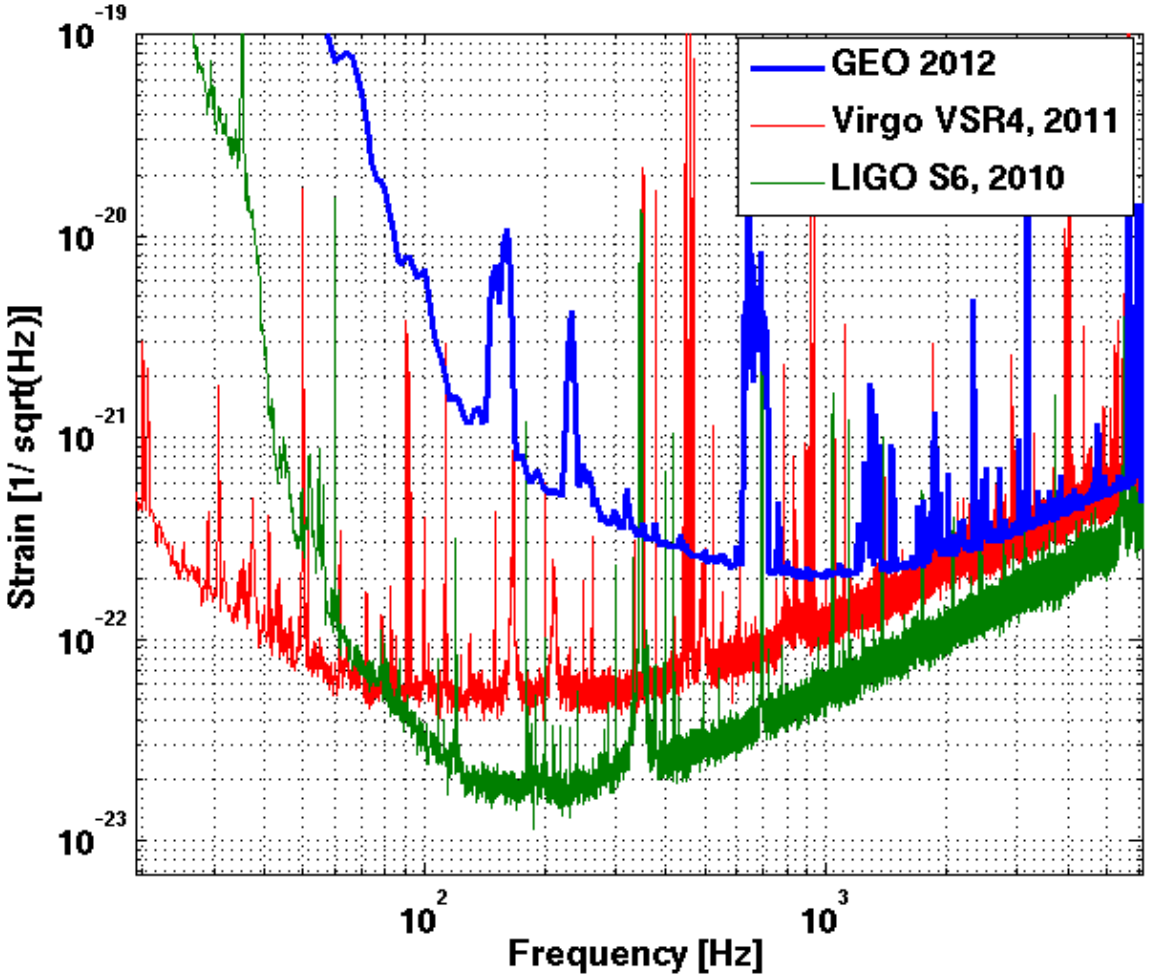

Figure 1.5: The noise spectral density as a function of frequency for the LIGO, Virgo and GEO600 detectors [51].

the world and coordinates operation of both the LIGO detectors as well as GEO600, measured science quality data from 2002 until 2007 through a series of Science Runs. Throughout this period the Virgo and GEO600 detectors also conducted Science Runs. Figure 1.5 shows the noise amplitude spectral density of these detectors i.e the frequency band and strain that the detectors were sensitive. A discusion of the noise and its sources can be found in Section 1.4. No detection of GWs were made and the LIGO and Virgo detectors were taken offline to undergo an upgrade to the Advanced detectors.

1.3.2 Second Generation of Ground Based Interferometers

In the coming years both LIGO and Virgo will be upgraded to the so called 2nd generation detectors, Advanced LIGO [121] and Advanced Virgo [30], which will both use existing sites and infrastructure. They will both have many improvements over their predecessors such as implementing higher laser power, new optics, monolithic suspensions and improved seismic isolation. There is a plan to move the second interferometer from Hanford to India which will greatly improve source localisation [118].It is expected that a five detector network comprising of the interferometers at Livingston (L) and Hanford (H), Virgo (V), the Indian detector known as LIGO India [118], as well as a Japanese detector known as KAGRA which is currently under construction in the Kamioka mine in Japan which will have 3km arm length [11], will reach full sensitivity over the next decade, (see Figure 1.6).

For Advanced LIGO there will be an increase of sensitivity of a factor of 10 which will increase the the number of GW emitting sources by a factor of a 1000. This is due to the fact that the distance to which a detection can be made will increase in every direction and will enable the study of a significant number of astrophysical sources.

1.3.3 Third Generation of Ground Based Interferometers

Looking further into the future there is a proposal to build a 3rd generation detector called the Einstein Telescope (ET) somewhere in Europe [42]. ET is expected to be composed of three 10km arm length detectors arranged in a triangle formation in three underground tunnels. The idea is that it will utilise new technologies to improve sensitivity, such as cryogenics, to reduce thermal noise.

This would greatly improve upon the sensitivity of the Advanced detectors, by approximately a factor of 10 as well as expanding the frequency band. This means that ET will be first detector expected to allow astrophysicists to begin regular gravitational wave astronomy [98].

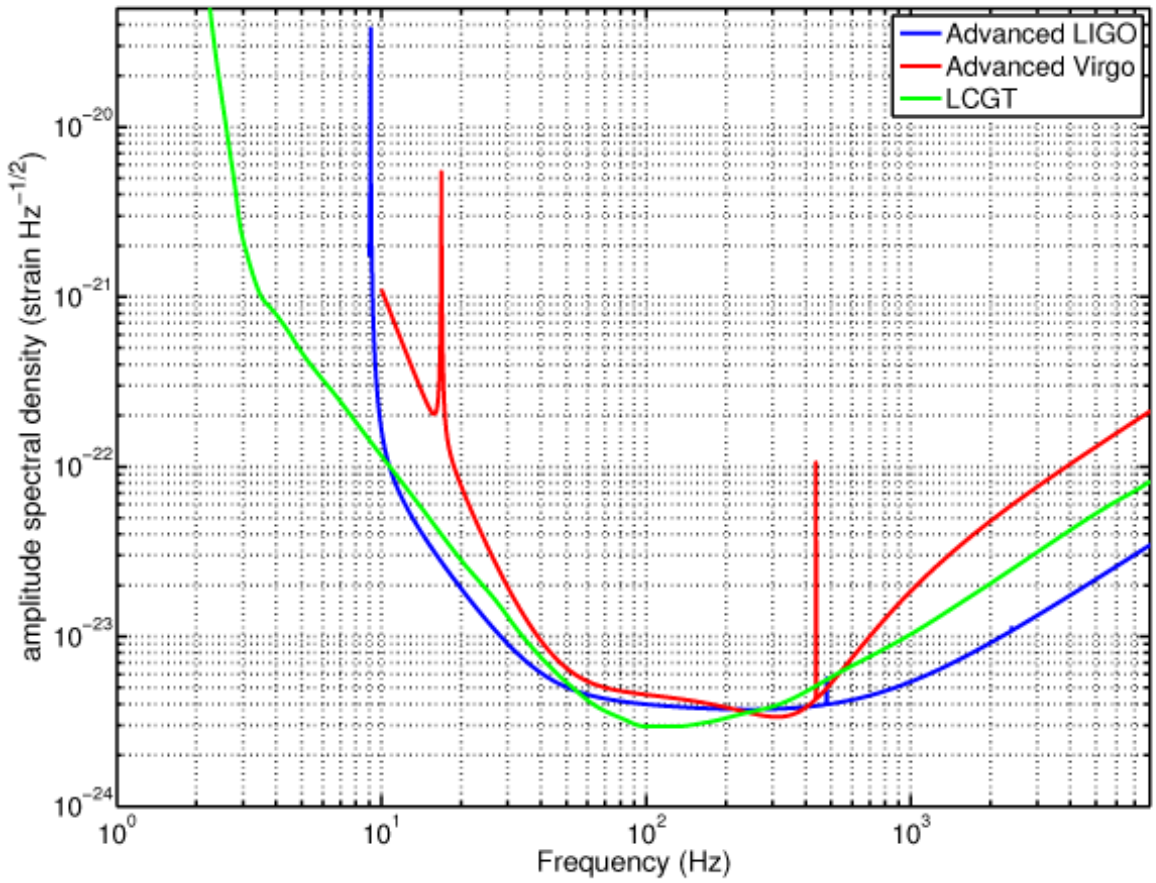

Figure 1.6: The amplitude noise spectral density as a function of frequency for the Advanced LIGO, Advanced Virgo and KAGRA (labelled as LGCT) detectors [99].

1.3.4 Future Space Based Detectors

One of the limitations of ground based interferometers is that of seismic and gravity gradient noise, (Section 1.4). The only way to avoid these sources of noise is to build space-based interferometers. This would allow signals at low frequencies to be detected. The latest design for such a detector is eLISA, the Evolved Laser Interferometer Space Antenna.

The detector will consist of two interferometer arms with three spacecraft in a triangular formation with arm lengths of 10^6 km [6]. The aim is to put the arrangement of spacecraft in a solar orbit at the the same distance from the Sun as the Earth. It would trail Earth's orbit by 20 degrees. The test masses which reflect the laser light are designed so that the spacecraft floats around the mass using extremely precise thrusters to ensure the mass can float freely in space. eLISA will have a frequency bandwidth of 0.1 mHz to 1 Hz and is expected to detect GWs from sources such as the merging of super-massive black holes and possible stochastic signals from the early universe [43], (see Section 1.6).

1.4 Noise Sources for Ground Based Interferometers

The typical bandwidth of ground based interferometric detectors range from 40 Hz to 6 kHz. Across this detection bandwidth the spectrum of the noise is not flat but shows three distinct regions, (see Figure 1.7 for the noise curves for Advanced LIGO). At lower frequencies (<50Hz), the dominant noise source comes from Seismic noise, represented by the brown curve in Figure 1.7, due to motion on the surface of the Earth as well as fluctuations underground. In the range of around 50 - 150 Hz thermal noise, represented by the blue curve in Figure 1.7, due to Brownian motion in the optics and suspensions dominates. At frequencies above 150 Hz the shot noise is the dominant cause of noise, represented by the purple curve in Figure 1.7.

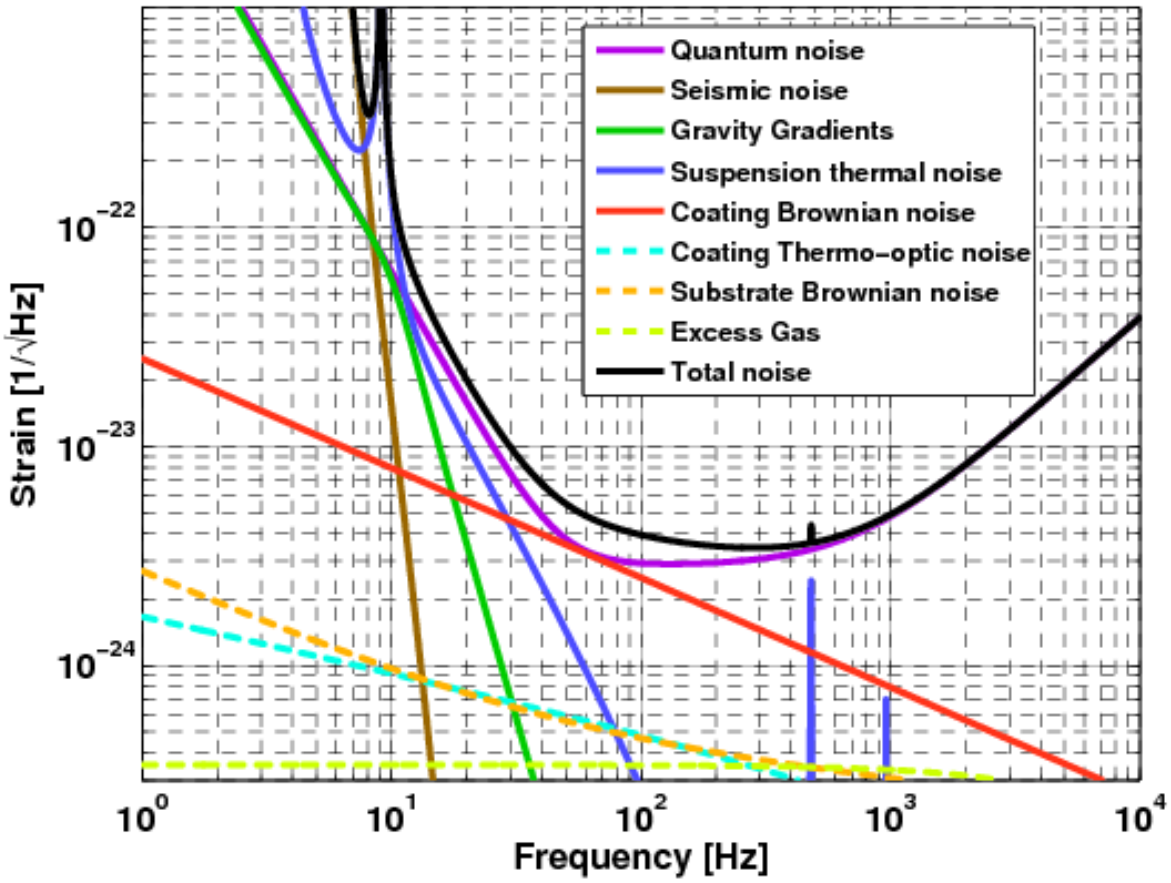

Figure 1.7: Plot of amplitude spectral density contributions representing each source of noise [57]. These contributions can be combined to calculate the total noise shown in the black curve.

1.4.1 Seismic Noise

Vibrations in the ground can come from seismic activity, man made objects such as trains or cars and the waves crashing into the continents. This will limit the sensitivity of interferometers at lower frequencies. A system of complicated isolation systems are used to suspend the main optics within the interferometer in an attempt to reduce the effects of seismic noise. Multi-stage pendulums, which are good filters for reducing motion above their natural frequency, are used and are located on isolation platforms [90]. Technologies such as Hydraulic External Pre-Isolators are now being employed in Advanced LIGO to further improve sensitivity at small frequencies [95].

1.4.2 Thermal Noise

In the interferometers most sensitive region, that of a few hundred Hz, vibrations of the optics or suspensions due to Brownian motion is the dominant source of noise. To reduce this noise the resonant frequency of the suspensions systems and optics are made to be far away from the frequencies of interest, on the order of a few Hz for the suspensions and several kHz for the optics. By using material with a high quality factor the noise can be reduced by confining it to a narrow bandwidth around the resonant frequency. This allows interferometers to operate at room temperature however thermal noise could also be reduced by employing cryogenic cooling which will be employed by the Japanese KAGRA detector [110].

1.4.3 Shot Noise

Above a few hundred Hz the noise caused by the random arrival time of the photons within the laser beam, which causes fluctuations in the intensity of the light detected, will dominate. Using a higher power laser which increases the number of photons would help reduce this source of noise. Shot noise can also be reduced by using power recycling techniques which increase the amount of power within the interferometer [9]. Advanced LIGO will employ a laser which is more powerful than that used in initial LIGO as well as installing a signal recycling mirror which will aid in reducing shot noise.

1.4.4 Radiation Pressure Noise

Increasing the power of the laser causes the momentum transferred to the mirrors, as photons are reflected by them, to increase. Therefore there must be a trade-off between this radiation pressure noise and shot noise. To do this the quadrature sum of the two is minimised which occurs when the two noise sources are of equal amplitude at some target frequency [44].

1.4.5 Gravity Gradient Noise

This is a form of noise is caused by the direct gravitational coupling of mass density fluctuations as well as noise from changes in air pressure [89]. This form of noise will limit the sensitivity of the Advanced detectors with a frequency limit of around 1 Hz and below. A possible option to eliminate this effect is to put detectors in space such as the proposed eLISA mission (Section 1.3.4). However, there are two solutions which reduce this effect on Earth. One is to build the detector underground where most of the gravitational field effects will be reduced as they mostly occur at the surface [14]. The Japanese KAGRA detector is currently being built in the Kamioka mine and this technique has also been proposed for the Einstein telescope. Another solution is to build seismometers and place them around the detector. By calculating the effect of motion it can be subtracted from the detector output [89].

1.5 Multi-messenger approach to detection

A network of GW detectors will greatly improve our understanding of many astrophysical phenomenon but there are many sources that will emit electromagnetic or neutrino signals as well. Thus the detection of a GW will complement and add to the data accumulated from a source.

In the case of a coalescing black hole binary, perturbations of huge magnetic fields could emit EM radiation. What is expected to be far more common is a variety of EM radiation such as radio and gamma rays being emitted from neutron star binaries, magnetars or core-collapse supernovae, see Section 1.6.

As discussed, GWs are difficult to detect and any correlation in direction with neutrino or EM telescopes would therefore greatly improve inferences of the source's sky position and possibly its host galaxy [45]. The reverse could also occur: if the triangulation of the source's position could be inferred accurately from the GW signal, optical telescopes could then be pointed in that direction and much more information about the source could be found. Similarly the light from a supernova or a gamma ray burst (GRB) could indicate the time of the event drastically reducing the amount of data needed to be searched over from the GW detectors.

The multimessenger approach will not just help in determining the time or arrival and sky position of the signal but will also complement the different types of physics that can be learned. For example, any GW detected will not be blocked by interstellar dust or any other light from the event thus allowing a direct probe of the internal physics of a system. This would greatly improve the understanding of events such as core collapse supernova and the mechanism behind the event, (see Section 1.6.4).

1.6 Sources of Gravitational Waves

GWs are caused by the acceleration of masses and ground based detectors are well suited to detect four different types of GWs: continuous wave, compact binary coalescence (CBC), stochastic and burst. These can be roughly separated into two categories. Burst and CBC signals are short duration signals of around a second for the first generation of detectors. In the case of second generation detectors, CBC signal may be a few minutes in length. The second category consists of continuous wave and stochastic signals which are long term signals. These different types of signal will be discussed in more detail in the following sections.

1.6.1 Continuous Emission

Sources of continuous emission come from Neutron Stars which are the products of a core collapse supernova, (see Section 1.6.4), and typically have a mass of around $1.4M_{\odot}$ and a radius of 10 km. Because of this they have an extremely high density

and a very high rotation speed due to the conservation of angular momentum with periods of a few seconds right up to a few milliseconds. Due to the conservation of magnetic flux they have very strong magnetic fields ranging from 10^4 T for recycled millisecond pulsars to 10^11 T for magnetars. To emit a GW signal a Neutron Star must be deformed or aspherical. These deformities could be due to precession, different vibrational modes such as fundamental modes excited by glitches, nuclear explosions which would lead to a short burst emission or by non-uniform heating of the crust through accretion in low-mass x-ray binary systems causing non-axisymmetric density perturbations. Continuous emission could be caused if the source is triaxial meaning they have bumps or mountains on the surface caused during its formation or by magnetic fields. If these triaxial neutron stars are detected via GW emission they could help determine the equation of state and the number of galactic millisecond pulsars that currently cannot be seen. Vibrational modes could also help constrain the equation of state and explain glitch mechanisms and the energetics during a soft gamma ray repeater and an anomalous X-ray pulsar flare [40, 39].

1.6.2 Stochastic

Stochastic GWs can be split into two possible sources. The first type of signal is thought to be from the early moments of the Universe, like the Cosmic Microwave Background Radiation in the electromagnetic spectrum. It is a flux of gravitons left over from when the Universe became optically thin to gravitons, just before Big Bang Nucleosynthesis occurred. It would show up as a flat spectrum and offer observations of the earliest possible moments in our Universe [94].

The second type of signal comprises a large number of weak, discrete GW signals which are too small and too numerous to be separately detected by ground based detectors. These signals could come from white dwarf binary systems or from extra-galactic black hole binary systems.

These signals are extremely difficult to detect by ground based detectors but future interferometers such the eLISA may have success in finding stochastic GWs [3]. This would allow a new field of study into the background of local sources as well as the early time cosmology of the Universe.

1.6.3 Compact Binary Coalescence

Compact Binary Coalescences occur in binary systems that contain two neutron stars or theoretically a neutron star and a black hole or two black holes [37]. Black Holes are the final stage of massive stars which have collapsed to the point that they form a singularity. They are so dense that even light cannot escape their gravitational field and can come in many different sizes. The smallest are as much as 100 times the mass of the Sun and occur either by themselves or in a binary system. Intermediate mass black holes [38] are still to be confirmed but are predicted to have masses ranging from $100 - 1000s\ M_{\odot}$ and could be the cause of Ultra-luminous X-ray sources in other galaxies. They are thought to be caused by mergers with other black holes and so they could be sources of GWs during these mergers although it is still not known what the best approach is to model these collisions. The most massive black holes are Super Massive Black Holes which exist at the centre of galaxies. They can have masses greater than $10^4\ M_{\odot}$ and are expected to be strong emitters of gravitational waves during galaxy mergers [103].

Many double neutron star systems are known to have a decay in their orbit which agrees with what would be seen in gravitational wave emission [125]. As their orbits decay they will eventually coalesce in a process composed of three stages; the inspiral, merger and ringdown phases which can all be modelled, albeit with many approximations. In particular the inspiral phase could be useful in cosmology as they can be used as "standard sirens". The amplitude of the wave only depends on its distance and the chirp mass,

$$M_{\text{chirp}} = \frac{(m_1 m_2)^{\frac{3}{2}}}{M^{\frac{1}{5}}} \tag{1.8}$$

where M is the sum of their masses. If there is an EM observation made the system's redshift can also be measured and these two values can be used to constrain cosmic acceleration much more accurately than other methods [59].

1.6.4 Bursts-Supernovae

One source of burst emission (non-repeating events that occur in the order of milliseconds) are supernovae. These are enormous stellar explosions which can briefly

outshine an entire galaxy which happen when a star is no longer able to support itself gravitationally and so undergoes a violent collapse. Supernovae are classified into different groups depending on the spectral lines found in their light curves. Type I show no hydrogen lines but do have helium or silicon lines and are caused by the collapse of a White Dwarf which undergoes a thermonuclear explosion after accreting mass from a star in orbit with it. This causes a mostly spherically symmetrical explosion and so will not emit gravitational waves, however they are very useful for use as standard candles in the cosmological distance ladder. Type II show hydrogen absorption lines and occur when a massive star is no longer able to support itself through nuclear fusion and undergoes a core collapse into either a neutron star or a black hole depending on its mass and are predicted to be good sources for gravitational waves [109]. They occur at a rate of about 0.1 to 0.01 per year for a Milky Way equivalent galaxy. This may seem like a very small number but due to the vast number of galaxies there are many of these every year, for example there are about 30 per year in the Virgo cluster.

The processes that occur during a supernova are described through the use of many complex theories including General Relativity, Magnetohydrodynamics (MHD) and nuclear physics. The first step is the core collapse of the iron core to form a protoneutron star followed by a supersonic infall of material onto the core. This material will then bounce off the core but does not have enough energy to escape its gravity and there are different theories as to what gives the material the extra boost it needs including neutrinos re-energising the material. All of these processes will show up in the gravitational waveform but different mechanisms will give a range of amplitudes for different stages of the supernova as well as having a different shape depending on the physical processes happening during the collapse, thus the chances of detection vary depending on the mechanism being used. The analysis of GWs along with neutrinos will enable us to discover what is happening in the core collapse and so if they are detected it could allow us to explain each stage of a supernova for the first time.

1.7 Gravitational Waves from Supernovae

1.7.1 Neutrino Mechanism

The gravitational collapse of the iron core and the subsequent evolution of the nascent hot puffed-up protoneutron star to a cold compact neutron star releases of order 300 B (1 B = 10^{51} erg) of energy, ∼99% of which is emitted in the form of neutrinos of all flavors [15]. If only a small fraction of the energy released in neutrinos is re-absorbed behind the stalled shock, leading to net heating, an explosion could be launched and endowed with the energy to account for the observed range of asymptotic explosion energies of 0.1-1 B of a typical core-collapse supernovae [53]. This is the main theory behind the neutrino mechanism of core-collapse supernovae, which, in its early form was proposed by Arnett [10] and Colgate & White [28], and in its modern form by Bethe & Wilson [16].

While this mechanism appears relatively simple, the neutrino mechanism, in its purest, spherically-symmetric (1D) form, fails to revive the shock in simulations for all but the lowest-mass massive stars with O-Ne cores [69, 93, 115, 61]. There is now strong evidence from axisymmetric (2D) [19, 74, 76, 111, 132, 86, 78] and first 3D [50, 80, 66, 77, 63, 60, 113, 54] simulations that the breaking of spherical symmetry is key to the success of the neutrino mechanism. In 2D and 3D, neutrino-driven convection in the region of net heating behind the shock, and the standing-accretion-shock instability (SASI) [18, 46, 47, 100] increase the efficiency of the neutrino mechanism [78, 80, 66, 113].

Apart from rapid rotation, the dominant multi-dimensional GW-emitting dynamics in neutrino-driven core-collapse supernovae are convection in the protoneutron star (e.g., [71, 75]) and SASI-modulated convection in the region behind the stalled shock. GW emission from convection and SASI has been extensively studied in simulations in 2D [71, 64, 75, 79, 132] and to some extent in 3D [49, 77, 62, 63]. The top panel in Fig. 1.8 shows a typical example waveform drawn from the catalogue of Murphy *et al.* [79]. Right after core bounce, an initial burst of GWs is emitted by strong, so-called prompt convection [84], driven by the negative entropy gradient left behind by the stalling shock. Subsequently, the GW signal settles at lower amplitudes, then picks up again as the SASI reaches its non-linear phase and high-velocity accretion downstreams penetrate deep into the region behind the

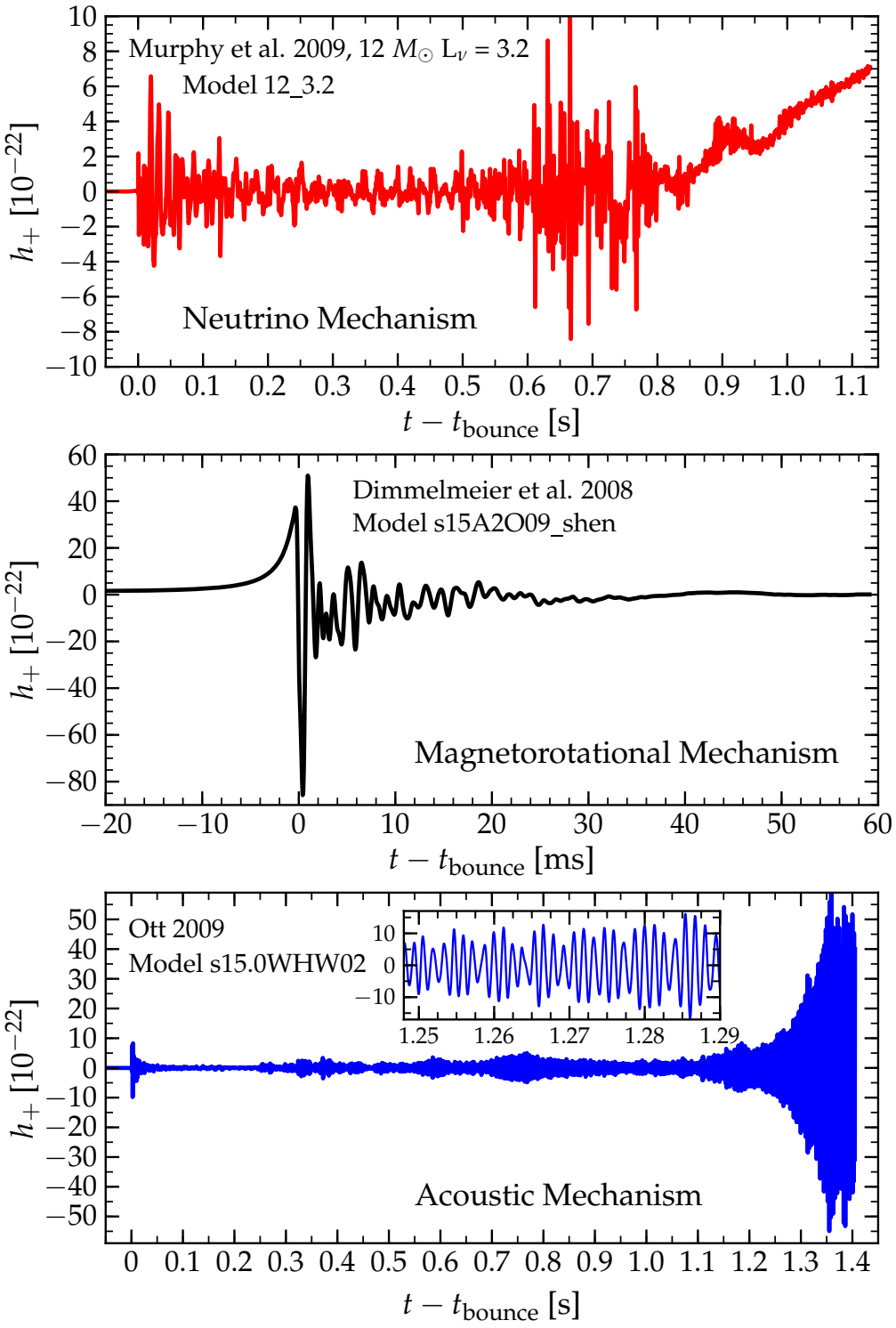

Figure 1.8: Linearly polarized GW signal predictions for a core collapse event located at 10 kpc from matter dynamics in axisymmetric simulations that can be associated with the neutrino mechanism (top panel, taken from [79]), the magnetorotational mechanism (center panel, taken from [34]), and the acoustic mechanism (bottom panel, taken from [84]). Note the varying ranges of the time and strain axes. Also note that the simulations of [34] did not include magnetic fields, since the GW signal from core bounce in magnetorotational explosions is due to rapid rotation and not influenced by magnetic fields. This, however, did not allow them to capture the expected secular rise of the waveform expected to occur once an explosion sets in [112]. See text for further discussion.

shock, where they are decelerated, leading to pronounced spikes in the wave signal [79]. The secular rise in the signal amplitude towards the end of the waveform is due to the onset of an aspherical explosion [79, 132, 77], but occurs at too low characteristic frequencies to be visible to Advanced LIGO-class detectors.

Overall, the detectable GW signal from a neutrino-driven nonrotating or slowly rotating core-collapse supernova will have random polarization, a broadband spectrum from $\sim$100$-$1000 Hz and typical strain amplitudes $|h|$ of order $10^{-22}\,(D/10\,\mathrm{kpc})^{-1}$, with individual peaks reaching $10^{-21}\,(D/10\,\mathrm{kpc})^{-1}$ [84, 77]. The typical duration of emission is the time from core bounce to the launch of the explosion, $0.3-1\,\mathrm{s}$, but convection inside the cooling protoneutron star can continue to emit GWs at lower amplitudes and higher frequencies for many seconds afterwards [71, 84]. Typical total emitted GW energies are in the range $10^{-11}-10^{-9}\,M_\odot\,c^2$ [84, 79, 132].

The effects of rotation on the neutrino mechanism and its GW signature are not yet fully understood (see, e.g., [48, 111, 74, 76, 86, 120, 83]) and it cannot be excluded that contributions from rotational dynamics may modify the GW signal of neutrino-driven core-collapse supernovae. However, results from the systematic rotating core collapse studies of [34, 120, 20, 112] suggest that once rotation rates become sufficiently high to alter the dynamics, the explosion is actually more likely to occur via the magnetorotational mechanism discussed in §1.7.2. This, however, is under the provision that the magnetorotational instability (e.g., [13, 82]) works robustly and builds up the required strong magnetic fields to drive an explosion. Therefore, for the purpose of this thesis, the assumption is made that the GW signature of neutrino-driven core-collapse supernovae is unaffected by rotational effects.

GW Signal Catalogues

In this study, the catalogue of Murphy *et al.* [79] is used. The Murphy *et al.* catalogue (in the following, these waveforms from this catalogue are labelled as `Mur` waveforms) encompasses 16 waveforms that were extracted via the quadrupole formula (e.g., [116]) from Newtonian axisymmetric core collapse simulations that used a parameterized scheme for electron capture and neutrino heating/cooling and included only the monopole component of the gravitational potential as described in [78, 79]. The Murphy et al. simulations are nonrotating and the parameter space

covered is spanned by progenitor ZAMS (zero age main sequence) mass ({12, 15, 20, and 40} $M_\odot$) and by the total electron and anti-electron neutrino luminosity.

Yakunin *et al.* [132] performed self-consistent axisymmetric Newtonian (with an approximate-GR monopole term of the gravitational potential [73]) radiation-hydrodynamics simulations of neutrino-driven core-collapse supernovae. They provide three waveforms at [25], obtained from simulations using progenitors of (12, 15, and 25) $M_\odot$. The Yakunin waveforms (denoted, in the following, as `Yak` waveforms) are used to test the robustness of the supernova mechanism determination algorithm which is the focus of this thesis.

Due to the limitations of the provided catalogues, only linearly polarized signals are considered. Gravitational waveforms with + and × polarizations from 3D simulations of neutrino-driven core-collapse supernovae [62, 63, 77] will not be considered in this thesis.

1.7.2 Magnetorotational Mechanism

The conservation of angular momentum in core collapse to a protoneutron star leads to a spin-up by a factor of ∼1000 [87]. Starting from a precollapse angular velocity distribution that may be expected to be more or less uniform in the inner core (e.g., [55]), homologous collapse preserves the uniform rotation of the inner core while the supersonic collapse of the outer core leads to strong differential rotation in the outer protoneutron star and in the region between protoneutron star and shock [87].

A rapidly spinning precollapse core with a period of order 1 s results in a ms-period protoneutron star, with a rotational energy of order 10 B, which is about ten times greater than the typical core-collapse supernova explosion energy. If only a fraction of this energy was tapped, a strong explosion could be triggered.

Theory and simulations (e.g., [128, 17, 65, 81, 104, 20, 32, 26, 112]) have shown that magnetorotational processes are efficient at extracting spin energy and can drive collimated outflows, leading to energetic bipolar jet-like explosions. Recent work [104, 20, 32, 26, 112] suggests that magnetic fields of the order of 10^{15} G with strong toroidal components are required to yield the necessary magnetic stresses to drive a strong bipolar explosion. If 10^{15} G fields were to arise from flux compression

in collapse alone, precollapse core fields would have to be of order 10^{12} G [20, 104], which is about 3 orders of magnitude larger than predicted by stellar evolution models (e.g., [55, 131]). It is more likely that the most significant amplification occurs after core bounce via rotational winding of poloidal into toroidal field (a linear process), the non-linear magnetorotational instability (MRI, which is not yet fully understood in the core collapse context [13, 82]). Both processes operate on the free energy stored in differential rotation, which is abundant in the outer core.

For the magnetorotational mechanism to work, precollapse spin periods $\lesssim 4-5$ s appear to be required [20]. Such rapid rotation leads to a strongly centrifugally-deformed inner core with a large quadrupole moment ($\ell = 2$; due to its oblateness), which rapidly changes during core bounce, leading to a strong burst of GWs. The GW signal from rotating collapse and bounce has been studied extensively and the most recent general-relativistic simulations have shown it to be of rather generic morphology with a single strong peak at bounce and a subsequent ringdown as the protoneutron star core settles into its new equilibrium [33, 34, 88]. A typical example GW signal taken from the catalogue of Dimmelmeier *et al.* [34, 24] is shown in the center panel of Fig. 1.8. The core collapse and bounce phase proceeds essentially axisymmetrically even in very rapidly spinning cores [88, 101, 102] and its GW signal is linearly polarized with vanishing amplitude seen by an observer located along the symmetry axis and maximum amplitude for an equatorial observer. Typical emission durations for the linearly polarized GWs from core bounce are of order 10 ms and peak GW amplitudes for rapidly spinning cores that may lead to magnetorotational explosions are of order $10^{-21} - 10^{-20}$ at 10 kpc with most of the energy being emitted around $500 - 800$ Hz in cores that reach nuclear density and bounce due to the stiffening of the nuclear equation of state. Cores with initial spin periods shorter than $\sim 0.5 - 1$ s experience a slow bounce at sub-nuclear densities strongly influenced or dominated by the centrifugal force. They emit most of the GW energy at frequencies below ~ 200 Hz [34, 84]. Typical emitted GW energies are in the range $10^{-10} - 10^{-8}\, M_\odot\, c^2$. The GW signal from rotating collapse and core bounce is unlikely to be affected by MHD effects, since the build up to dynamically relevant field strengths occurs only after bounce [65, 81, 112, 20].

Due to the strong rotational deformation of the protoneutron star, neutrinos decouple from the matter at smaller radii and hotter temperatures in polar regions than near the equator. This leads to the emission of a larger neutrino flux with a harder neutrino spectrum in polar regions (e.g., [86]). This globally asymmetric

neutrino emission results in a secularly rising low-frequency GW signal [84]. Similar low-frequency contributions will come from the bipolar outflow characteristic for a magnetorotational explosion and from magnetic stresses [65, 81, 112]. The low-frequency waveform components are not shown in the center panel of Fig. 1.8 and are not detectable by the upcoming second-generation earthbound GW observatories.

GW Signal Catalogs

The large (128 waveforms) GW signal catalogue of Dimmelmeier *et al.* [34, 24] (`Dim` in the following) is employed in this thesis. Dimmelmeier *et al.* performed 2D general relativity simulations of rotating iron core collapse for (11.2, 15, 20, and 40) $M_\odot$ progenitors and two different nuclear EOS, varying initial rotation rate and degree of differential rotation. They approximated the effects of electron capture during collapse by parametrizing the electron fraction Y_e as a function of density, which yields inner core sizes that are very close to those obtained with full neutrino transport [68]. The inner core size determines the amount of mass and angular momentum that can be dynamically relevant during core bounce and, hence, is a determining factor in the GW signal [33]. The `Dim` catalogue was also used by the previous parameter estimation work of Röver *et al.* [97]. For testing, the three additional `Dim` waveforms computed for [97] are used that are not part of the original `Dim` catalogue and were used to test their algorithm. This set of extra waveforms is labelled as `DimExtra`.

For studying the robustness of the mechanism-determination approach, gravitational waveforms of rotating models are drawn from the catalogue of Scheidegger *et al.* [102, 23], (`Sch` in the following) who performed 3D Newtonian-MHD rotating iron core collapse calculations with a spherical approximate-GR gravitational potential and employed the same EOS and electron capture treatment as Dimmelmeier *et al.* [34], but used different progenitor models.

Furthermore, the GW signal catalogue of Abdikamalov *et al.* [1] is used (`Abd` in the following) who used the same numerical code as Dimmelmeier *et al.* [34], but studied the rapidly spinning accretion-induced collapse (AIC) of massive white dwarfs to neutron stars. This process yields a GW signal very similar to rotating iron core collapse and explosions in AIC may occur also via the magnetorotational mechanisms [31]. This catalogue of 106 waveforms is included to see if the algorithm

described in Chapter 3 can differentiate between rotating iron core collapse and rotating AIC assuming the `Dim` and `Abd` catalogues correctly predict the respective GW signals.

1.7.3 Acoustic Mechanism

The core-collapse supernova evolution in the *acoustic mechanism* proposed by Burrows *et al.* [21, 22, 85] is initially identical to the one expected for the neutrino mechanism. Neutrino heating, convection and the SASI set the stage, but no explosion is triggered for $\gtrsim$500 ms after bounce. At this point, the SASI is in its highly non-linear phase and modulates high-velocity accretion downflows that impact on the protoneutron star and excite core pulsations (primarily $\ell = \{1, 2\}$ g-modes). Over hundreds of milliseconds, these pulsations reach large amplitudes and damp via the emission of strong sound waves. Traveling down the steep density gradient in the region behind the shock, the sound waves frequenices steepen to shocks and dissipate their energy behind and in the shock. This mechanism is robust in the simulations by Burrows *et al.* [21, 22, 85], but requires $\gtrsim$1 s to develop, thus leads to massive NSs, and tends to yield explosion energies on the lower side of what is observed.

The GW signature of the acoustic mechanism is dominated by the strong emission from the quadrupole components of the protoneutron star core pulsations that are quasi-periodic (their frequency shifts secularly along with the changing protoneutron star structure) and become very strong $\gtrsim 800 - 1000$ ms after core bounce [85, 84]. The lower panel of Fig. 1.8 depicts a typical example waveform from Ott *et al.* [84, 85], who studied the GW signature of the acoustic mechanism based on the simulations of Burrows *et al.* [21, 22]. At early times, the GW signal is essentially the same as expected for the neutrino mechanism, but once the protoneutron star core pulsations grow strong, they are hard to miss. The simulations of Burrows *et al.* [21, 22, 85] were axisymmetric and the resulting GW signals are linearly polarized, though in 3D, one would expect oscillation power also in non-axisymmetric components. Typical maximum strain amplitudes are of order few $\times 10^{-21} - 10^{-20}$ and multiple modes with frequencies between $\sim 600 - 1000$ Hz contribute to the emission. Since the pulsations last for many cycles, the emitted GW energies may be large and are predicted to be of order $10^{-8} - 10^{-7} M_\odot c^2$ and extreme models reach few $\times 10^{-5} M_\odot c^2$ [85, 84].

There are multiple caveats associated with the acoustic mechanism that must be mentioned. Most importantly, the acoustic mechanism has been found in simulations of only one group with a single simulation code, but others have not yet ruled out the possibility of strong protoneutron star pulsations at late times (e.g., [74]). In a non-linear perturbation study, Weinberg & Quataert [123] found that the protoneutron star pulsation amplitudes may be limited by a parametric instability involving high-order modes that damp efficiently via neutrino emission and are not presently resolved in numerical simulations. This would limit the protoneutron star pulsations to dynamically insignificant amplitudes. Moreover, the simulations of Burrows *et al.* were axisymmetric and nonrotating or only very slowly rotating. It is not clear to what amplitudes individual protoneutron star pulsation modes would grow in 3D. Rapid rotation, due to its stabilizing effect on convection and SASI [86, 83], may likely inhibit the growth of pulsations. Both 3D and rotational effects remain to be explored.

GW Signal Catalogs

A set of 7 waveforms from the models of [22] analyzed by Ott [84] are employed here. This catalogue is referred to as the `Ott` catalogue in the following Chapters. All waveforms were computed on the basis of the Burrows *et al.* [21, 22, 85] simulations and differ only in the employed progenitor model, covering a range in ZAMS mass from 11.2 to 25 $M_{\odot}$.

Three additional waveforms of an earlier study of Ott *et al.* [85] are used. This small set is labelled as `OttExtra` and is used for testing the capability of correctly identifying them as coming from stars exploding via the acoustic mechanism.

Chapter 2

Bayesian Inference Techniques

As discussed in Sections 1.6.4 and 1.7 there is no agreed upon mechanism which drives a supernova and there are many theories of the physical processes behind the supernova mechanism. GWs, along with neutrinos, provide an opportunity to see through to the core of a collapsing star. Thus if a gravitational wave from a core collapse supernova is detected it could provide information as to which supernova mechanism is reenergising the supernova. The challenge is to design an algorithm that will analyse a detected GW and identify the mechanism responsible for the observed GW. Achieving this would immediately provide inference on the physics behind a core collapse supernova, which would be a great advancement in the understanding of one the most important processes in the universe.

To achieve this goal the technique of Bayesian model selection is employed as a method for comparing data with a choice of different models. This chapter introduces Bayesian Inference in Section 2.1 and follows with an explanation of the different analysis techniques to perform bayesian model selection and infer the physics behind a core collapse supernova.

2.1 Bayesian Inference

Bayesian Inference [106] has been widely used throughout the astrophysics community and has become a powerful tool used to analyse data. The most powerful

and useful derivation from Bayesian Inference is Bayes' Theorem. Bayes' Theorem provides a learning process in which the probability of each hypothesis is considered and adjusted according to any new data that is acquired. It can be thought of as relating the probability that a hypothesis is true to the more useful probability that the measured data has been observed given that the hypothesis is true and I represents all the information, or

$$prob(hypothesis|data, I) \propto prob(data|hypothesis, I) \times prob(hypothesis|I). \quad (2.1)$$

The terms in Bayes' Theorem have been given names which reflect their purpose. The term $prob(hypothesis|I) = p(H|I)$ is called the prior probability and relates the state of knowledge about the truth of the hypothesis before any data has been analysed. The prior can then be modified by the experimental measurements through the likelihood function, $prob(data|hypothesis, I) = p(D|H, I)$. This then yields the posterior probability, $prob(hypothesis|data, I) = p(H|D, I)$ which represents the state of knowledge about the truth of the hypothesis considering the data. There is an extra term, $p(D|I) = prob(data|I)$ which has been omitted due to the use of a proportionality and in most cases of parameter estimation this is treated as a normalisation term. However when considering model selection this term becomes extremely important. To reflect this importance it is given the name evidence. Thus Bayes' Theorem can be written as,

$$p(H|D, I) = \frac{p(H|I)p(D|H, I)}{p(D|I)}, \quad (2.2)$$

given a set of data, D.

When considering all hypotheses the sum of all the posterior probabilities must equal to one i.e. $\int_\theta p(\theta|D, H, I)d\theta = 1$. Thus by rearranging Bayes' Theorem the evidence, Z, can be obtained by,

$$Z = p(D|H) = \int_\theta p(\theta)p(D|\theta, H)\, d\theta, \quad (2.3)$$

where θ represents the hypothesis parameters. This integral often cannot be solved analytically and is, instead, evaluated using numerical methods such as the nested sampling algorithm, (see Section 2.2).

As is often the case with any experimental result, there may be multiple hypotheses that can describe the data and there is a question which hypothesis, or model, best fits the measured data. The ratio of the posterior probabilities is used to compare two models, i.e. $H = M_i$ or M_j. This is known as an Odds Ratio,

$$O_{ij} = \frac{p(M_i|D,I)}{p(M_j|D,I)} = \frac{p(M_i|I)}{p(M_j|I)} \frac{p(D|M_i,I)}{p(D|M_j,I)}. \tag{2.4}$$

If neither model prior is preferred over the other, the prior ratio is set to unity and the Odds Ratio reduces to the ratio of the likelihoods,

$$O_{ij} = B_{ij} = \frac{p(D|M_i,I)}{p(D|M_j,I)}, \tag{2.5}$$

where B_{ij} is known as the Bayes Factor. By marginalising over a set of model parameters, the Bayes Factor becomes the ratio of the marginalised likelihoods for the 2 models. Thus the Bayes Factor becomes,

$$B_{ij} = \frac{\int p(\theta_i)p(D|\theta_i,M_i)d\theta_i}{\int p(\theta_j)p(D|\theta_j,M_j)d\theta_j}. \tag{2.6}$$

From Eq 2.3, the Bayes Factor can then be expressed as a ratio of the evidence calculated for each competing model,

$$B_{ij} = \frac{p(D|M_i)}{p(D|M_j)}. \tag{2.7}$$

The Bayes' Factor will then be greater than or less than one depending on whether M_i or M_j is the favoured model. If it is of order unity, then the current data is insufficient to make an informed judgement. However for the majority of the results it is the logarithm of the evidence which is found by the nested sampling algorithm, so instead the logarithm of the Bayes Factor will be used to compare different models. Thus instead of using the equation above, the expression

$$\log B_{ij} = \log(p(D|M_i)) - \log(p(D|M_j)). \tag{2.8}$$

is needed. In this case choosing between the two models will depend on whether $\log B_{ij}$ is less than or greater than zero. $\log B_{ij} > 0$ will mean M_i is the preferred model whereas $\log B_{ij} < 0$ will point to M_j being favoured [119].

The evidence will be greater for a model that is supported by the data. There-

fore, the Bayes Factor indicates which of the two competing models best describes the data and thus infer which mechanism is being employed in a core collapse supernova.

2.2 The Nested Sampling Algorithm

For evaluating $\log B_{ij}$, first the evidences $\log(p(D|M_i))$ and $\log(p(D|M_j))$ for the two models M_i and M_j need to be calculated. In some cases, or for some set of parameters, the integral in Equation 2.3 can be computed analytically. But, more generally, it can be discretised so that the evidence is the sum of the likelihood times the prior determined for all possible parameter values of the desired model. For likelihoods dependent on more than a few parameters a brute force approach to evaluate the integral on a grid of values becomes computationally prohibitive. It is also an inefficient way of determining the evidence since the likelihood values will be most significant, and therefore contribute most to the evidence, for a small subset of parameter values which best models the data for a desired model. For most other combinations of the model's parameters, the likelihood will be insignificant and will not contribute to the evidence. Therefore, the approach of Veitch *et al.* [119] is chosen and nested sampling [108, 106] is employed to efficiently calculate the evidence integral.

The nested sampling algorithm determines the evidence integrals by calculating the likelihood for a selected sample of parameter values for the desired model. From Eq 2.3 the evidence can be written as,

$$Z = \int \mathcal{L}(\theta)\pi(\theta)d\theta = \int \mathcal{L}dX, \tag{2.9}$$

where $\mathcal{L}(\theta)$ is the likelihood and $\pi(\theta)$ represents the prior. Here, $dX = \pi(\theta)d\theta$ and is the element of probability mass associated with the prior density $\pi(\theta)$. Z can be calculated using the nested sampling algorithm by using the prior mass, X, directly. Prior mass, X, is defined as the cumulant prior mass covering all likelihood values greater than ν,

$$X(\nu) = \int\limits_{\mathcal{L}(\theta)>\nu} \pi(\theta)d\theta. \tag{2.10}$$

As ν increases, the prior mass, X, will decrease from 1 to 0. The inverse of this

function is then $\mathcal{L}(X(\nu)) \equiv \nu$ and so the evidence becomes a one-dimensional integral over unit range

$$Z = \int_0^1 \mathcal{L}(X)dX \tag{2.11}$$

in which the integrand must always be positive and decreasing.

Initially, the model's parameter values are randomly selected with respect to the prior. The algorithm then iterates over different sets of the model's parameter values, calculating the likelihood for each of the parameter values obtained and moves towards regions of higher likelihood. This is done through the use of a Markov Chain Monte Carlo (MCMC) algorithm [7] which randomly picks a point and moves towards another point with the highest likelihood. A description of the MCMC used in this analysis can be found in [119]. This point is then replaced by one with a higher likelihood found by the MCMC and the nested sample repeats. Therefore, as the algorithm stochastically samples the parameter space, it iteratively converges on the set of parameter values that produce the most significant likelihood values and smallest values for X, see Figure 2.1.

For every new iteration, there are m objects (called live points) which are restricted to the prior mass such that $X < X^*$ where X^* is the prior limit from the previous iteration. The object with the largest X and therefore the lowest likelihood is the largest of m numbers uniformly distributed in $X = 0$ to X^*. This point is then taken as the new limit on the likelihood and prior space (X^*, $\mathcal{L}^*$) and a new point within this space is created. For each iteration, i, a contribution to the evidence is calculated by finding $\mathcal{L}_i w_i$ where w_i is the width and is equal to $w_i = X_{i-1} - X_i$. This then accumulates for every iteration,

$$Z_i = Z_{i-1} + \mathcal{L}_i w_i. \tag{2.12}$$

During this process the desired regions of parameter space will be found and the increasing likelihood will start to flatten off and reach a maximum. Thus most of the evidence, Z, will have been found and the algorithm will need to be terminated. This is done at the iteration where no more contribution to the evidence can be made. This can be done by using the limit that the nested sampling algorithm will continue iterating until the number of iterations, i, exceeds mH_i where m is the

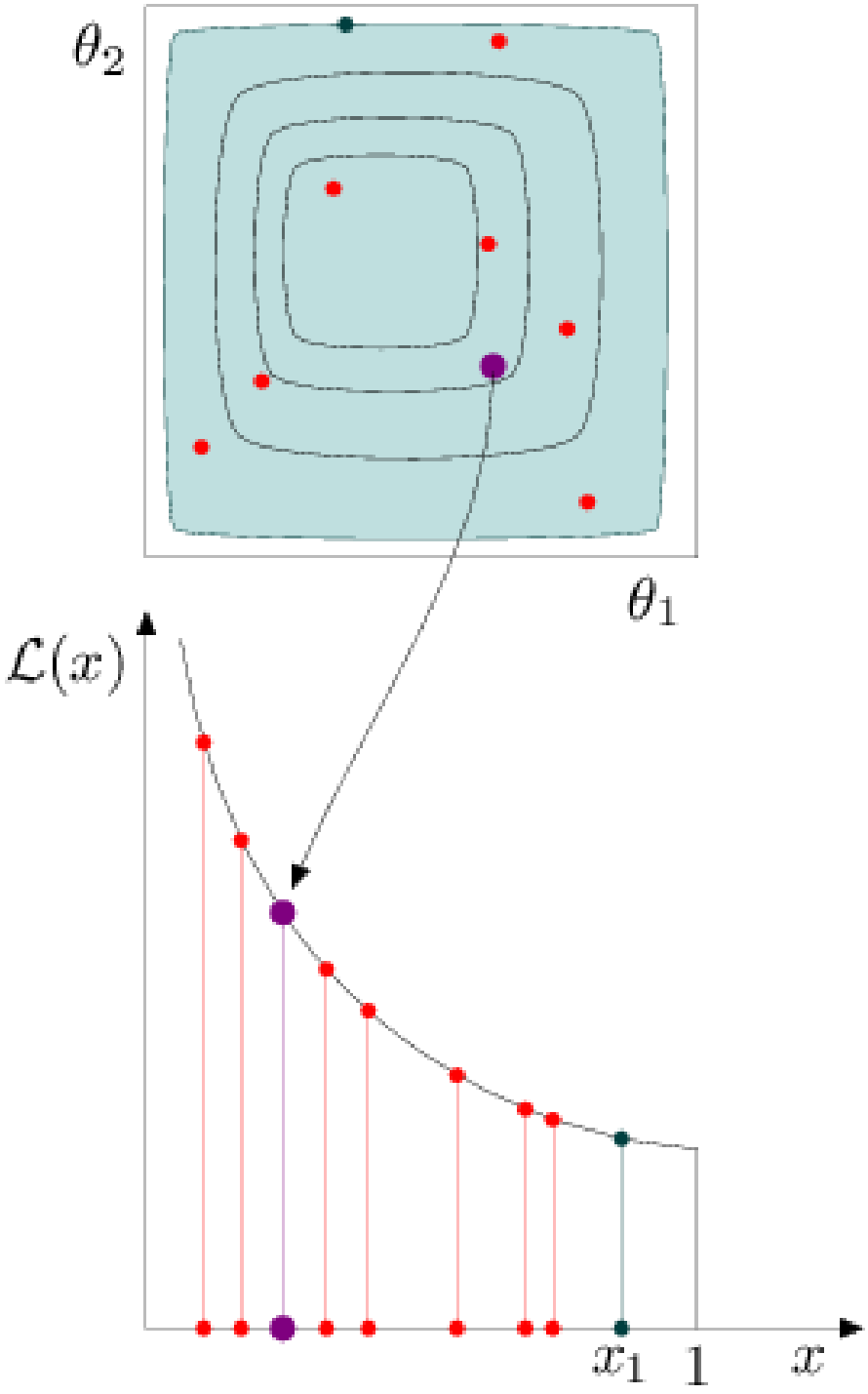

Figure 2.1: Figure representing the evolution of the nested sampling algorithm. Contours enclose shrinking prior mass regions and evidence is found by adding areas under the graph for each iteration. For example the point x_1 here has the smallest likelihood and so the MCMC finds a point with a higher likelihood and replaces x_1. This reduces the parameter space and shrinks the prior mass, from [107].

number of live points and,

$$H = \int \log\Big(\frac{dP}{dX}\Big) dP. \tag{2.13}$$

H is known as the information and is the logarithm of the fraction of the prior mass, X, that contains the bulk of the posterior mass, P, and is calculated for every iteration. So that when $i > mH$ the majority of the evidence (and therefore the majority of the posterior) has been found and continuing the iterations will provide no extra value. In this work, $m = 50$ unless otherwise stated and has been chosen as the number of live points as well as the number of points in the MCMC chain used to create a new point for each iteration. Using as many objects as possible would improve accuracy but would greatly increase the computation time. Thus, a value was chosen to keep the algorithm running quickly while still calculating evidence values which were sufficient to do model selection. For a study on the number of live points to use, see Section 5.1.

2.3 The Likelihood Distribution

For every iteration of the nested sampling algorithm a likelihood, $\mathcal{L}$, is found. This likelihood compares the input data, which for this thesis is taken as a GW signal plus the detector noise, to the trial gravitational waveform calculated for each iteration which is known as the reconstructed waveform. If the trial waveform is successful and matches the input data, it will be when the likelihood is at its maximum. In the analysis pipeline that will be described in the next Chapter, three different types of signal are used which employ two different likelihood functions. Firstly, the likelihood for a gravitational waveform in the time domain in Gaussian noise that has undergone a Fast Fourier Transform and is considered to have a Gaussian distribution. The likelihood for a single data sample, n, is given as,

$$p(D_n|\theta, M) = \frac{1}{\sigma_n\sqrt{2\pi}} \exp\Big(-\frac{(|D_n - \mu_n)|^2}{2\sigma_n^2}\Big), \tag{2.14}$$

where D is the input data, μ is the theorised data calculated in the nested sampling algorithm and σ represents the detector noise i.e the standard deviation of the Gaussian detector noise. Therefore the likelihood for a series of points comes from

the multiplication of all the individual probabilities,

$$p(D|\theta, M) = \mathcal{L} = \prod_{n=1}^{N/2} \frac{1}{\sigma_n \sqrt{2\pi}} \exp\Big(- \frac{|(D_n - \mu_n)|^2}{2\sigma_n^2}\Big). \tag{2.15}$$

It is often convenient to work with the logarithm of the likelihood and this is what will be used in this thesis:

$$\log \mathcal{L} = \frac{-N}{2} \log(2\pi) - N \log(\sigma) - \sum_{n=1}^{N/2} \frac{|(D_n - \mu_n)|^2}{2\sigma_n^2} \tag{2.16}$$

The other two forms of data employed are in the power spectrum and spectrogram domains which have independent, Gaussian distributed random variables with a nonzero mean and variance. In this case the random variable

$$d = \sum_{i=1}^{k} \Big(\frac{D_i}{\sigma_i}\Big)^2, \tag{2.17}$$

where D contains a vector of independent, Gaussian distributed variables, is said to be distributed according to a noncentral χ^2 distribution where k represents the number of degrees of freedom. Associated with this is a noncentrality parameter, λ, which is related to the mean, μ, by

$$\lambda = \sum_{i=1}^{k} \Big(\frac{\mu_i}{\sigma_i}\Big)^2. \tag{2.18}$$

The probability density function for a noncentral χ^2 distribution [8] is written as,

$$p(y|\lambda) = \frac{1}{2} \exp\Big(- \frac{(d+\lambda)}{2}\Big) \frac{d}{\lambda}^{(k/4-1/2)} I_{(k/2-1)}(\sqrt{\lambda d}), \tag{2.19}$$

where $I_{(k/2-1)}$ represents a Bessel function. For data in the power spectrum and spectrogram domains there are two degrees of freedom, the real and imaginary part of the data, so $k = 2$ and the above equation simplifies to

$$p(y|\lambda) = \frac{N}{2} \exp\Big(- \frac{(d+\lambda)}{2}\Big) I_0(\sqrt{\lambda d}). \tag{2.20}$$

This can then be rewritten using Equations 2.17 and 2.18 and the logarithm of the

likelihood is found, thus

$$\log \mathcal{L} = \log(1/2) + \sum_{n=1}^{N} \frac{-(D_n^2 + \mu_n^2)}{2\sigma_n^2} + \log\Big(I_0\Big(\frac{\sqrt{D_n \mu_n}}{\sigma_n^2}\Big)\Big). \tag{2.21}$$

2.4 The Posterior Distribution

The primary output of the nested sampling algorithm is the evidence, Z. The posterior probability for each parameter can be calculated from the outputs of the Nested Sample in logarithm space as,

$$\log(posterior) \propto \log(prior) + \log(likelihood) \tag{2.22}$$

which is weighted by the evidence. Thus, for any reconstruction of a waveform obtained through the use of the nested samples, a posterior distribution for each parameter can be found. While this is not necessary for model selection it can be a useful tool to guage how successful the algorithm is at parameter estimation which could be used to infer information about the source such as the mass of the core.

2.5 Principal Component Analysis

Each core-collapse supernova waveform catalogue consists of a number of gravitational waveforms obtained for different initial conditions and simulation parameters (e.g., progenitor star mass, Equation of State, rotational configuration etc.). While individual waveforms of one catalogue are different in detail, they generally exhibit strong common general features. This can be exploited by principal component analysis (PCA) [72], which isolates the most common features of waveforms in linearly independent principal components (PCs) ordered by their relevance. The first few PCs may already be sufficient to efficiently span their entire catalogue, as was shown in [56] and [97] for the `Dim` catalogue (see Sect. 1.7).

The PCs are obtained via singular value decomposition (SVD) (e.g., [72]). In singular value decomposition, a set of waveforms are decomposed into an orthonormal basis. Each waveform catalogue is arranged into a $m \times n$ matrix A, where

m is the number of waveforms each of length n. The covariance matrix for A is calculated by

$$C = \frac{1}{m} A A^T. \tag{2.23}$$

By finding the normalised eigenvectors of C, a set of basis vectors which span the linear space of each column in A are found. This means that each waveform can now be uniquely represented as a linear combination of these eigenvectors. How well each eigenvector spans this space is determined by the eigenvalues of C and so each eigenvector can be ranked by their corresponding eigenvalue. The eigenvector which corresponds to the largest eigenvalue is known as the first principal component (PC) which consists of the most significant common features of all waveforms in the catalogue. It follows that the PC with the second largest corresponding eigenvalue is the second PC and of the second most significant common features and so on.

This method can be computationally expensive as n can be typically 1000 to 10000 samples long. This can be avoided by calculating the eigenvectors, Σ, of $A^T A$ such that

$$A^T A \Sigma_i = u_i \Sigma_i, \tag{2.24}$$

where u_i is the corresponding eigenvalue for each eigenvector. Each side is then pre-multiplied with A to obtain

$$A A^T A \Sigma_i = u_i A \Sigma_i. \tag{2.25}$$

If equation 2.23 is rewritten as $C = A A^T$ then $U = A\Sigma_i$ are the eigenvectors of the covariance matrix. So the eigenvectors of the covariance matrix can be determined by calculating the eigenvectors of $A^T A$ which is a smaller $m \times m$ matrix, therefore significantly reducing computing costs [56].

The main advantage of this technique is that only a small number of principal components are required to reconstruct any of the waveforms used to create the matrix A. This means that any of the waveform catalogues discussed in Section 1.7 can be decomposed into a set of basis vectors and only the first few principal components are required to reconstruct any injected waveform. The waveforms in A can be reconstructed by taking a linear combination of PCs,

$$h_i \approx \sum_{j=1}^{k} U_j \beta_j \ , \tag{2.26}$$

where h_i is the desired waveform from the catalogue, U_j is the j'th PC and β_j is the corresponding PC coefficient, which can be obtained by projection of h_i onto U_j. The sum of k PCs produces an approximation of the desired waveform since $k \leq m$.

So to successfully reconstruct an injected waveform using a selected set of principal components and obtain a maximum value for the evidence, the correct values for β must be found by the nested sampling algorithm. This is the process used by the analysis pipeline SMEE (Supernova Model Evidence Extractor) by which the physics behind a core collapse supernova can be inferred and will be described in detail in Chapter 3.

Chapter 3

Supernova Model Evidence Extractor

In the following chapter, the components of a Bayesian data analysis algorithm called the Supernova Model Evidence Extractor (SMEE) are described. SMEE is designed to classify detected gravitational waveforms from core-collapse supernovae. A block diagram of the analysis algorithm is shown in Fig. 3.1. SMEE is implemented in `MATLAB`[1].

In a first step, SMEE performs principal component analysis (PCA) (Section 2.5) via singular value decomposition (SVD) on the waveforms in each catalogue to create sets of orthogonal basis vectors, the principal components (PCs). Using a complete set of PCs, each waveform can be reconstructed as a linear combination of PCs for the corresponding catalogue, allowing each waveform to be simply parameterized by the PC coefficients, β, in the linear combination. Non-catalogue waveforms (i.e., waveforms which have not been used in creation of the principal components) may be identified as belonging to the same class of waveforms as catalogue waveforms if they can be approximately matched with the first few PCs of a catalogue.

SMEE then uses Bayesian model selection and computes the logarithm of the Bayes Factor (Section 2.1) to distinguish between the waveform catalogues which represent different supernova waveform models. This requires summing up the like-

[1]The MathWorks Inc., Natick, MA 01760, USA. `http://www.mathworks.com/products/matlab/`.

lihood function multiplied by the prior across all possible waveform parameters (in our case, values of PC coefficients) to determine the evidence for two different waveform models. SMEE accomplishes this efficiently via the nested sampling algorithm (Section 2.2).

3.1 GW Preparation and PCA

In the development of the Supernova Model Evidence Extractor (SMEE) three separate versions have been investigated. These three versions depend on which type of data is used to create the principal components, the idea being that each signal should be analysed in multiple ways so as to learn as much as possible about the source. The three versions of SMEE are as follows: firstly a version where the PCs are created in the time domain (TD_SMEE), a version where the PCs are created in the power spectrum domain (PSD_SMEE) and finally a version where the PCs are constructed in the spectrogram domain (Spec_SMEE). Having the data in the time domain was chosen as this is the form that the waveform catalogues were created in and so would need the least manipulation before being analysed. As can be seen in Figure 1.8, gravitational waveforms from supernovae vary greatly in the time domain thus potentially aiding the ability of SMEE to accurately perform Bayesian model selection. The power spectrum domain (PSD) is chosen to explore SMEE's ability in the frequency domain as well as the effect of removing any phase information from the waveforms. Finally, the spectrogram domain is chosen as this combines both time and frequency information and allows SMEE to analyse both previous types of information about any given waveform at the same time. In this section there will be a discussion on how each one of these sets of PCs are created as well as how the gravitational waveform is prepared before being analysed in the nested sampling algorithm.

All of the waveform catalogues were initially generated in the time domain so the model catalogues must first be prepared in this form. It must be ensured that the longest available core-collapse supernova GWs can be used. To do this all waveforms are buffered with zeroes to be of length n, which is chosen to correspond to 3 s as this will ensure that each waveform file is the same length and comfortably contains the whole length of any waveform. A sampling rate of 4096 Hz is chosen to reduce the length of the waveforms, thus decreasing the time it takes to analyse

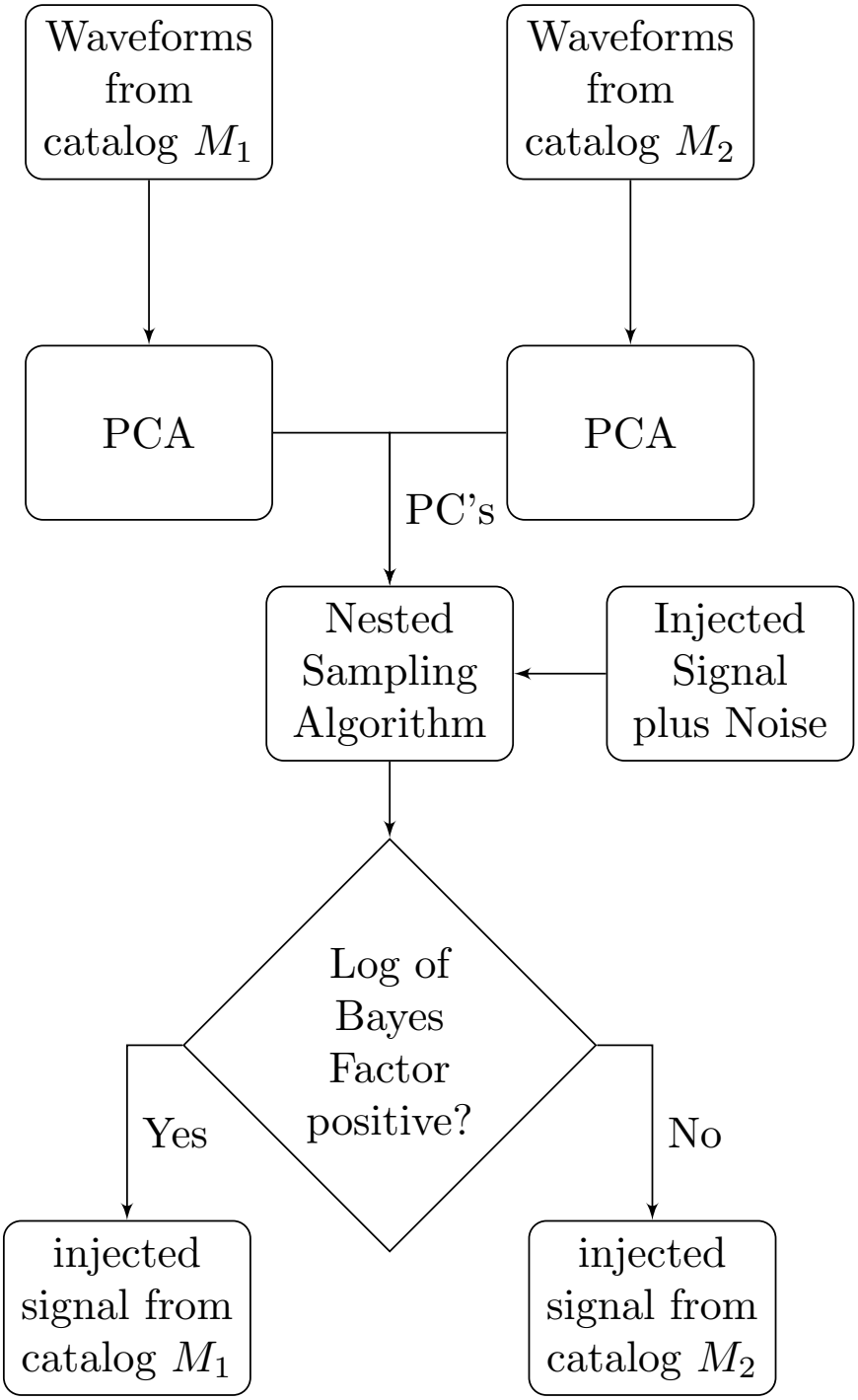

Figure 3.1: Block diagram of the Supernova Model Evidence Extractor (SMEE). A desired core-collapse supernova gravitational waveform is injected into noise, and the algorithm compares it to the principal components (PCs) of a given waveform catalogue representing a particular model. The PCs are constructed via singular value decomposition (SVD). The sign of the log Bayes Factor between two PC sets indicates which model is favored by the data.

a waveform, while still having a large enough resolution that will contain sufficient information about the waveform. This is completed before carrying out PCA and adding detector noise to the waveforms. While the Advanced LIGO sampling rate is 16 kHz the reduced sampling rate chosen saves computation time and is sufficient to capture the frequency content of the core-collapse supernova waveforms considered here, which have most of their power at $\sim 50 - 1000$ Hz.

Waveforms from the `Dim` catalogue are aligned at their maximum (the spike at core bounce, see Figure 1.8). Waveforms from the `Mur` and `Ott` catalogues are aligned so that the onsets of emission coincide. All waveforms are shifted so that they are aligned to the 4000-th point in the SMEE input data file. This corresponds to about the 1 s mark in the 3 s interval and is done to leave ample space to the left and right of the waveform. Once each waveform from a corresponding catalogue is aligned and made the same length they are organised into a matrix where every column contains one waveform. Thus we are able to create a matrix of waveforms for each of the catalogues we want to use to create PCs. Each of these catalogues thus represent a model that SMEE is set up to compare.

3.1.1 Time Domain

The simplest family of PCs to create is in the time domain. For this the time domain catalogues that were created are used to produce a set of PCs for each of our models using the method discussed in Section 2.5. The first three PCs computed for the `Dim` (magnetorotational mechanism; left panel), `Mur` (neutrino mechanism; center panel), and `Ott` (acoustic mechanism; right panel) catalogues are presented in Fig. 3.2. Before generating PCs for the `Mur` catalogue the secular low-frequency drifts present in the `Mur` waveforms (see Fig. 1.8) are filtered out by high pass filtering the signal above 30 Hz. Since the low-frequency components are hidden in detector noise even when the source is nearby, removing them improves the efficiency of our subsequent Bayesian analysis and waveform reconstruction. This is repeated for all trial waveforms utilising the neutrino mechanism before they are added to detector noise.

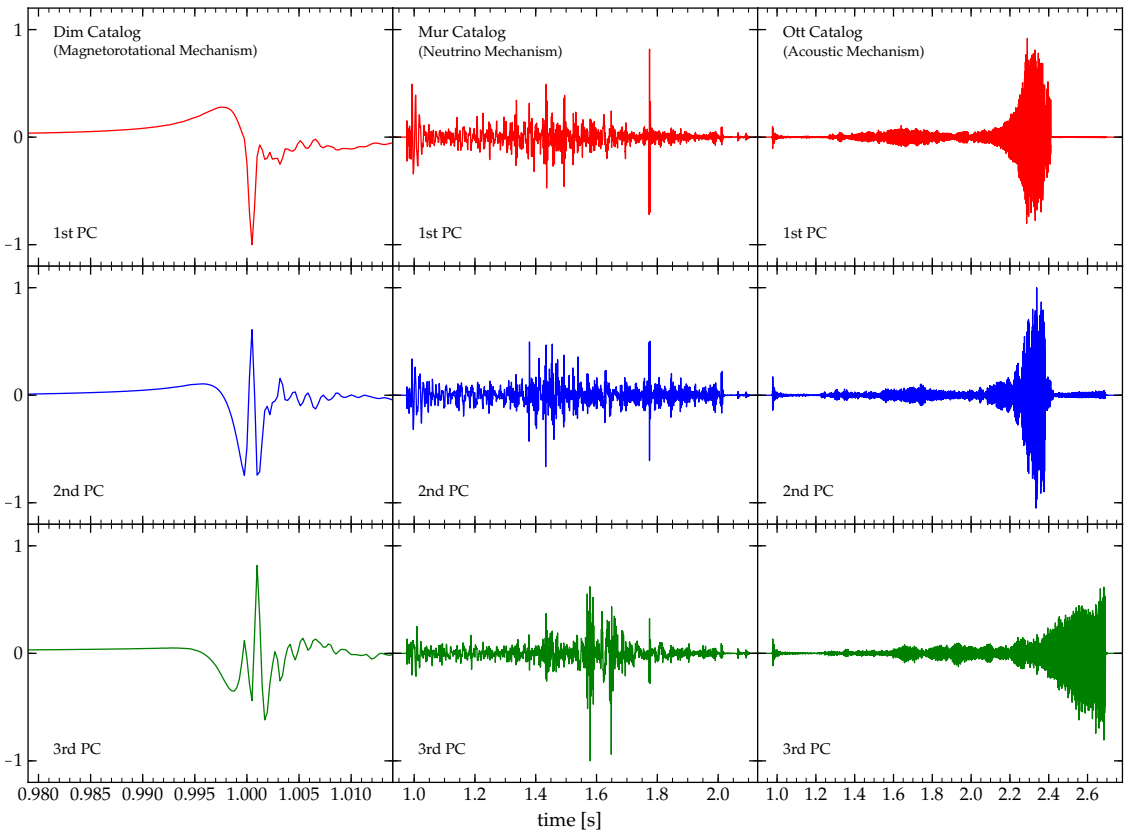

Figure 3.2: The first three principal components (PCs) for the waveforms from the Dimmelmeier (`Dim`) [34, 24], Murphy (`Mur`) [79], and `Ott` [84] catalogues, which is taken to be representative of the magnetorotational, neutrino and acoustic mechanisms, respectively (see Section 1.7). In calculating the PCs, the waveforms of each catalogue are placed in a systematic way in a 3 s interval and padded left and right by zeros. The vertical axis is a dimensionless scale which represents the amplitude, which is normalized by the maximum amplitude over all 3 PCs of each catalogue shown here, from Logue et al. [70].

3.1.2 Power Spectrum Domain

In the power spectrum domain before creating the PCs we first perform a Fast Fourier Transform (FFT) on each of our catalogues. We then only take the first half of our FFT'd catalogue as it will be repeated due the input catalogue being real. Finally the FFT'd catalogue is scaled by a normalisation factor,

$$n_{\text{norm}} = \sqrt{\frac{1}{LF_s}} \tag{3.1}$$

where $F_s = 4096Hz$ is the sampling frequency and L is the length in samples of the time domain waveform before the waveform has been zero padded. This is done to ensure the waveforms in each catalogue have the correct dimensions of $(\text{Hz})^{-1/2}$. Once this has been done the absolute value squared of each of our Fourier transformed waveforms is found thus converting them into the power spectrum domain. To be clear, we have gone from having a catalogue of waveforms in the time domain to one in the power spectrum domain. We then use the same technique to create a set of PCs for each catalogue thus creating a set of models in the power spectrum domain that can be tested in SMEE, (see Figure 3.3).

3.1.3 Spectrogram Domain

For the spectrogram domain, we select each waveform in a catalogue and use the MATLAB spectrogram function and calculates a short-time Fourier transform of each waveform. This function allows the choice of window, FFT length, overlap and sampling frequency. For simplicity, the standard Hamming window is used with the sampling frequency of 4096 Hz and an overlap of 90% is adopted. The FFT length is kept as a free parameter that the user can input. For the results shown in this thesis a FFT length of 128 is used, thus creating spectrograms with a frequency resolution of 32 Hz and a time resolution of approximately 3 microseconds. These values were chosen to ensure that there is sufficient time and frequency information for each waveform. We then introduce a frequency cutoff so that the first 32 Hz of data is ignored as ground based interferometers do not perform well at these lower frequencies, any part of the waveform at this frequency would be undetectable.

Since the spectrogram function takes the waveforms from a catalogue, which is

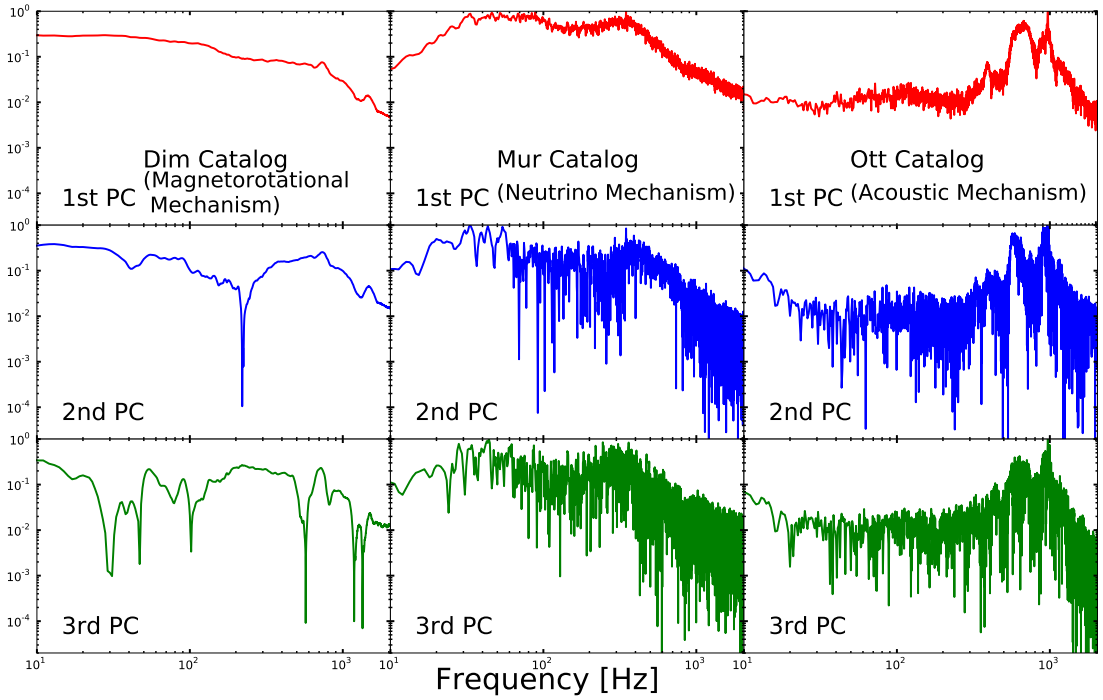

Figure 3.3: The first three principal components (PCs) in the power spectrum domain for the waveforms from the Dimmelmeier (`Dim`) [34, 24], Murphy (`Mur`) [79], and `Ott` [84] catalogues, which is taken to be representative of the magnetorotational, neutrino and acoustic mechanisms, respectively (see Section 1.7). The vertical axis is a dimensionless scale which represents the amplitude, which is normalized by the maximum amplitude over all 3 PCs of each catalogue shown here.

a vector, and creates a spectrogram which is essentially a matrix, each column in the catalogue needs to be organised into a vector so the PCs can be created. This is simply done by taking the columns in the spectrogram matrix of a waveform and adding the beginning of a column onto the end of preceding column. This means that for every waveform in the catalogue a vector can be created with a length that is the number of frequency bins multiplied by the number of time bins.

As in the power spectrum domain the outputs of the spectrogram function need to be normalised to ensure they have the correct dimensions as we want them to have the same dimensions as the power spectrum ($(\mathrm{Hz})^{-1/2}$). The normalisation is a real scaler value, n_{norm}, where the waveform in the dimensions of the power spectrum domain (PSD) equals,

$$P = (n_{\mathrm{norm}}|S|)^2 \tag{3.2}$$

and S is the output of the spectrogram function. For the spectrogram domain,

$$n_{norm} = \sqrt{\frac{1}{F_s \sum_{i=1}^{j} |w(i)|^2}} \tag{3.3}$$

where j is the number of frequency bins and $w(n)$ represents the window function which is kept as a Hamming window. F_s is the sampling frequency which is kept as 4096 Hz. Once this has been done the PCs are created for each catalogue and thus a set of models in the spectrogram domain are made which can be tested in SMEE, (see Figure 3.4).

3.1.4 Priors for the PC coefficients

The nested sampling algorithm which is the bulk of SMEE is set up to calculate the PC coefficients that are used to reconstruct a given gravitational waveform, see Equation 2.26. To find these coefficients a parameter space for the nested sample to search over must be established. This is known as the prior as it contains any previous knowledge about what each PC coefficient should equal. The prior for each PC coefficient, β_k, is taken to be flat and uniform meaning that any value in a given range is given equal weight. The prior range for each β_k is determined by first reprojecting all waveforms of a given catalogue back onto the PCs to compute

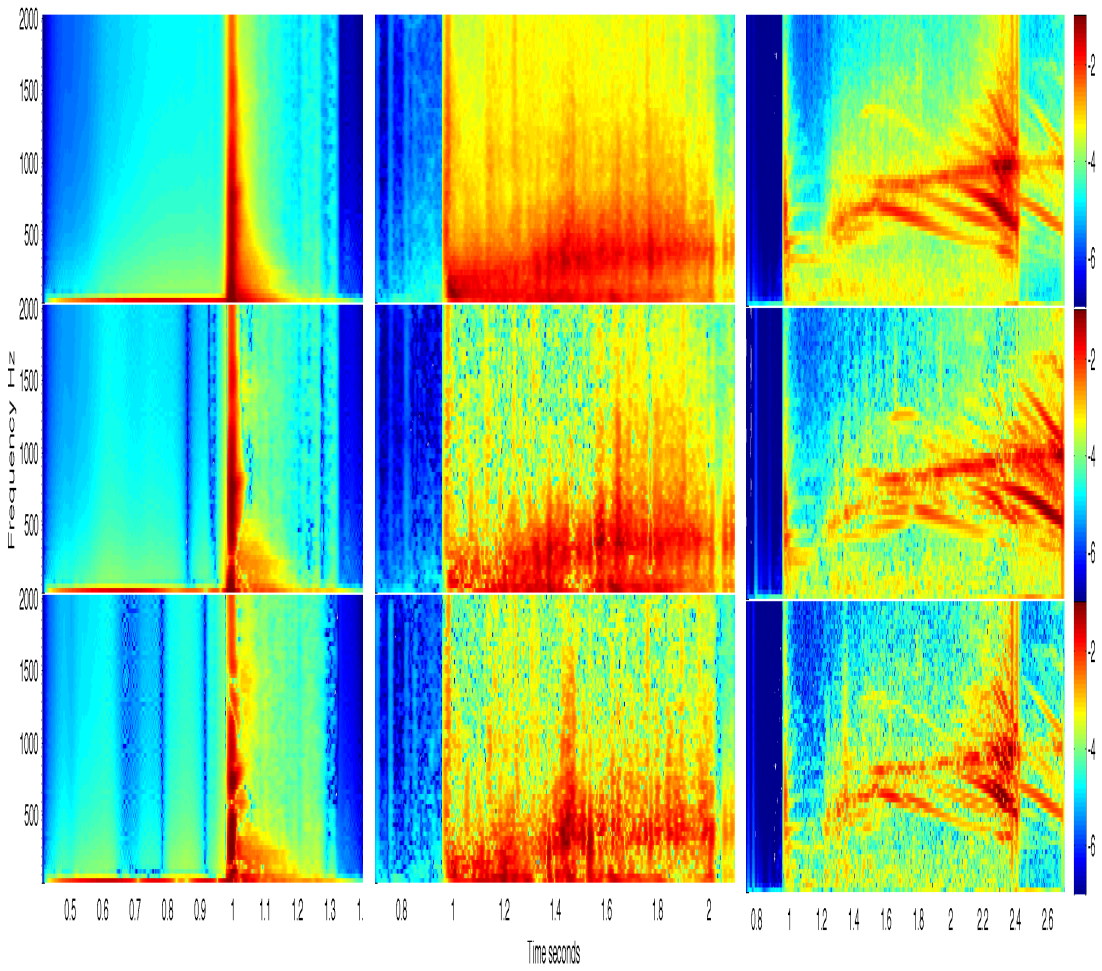

Figure 3.4: The first three principal components (PCs) in the spectrogram domain for the waveforms from the Dimmelmeier (`Dim`) [34, 24], Murphy (`Mur`) [79], and `Ott` [84] catalogues, which is taken to be representative of the magnetorotational, neutrino and acoustic mechanisms, respectively (see Section 1.7). The vertical axis is a dimensionless scale which represents the amplitude, which is normalized by the maximum amplitude over all 3 PCs of each catalogue shown here.

the correct value, $\hat{\beta}_{kl}$, for each PC k and waveform l of the catalogue. The range of expected possible values of β_k is then found by taking the minimum and maximum of $\hat{\beta}_{kl}$ over all l. To account for uncertainty due to the noise, motivated by the findings of [97], 10% of the maximum added to the maximum and 10% of the minimum is subtracted from the minimum $\hat{\beta}_{kl}$. This ensures that the value calculated by the nested sample will lie within the desired range. This is repeated for each PC catalogue and so a global maximum and minimum value over all three PC catalogues can be found.

This technique is used for each version of SMEE ensuring that there is a set of priors for the time domain, power spectrum domain and spectrogram domain version of SMEE.

3.2 Time Delays and Antenna Response with Multiple Detectors

It was shown in Figures 1.3 and 1.4 that a GW detector is sensitive to the direction of the source, in this case a core collapse supernova. It is most sensitive when the GW is travelling perpendicular to the detector and least sensitive when it is parallel. This effect is called the antenna response and can be calculated using Equation 1.7. However the supernova data employed in this thesis only contains the plus polarisation so only F_+ is needed,

$$\begin{aligned} F_+ = \frac{1}{2}(1+\cos^2\theta)\cos 2\phi \cos 2\psi \\ - \cos\theta \sin 2\phi \sin 2\psi, \end{aligned} \tag{3.4}$$

where θ is the local polar angle of the sky position of a source of gravitational waves and ϕ is the local azimuthal angle of the sky position of the source. ψ is the local polarisation angle of the source [96].

This can be simulated in SMEE by calculating the antenna response for a chosen right ascension, declination (which can be converted into polar angle and azimuthal angle) and the polarisation angle of the source. It is expected that a Galactic supernova will be an extremely bright event and so finding its right ascension and

declination will be trivial so these are kept as fixed parameters in SMEE. This polarisation angle, ψ, is more difficult to predict as it will not be immediately calculated from EM observations and so it treated as a free parameter. This means that in addition to marginalising over the PC coefficients, the polarisation angle is also marginalised in the nested sampling algorithm. This means that for every iteration there will be a trial antenna response which scales the reconstructed waveform and will be closest to the chosen waveform (which has been scaled by the correct antenna response) when the polarisation angle matches the correct value. The prior for this is uniform over the range 0 to π and is chosen to encompass all possible angles in the sky frame.

Due to the fact that GWs are travelling at the speed of light there will be a small time delay (T_d)when the signal arrives at different detectors around the world. Thus for every interferometer which successfully detects a gravitational waveform there will be a different time of arrival. These can be adjusted to a single frame of reference by using the time at which the GW reaches the centre of the Earth. To successfully reconstruct a GW this Earth centre time must be known so that for each detector the PCs can be correctly aligned with the GW which has been detected by an individual detector. Because of this, when SMEE is run using detected waveforms from multiple detectors the Earth centre time is kept as a free parameter and is marginalised in the nested sampling algorithm. For the purposes of improving the efficiency of SMEE this is achieved by first creating a set of PCs for each detector that have been shifted by T_d from the GW arriving at the centre of the Earth. This is done by shifting each of the waveforms in the time domain by the number of samples that are equal to T_d i.e each waveform is 3 seconds long and is 12288 samples long, so each sample represents 2.4×10^{-4} seconds. Once this is done PCA is performed using the techniques discussed in Section 3.1. In the nested sampling algorithm a trial Earth centre time is chosen and T_d for each detector is calculated and the chosen waveform is shifted by this value before being added to the detector noise. When dealing with real data where T_d does not need to be simulated this process can be reversed and the PCs will be shifted for every trial Earth centre time. This would greatly slow down SMEE as a new set of PCs would be required for each iteration of the nested sampling algorithm so this technique is not used when using simulated waveforms. Thus a prediction of the T_d and therefore the Earth centre time is found when the maximum likelihood is found and the reconstructed waveform is aligned with the desired waveform. It is expected that there will be some information about when the GW arrives at Earth and that a Earth centre

time will be inferred so the priors for the Earth centre are kept fairly tight over a uniform range. The maximum time is 50 ms above the inferred value and the minimum time is 50 ms below the inferred value. If there is less confidence in the prediction of Earth centre time the prior would be expanded over a wider range.

3.3 Generation of Simulated Noise

Assuming a single Advanced LIGO detector, Gaussian coloured noise is generated in the proposed broadband configuration (the so-called "zero detuning, high-power" mode). The data file `ZERO_DET_high_P.txt` is employed, provided by [105], which contains $\sqrt{S(f)}$, the square root of the one-sided detector noise power spectral density in units of $(\text{Hz})^{-1/2}$.

This function reads in the amplitude spectral density and resamples it to match the sampling rate of the data (4096 Hz). This noise vector is then used as the variance in the likelihood function i.e. $\sigma = \sqrt{S(f_k)}$. When running SMEE in the power spectrum and spectrogram domains the data also has dimensions $(\text{Hz})^{-1/2}$ so the function outputs Fourier domain random Gaussian noise which is generated as,

$$\Re(\hat{n}(f_k)) = \sqrt{\frac{S(f_k)}{2}} \times \text{RANDN}, \tag{3.5}$$

$$\Im(\hat{n}(f_k)) = \sqrt{\frac{S(f_k)}{2}} \times \text{RANDN} \tag{3.6}$$

where RANDN denotes a random number drawn from a Gaussian probability distribution with zero mean and unit variance. By extension, this term will then also have dimensions of $(\text{Hz})^{-1/2}$. This technique works for both PSD and spectrogram versions of SMEE however one difference needs to be made for the spectrogram domain. Here a single power spectrum of the noise is created with the same frequency resolution as the spectrogram data (32 Hz). This data is then repeated r times, where r is the number of time bins, and is added together in the same manner as the spectrogram data, see Section 3.1.3. This ensures that the length of the noise file is the same as the signal.

When using SMEE with principal components generated in the time domain, the injected waveform has dimensions of $(\text{Hz})^{-1}$ thus the noise added to the waveform

must have the same dimensions. This can be done by considering the definition of $S(f_k)$ as

$$\langle \tilde{n}(f)\tilde{n}^*(f')\rangle = \frac{1}{2}S(f)\delta(f-f'), \tag{3.7}$$

where

$$\langle |\tilde{n}(f_k)|^2\rangle = \frac{T}{2}S(f_k). \tag{3.8}$$

T is the total observation time, $f_k = k\Delta f$ is the frequency in the k^{th} frequency bin, where Δf denotes the frequency resolution, and $\langle . \rangle$ denotes ensemble average. The real and imaginary components of the Fourier domain noise can be expressed as

$$\langle |\tilde{n}(f_k)|^2\rangle = \langle |\tilde{x}(f_k)|^2\rangle + \langle |\tilde{y}(f_k)|^2\rangle, \tag{3.9}$$

where $\tilde{x}(f_k) \in \Re$ and $\tilde{y}(f_k) \in \Im$. The noise variance σ_k^2 can be defined in terms of $\tilde{n}_k$ where,

$$\tilde{n}_k = \frac{\tilde{n}(f_k)}{\Delta t}. \tag{3.10}$$

Δt is the time resolution and has units $(\text{Hz})^{-1}$, so

$$\begin{aligned} \sigma_k^2 &= \langle |\tilde{n}_k|^2\rangle, \\ &= \frac{TS(f_k)}{2\Delta t^2}, \\ &= \frac{NS(f_k)}{2\Delta t} \end{aligned} \tag{3.11}$$

where $N = T/\Delta t$ is the number of samples. Since σ_k^2 is dimensionless, the real and imaginary components of the simulated Gaussian detector noise can be expressed in terms of $\sigma_k^2/2$, such as

$$\begin{aligned} \Re(\tilde{n}(f_k)) &= \Delta t\sqrt{\frac{\sigma_k^2}{2}} \times \text{RANDN}, \\ &= \Delta t\sqrt{\frac{NS(f_k)}{4\Delta t}} \times \text{RANDN}, \\ &= \sqrt{\frac{NS(f_k)\Delta t^2}{4\Delta t}} \times \text{RANDN}, \\ &= \sqrt{\frac{TS(f_k)}{4}} \times \text{RANDN}, \\ &= \sqrt{\frac{S(f_k)}{4\Delta f}} \times \text{RANDN}, \end{aligned} \tag{3.12}$$

and

$$\Im(\tilde{n}(f_k)) = \sqrt{\frac{S(f_k)}{4\Delta f}} \times \text{RANDN}. \tag{3.13}$$

This results in $\tilde{n}(f_k)$ having units of $(\text{Hz})^{-1}$ as required.

For convenience, the matched filter signal-to-noise ratio (SNR) of a GW, h, is defined as

$$\text{SNR}^2 = 4\int_0^\infty \frac{\left|\tilde{h}(f)\right|^2}{S(f)} df \tag{3.14}$$

$$= 4\Delta f \sum_{k=1}^{N_f} \frac{\left|\tilde{h}(f_k)\right|^2}{S(f_k)} \ , \tag{3.15}$$

where the term $4\Delta f$ ensures that this term is dimensionless as the term in the sum as dimension $(\text{Hz})^{-1}$ and $4\Delta f$ has dimension $(\text{Hz})^1$

3.4 SNR and Distance Scaling

The results of SMEE's computations will depend on the SNR of the waveform, i.e. the distance to the core collapse event, and on the amount of information that can be provided to SMEE about expected waveforms in the form of principal components. The SNR (and distance) of the waveform can be adjusted in SMEE to test this dependence. This is done by introducing a scale factor which is equal to 1 when the waveform is at 10kpc. The scale factor is then the chosen SNR divided by the network SNR of the waveform at 10kpc. When scaling by distance the scale factor is 10 divided by the chosen distance. The waveform (before any detector noise has been added) and the PCs are then multiplied by this value.

This scale factor, s_f, can be used as a free parameter in SMEE when the distance to the source is treated as an unknown value. Thus, instead of multiplying s_f by the PCs, a trial s_f is chosen for each iteration of the nested sample. Any reconstructed trial waveform will then give a maximum likelihood when the true s_f that was used to adjust the chosen waveform and the correct signal parameters are found. If this s_f can be predicted accurately, the distance to the source can be predicted. The prior range for this value is chosen as the given distance of the simulated signal

+/− 10% i.e. if the distance is 10 kpc, s_f will be 1 and so the prior will be over the range of 0.9 to 1.1. This makes the assumption that the distance to the source is measured accurately before any GW data is analysed i.e an EM counterpart has been measured.

3.5 Signal and Noise Models

For the analysis described here, two types of models are considered. The first model which tests the presence of a waveform $h(\beta)$ in the data, where β represents the PC coefficients, is called the signal model, M_s. To test this model an evidence must be calculated thus a likelihood function is required.

In the time domain the Gaussian likelihood function was shown to be,

$$\log \mathcal{L} = \frac{-N}{2}\log(2\pi) - N\log(\sigma) - \sum_{n=1}^{N/2} \frac{|(D_n - h(\theta)_n)|^2}{2\sigma_n^2} \tag{3.16}$$

in Section 2.3 with the sum performed only over positive frequencies. The terms $(-N/2)\log(2\pi)$ and $N\log(\sigma)$ will always be constant so these terms can be ignored and σ^2 is the one sided detector noise, $S(f)$. D here is the sum of the detector noise which was generated in Section 3.3 and the time domain signal, which has been first shifted by a trial T_d in the nested sampling algorithm for a particular detector, and then FFT'd and normalised such that,

$$D = \tilde{d}(f_k) = (s_f F_+ \times \tilde{h}(f_k)\Delta t) + \tilde{n}(f_k), \tag{3.17}$$

where Δt ensures the waveform and noise have the same dimensions of $(\mathrm{Hz})^{-1}$. F_+ is the antenna response ands_f is the scale factor which adjusts the waveform to a particular distance. As in Eq. 3.15 the term $4\Delta f$ is used to ensure that the likelihood is dimensionless. Thus the likelihood is given as,

$$\log \mathcal{L} = -4\Delta f \sum_{n=1}^{N/2} \frac{(|\tilde{d}_n - (s'_f F'_+ \tilde{h}(\beta)_n)|^2}{2S(f_n)} \tag{3.18}$$

where $\tilde{h}_n(\beta)$ is the desired waveform reconstructed from the PCs which, as dis-

cussed in Section 3.2 have already been shifted by T_d, and the PC coefficients β, and N is the length of the data with a corresponding index n. F'_+ is the estimation of the antenna response from the desired polarisation angle. s'_f is the estimation of the scale factor. When considering combining data from multiple detectors a $\log \mathcal{L}$ is found for each detector and a final likelihood is found from finding the sum,

$$\log \mathcal{L}_{\mathcal{M}} = \sum_{m=1}^{M} \log \mathcal{L}_j = \sum_{m=1}^{M} -4\Delta f \sum_{n=1}^{N} \frac{(|(\tilde{d}_n)_m - s'_f(F'_+ \tilde{h}(\beta)_n)_m)|^2}{2S(f_n)_m}. \tag{3.19}$$

Due to the fact that we are adding real and imaginary parts of the signal in the PSD and spectrogram versions of SMEE we choose to utilise a non-central χ^2 likelihood distribution (Section 2.3) for the signal model. $\log \mathcal{L}$ in this case was shown to be

$$\log \mathcal{L} = N \log(1/2) + \sum_{n=1}^{N} \frac{-(|D_n|^2 + |h(\theta)_n|^2)}{2\sigma_n^2} + \log\Big(I_0\Big(\frac{\sqrt{D_n h(\theta)_n}}{\sigma_n^2}\Big)\Big). \tag{3.20}$$

As in the Gaussian likelihood, $\sigma^2 = S(f)$ and D is the sum of the detector noise and the injected signal, which has been first shifted by a trial T_d in the nested sampling algorithm for a particular detector before being transformed into the PSD or spectrogram domain, such that,

$$D = \hat{d}(f_k) = |(s_f F_+ \times \hat{h}(f_k) \times n_{\text{norm}}) + \hat{n}(f_k)|, \tag{3.21}$$

and n_{norm} is a normalisation constant used to ensure the signal has the same dimensions as the detector noise. These are the same terms used to normalise the principal components in equations 3.1 and 3.3. $h(\theta) = \hat{h}(\beta)$ and again is the desired waveform reconstructed from the PCs which, as in the case for time domain PCs, have already been shifted by T_d. By ignoring the term $N \log(1/2)$ which remains constant, the likelihood function is as follows,

$$\log \mathcal{L} = \sum_{n=1}^{N} \frac{-(\hat{d}_n^2 + |(s'_f F'_+ \hat{h}(\beta)_n)|^2)}{2S(f)} + \log\Big(I_0\Big(\frac{\sqrt{\hat{d}_n |(s'_f F'_+ \hat{h}(\beta)_n)|}}{S(f_n)}\Big)\Big). \tag{3.22}$$

Thus when employing multiple detectors the final likelihood is,

$$\log \mathcal{L}_M = \sum_{m=1}^{M}\sum_{n=1}^{N} \frac{-((\hat{d}_n)_m^2 + s'_f|F'_+\hat{h}(\beta)_n|_m^2)}{2S(f_n)_m} + \log\Big(I_0\Big(\frac{\sqrt{(\hat{d}_n)_m s'_f|F'_+\hat{h}(\beta)_n|_m}}{S(f_n)_m}\Big)\Big). \tag{3.23}$$

To determine the evidence (in logarithm space) for the signal model, M_s, the integral in Eq. 2.3 is solved numerically, using uniformly-distributed priors over a chosen number of PCs, (see Section 3.1.4). The priors for the extra parameters, s_f, T_d and ψ are also included. So, summing up over multiple detectors,

$$\log Z_{\text{signal}} = \sum_{m=1}^{M} \log(p(D|M_s))_m = \Big[\sum_{m=1}^{M}\sum_{n=1}^{N}(\log(p(\beta, s_f, T_d, \psi|M_s)_n)_m\Big] + \log\mathcal{L}_M. \tag{3.24}$$

The second model considered is the noise model, M_n, which tests the data's consistency with detector noise. The likelihood function for the noise model is the same as that in Eq. 3.18 and 3.22, but with $h(\beta) = 0$. It is then straightforward to perform the integration in Eq. 2.3 and obtain an analytic form for the noise evidence function when summing up over multiple detectors,

$$\log Z_{\text{noise}} = \sum_{m=1}^{M} log(p(D|M_n))_m = \sum_{m=1}^{M} 4\Delta f \sum_{n=1}^{N} -\frac{(|\tilde{d}^2|_n)_m}{2S(f_n)_m}, \tag{3.25}$$

when a Gaussian likelihood is used and

$$\log Z_{\text{noise}} = \sum_{m=1}^{M} log(p(D|M_n))_m = \sum_{m=1}^{M}\sum_{n=1}^{N} -\frac{(\hat{d}_n^2)_m}{2S(f_n)_m}, \tag{3.26}$$

when a non-central χ^2 likelihood is used.

To compare the signal model to the noise model the natural logarithm of the Bayes Factor, see Equation 2.8, is then used and is simply,

$$\log B_{SN} = \log Z_{signal} - \log Z_{noise}, \tag{3.27}$$

where a positive $\log B_{SN}$ indicates M_s is favoured and a negative value indicates

that M_n is favoured.

3.6 Signal Injection and Model Selection

Trial GWs are added to detector noise such as simulated Gaussian Advanced LIGO noise and SMEE is used to determine which signal model (e.g., which core-collapse supernova explosion mechanism) a given waveform belongs to. This is done via the evaluation of the logarithmic Bayes Factors $\log B_{SN}$ (Eq. 3.27) for an injected signal for each signal model S and the noise model N. Comparing two signal models $S = i$ or $S = j$ is then accomplished by computing $\log B_{ij} = \log B_{iN} - \log B_{jN}$.

SMEE's model selection operates in either the frequency domain, power spectrum domain or spectrogram domain. In the version of SMEE where PCA is performed in the time domain, trial GW and the PCs belonging to the signal model under consideration are transformed into the frequency domain via DFT and the trial GW is added to the complex frequency-domain noise, retaining phase information. This version of SMEE will still be referred to as time domain SMEE as this the form the principal components are created in. The PSD version is the same except that it is a power spectrum of the trial GW that is used so we lose all phase information. As for the spectrogram version, signals are prepared and normalised in the same way described in Section 3.1 to create the PCs. The PC coefficients β_k, polarisation angle, Earth centre time and distance (through the use of a scale factor) are marginalised by invoking the nested sampling algorithm.

The maximum number of PCs at SMEE's disposal is limited by the number of waveforms used to determine the set of PCs. While each catalogue used in this study has a different number of waveforms, analysis is simplified by using the same number of PCs for all catalogues. Hence, the maximum number of PCs used is 7 and is set by the number of waveforms in the `Ott` catalogue (see §1.7). This gives SMEE complete information about waveforms belonging to the `Ott` catalogue. It also gives significant, but incomplete information about waveforms from the `Dim` and `Mur` catalogues. This limits SMEE's ability to precisely reconstruct waveforms from the `Dim` and `Mur` catalogues, but it represents the real-life situation that the a priori information about a detected signal is severely limited.

Reconstructions of a waveform along with plots of the posterior distribution for each PC coefficient are shown for the same `Dim` waveform for all versions of SMEE with 7 PCs at a distance of 10kpc using a single Advanced LIGO detector in Figures 3.5 (time domain), 3.6 (power spectrum domain) and 3.7 (spectrogram domain). Reconstructions for the extra parameters are shown in Section 6.1. While these reconstructions are adequate, the goal here is not to ideally reconstruct waveforms but to show that determining the underlying physical model of an observed signal is possible with limited advance knowledge. For a complete study on how the number of PCs used affects the results see Chapter 5.

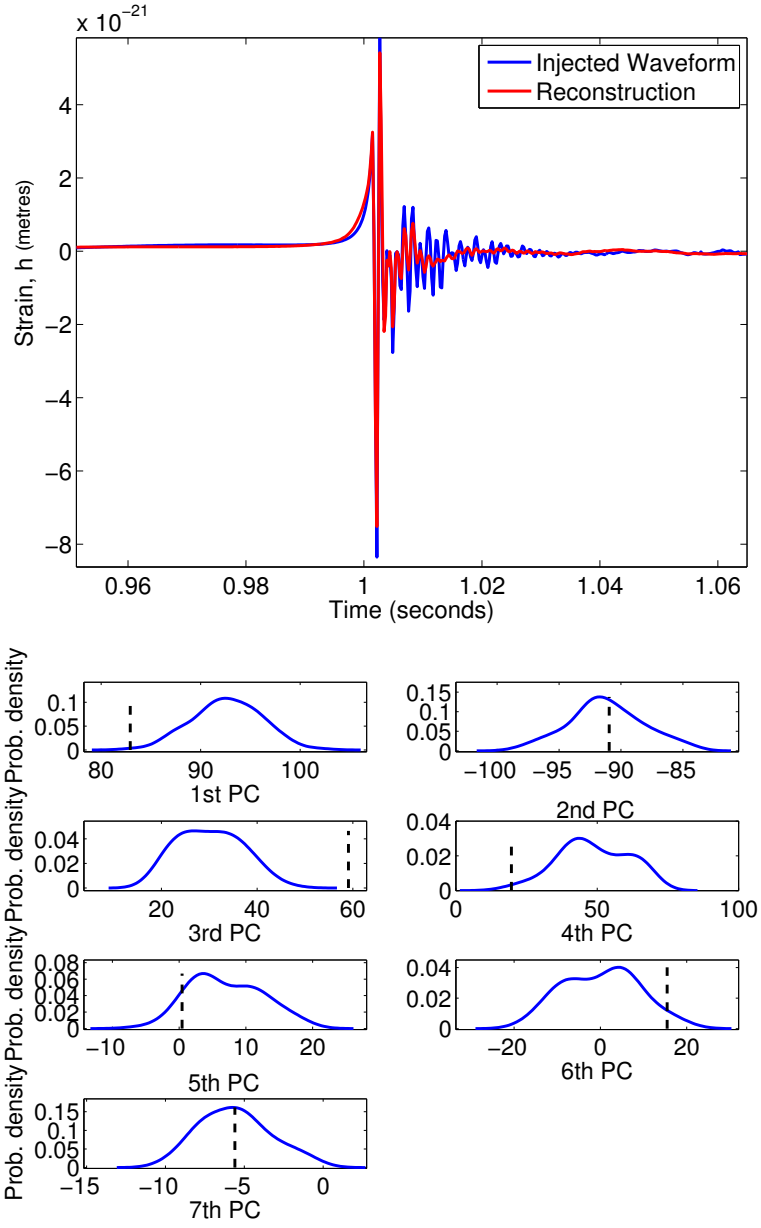

Figure 3.5: **Top Plot:** Plot of a `Dim` waveform with the reconstruction from TD_SMEE. Note that the waveform has been shifted and padded with zeroes so that the first peak occurs at around 1 second. **Bottom Plot:** Posterior distributions for the 7 PCs used to reconstruct a `Dim` waveform using time domain SMEE. The dashed line shows where the correct value for each PC coefficient lies.

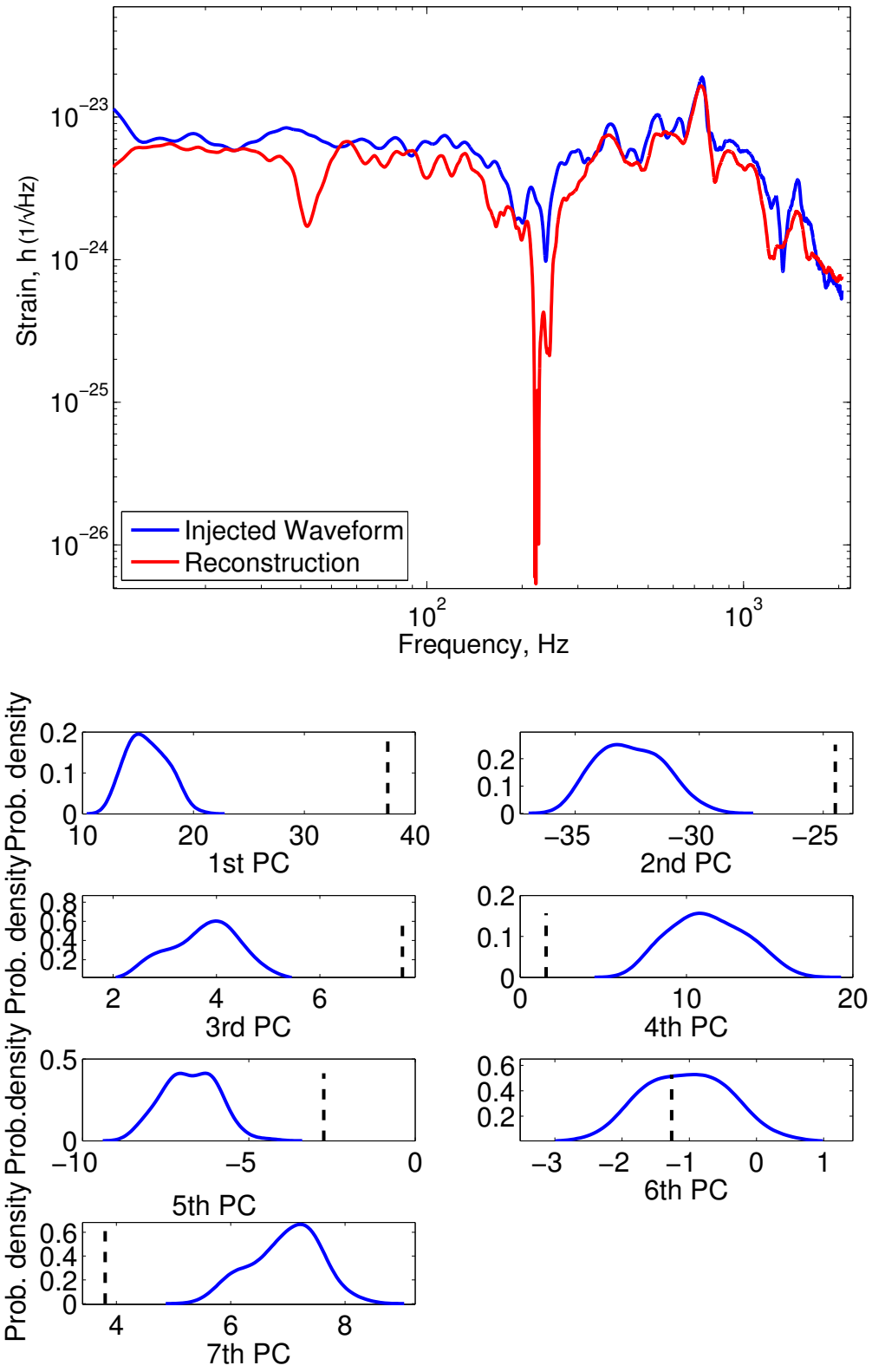

Figure 3.6: Same as Figure 3.5 but using PSD_SMEE to reconstruct the waveform.

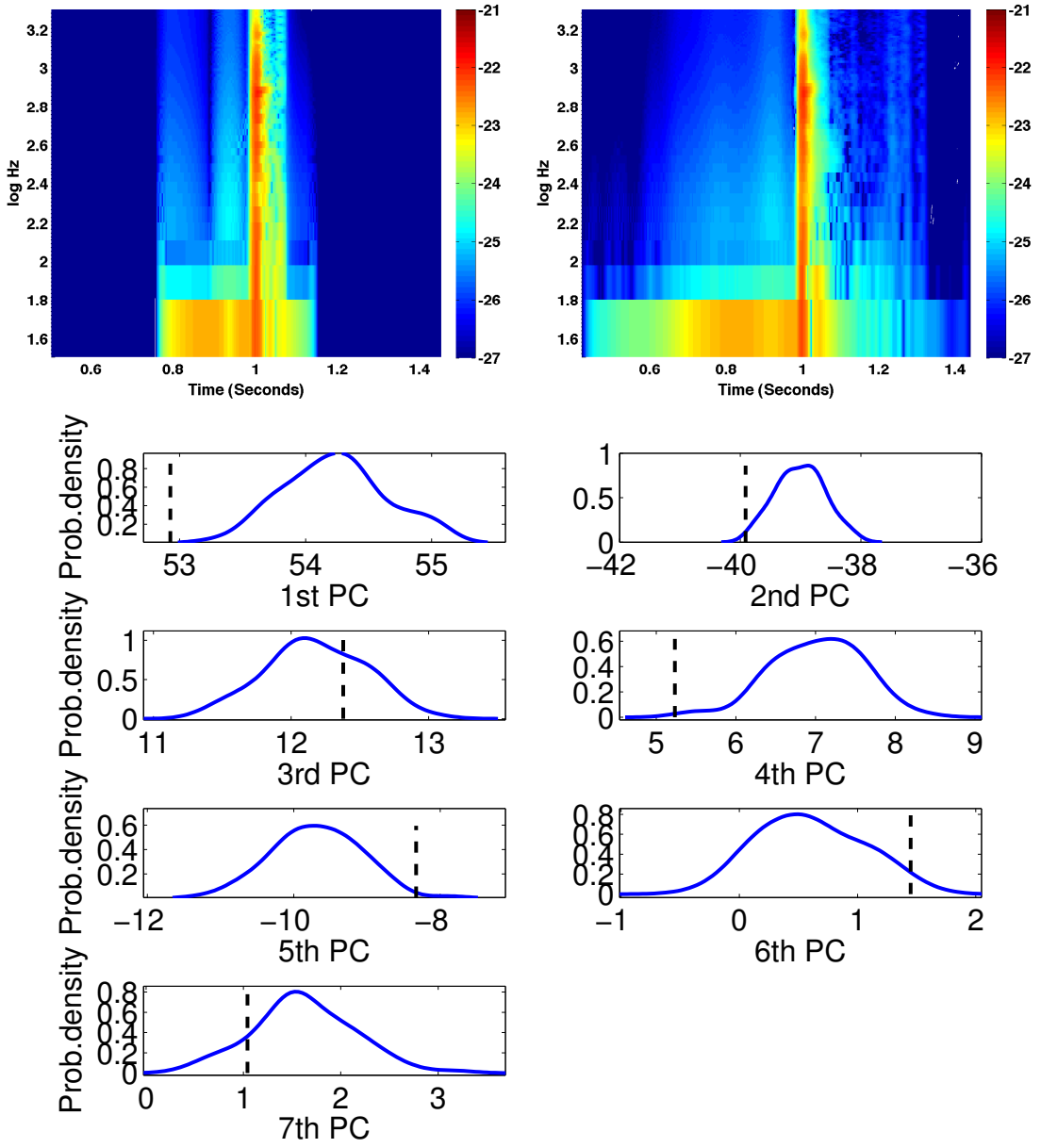

Figure 3.7: **Top Plot:** On the left is a spectrogram of a `Dim` waveform with the reconstruction on the right. Note that the `Dim` waveforms have been zero buffered in the time domain and appears dark blue when zero. The PCs will contain time domain information and will attempt to reconstruct areas which are at zero for this particular waveform. In both these plots the colour represents the strain, h. **Bottom Plot:** Posterior distributions for the 7 PCs used to reconstruct a `Dim` waveform using Spec_SMEE. The dashed line shows where the correct value for each PC coefficient lies.

Chapter 4

SMEE with One Detector

Chapter 3 described a Bayesian model selection pipeline known as the Supernova Model Evidence Extractor (SMEE). The purpose of SMEE is to determine if a detected gravitational wave from a supernova resembles any of the waveform mechanisms described in Section 1.7. Any gravitational wave detected will have been emitted directly from the core of the collapsing star which is entirely blocked from view in the electromagnetic spectrum. If SMEE is successful an inference can be made on the supernova mechanism which drives the explosion, and would therefore provide an enormous leap forward in the understanding of the physics of supernovae.

In this Chapter, the results for a simplified idealised version of SMEE is discussed. All results shown use 7 PCs (see Section 3.6) unless otherwise stated for one gravitational wave detector. In this chapter the detector is chosen to be an Advanced LIGO detector and all effects of sky position and the time of arrival of the signal are ignored i.e. $F_+ = 1$ and $T_d = 1$ in Equations 3.18 and 3.22. The scale factor s_f used to scale the distance or SNR of a waveform is kept as a fixed parameter and is not marginalised in the Nested Sampling Algorithm. As well as this, only the linear polarisation of the waveform is employed here as most supernova catalogues only contain this data.

In Section 4.1, SMEE will be tested with only noise (no signal is injected), the purpose of this being to investigate how SMEE works when it should agree with the model that there is only noise in the data. In Sections 4.2.1 to 4.2.4 the performance of time domain SMEE (TD_SMEE) is characterised through a series

of tests using simulated detector noise and gravitational waveforms. These tests are then repeated for the power spectrum (PSD_SMEE) and spectrogram domain (Spec_SMEE) versions of SMEE to investigate the strengths and limitations of each version of SMEE.

4.1 Response to Simulated Noise

It is necessary to quantify and understand SMEE's response to pure Gaussian detector noise without a signal being present in order to interpret the results of SMEE's bayesian model selection on the basis of Eq. 2.8. To this end, all three versions of SMEE are run on 10,000 randomised instances of Advanced LIGO detector noise (generated as described in Section 3.3) without the addition of a waveform. $\log B_{SN}$ (Eq. 3.27) is then computed in the absence of a waveform for each waveform model, S, with each model representing a different supernova mechanism.

4.1.1 Time Domain

The results for TD_SMEE, shown in Fig. 4.1, follow a Gaussian distribution with a mean corresponding to the expected value $-4\Delta f \sum_{i=1}^{N/2} \frac{h_i(\beta)^2}{2\sigma_i^2}$, where N is the length of the time domain data. This equation follows from equation 3.18 where the data is equal to zero and s'_f, $F'+$ and T'_d are equal to 1. The average logarithmic Bayes Factors obtained for 10,000 instances of noise indicate that noise, or any signal fully consistent with noise, is most likely to have a logarithmic Bayes Factor of -54.0 when TD_SMEE is run with 7 PCs of the `Dim` catalogue. For the `Ott` and `Mur` catalogues, the expected logarithmic Bayes Factors for pure Gaussian noise and 7 PCs are -52.1 and -52.3, respectively. The observed expectation values are very comparable to those calculated for the `Dim` (-53.9), `Ott` (-52.2), and `Mur` (-52.3) catalogues, respectively, verifying that TD_SMEE is operating as expected.

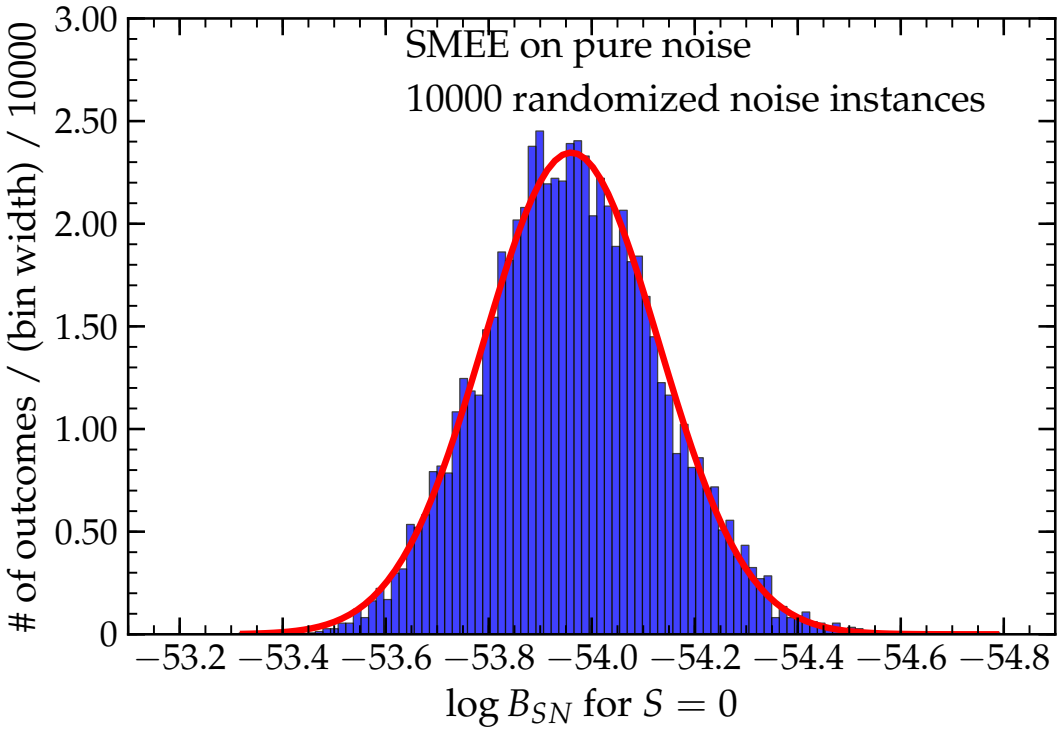

Figure 4.1: Results from running TD_SMEE with 7 PCs of the `Dim` catalogue and without an injected signal on 10,000 randomized instances of Gaussian Advanced LIGO noise, generated as described in Sec. 3.3. A signal consistent with noise is most likely to have a logarithmic Bayes Factor of ~ -54.0. The red line plots a fit to the data with a mean of -53.96 and a standard deviation $\sigma = 0.17$, from Logue et al. [70].

4.1.2 Power Spectrum Domain

In the case for PSD_SMEE, shown in Fig. 4.2 are a non-central χ^2 likelihood is used which has a mean corresponding to the expected value $-\sum_{i=1}^{N/2} \frac{h_i(\beta)^2}{2\sigma_i^2}$ where N is the length of the data seen in the time domain. This is the same as Equation **??** where the data term is equal to zero and s'_f, F'_+ and T'_d are all equal to one. Thus the distribution will appear to follow a Gaussian distribution as in the case of time domain data which has undergone a FFT. In the case of the power spectrum domain a signal fully consistent with noise is expected to give logarithmic Bayes Factor of -31.1, -30.6 and -30.8 when PSD_SMEE is run with 7 PCs of the `Dim`, `Ott` and `Mur` catalogues respectively. The observed values are consistent to those calculated for the `Dim` (-31.6), `Ott` (-30.8) and `Mur` (-30.8) catalogues so PSD_SMEE is operating as expected.

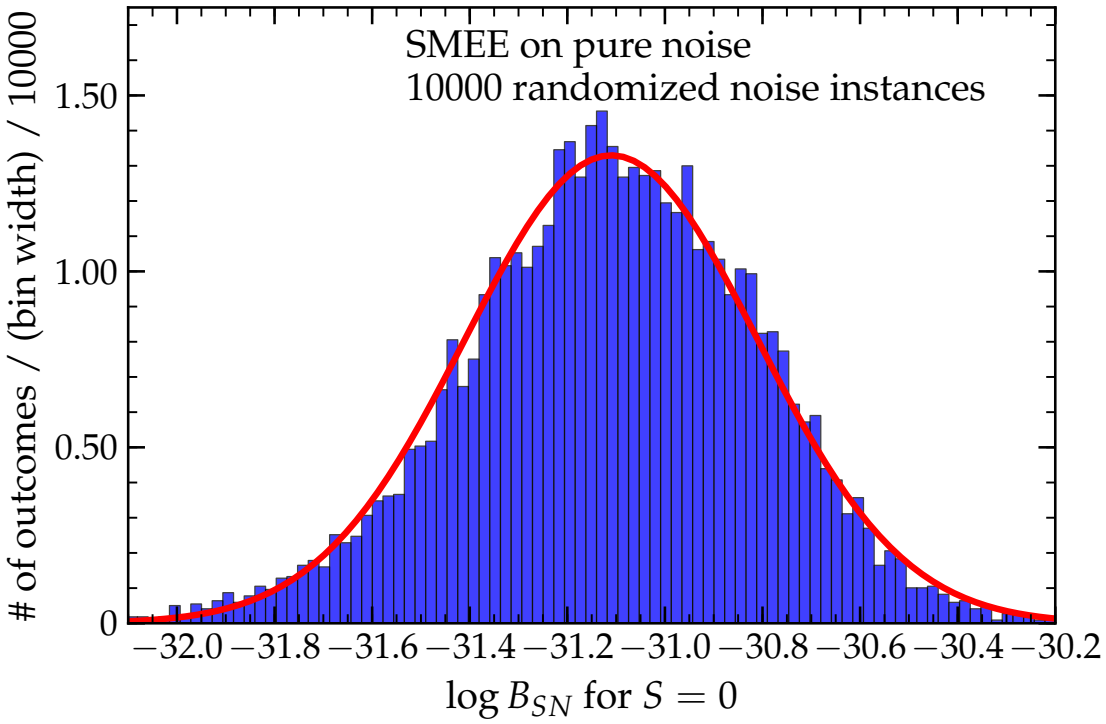

Figure 4.2: Results from running SMEE in the power spectrum domain with 7 PCs of the `Dim` catalogue and without an injected signal on 10,000 randomized instances of Gaussian Advanced LIGO noise, generated as described in Sec. 3.3. A signal consistent with noise is most likely to have a logarithmic Bayes Factor of ~ -31.6. The red line plots a fit to the data with a mean of -31.11 and a standard deviation $\sigma = 0.3$.

4.1.3 Spectrogram Domain

The results for Spec_SMEE, shown in Fig. 4.3, a signal fully consistent with noise is expected to give logarithmic Bayes Factor of -40.5, -40 and -40 when SMEE is run with 7 PCs of the `Dim`, `Ott` and `Mur` catalogues respectively. The observed values are consistent to those calculated for the `Dim` (-39.6), `Ott` (-39.1) and `Mur` (-39.3) catalogues so Spec_SMEE is operating as expected.

4.1.4 Threshold for Detection

Since the logarithmic Bayes Factors appear to follow a Gaussian distribution for all versions of SMEE, a threshold can be set using the standard deviations as an indicator for the expected false alarm rate. Ideally, for the `Dim` catalogue, a 1% false alarm rate would correspond to a threshold that is $\sim$2.6 times the standard deviation, corresponding to $\sim$0.44 above the mean. However, it is noted that the

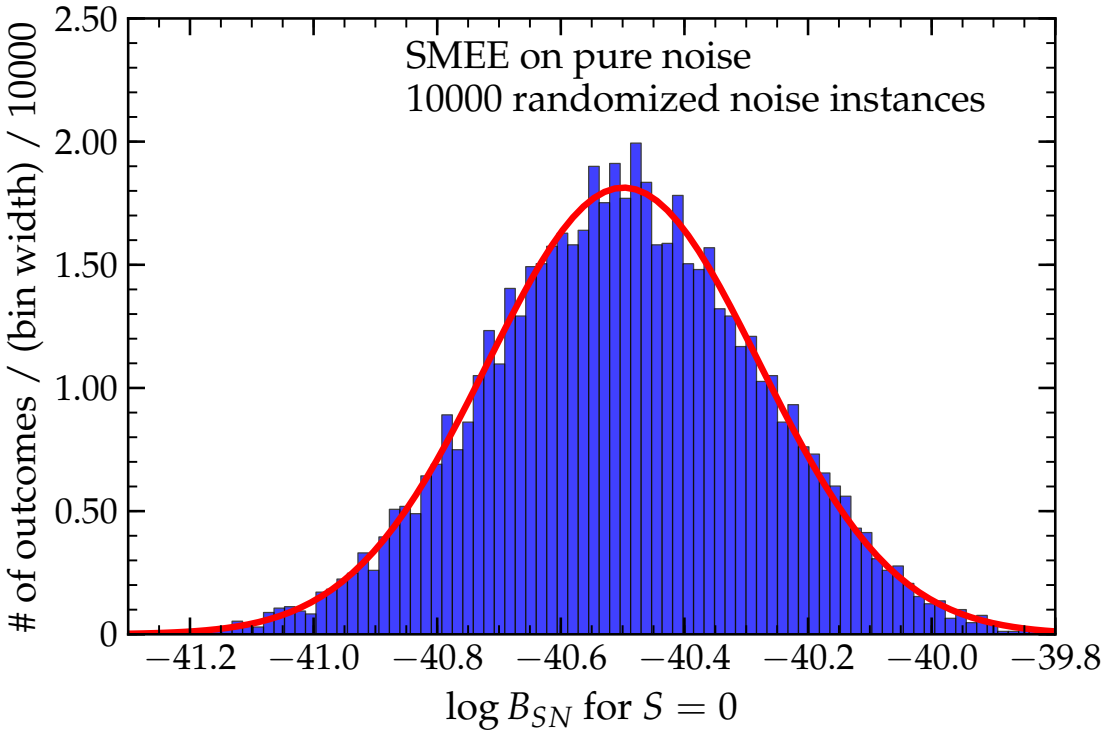

Figure 4.3: Results from running Spec_SMEE with 7 PCs of the `Dim` catalogue and without an injected signal on 10,000 randomized instances of Gaussian Advanced LIGO noise, generated as described in Sec. 3.3. A signal consistent with noise is most likely to have a logarithmic Bayes Factor of ~ -39.6. The red line plots a fit to the data with a mean of -40.49 and a standard deviation $\sigma = 0.22$.

expected logarithmic Bayes Factor value varies between different catalogues as well as the fact that different likelihood distributions are used. Because of this, for a fixed false alarm rate, a different threshold would be required for each catalogue. Since the focus here is to distinguish between different waveforms catalogues and not to perform a study on the detection efficiency of GWs, a conservative approach of simply setting a higher threshold is chosen. Therefore, to identify a waveform as being distinct from noise its $\log B_{SN}$ is first recalibrated such that $\log B_{SN} = 0$ when only noise is injected. This means that results from each version of SMEE can be easily compared. A $\log B_{SN} \geq 5$ is then chosen as the threshold where a confident statement that a waveform has been added to the noise. This threshold can then be carried forward to the case when comparing two waveform models M_i and M_j, i.e. M_i is favoured if $\log B_{ij} \geq 5$ and M_j is favoured if $\log B_{ij} \leq 5$.

4.2 Characterising SMEE in the Time Domain

4.2.1 Signal Model versus Noise Model

The minimal GW strength required for SMEE to be able to select the core-collapse supernova mechanism is an important question. The primary prerequisite for an incident GW to be useful for model selection is that SMEE can distinguish it from detector noise, i.e., the minimum signal strength (i.e., SNR) so that $\log B_{SN} \geq 5$ must be found (when 7 PCs are used; Eq. 3.27 and Section 4.1). The waveform SNR when the waveform can distinguish itself from the other models (supernova mechanisms) being tested can also be found. For the majority of results shown in this chapter, three models are used (the `Dim` PCs for the magnetorotational mechanism, `Mur` PCs for the neutrino mechanism, and `Ott` PCs for the acoustic mechanism), so to find the minimum signal strength we use Eq. 2.8 twice i.e. when $i = Dim$ and $j = Mur$ followed by $i = Dim$ and $j = Ott$. Out of the two Bayes Factors calculated the minimum one is chosen to ensure the signal is distinguished from both of the other models, this value is labelled as $\log B$.

All waveforms from the `Dim`, `Mur`, and `Ott` catalogues are processed by TD_SMEE where the SNR increases by 1 from 0 up to an SNR of 10, using 7 PCs generated from the model to which each waveform belongs. This is done in order to determine the range of minimum SNR required across and within core-collapse supernova GW types. The result of this exercise is shown in the in Figure 4.4 for TD_SMEE. In general a SNR of $\gtrsim 3 - 5$ is required for TD_SMEE to find $\log B_{SN} \geq 5$ in the idealized setting that is considered here. This is also the case for $\log B$ when all of the sets of PCs are compared in the bottom plot in Figure 4.4. This indicates that TD_SMEE can comfortably distinguish between the waveforms representing the 3 supernova mechanisms. In a more realistic scenario where there is no information about the sky position and there is an unknown arrival time along with the non-Gaussianity of real detector noise, a SNR in excess of 8 would be required for a detection statement (e.g., [41]).

In Figure 4.4, the waveforms associated with the acoustic mechanism (`Ott` catalogue) require the smallest SNR, followed by those of the magnetorotational mechanism (`Dim` catalogue) and the neutrino mechanism (`Mur` catalogue). This hierarchy in minimum SNR is not fundamental but a consequence that this test has been

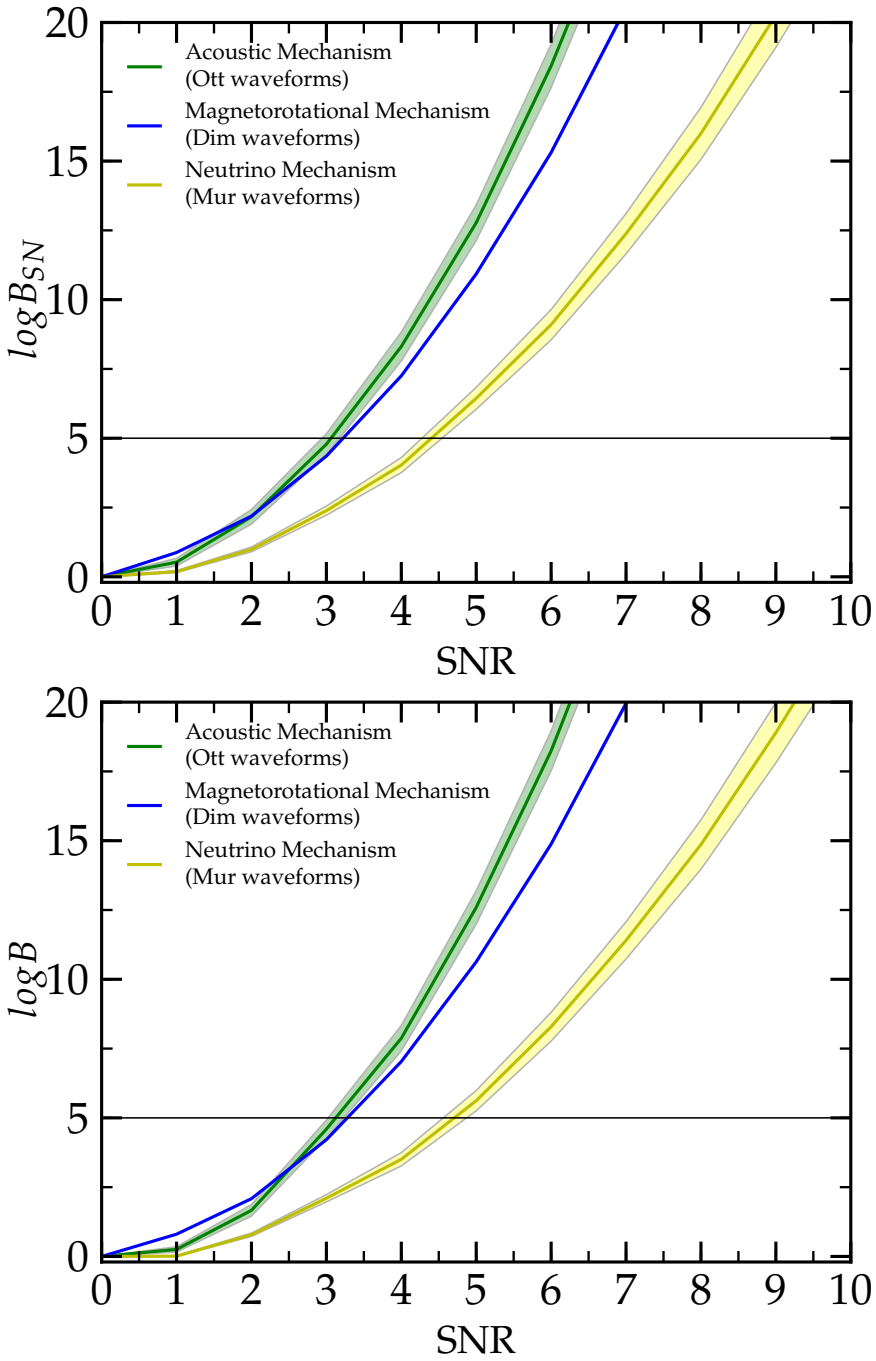

Figure 4.4: **Top panel:**Mean $\log B_{SN}$ as a function of signal-to-noise ratio (SNR; Eq. 3.15) for all waveforms from the `Mur`, `Ott` and `Dim` catalogues using 7 principal components (PCs) with TD_SMEE. The shaded areas represent the standard error in the mean value of $\log B_{SN}$ for each waveform catalogue computed as $\sigma = \pm N^{-1}(\Sigma_i(\bar{x} - x_i)^2)^{1/2}$, where $\bar{x}$ is the mean and x_i are the individual SNRs and N is the number of waveforms. Values of $\log B_{SN}$ below 5 in the 7-PC case indicate that the algorithm considers it more likely that there is no signal detectable in the noise. **Bottom panel:** This shows results for the same waveform catalogues when the results from the top panel are compared with the $\log B_{SN}$ found when attempting to reconstruct the supernova waveform with the other two sets of PCs. The log Bayes Factor is then found i.e. in the case of the `Dim` catalogue, $\log B$ is found for the `Dim` PCs versus the `Mur` and the `Ott` PCs. Out of the two results the minimum is plotted here to ensure that TD_SMEE can distinguish between all sets of PCs.

carried out using 7 PCs for each waveform catalogue. Since the `Ott` catalogue comprises only 7 waveforms, the set of 7 PCs completely spans it and allows near perfect reconstruction, maximizing $p(D|M_s)$ (Eq. 3.18). In the case of less than perfect knowledge of the signal, the minimum SNR will always be greater. This is why the `Dim` and `Mur` catalogues, which have many more than 7 waveforms, require larger minimum SNR than the `Ott` waveforms.

4.2.2 Distinguishing the Supernova Mechanism

The basic assumption of this work is that the neutrino, magnetorotational, and acoustic core-collapse supernova explosion mechanisms have robustly distinct GW signatures. This assumption can be tested by injecting waveforms into simulated noise and running TD_SMEE on the data using PCs of waveform catalogues representative of the neutrino, magnetorotational, and acoustic mechanisms. If this assumption is correct and the GW signatures of these mechanisms are truly distinct, then TD_SMEE should firstly yield the largest value of $\log B_{SN}$ when the set of PCs is used that corresponds to the mechanism the waveform is representative of. Secondly $\log B_{ij}$ (Eq. 2.8) should be positive (and larger than $\sim$5; see §4.1) if the injected waveform is most consistent with mechanism i, negative if it is most consistent with mechanism j, and near zero if the result is inconclusive.

TD_SMEE calculations are carried out for events located at 2 kpc, and 10 kpc and with 7 PCs. 2 kpc is nearby on the galactic scale, but the Galactic volume out to this radius already contains hundreds of supergiants, one of which may make the next galactic supernova [58]. 10 kpc is the fiducial Galactic distance scale and is considered to state what can be inferred throughout the Milky Way.

In Figure 4.5, results are shown for injection studies of *all* waveforms from the `Dim`, `Mur`, and `Ott` catalogues run through TD_SMEE and analysed with the `Dim`, `Mur`, and `Ott` PCs at a source distance of 10 kpc. The top left panel depicts the $\log B_{\texttt{DimMur}}$ result for waveforms from the `Dim` and `Mur` catalogues, that are taken to be representative of the magnetorotational and neutrino mechanism, respectively. Even at 10 kpc all waveforms characteristic for magnetorotational explosions are clearly identified as belonging to this mechanism. For the neutrino mechanism, the evidence is generally significantly weaker and only $\sim$44% of the `Mur` waveforms are identified with $\log B_{\texttt{DimMur}} < -100$ and none have $\log B_{\texttt{DimMur}} < -1000$, while $\sim$19%

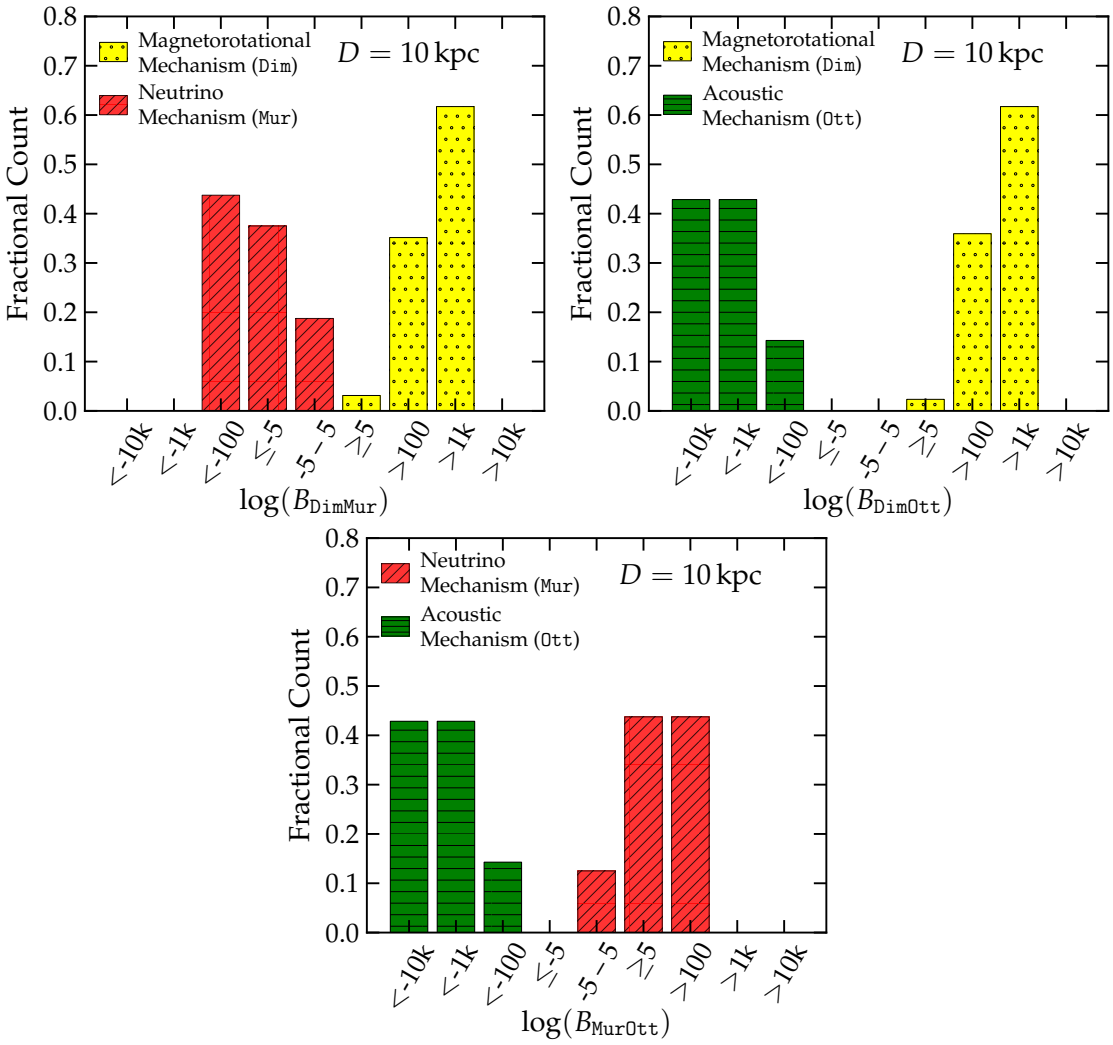

Figure 4.5: Histograms describing the outcome of signal model comparisons in the time domain by means of the Bayes Factors $\log B_{ij} = \log p(D|M_i) - \log p(D|M_j)$, where $i \neq j$ and M_i and M_j are signal models described by the `Dim` (magnetorotational mechanism), `Mur` (neutrino mechanism), and `Ott` (acoustic mechanism) waveform catalogues. The Bayes Factors are computed with 7 PCs and for a source distance of 10 kpc. A positive value $\log B_{ij}$ indicates that the injected waveform most likely belongs to model M_i, while a negative value suggest that model M_j is the more probable explanation. The bars are color-coded according to the type of injected waveform. The results are binned into ranges of varying size from < -10000 to > 10000 and the height of the bars indicates what fraction of the waveforms of a given catalogue falls into a given bin of $\log B_{ij}$. A range of $(-5, 5)$ of $\log B_{ij}$ is considered as inconclusive evidence (see §4.1), from Logue et al. [70].

are in the inconclusive regime of $-5 < \log B_{\mathtt{DimMur}} < 5$.

In the top right panel of Fig. 4.5, results are shown for $\log B_{\mathtt{DimOtt}}$ for waveforms corresponding to the magnetorotational (`Dim`) and the acoustic (`Ott`) mechanisms. All waveforms are correctly identified as most likely belonging to their respective catalogue/mechanism. Finally, the bottom panel of Fig. 4.5 presents $\log B_{\mathtt{MurOtt}}$

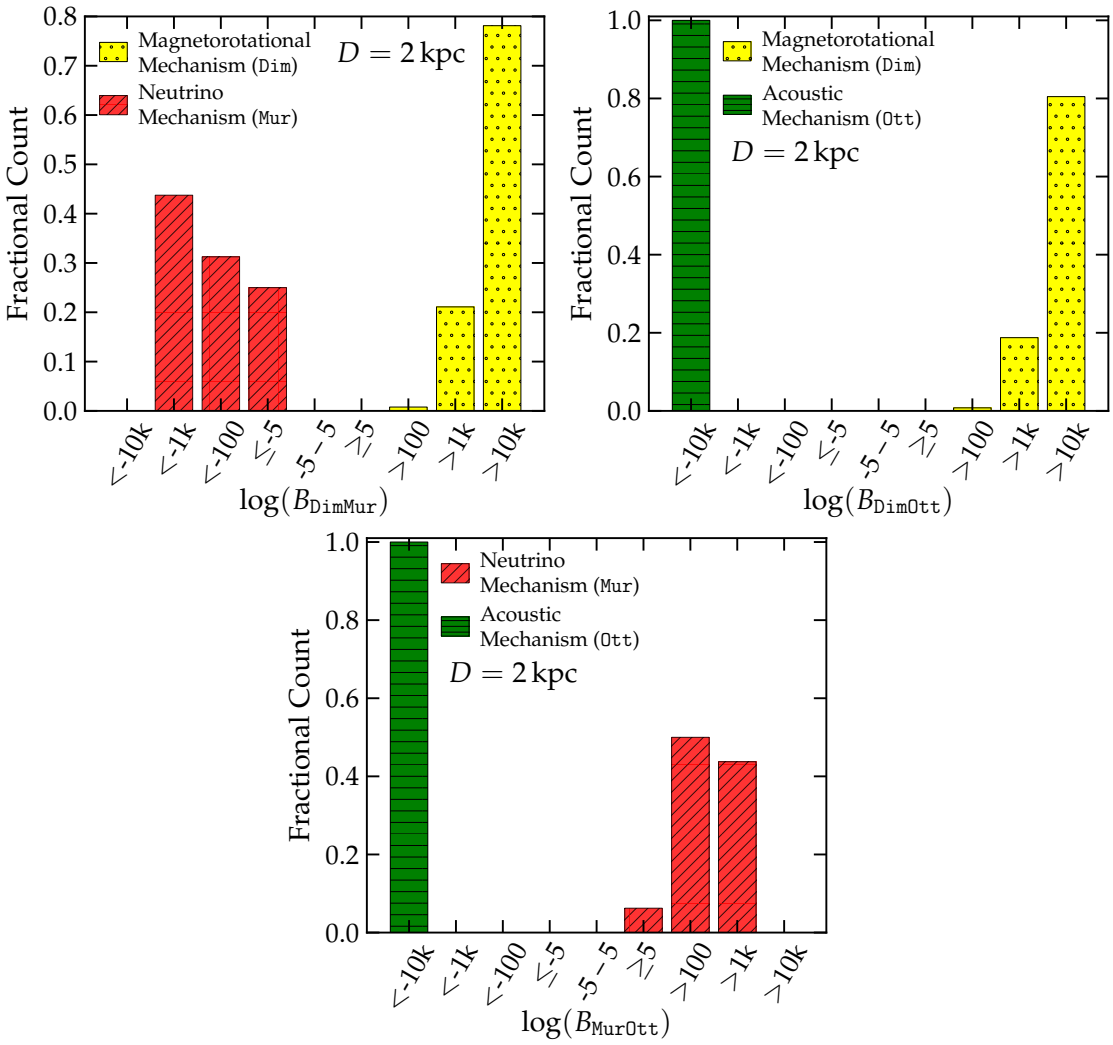

Figure 4.6: Same as Fig. 4.5, but computed for a source distance of 2 kpc, from Logue et al. [70].

for waveforms representative of the neutrino (`Mur`) and acoustic (`Ott`) mechanism. As in the previous panel, TD_SMEE associates the waveforms corresponding to the acoustic mechanism with high confidence to the `Ott` catalogue. The evidence suggesting correct association of the neutrino mechanism waveforms is considerably less strong, but $\log B_{\mathtt{MurOtt}}$ is still conclusive for ∼88% of the `Mur` waveforms.

Figure 4.6 shows the results for $\log B_{\mathtt{DimMur}}$, $\log B_{\mathtt{DimOtt}}$, and $\log B_{\mathtt{MurOtt}}$ obtained by TD_SMEE with 7 PCs at a source distance of 2 kpc. Here, all acoustic mechanism waveforms (`Ott` catalogue), all magnetorotational mechanism waveforms (`Dim` catalogue), and all neutrino mechanism waveforms (`Mur` catalogue) are correctly identified as belonging to their respective catalogue and explosion mechanism.

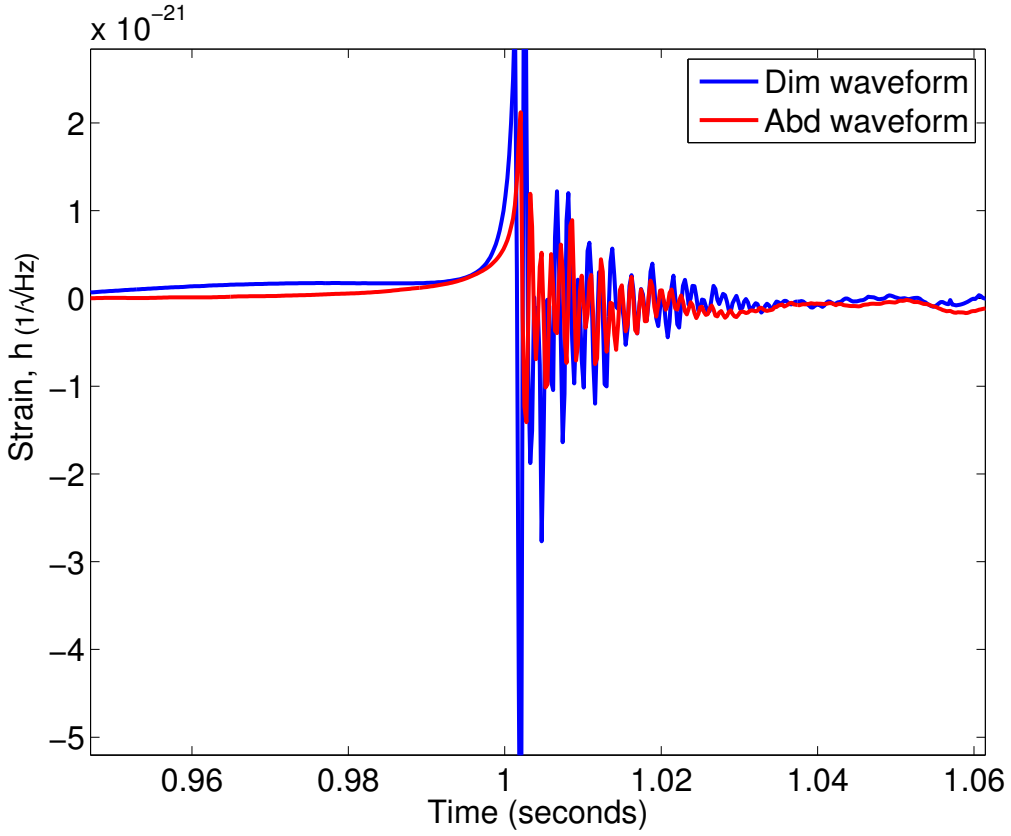

Figure 4.7: Plot of an `Abd` waveform on top of a `Dim` waveform. Both waveforms have a very similar length and shape. This will potentially make it more difficult for SMEE to distinguish these two catalogues.

4.2.3 Rotating Accretion-Induced Collapse or Rotating Iron Core Collapse?

The waveforms of the `Dim` catalogue are representative of the GW emitted by rotating collapse and bounce of iron cores of massive stars with ZAMS masses $\gtrsim 8 - 10\,M_{\odot}$. In the accretion-induced collapse (AIC) of rapidly rotating O-Ne white dwarfs, very similar dynamics occur and the corresponding GWs, as predicted by Abdikamalov *et al.* [1], share many of the basic features of the rotating iron core collapse and bounce waveforms of, e.g., the `Dim` catalogue (see the discussion in Sec. IV.C. of [1]). Hence, it is interesting to see if the SMEE model selection algorithm can tell them apart.

The PCs for the `Abd` catalogue are computed in the same fashion as done previously for the `Dim`, `Mur`, and `Ott` catalogues for each version of SMEE. All `Abd` and `Dim` waveforms are then injected into simulated Advanced LIGO noise. Since

the `Abd` and `Dim` catalogues are very similar (see Fig 4.7), the results found for `Dim` waveforms in Sec. 4.2.1 carry over directly to `Abd` waveforms. TD_SMEE is then run with 7 PCs to calculate $\log B_{\texttt{AbdDim}}$. The result for TD_SMEE is shown in Fig. 4.8 for source distances of 10 kpc and 2 kpc.

In spite of the strong general similarity of rotating iron core collapse and rotating AIC waveforms, TD_SMEE correctly identifies the majority of waveforms as most likely being emitted by a rotating iron core collapse or by rotating AIC. However, for a source at 10 kpc (top panel of Fig. 4.8), ∼6% of the `Dim` and ∼5% of the `Abd` are incorrectly identified as belonging to the respective other catalogue. For an additional 2% of the `Dim` waveforms and ∼14% of the `Abd` waveforms, $\log B_{\texttt{AbdDim}}$ is in the inconclusive region. At a source distance of 2 kpc (bottom panel of Fig. 4.8), 88% of the AIC (`Abd`) and 93% of the rotating core collapse (`Dim`) waveforms are correctly identified.

If one placed trust in the reliability of less dominant and more particular features of waveforms in the underlying catalogues, one could use a larger number of PCs in the analysis. In order to study the effect of using an increased number of PCs, the `Abd` vs. `Dim` comparison is repeated in the time domain with 14 PCs and it is found that the result is significantly worse than with 7 PCs: ∼61% of the `Abd` waveforms and ∼23% of the `Dim` catalogue are now incorrectly attributed to the respective other catalogue at 10 kpc. This counter intuitive and at first surprising result is readily explained by the overall great similarity of the AIC and iron core collapse waveforms and the nature of PCA and SMEE's bayesian model selection. The most robust features of each waveform catalogue are encapsulated in its first few PCs. The first `Dim` and `Abd` PCs are indeed significantly different, but subsequent `Abd` and `Dim` PCs exhibit rather similar secondary features. Since each PC carries the same weight in SMEE's evidence calculation, including a larger number of PCs dilutes SMEE's judgment in this case and leads to the observed false identifications.

4.2.4 Testing Robustness of SMEE using Non-catalogue Waveforms

In the previous sections, TD_SMEE's ability to identify a trial GW as belonging to a particular physical model (i.e., emission mechanism and/or explosion mechanism)

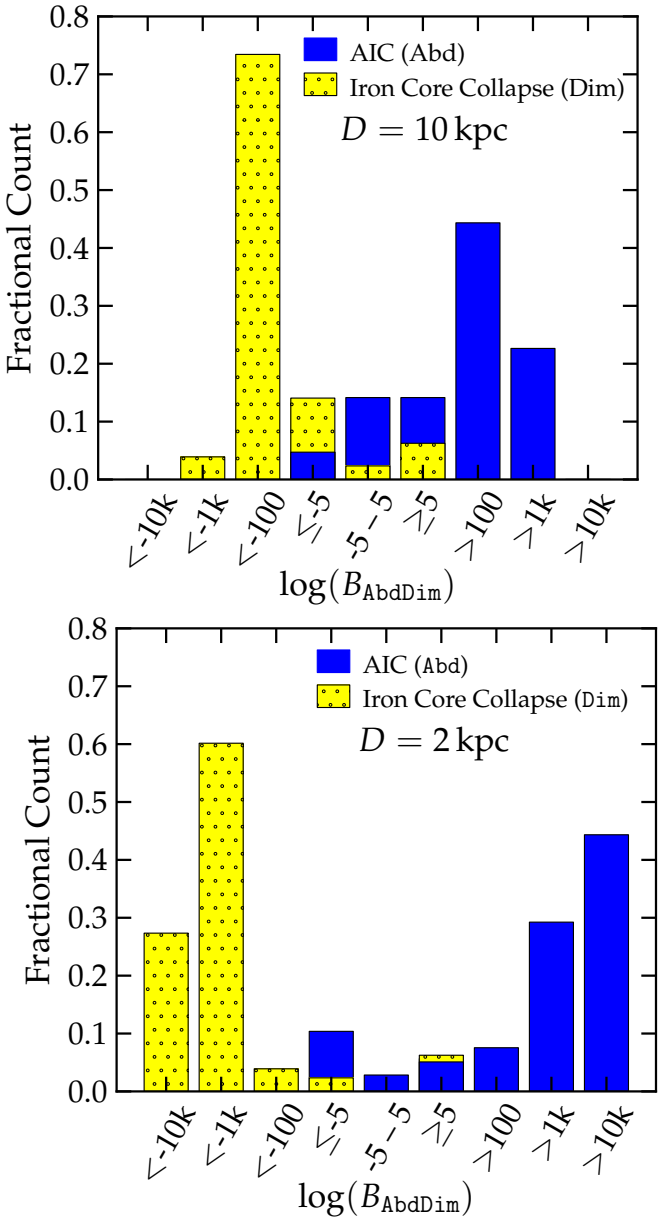

Figure 4.8: Outcome of the SMEE analysis in the time domain of injected rotating iron core collapse (`Dim` catalogue) and rotating accretion-induced collapse (AIC, `Abd` catalogue) waveforms. The top panel shows results for a source distance of 10 kpc and the bottom panel depicts the results for a distance of 2 kpc. The Bayes Factors $\log B_{\mathtt{AbdDim}}$ are computed on the basis of 7 PCs from the `Abd` and `Dim` catalogue. A positive value of $\log B_{\mathtt{AbdDim}}$ indicates that an injected waveform is most likely associated with rotating AIC and a negative value suggests it to be more consistent with rotating iron core collapse. The results are binned into ranges of varying size from < -10000 to > 10000 and the height of the colour-coded bars indicates what fraction of the waveforms of a given catalogue falls into a given bin of $\log B_{\mathtt{AbdDim}}$. A range of $(-5, 5)$ of $\log B_{ij}$ is considered as inconclusive evidence (see §4.1).

has been demonstrated. In this, however, the injected waveforms has been drawn directly from the catalogues used to generate the PCs. In other words, TD_SMEE has been given (limited) advanced knowledge about the injected waveforms.

Here, a much more stringent test of TD_SMEE's ability is carried out by injecting waveforms that were not employed in the initial PC generation and/or stem from completely independent catalogues.

Magnetorotational Mechanism

For the magnetorotational mechanism, three additional `Dim` waveforms (`DimExtra`, Sec. 1.7), are employed that were not included in the calculation of the `Dim` PCs. Furthermore, waveforms from rotating models of the `Sch` catalogue of Scheidegger *et al.* [102, 23] are tested (see Sec. 1.7). The results of both the $\log B_{SN}$ calculation for the magnetorotational, neutrino, and acoustic mechanism signal models are summarised in Tab. 4.1. `DimExtra` waveforms are identified as being most consistent with the `Dim` catalogue and, hence, the magnetorotational mechanism for all `DimExtra` signals out to distances $\gtrsim$10 kpc.

The `Sch` waveforms were generated with a completely different numerical code and thus allow for a truly independent test of TD_SMEE. Also, unlike the `Dim` waveforms, the `Sch` waveforms are based on 3D simulations. Hence, they are not linearly polarized. For consistency with our current approach, $h_\times$ is neglected and only h_+ as seen by an equatorial observer is injected. Results of TD_SMEE $\log B_{SN}$ calculations for all `Sch` waveforms are summarized in Tab. 4.1. TD_SMEE correctly identifies *all* injected `Sch` waveforms as indicative of magnetorotational explosions at a source distance of 2 kpc. At 10 kpc, still 91% of the injected `Sch` waveforms are attributed to the magnetorotational mechanism, which is an indication of the robustness of the GW associated with rapid rotation and magnetorotational explosions. The very few `Sch` waveforms that TD_SMEE is not able to clearly associated with the magnetorotational mechanism have such weak SNRs that they are more consistent with noise than with any of the catalogues at 10 kpc.

Table 4.1: $\log B_{SN}$ for gravitational waveforms that were not included in the catalogues used for PC computation using TD_SMEE. The `DimExtra`, `Sch`, `OttExtra`, and `Yak` waveforms are discussed in §1.7. Results are shown for source distances of 2 kpc and 10 kpc and for evaluations using 7 PCs. Larger values indicate stronger evidence that the waveform is matched to the model catalogue from which the PCs were constructed. $\log B_{SN} < 5$ when 7 PCs are used indicates that the injected signal is likely consistent with noise while larger values suggests that the signal belongs to the signal model whose PCs were used in the analysis.

Waveform	$\log B_{SN}$ Dim PCs		$\log B_{SN}$ Mur PCs		$\log B_{SN}$ Ott PCs	
	2 kpc	10 kpc	2 kpc	10 kpc	2 kpc	10 kpc
`DimExtra` [97]						
s20a1o05_shen	31227	1322	1952	85	78	5
s15a1o03_LS	95280	3933	2627	108	434	22
s40a1o10_LS	189967	7593	7054	243	139	7
`Sch` [102]						
R1E1CA	336	15	1	2	3	1
R1E1CA_L	163	9	1	2	2	0
R1E1DB	276	13	1	1	3	0
R1E3CA	456	22	3	2	4	1
R1STCA	120	7	4	2	1	0
R2E1AC	4489	204	13	2	15	1
R2E3AC	4105	187	15	1	9	1
R2STAC	8000	346	16	2	21	2
R3E1AC	37787	1592	121	6	116	7
R3E1AC_L	25817	1099	117	5	63	4
R3E1CA	30743	1301	119	6	91	5
R3E1DB	30862	1305	160	9	87	5
R3E2AC	27743	1180	82	6	86	5
R3E3AC	39922	1683	81	3	157	9
R3STAC	50646	2113	176	7	121	7
R4E1AC	103019	4259	259	10	429	21
R4E1CF	533131	21506	22451	827	1537	70
R4E1EC	81799	3401	248	11	380	20
R4E1FC	411834	16671	5404	186	1362	62
R4E1FC_L	95939	3968	233	8	370	19
R4STAC	127311	5233	669	27	408	20
R5E1AC	74266	3078	492	18	377	19
`OttExtra` [85]						
m15b6	14	0	4	1	296	17
s11WW	66	0	20	2	353	9
s25WW	88	4	3719	160	127736	5157
`Yak` [132]						
s12_matter	3	0	28	4	0	0
s15_matter	5	0	28	3	0	0
s25_matter	8	0	13	2	0	0

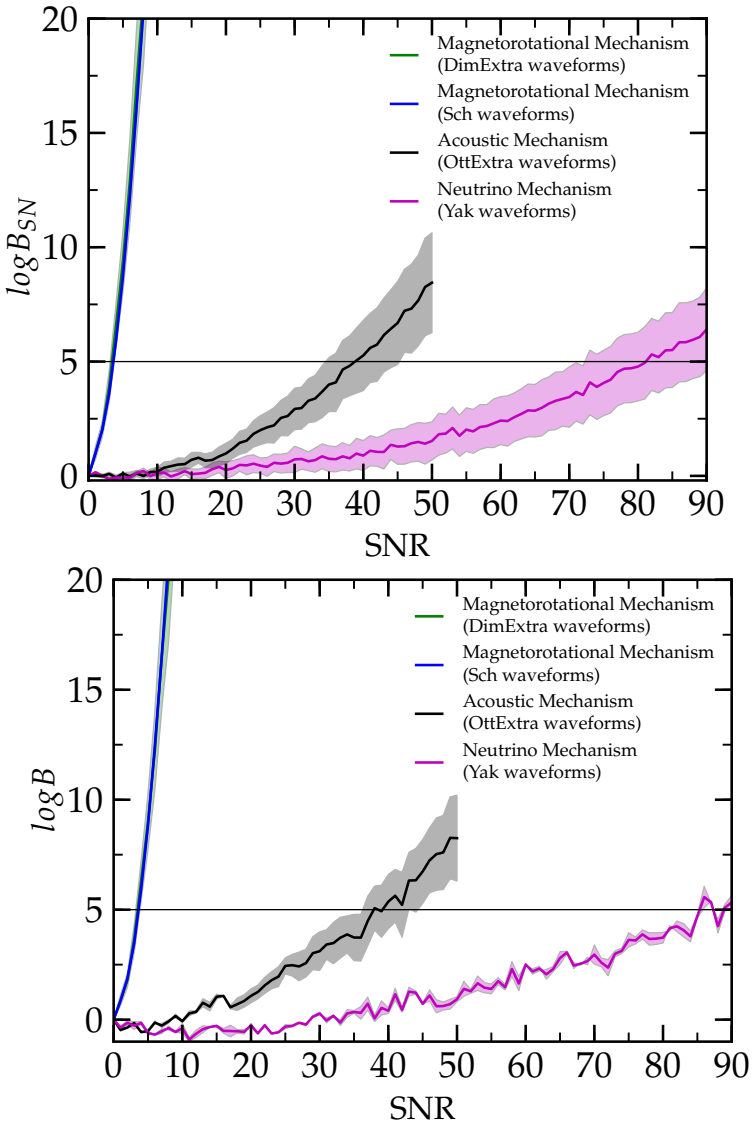

Figure 4.9: Mean and 1-σ range of $\log B_{SN}$ as a function of signal-to-noise ratio SNR comparing the waveform with noise evidence using TD_SMEE. The horizontal lines mark the threshold values of $\log B_{SN}$ above which it is considered a waveform to be distinct from Gaussian noise. **Top panel:** Results for the `Sch` and `DimExtra` in green and blue. These two were both reconstructed with 7 `Dim` PCs. Results for the `Yak` in mauve and `OttExtra` waveforms in black as reconstructed with 7 `Mur` for the first and 7 `Ott` PCs for the latter. The `Dim` PCs very efficiently reconstruct the `Sch` and `DimExtra` waveforms at moderate SNRs while the `Yak` and `OttExtra` require very high SNRs to be distinguished from noise by the `Mur` and `Ott` PCs, respectively. **Bottom panel:** This shows results for the same waveform catalogues when the results from the top panel are compared with the $\log B_{SN}$ found when attempting to reconstruct the desired waveform with the other two sets of PCs. The log Bayes Factor is then found i.e. in the case of the `Yak` catalogue $\log B$ is found for the `Mur` PCs versus the `Dim` and the `Ott` PCs. Out of the two results the minimum is plotted here to ensure that SMEE can distinguish between all sets of PCs. As in the results shown in the left panel the `Dim` PCs very efficiently reconstruct the `Sch` and `DimExtra` waveforms at moderate SNRs while the `Yak` and `OttExtra` require very high SNRs to be distinguished from both the noise and the other two sets of PCs.

Acoustic Mechanism

TD_SMEE's ability to identify core-collapse supernovae exploding via the acoustic mechanism is tested by utilising the three `OttExtra` waveforms (see Sec. 1.7). The results of this test are again summarized in Tab. 4.1. They suggest that the a-priori unknown `OttExtra` waveforms can be identified as belonging to the acoustic mechanism out to 2 kpc with great confidence when 7 PCs are used in the analysis. At 10 kpc, the waveforms are still correctly attributed to the acoustic mechanism, but the evidence is much weaker. The `OttExtra` 3 waveform (labelled as s25WW), which is clearly identified at 10 kpc, has an extreme SNR of $\sim$2530 at this distance, while the two other waveforms have SNRs of $\sim$50. TD_SMEE's difficulty is illustrated in the bottom panel of Fig. 4.9, which indicates that the `OttExtra` waveforms reach the threshold of $\log B \geq 5$ only for SNRs $\gtrsim$35, whereas `Ott` waveforms are identified already at SNRs $\gtrsim$4, if the full set of 7 PCs is used, see Figure 4.4 for the `Ott` results. This is a strong indication that the range of possible waveform features associated with the acoustic mechanism is not efficiently covered by the 7 PCs generated from the `Ott` catalogue. This could simply be attributed to the very small number of waveforms in this catalogue. However, when studying the `Ott` and `OttExtra` waveforms, one immediately notes that the time between the first peak (associated with core bounce) and the second peak (the global maximum, associated with the non-linear phase of the protoneutron star pulsations) varies significantly between waveforms. Since PCs are computed in the time domain, such large-scale features are imprinted onto the PCs and make it difficult to identify waveforms whose two peaks are separated by significantly different intervals. An alternative method that may work much better for waveforms of this kind is to compute PCs based on waveform power spectra, which would remove any potentially problematic phase information.

Neutrino Mechanism

TD_SMEE's ability to identify GWs emitted by core-collapse supernovae exploding via the neutrino mechanism is tested using the waveforms of the `Yak` catalogue (see Sec. 1.7) that were obtained with a completely different numerical code. The three available `Yak` waveforms are injected into Advanced LIGO noise and TD_SMEE is run on them to compute $\log B_{SN}$. The results are listed in Tab. 4.1. TD_SMEE

correctly and clearly associates the `Yak` waveforms with the `Mur` PCs at 2 kpc. However at 10 kpc the `Yak` waveforms appear to be most consistent with noise. The bottom panel of Fig. 4.9 shows that the `Yak` waveforms require an SNR to be clearly associated with the neutrino mechanism that is more than ∼18 times higher than for `Mur` waveforms. This rather disappointing result can be explained as follows: While the `Yak` waveforms are qualitatively very similar to the `Mur` waveforms, they differ significantly in quantitative aspects. The `Yak` waveforms are generally only half as long (∼1 s for `Mur` and 0.5 s for `Yak`, whose models explode much earlier than the `Mur` models). This may be due to the more simplified treatment of gravity and neutrino microphysics and transport in the study of Murphy *et al.* [79] underlying the `Mur` catalogue compared to the work of Yakunin *et al.* [132] that led to the `Yak` catalogue.

4.3 Characterising SMEE in the Power Spectrum Domain

4.3.1 Signal Model versus Noise Model

The results shown in Section 4.2.1 are repeated for the power spectrum domain version of SMEE (PSD_SMEE), see Fig. 4.10. In this case a larger SNR compared to the time domain is required for PSD_SMEE to find $\log B_{SN} \geq 5$ in the idealized setting that is considered here. The `Dim` waveforms requires the smallest SNR of 18 followed by those of the `Mur` catalogue with 24 and finally the `Ott` catalogue which requires a SNR of 27.

The SNR required to correctly determine the correct model increases with the `Dim` and `Mur` catalogues. This indicates that $\log B_{SN}$ may be greater than zero when the wrong set of PCs is used to reconstruct the signal. In this case $\log B_{SN}$ is always greatest when the correct set of PCs is used meaning that all waveforms can still be matched to the correct explosion mechanism.

As in the case of the time domain the `Ott` catalogue comprises only 7 waveforms, so it is expected that they will be accurately reconstructed. However in this case the `Ott` waveforms are the last catalogue to reach the detection threshold. This

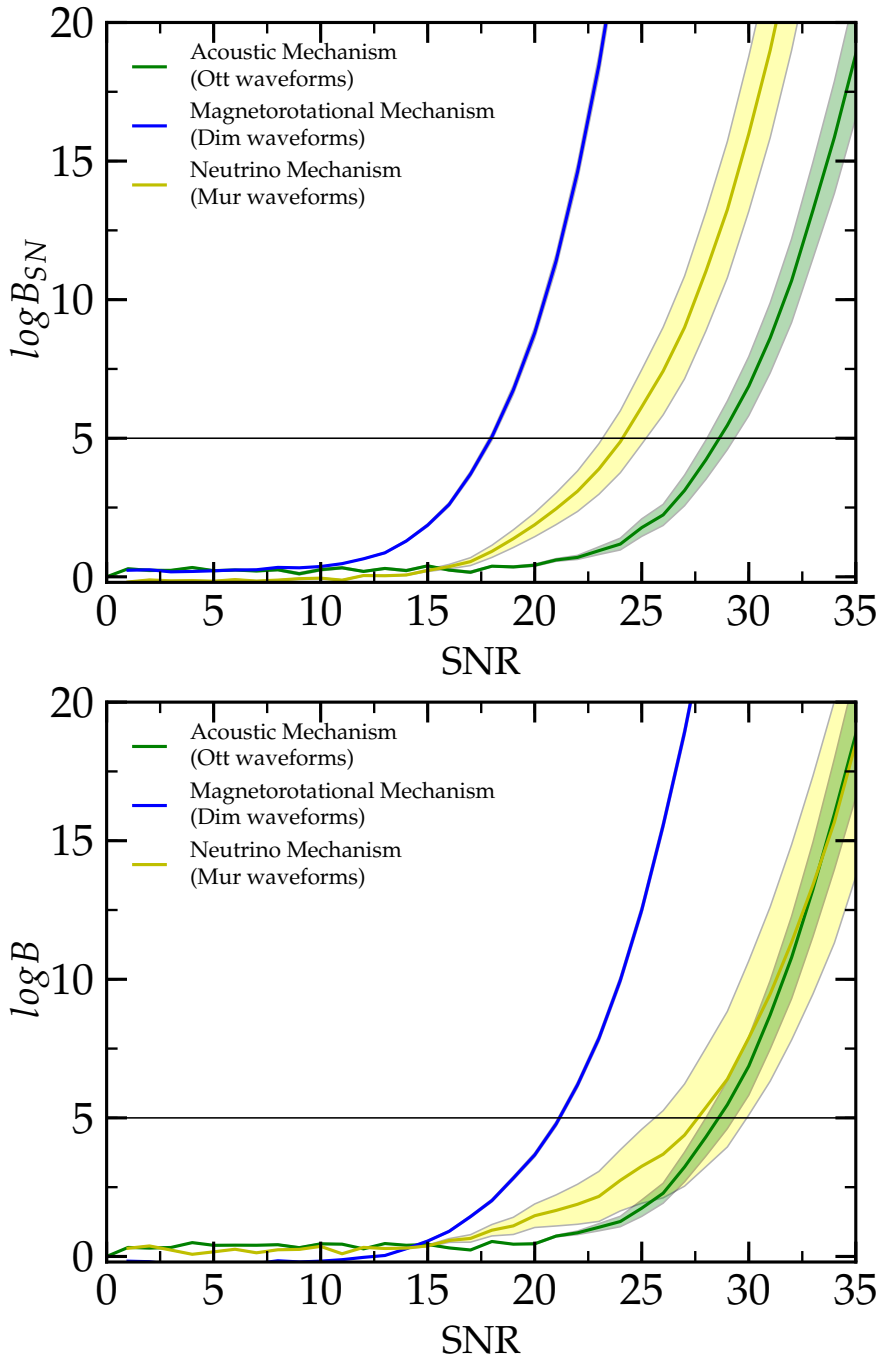

Figure 4.10: **Top panel:** Mean $\log B_{SN}$ using the PSD_SMEE as a function of signal-to-noise ratio (SNR; Eq. 3.15) for all waveforms from the `Mur`, `Ott` and `Dim` catalogues 7 principal components (PC). The shaded areas represent the standard error in the mean value of $\log B_{SN}$ for each waveform catalogue computed as $\sigma = \pm N^{-1}(\Sigma_i(\bar{x} - x_i)^2)^{1/2}$, where $\bar{x}$ is the mean and x_i are the individual SNRs and N is the number of waveforms. Values of $\log B_{SN}$ below 5 indicate that the algorithm considers it more likely that there is no signal detectable in the noise. **Bottom panel:** This shows results for the same waveform catalogues when the results from the top panel are compared with the $\log B_{SN}$ found when attempting to reconstruct the injected waveform with the other two sets of PCs. The log Bayes Factor is then found i.e. in the case of the `Dim` catalogue $\log B$ is found for the `Dim` PCs versus the `Mur` and the `Ott` PCs. Out of the two results the minimum is plotted here to ensure that SMEE can distinguish between all sets of PCs.

is due to the fact that when calculating the power spectrum all time and phase information is lost which means the waveforms are no longer as distinct. As well as this the waveforms peak at around 10^3 Hz where Advanced LIGO noise is higher, see Fig 4.11. This also applies to the `Mur` catalogue where losing the phase data has diminished PSD_SMEE's ability to distinguish the waveform from the noise as well as the fact that due to using only 7 PCs there is less than perfect knowledge of the waveform. The `Dim` catalogue on the other hand performs the best out of all three catalogues due to the fact that even with only 7 PCs there is enough information to satisfactorily reconstruct the injected signals thus giving a larger value for the evidence.

4.3.2 Distinguishing the Supernova Mechanism

Following the same process as described in Section 4.2.2, results are shown in Fig. 4.12 using PSD_SMEE. The top left panel depicts the $\log B_{\texttt{DimMur}}$ result and like TD_SMEE, the vast majority of waveforms characteristic for magnetorotational explosions are clearly identified as belonging to this mechanism. For the neutrino mechanism, the evidence is significantly weaker and none of the `Mur` waveforms are outside the inconclusive regime of $-5 < \log B_{\texttt{DimMur}} < 5$. This is due to the low SNR of the waveforms at 10 kpc, neither the `Dim` nor `Mur` PCs can distinguish the waveform from the noise.

In the top right panel of Fig. 4.12, results are shown for $\log B_{\texttt{DimOtt}}$. Most waveforms are correctly identified as most likely belonging to their respective catalogue/mechanism. Finally, the bottom panel of Fig. 4.12 presents $\log B_{\texttt{MurOtt}}$. As in the previous panel, PSD_SMEE associates the waveforms corresponding to the acoustic mechanism with high confidence to the `Ott` catalogue. The evidence suggesting correct association of the neutrino mechanism waveforms is considerably less strong, with $\log B_{\texttt{MurOtt}}$ being in the inconclusive region for all of the `Mur` waveforms.

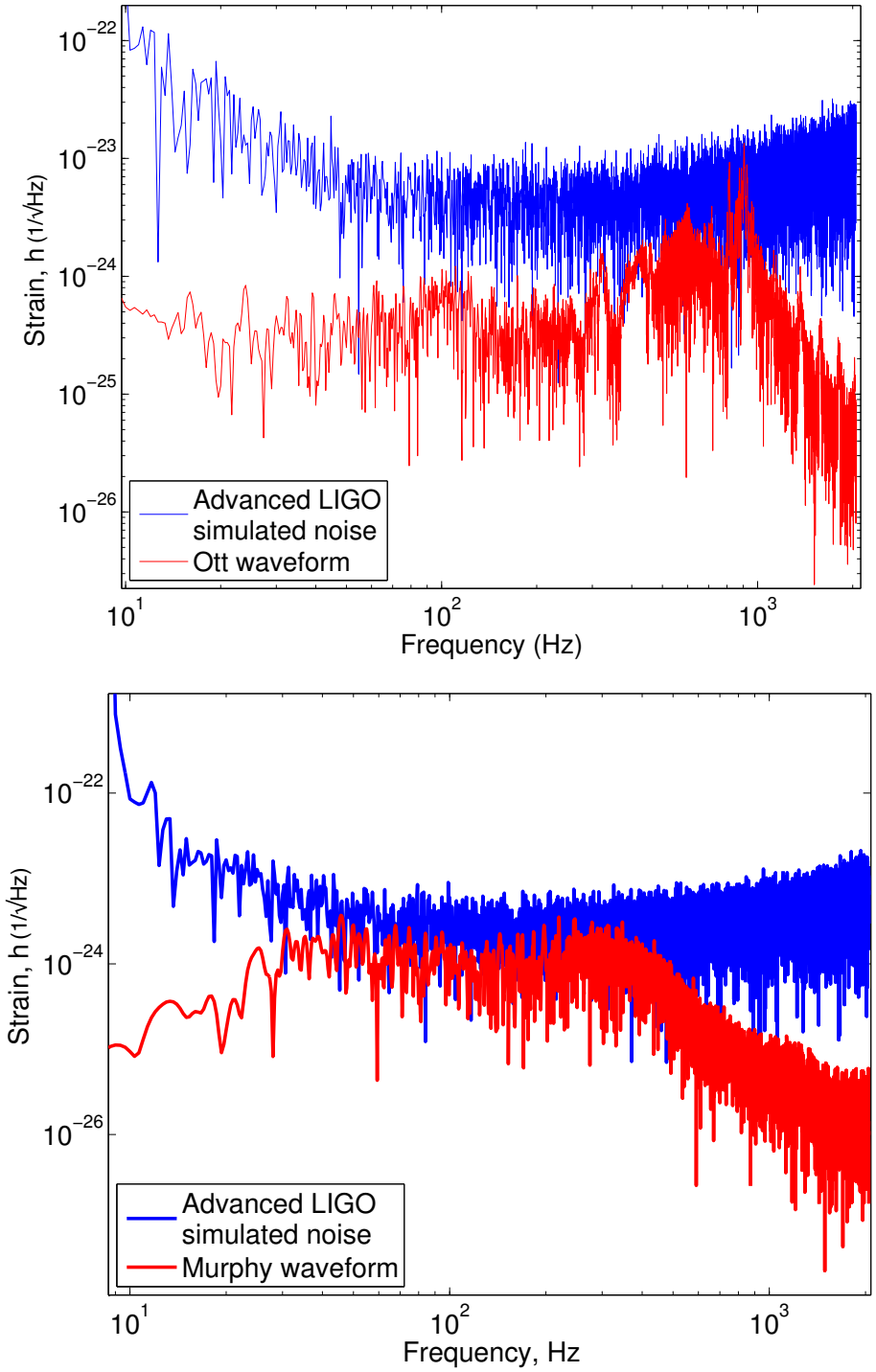

Figure 4.11: **Top panel:** Plot showing an `Ott` waveform with a SNR of 30 at 10kpc. This highlights the point that there are no distinct features in this signal until a frequency of around 10^3 Hz which makes it difficult for PSD_SMEE to distinguish signals from the noise at SNR values smaller than 30. **Bottom panel:** Plot showing a `Mur` waveform with a SNR of 20 at 10kpc. This shows that there are few distinct features in the PSD making it difficult for PSD_SMEE to distinguish the signal from the noise at this SNR.

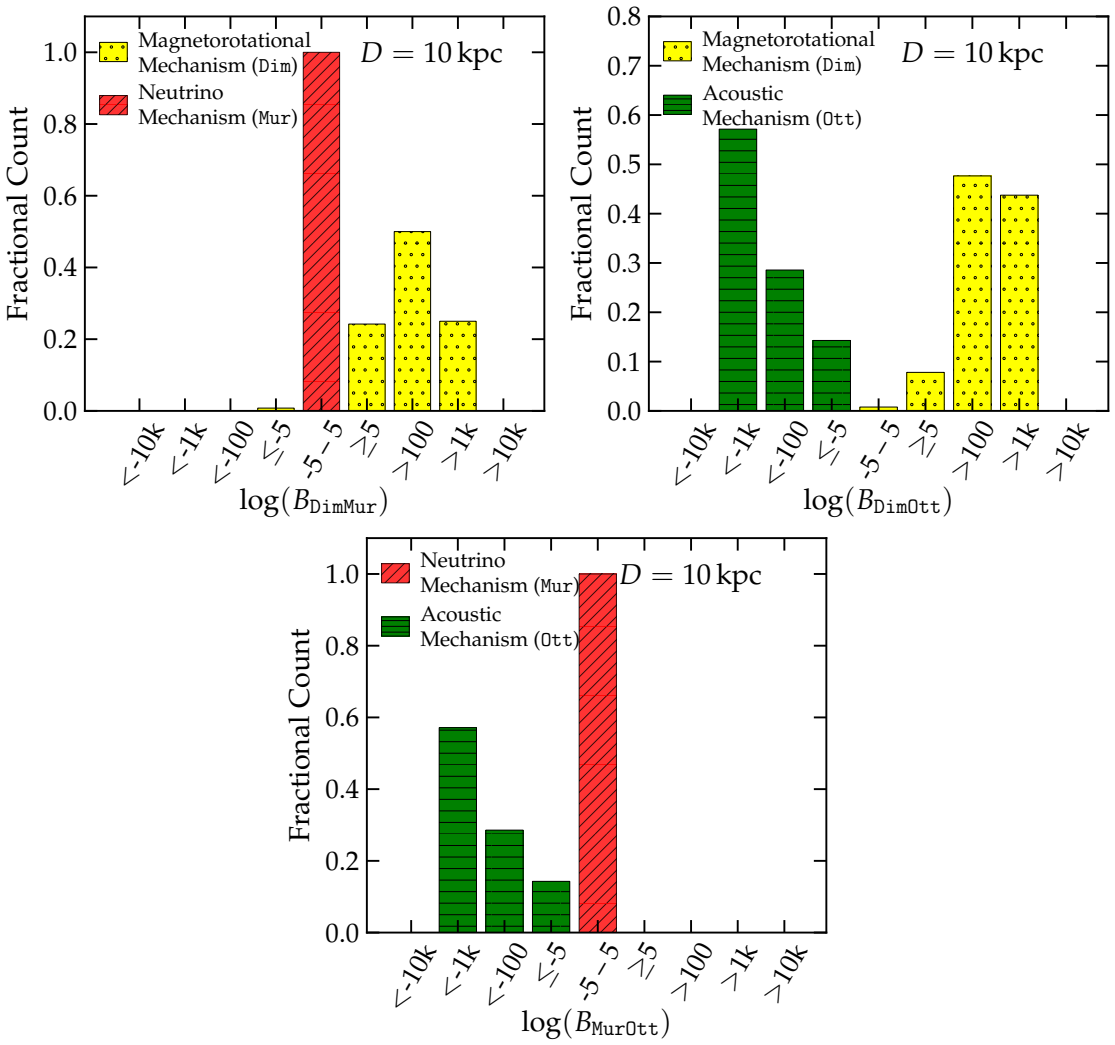

Figure 4.12: Histograms describing the outcome of signal model comparisons in the power spectrum domain by means of the Bayes Factors $\log B_{ij} = \log p(D|M_i) - \log p(D|M_j)$, where $i \neq j$ and M_i and M_j are signal models described by the `Dim` (magnetorotational mechanism), `Mur` (neutrino mechanism), and `Ott` (acoustic mechanism) waveform catalogues. The Bayes Factors are computed with 7 PCs and for a source distance of 10 kpc. A positive value $\log B_{ij}$ indicates that the injected waveform most likely belongs to model M_i, while a negative value suggest that model M_j is the more probable explanation. The bars are colour-coded according to the type of injected waveform. The results are binned into ranges of varying size from < -10000 to > 10000 and the height of the bars indicates what fraction of the waveforms of a given catalogue falls into a given bin of $\log B_{ij}$. A range of $(-5, 5)$ of $\log B_{ij}$ is considered as inconclusive evidence (see §4.1).

Figure 4.13 shows the results for $\log B_{\mathtt{DimMur}}$, $\log B_{\mathtt{DimOtt}}$, and $\log B_{\mathtt{MurOtt}}$ obtained by PSD_SMEE with 7 PCs at a source distance of 2 kpc. Here, all acoustic mechanism waveforms (`Ott` catalogue) and the majority of all neutrino mechanism waveforms (`Mur` catalogue) are correctly identified as belonging to their respective catalogue and explosion mechanism however ∼12.5% still do not have a large enough SNR to be distinguished from the noise. In the case of the magnetorotational mech-

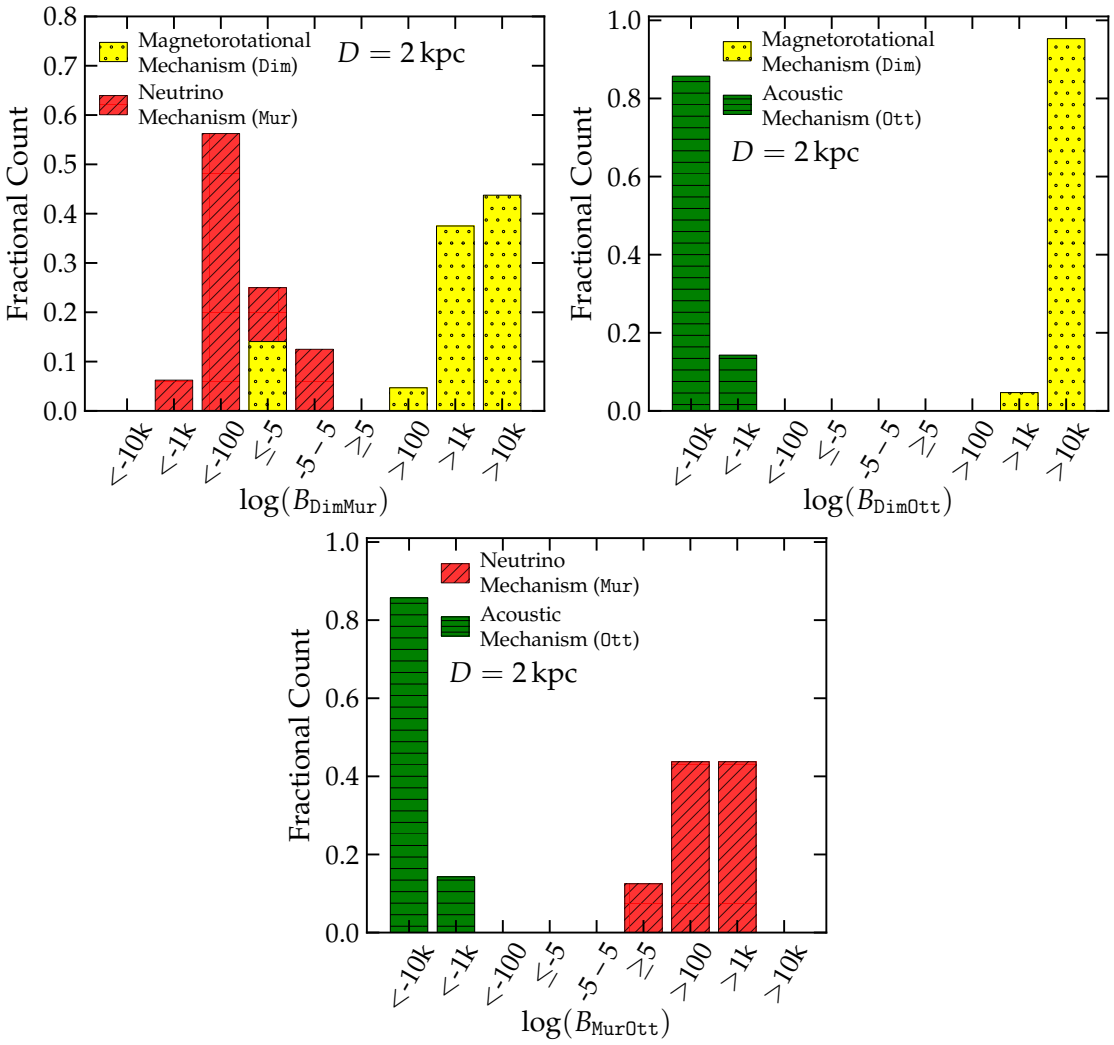

Figure 4.13: Same as Fig. 4.12, but computed for a source distance of 2 kpc.

anism, ∼13% of the `Dim` waveforms incorrectly favour the neutrino mechanism. This is due to the fact that we do not have complete information on either of these catalogues. These `Dim` waveforms have features which are not reconstructed well using the `Dim` PCs so that the `Mur` PCs are able to reconstruct the waveform with a higher evidence, see Fig 4.14.

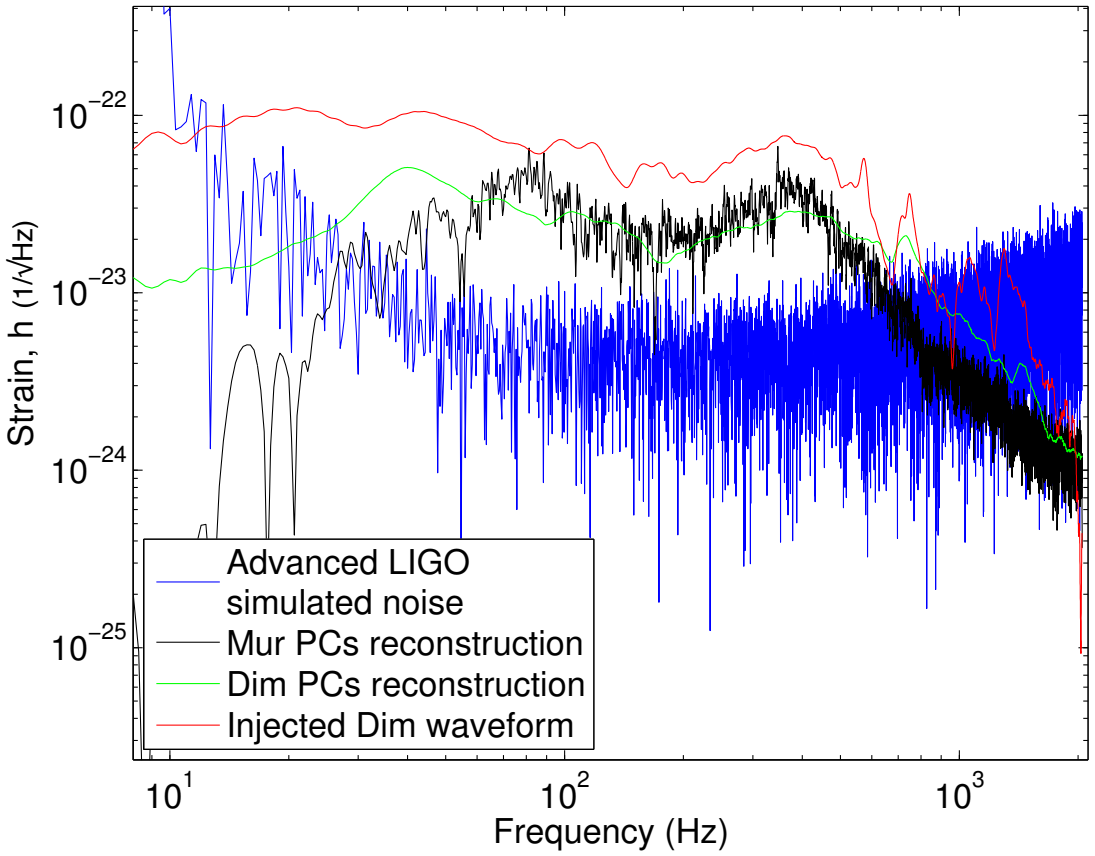

Figure 4.14: Figure showing the reconstruction of a `Dim` waveform using the `Mur` and `Dim` PCs. In the frequency band that Advanced LIGO is most sensitive, between 10^2 and 10^3 Hz the reconstruction using the `Mur` PCs is closer in scale to the injected waveform. Because of this it has a higher evidence value and thus PSD_SMEE incorrectly favours this over the reconstruction using the `Dim` PCs.

4.3.3 Rotating Accretion-Induced Collapse or Rotating Iron Core Collapse?

In the power spectrum domain, SMEE performs significantly worse than in the time domain version of SMEE. In this case, for a source at 10 kpc (top panel of Fig. 4.15), the majority of the `Dim` are correctly identified as most likely being emitted by a rotating iron core collapse with only ∼10% being in the inconclusive region or incorrectly identified as belonging to the `Abd` catalogue. However, for the `Abd` waveforms ∼40% of the `Abd` are incorrectly identified as belonging to the respective other catalogue or have a Bayes Factor between -5 and 5.

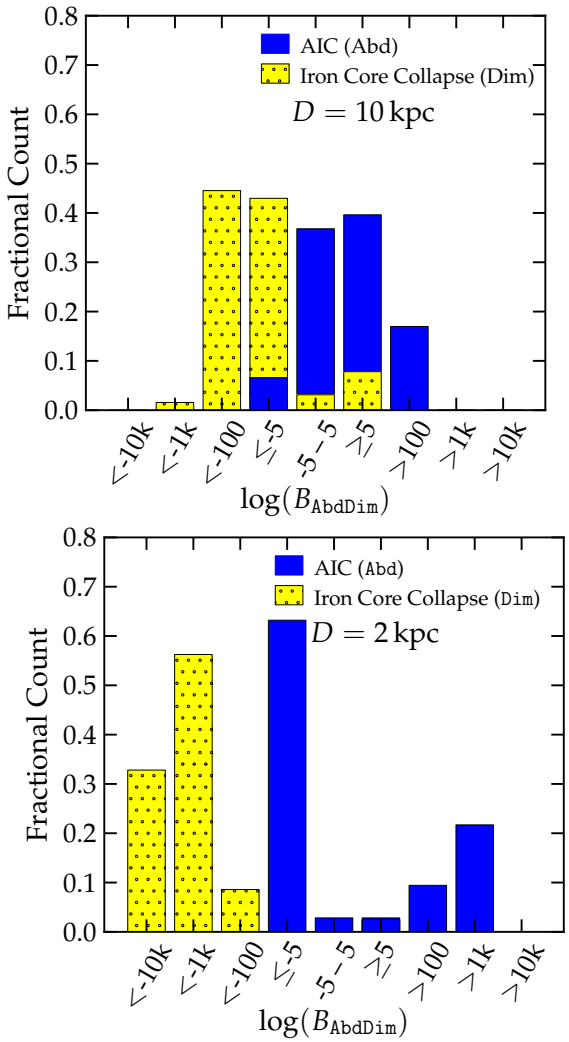

Figure 4.15: Outcome of the SMEE analysis in the power spectrum domain of injected rotating iron core collapse (`Dim` catalogue) and rotating accretion-induced collapse (AIC, `Abd` catalogue) waveforms. The upper panel shows results for a source distance of 10 kpc and the lower panel depicts the results for a distance of 2 kpc. The Bayes Factors $\log B_{\mathtt{AbdDim}}$ are computed on the basis of 7 PCs from the `Abd` and `Dim` catalogue. A positive value of $\log B_{\mathtt{AbdDim}}$ indicates that an injected waveform is most likely associated with rotating AIC and a negative value suggests it to be more consistent with rotating iron core collapse. The results are binned into ranges of varying size from < -10000 to > 10000 and the height of the color-coded bars indicates what fraction of the waveforms of a given catalogue falls into a given bin of $\log B_{\mathtt{AbdDim}}$. A range of $(-5, 5)$ of $\log B_{ij}$ is considered as inconclusive evidence (see §4.1).

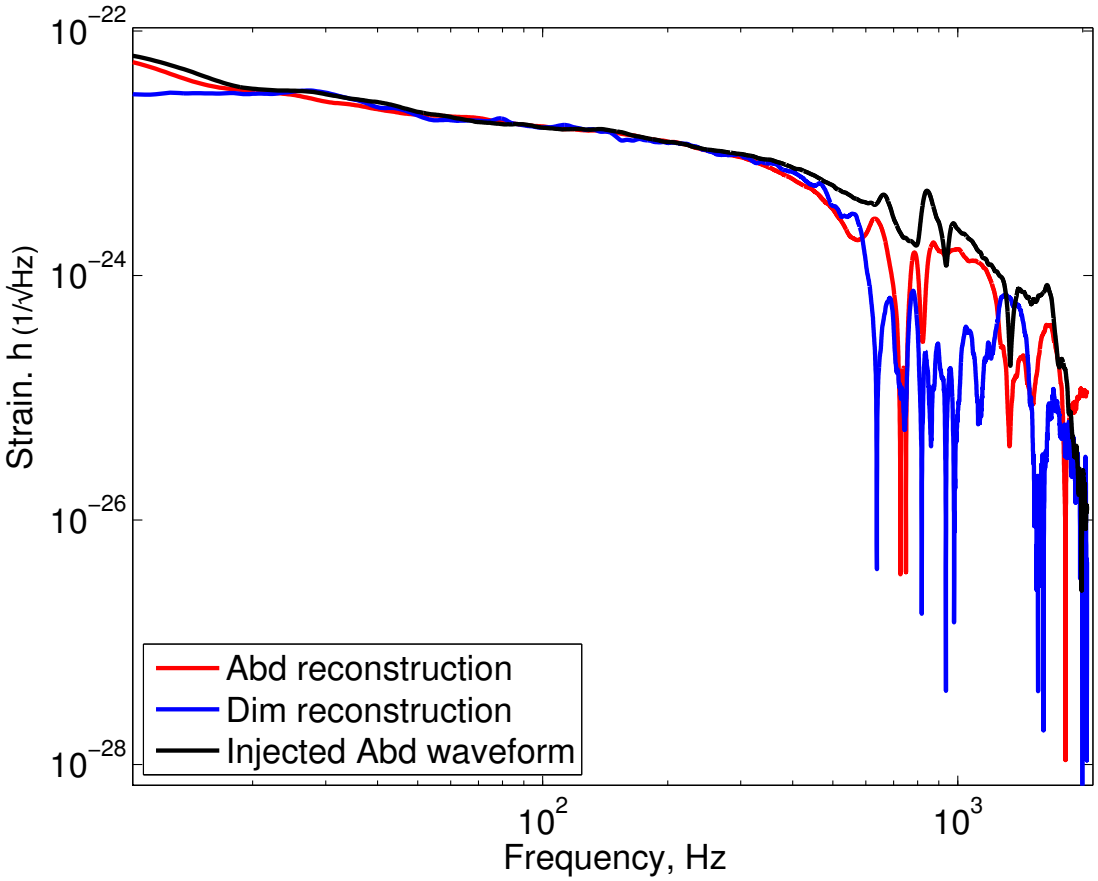

Figure 4.16: Reconstruction of an `Abd` waveform (injected waveform shown in black) using the `Abd` PCs in red and the `Dim` PCs in blue. Both waveforms occur across a very similar frequency band, especially in the frequency band between 10 and 400 Hz where there are no obvious distinct features between the two catalogues. This highlights the increased difficulty for SMEE to distinguish these two catalogues in the power spectrum domain.

At a source distance of 2 kpc (bottom panel of Fig. 4.15), 100% of the rotating core collapse (`Dim`) waveforms are correctly identified. However, ∼65% of the AIC `Abd` waveforms are incorrectly identified. Figure 4.16 highlights the difficulty in separating these two catalogues, even more so than in the time domain.

4.3.4 Testing Robustness of SMEE using non-catalogue waveforms

Magnetorotational Mechanism

As in the time domain, `Dim Extra` and `Sch` waveforms are employed here. The results of the $\log B_{SN}$ calculation for the magnetorotational, neutrino, and acoustic mechanism waveform models are summarized in Tab. 4.2. `DimExtra` waveforms are identified as being most consistent with the `Dim` catalogue and, hence, the magnetorotational mechanism for all `DimExtra` waveforms out to distances $\gtrsim$10 kpc.

Results of PSD_SMEE $\log B_{SN}$ calculations for all injected `Sch` waveforms are summarized in Tab. 4.2. PSD_SMEE correctly identifies *all* injected `Sch` waveforms as indicative of magnetorotational explosions at a source distance of 2 kpc. At 10 kpc, still 72% of the injected `Sch` waveforms are attributed to the magnetorotational mechanism, which is an indication of the robustness of the gravitational wave associated with rapid rotation and magnetorotational explosions. The very few `Sch` waveforms that PSD_SMEE is not able to clearly associate with the magnetorotational mechanism have such weak SNRs that they are more consistent with noise than with any of the catalogues at 10 kpc.

Acoustic Mechanism

As in the time domain the three `OttExtra` waveforms (see Sec. 1.7) are utilised here. The results of this test are again summarized in Tab. 4.2. They suggest that the a-priori unknown `OttExtra` waveforms can be identified as belonging to the acoustic mechanism out to 10 kpc with great confidence when 7 PCs are used in the analysis. PSD_SMEE's improvement is illustrated in the bottom panel of Fig. 4.17, which indicates that the `OttExtra` waveforms reach the threshold of $\log B \geq 5$ only for SNRs $\gtrsim$28 compared to $\gtrsim$35 for the time domain. This SNR is very close to the SNR required to reach the detection threshold when testing the `Ott` waveforms, see Section 4.3.1. This is a strong indication that the range of possible waveform features associated with the acoustic mechanism is much more efficiently covered by the 7 PCs generated from the `Ott` catalogue in the power spectrum domain confirming that any problems seen with the time domain results has been removed.

Table 4.2: power spectrum: $\log B_{SN}$ for gravitational waveforms that were not included in the catalogues used for PC computation. The `DimExtra`, `Sch`, `OttExtra`, and `Yak` waveforms are discussed in §1.7. Results are shown for source distances of 2 kpc and 10 kpc and for evaluations using 7 PCs. Larger values indicate stronger evidence that the waveform is matched to the model catalogue from which the PCs were constructed. $\log B_{SN} < 5$ when 7 PCs are used indicates that the injected signal is likely consistent with noise while larger values suggests that the signal belongs to the signal model whose PCs were used in the analysis.

Waveform	$\log B_{SN}$ Dim PCs		$\log B_{SN}$ Mur PCs		$\log B_{SN}$ Ott PCs	
	2 kpc	10 kpc	2 kpc	10 kpc	2 kpc	10 kpc
`DimExtra` [97]						
s20a1o05_shen	50449	736	52608	712	7646	1
s15a1o03_LS	105158	3493	110111	3236	17572	59
s40a1o10_LS	100357	5016	91035	3900	867	0
`Sch` [102]						
R1E1CA	1352	0	1307	0	0	0
R1E1CA_L	288	0	268	0	18	0
R1E1DB	969	1	958	0	0	0
R1E3CA	2811	1	2245	0	25	0
R1STCA	775	1	450	0	0	1
R2E1AC	5935	1	2804	0	4776	1
R2E3AC	6520	1	2389	0	4384	0
R2STAC	19357	27	8308	1	13610	20
R3E1AC	73018	1125	56375	540	55395	586
R3E1AC_L	105650	4233	79334	2087	73921	2204
R3E1CA	68186	848	51175	377	51972	476
R3E1DB	69328	886	52032	402	52980	504
R3E2AC	58258	555	41131	228	47143	332
R3E3AC	80412	1346	66150	815	55327	559
R3STAC	191988	11585	160628	5817	160295	7606
R4E1AC	137118	5030	125902	3846	76042	1411
R4E1CF	425485	54724	464719	53862	24441	575
R4E1EC	117529	3648	108240	2853	63920	905
R4E1FC	325979	35035	348117	33004	21984	430
R4E1FC_L	216629	15722	174432	7499	183179	10956
R4STAC	185035	10170	175705	7820	109781	3632
R5E1AC	109576	4605	123752	4160	14162	18
`OttExtra` [85]						
m15b6	10010	143	2145	0	14670	202
s11WW	9998	100	2608	0	13737	166
s25WW	560645	84571	165602	10275	1143494	201570
`Yak` [132]						
s12_matter	4669	1	2550	0	2696	0
s15_matter	11290	2	5387	0	7134	1
s25_matter	4289	1	1272	0	3424	0

Neutrino Mechanism

As in the time domain case the waveforms of the `Yak` catalogue (see Sec. 1.7) that were obtained with a completely different numerical code are tested. The results are listed in Tab. 4.2. PSD_SMEE correctly and clearly associates the `Yak` waveforms with the `Mur` PCs at 2 kpc but at 10 kpc the `Yak` waveforms appear to be most consistent with noise. However the results found show that $\log B_{SN}$ for the `Dim` and `Ott` PCs is considerably higher than those of the `Mur` PCs indicating that PSD_SMEE favours the incorrect models. The bottom panel of Fig. 4.17 confirms this by showing that $\log B$ decreases with SNR which shows that the $\log B_{SN}$ is higher for the other two sets of PCs. This rather disappointing result can be explained as follows: The `Yak` waveforms have considerably more power at frequencies above ∼800 Hz and their energy spectra peak at ∼1000 Hz while most of the emission in the `Mur` waveforms occurs at or below ∼400 Hz, see Figure 4.18. This peak in frequency occurs at a similar peak in both the `Dim` and `Ott` PCs which may be the reason they provide larger log Bayes Factors. This may be due to the more simplified treatment of gravity and neutrino microphysics and transport in the study of Murphy *et al.* [79] underlying the `Mur` catalogue compared to the work of Yakunin *et al.* [132] that led to the `Yak` catalogue.

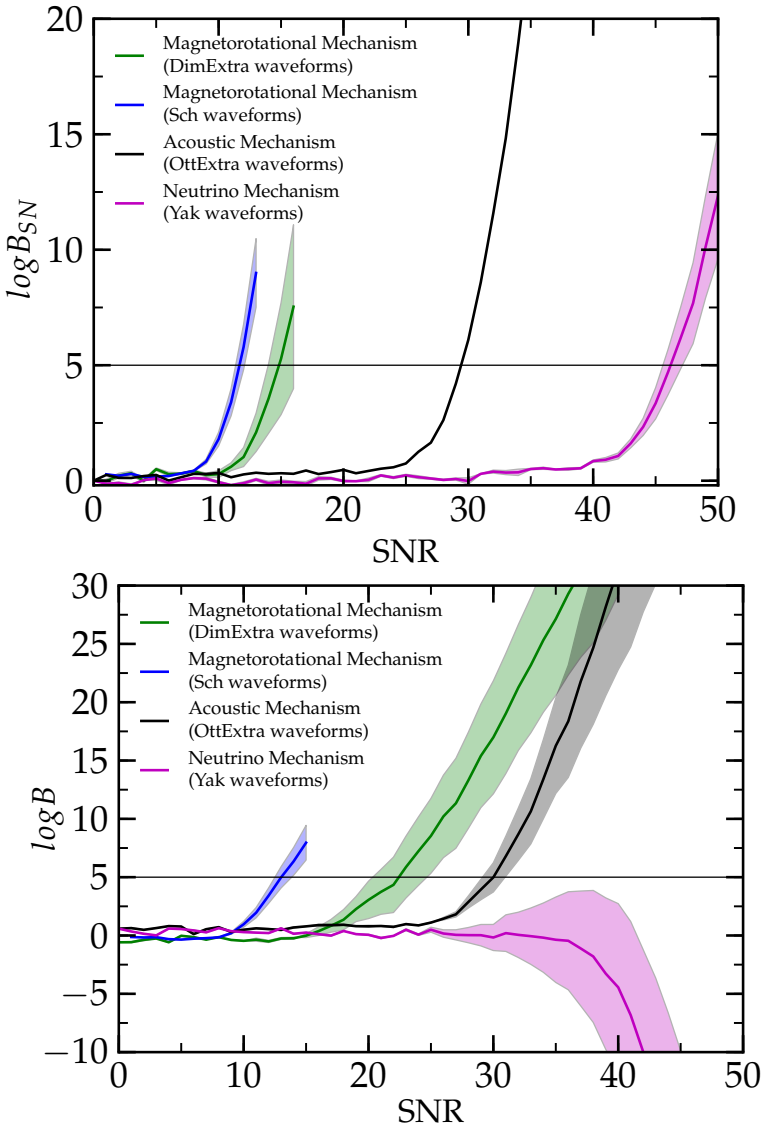

Figure 4.17: Mean and 1-σ range of $\log B_{SN}$ as a function of signal-to-noise ratio SNR comparing signal with noise evidence for non-catalogue waveforms for power spectrum domain **Top panel:** Results for the `Sch` and `DimExtra` in green and blue. These two were both reconstructed with 7 `Dim` PCs. Results for the `Yak` in mauve and `OttExtra` waveforms in black as reconstructed with 7 `Mur` for the first and 7 `Ott` PCs for the latter. The `Dim` PCs very efficiently reconstruct the `Sch` and `DimExtra` waveforms at moderate SNRs while the `Yak` and `OttExtra` require very high SNRs to be distinguished from noise by the `Mur` and `Ott` PCs, respectively. **Bottom panel:** This shows results for the same waveform catalogues when the results from the left panel are compared with the $\log B_{SN}$ found when attempting to reconstruct the injected waveform with the other two sets of PCs. The log Bayes Factor is then found i.e. in the case of the `Yak` catalogue $\log B$ is found for the `Mur` PCs versus the `Dim` and the `Ott` PCs. Out of the two results the minimum is plotted here to ensure that SMEE can distinguish between all sets of PCs. As in the results shown in the top panel the `Dim` PCs very efficiently reconstruct the `Sch` and `DimExtra` waveforms at moderate SNRs while the `Yak` and `OttExtra` require very high SNRs to be distinguished from both the noise and the other two sets of PCs.

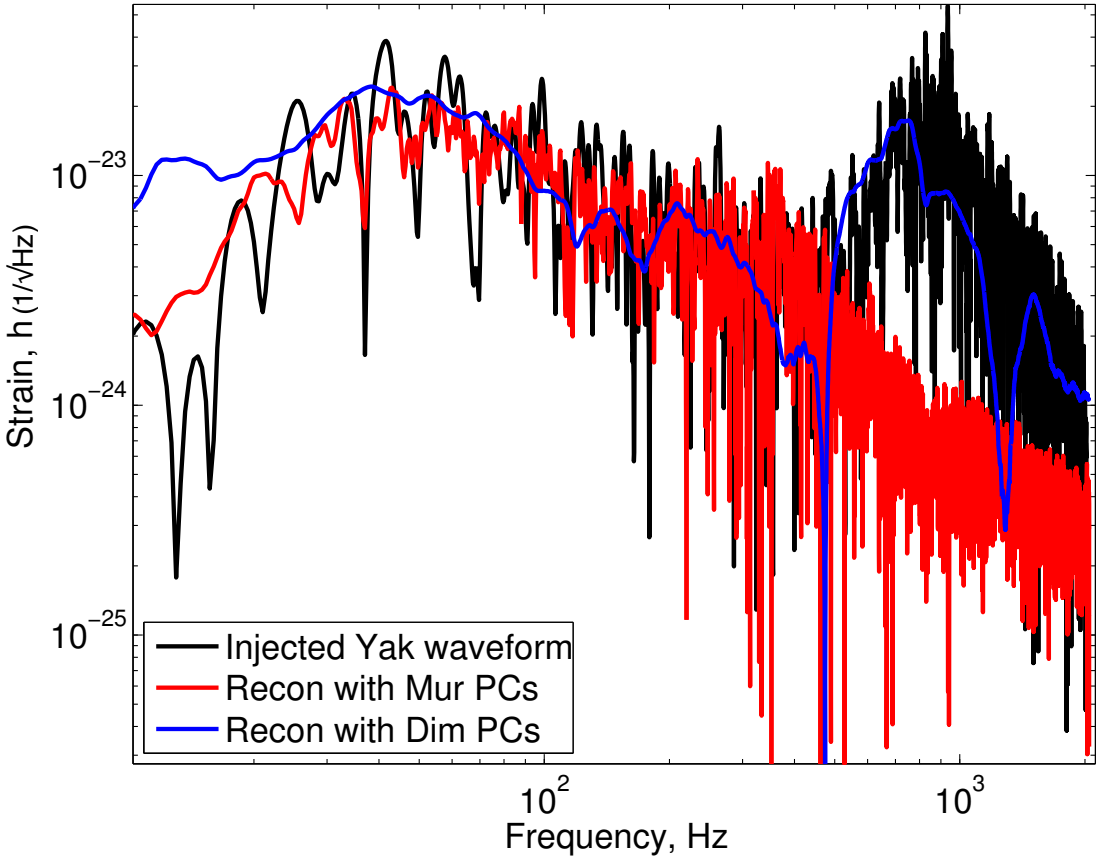

Figure 4.18: Reconstruction of a `Yak` waveform (injected waveform shown in black) using the `Mur` PCs in red and the `Dim` PCs in blue. This shows that the `Mur` PCs are unable to reconstruct the peak of the `Yak` waveform at 10^3 Hz whereas the `Dim` PCs are able to reconstruct this part of the waveform.

4.4 Characterising SMEE in the Spectrogram Domain

4.4.1 Signal Model versus Noise Model

The results shown in Section 4.2.1 are repeated in the spectrogram domain version of SMEE (Spec_SMEE), see Fig. 4.19. In this case a larger SNR compared to the time domain is required for Spec_SMEE to find $\log B_{SN} \geq 5$ in the idealized setting that is considered here. However there is a large improvement from the power spectrum results (Section 4.3.1). In this case the `Dim` waveforms require the smallest SNR

of 5 followed by those of the `Ott` catalogue with 7.5 and finally the `Mur` catalogue which requires a SNR of 9.5.

In the case where all three sets of PCs are compared, the `Dim` and `Ott` waveforms are easily distinguished from the other models. However with the `Mur` waveforms, the reconstructed waveform initially agrees with another one of the models (in this case the `Dim` PCs) and only begins to agree with the `Mur` PCs at an SNR of 13. The Bayes Factor below this SNR never goes below -5 so all results are still within the inconclusive region of between 5 and -5 where it is concluded that the models can not be distinguished. This highlights the need for such a conservative threshold as if it was smaller an incorrect result could have been registered in this case.

The `Ott` catalogue is much improved here over the power spectrum case as time domain information is included here. However, due to the frequency information also being included, the threshold for detection is larger than in the time domain case. For this same reason the results for the `Mur` catalogue has improved however Spec_SMEE is still limited due to having only 7 PCs to reconstruct the waveform. In the case of the `Dim` catalogue it performs very well for the same reasons as before i.e. that we are including the time domain information where the `Dim` waveforms have a simple structure which can be very successfully distinguished from the noise. The `Dim` catalogue also doesn't suffer as much from the limitations of the power spectrum domain so the results are not hampered by including this information.

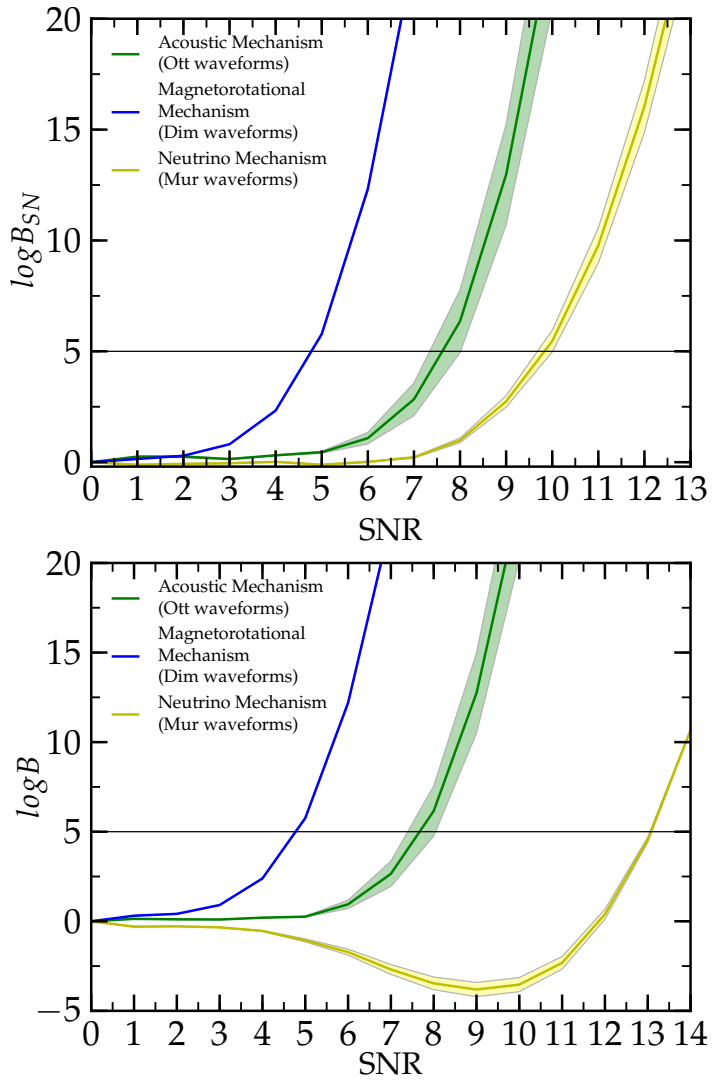

Figure 4.19: **Top panel:**Mean $\log B_{SN}$ using Spec_SMEE as a function of signal-to-noise ratio (SNR; Eq. 3.15) for all representative waveforms from the `Mur`, `Ott` and `Dim` catalogues using 7 principal components (PC). The shaded areas represent the standard error in the mean value of $\log B_{SN}$ for each waveform catalogue computed as $\sigma = \pm N^{-1}(\Sigma_i(\bar{x} - x_i)^2)^{1/2}$, where $\bar{x}$ is the mean and x_i are the individual SNRs and N is the number of waveforms. Values of $\log B_{SN}$ below 5 indicate that the algorithm considers it more likely that there is no signal detectable in the noise. **Bottom panel:** This shows results for the same waveform catalogues when the results from the top panel are compared with the $\log B_{SN}$ found when attempting to reconstruct the injected waveform with the other two sets of PCs. The log Bayes Factor is then found i.e. in the case of the `Dim` catalogue $\log B$ is found for the `Dim` PCs versus the `Mur` and the `Ott` PCs. Out of the two results the minimum is plotted here to ensure that SMEE can distinguish between all sets of PCs.

4.4.2 Distinguishing the Supernova Mechanism

In Fig. 4.20, results are shown for injection studies of *all* waveforms from the `Dim`, `Mur`, and `Ott` catalogues run through Spec_SMEE and analyzed with the `Dim`, `Mur`, and `Ott` PCs at a source distance of 10 kpc. The top left panel depicts the $\log B_{\texttt{DimMur}}$ results and at 10 kpc all waveforms characteristic for magnetorotational explosions are clearly identified as belonging to this mechanism. For the neutrino mechanism, the evidence is generally significantly weaker and only ∼30% of the `Mur` waveforms are identified with $\log B_{\texttt{DimMur}} < -100$ and none have $\log B_{\texttt{DimMur}} < -1000$, while ∼7% are in the inconclusive regime of $-5 < \log B_{\texttt{DimMur}} < 5$. Most damning of all is that ∼44% of `Mur` waveforms are incorrectly identified as `Dim` waveforms. This is due to the fact that at SNRs, typically less than 10, these waveforms favour the magnetorotational mechanism and only start agreeing with the neutrino waveforms at higher SNRs.

In the top right panel of Fig. 4.20, results are shown for $\log B_{\texttt{DimOtt}}$ for injected waveforms corresponding to the magnetorotational (`Dim`) and the acoustic (`Ott`) mechanisms. All waveforms are correctly identified as most likely belonging to their respective catalogue/mechanism. Finally, the bottom panel of Fig. 4.20 presents $\log B_{\texttt{MurOtt}}$ for waveforms representative of the neutrino (`Mur`) and acoustic (`Ott`) mechanism. As in the previous panel, Spec_SMEE associates the waveforms corresponding to the acoustic mechanism with high confidence to the `Ott` catalogue. The evidence suggesting correct association of the neutrino mechanism waveforms is not as strong, but $\log B_{\texttt{MurOtt}}$ is still conclusive for ∼93% of the `Mur` waveforms with the other ∼7% being in the inconclusive region.

Figure 4.21 shows the results for $\log B_{\texttt{DimMur}}$, $\log B_{\texttt{DimOtt}}$, and $\log B_{\texttt{MurOtt}}$ obtained by Spec_SMEE with 7 PCs at a source distance of 2 kpc. Here, all acoustic mechanism waveforms (`Ott` catalogue) and all magnetorotational mechanism waveforms (`Dim` catalogue) are correctly identified as belonging to their respective catalogue and explosion mechanism. Only 1 neutrino mechanism waveforms (`Mur` catalogue) still incorrectly identifies with the magenetorotational mechanism which highlights that even at 2kpc some `Mur` waveforms still do not have a high enough SNR to start agreeing with the correct mechanism.

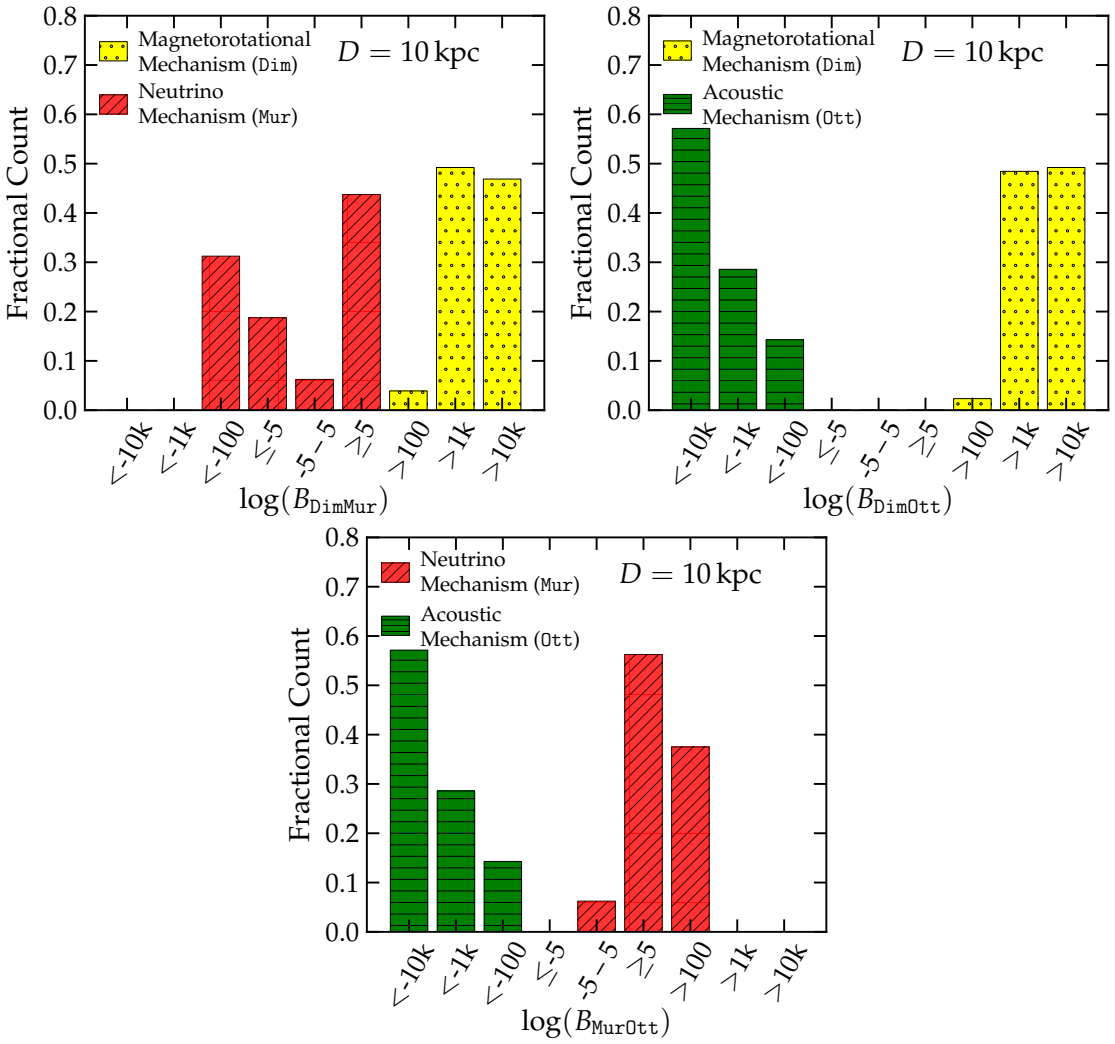

Figure 4.20: Histograms describing the outcome of signal model comparisons in the spectrogram domain by means of the Bayes Factors $\log B_{ij} = \log p(D|M_i) - \log p(D|M_j)$, where $i \neq j$ and M_i and M_j are signal models described by the `Dim` (magnetorotational mechanism), `Mur` (neutrino mechanism), and `Ott` (acoustic mechanism) waveform catalogues. The Bayes Factors are computed with 7 PCs and for a source distance of 10 kpc. A positive value $\log B_{ij}$ indicates that the injected waveform most likely belongs to model M_i, while a negative value suggest that model M_j is the more probable explanation. The bars are color-coded according to the type of injected waveform. The results are binned into ranges of varying size from < -10000 to > 10000 and the height of the bars indicates what fraction of the waveforms of a given catalogue falls into a given bin of $\log B_{ij}$. A range of $(-5, 5)$ of $\log B_{ij}$ is considered as inconclusive evidence (see §4.1).

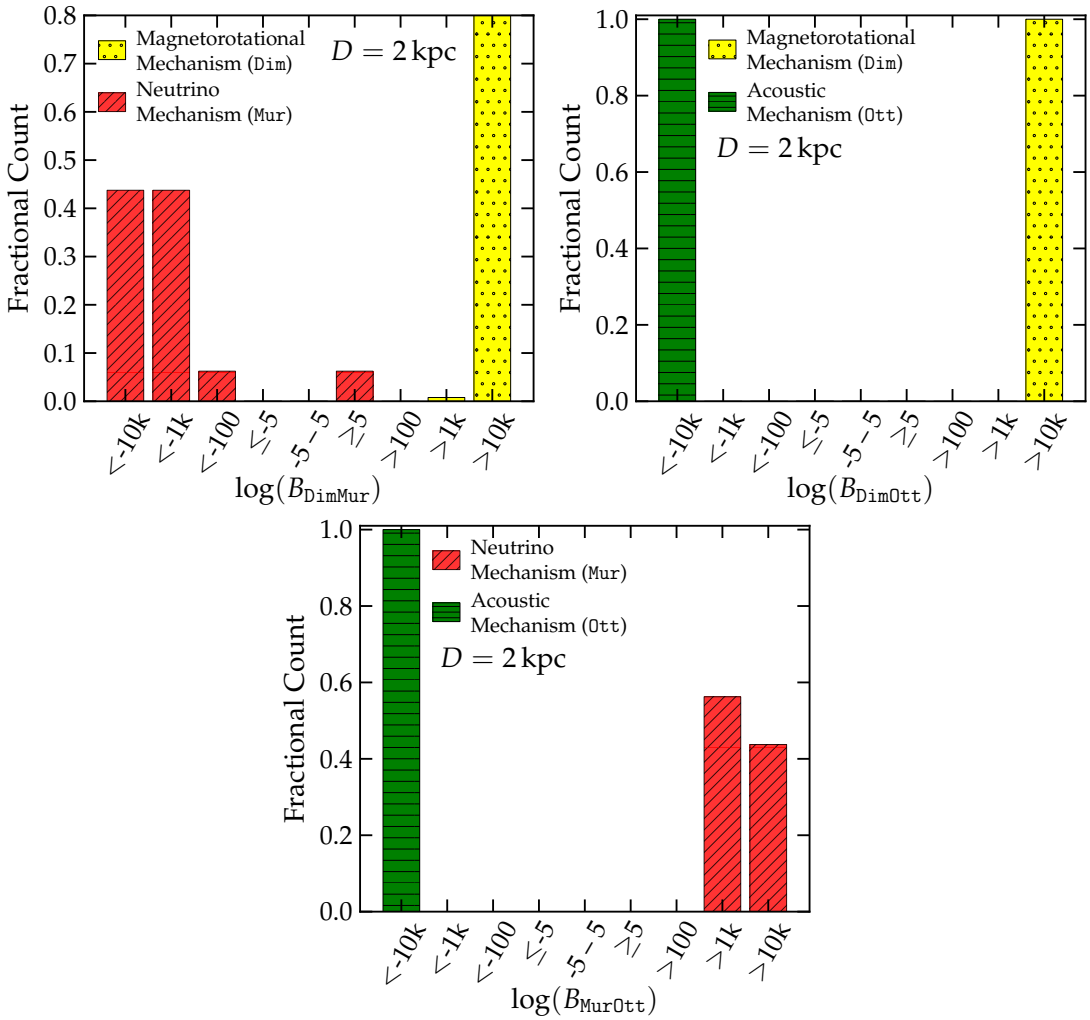

Figure 4.21: Same as Fig. 4.20, but computed for a source distance of 2 kpc.

4.4.3 Rotating Accretion-Induced Collapse or Rotating Iron Core Collapse?

For this test, Spec_SMEE performs better than both the time domain and power spectrum versions of SMEE. In this case, for a source at 10 kpc (top panel of Fig. 4.22), all of the `Dim` are correctly identified as most likely being emitted by a rotating iron core collapse. For the `Abd` waveforms, only ∼13% of the `Abd` are incorrectly identified as belonging to the respective other catalogue or have a Bayes Factor between -5 and 5.

At a source distance of 2 kpc (bottom panel of Fig. 4.22), 100% of the rotating core collapse (`Dim`) waveforms are correctly identified. However, ∼8% of the AIC `Abd` waveforms are incorrectly identified.

4.4.4 Testing Robustness of SMEE using non-catalogue waveforms

Magnetorotational Mechanism

Once again the (`DimExtra` waveforms, Sec. 1.7), are employed that were not included in the calculation of the `Dim` PCs as well as waveforms from rotating models of the `Sch` catalogue of Scheidegger *et al.* [102, 23] are injected (see Sec. 1.7). The results of the $\log B_{SN}$ calculation for the magnetorotational, neutrino, and acoustic mechanism signal models are summarized in Tab. 4.3. `DimExtra` waveforms are identified as being most consistent with the `Dim` catalogue and, hence, the magnetorotational mechanism. This is true with high confidence signals out to distances $\gtrsim$10 kpc.

Results of Spec_SMEE $\log B_{SN}$ calculations for all injected `Sch` waveforms are summarized in Tab. 4.3. Spec_SMEE correctly identifies *all* injected `Sch` waveforms as indicative of magnetorotational explosions at a source distance of 2 kpc. At 10 kpc, still 91% of the injected `Sch` waveforms are attributed to the magnetorotational mechanism, which is an indication of the robustness of the GW associated with rapid rotation and magnetorotational explosions. The very few `Sch` waveforms

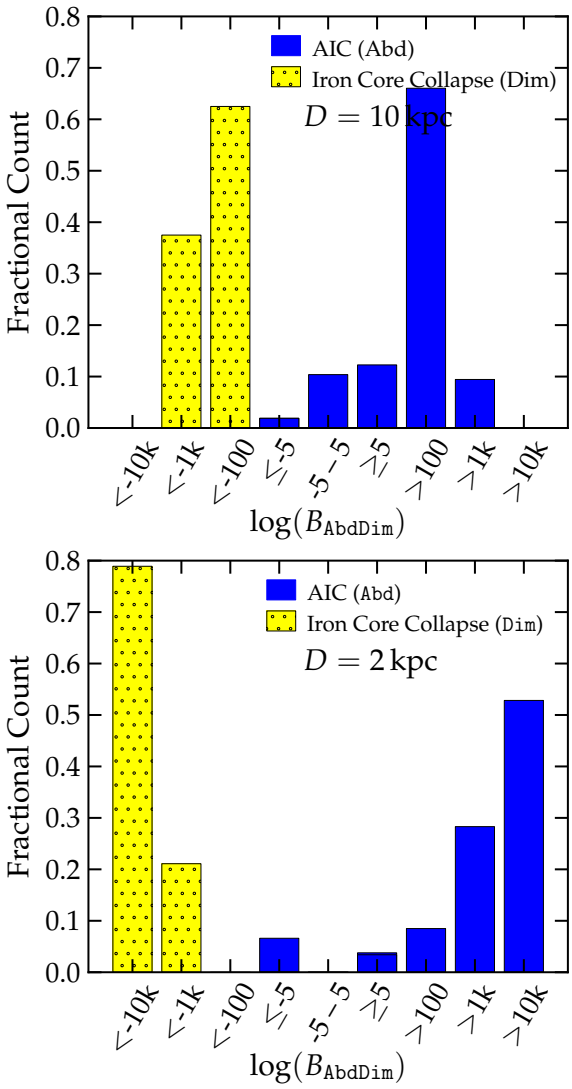

Figure 4.22: Outcome of the SMEE analysis in the spectrogram domain of injected rotating iron core collapse (`Dim` catalogue) and rotating accretion-induced collapse (AIC, `Abd` catalogue) waveforms. The left panel shows results for a source distance of 10 kpc and the right panel depicts the results for a distance of 2 kpc. The Bayes Factors $\log B_{\mathtt{AbdDim}}$ are computed on the basis of 7 PCs from the `Abd` and `Dim` catalogue. A positive value of $\log B_{\mathtt{AbdDim}}$ indicates that an injected waveform is most likely associated with rotating AIC and a negative value suggests it to be more consistent with rotating iron core collapse. The results are binned into ranges of varying size from < -10000 to > 10000 and the height of the color-coded bars indicates what fraction of the waveforms of a given catalogue falls into a given bin of $\log B_{\mathtt{AbdDim}}$. A range of $(-5, 5)$ of $\log B_{ij}$ is considered as inconclusive evidence (see §4.1).

that Spec_SMEE is not able to clearly associated with the magnetorotational mechanism have such weak SNRs that they are more consistent with noise than with any of the catalogues at 10 kpc.

Acoustic Mechanism

For the three `OttExtra` waveforms (see Sec. 1.7), the results of this test are again summarized in Tab. 4.3. They suggest that the a-priori unknown `OttExtra` waveforms can be identified as belonging to the acoustic mechanism out to 2 kpc with great confidence when 7 PCs are used in the analysis. At 10 kpc, the waveforms are still correctly attributed to the acoustic mechanism, but the evidence is much weaker.

Spec_SMEE's difficulty is illustrated in the bottom panel of Fig. 4.23, which indicates that the `OttExtra` waveforms reach the threshold of $\log B_{SN} \geq 5$ only for SNRs $\gtrsim$38, whereas `Ott` waveforms are identified already at SNRs $\gtrsim$8, if the full set of 7 PCs is used. This is a strong indication that, as in the case of the time domain, the range of possible waveform features associated with the acoustic mechanism is not efficiently covered by the 7 PCs generated from the `Ott` catalogue and that since we retain the time domain information when computing the spectrogram PCs, such large-scale features are again imprinted onto the PCs.

Neutrino Mechanism

For the `Yak` catalogue (see Sec. 1.7) the results are listed in Tab. 4.3. Spec_SMEE correctly and clearly associates the `Yak` waveforms with the `Mur` PCs at 2 kpc. At 10 kpc the `Yak` waveforms appear to be most consistent with noise for Spec_SMEE. The bottom panel of Fig. 4.23 shows that the `Yak` waveforms require an SNR to be clearly associated with the neutrino mechanism of 37. This is a significant improvement on the time and power spectrum versions of Spec_SMEE. This indicates that including the frequency information improves the reconstruction but by also having the time domain information the errors seen in the power spectrum domain are removed.

Table 4.3: Spectrogram: $\log B_{SN}$ for gravitational waveforms that were not included in the catalogues used for PC computation. The `DimExtra`, `Sch`, `OttExtra`, and `Yak` waveforms are discussed in §1.7. Results are shown for source distances of 2 kpc and 10 kpc and for evaluations using 7 PCs. Larger values indicate stronger evidence that the waveform is matched to the model catalogue from which the PCs were constructed. $\log B_{SN} < 5$ when 7 PCs are used indicates that the injected signal is likely consistent with noise while larger values suggests that the signal belongs to the signal model whose PCs were used in the analysis.

Waveform	$\log B_{SN}$ Dim PCs		$\log B_{SN}$ Mur PCs		$\log B_{SN}$ Ott PCs	
	2 kpc	10 kpc	2 kpc	10 kpc	2 kpc	10 kpc
`DimExtra` [97]						
s20a1o05_shen	308019	11426	48143	1555	6104	88
s15a1o03_LS	692386	26678	72783	2848	12645	326
s40a1o10_LS	1071939	41768	274761	11476	6223	119
`Sch` [102]						
R1E1CA	2132	17	192	0	0	0
R1E1CA_L	747	0	0	0	0	0
R1E1DB	1816	10	150	0	0	0
R1E3CA	3927	49	102	0	8	0
R1STAC	584	1	6	0	0	0
R2E1AC	25596	676	1031	0	152	0
R2E3AC	25771	695	761	0	103	0
R2STAC	48548	1520	1490	0	296	0
R3E1AC	223107	8028	9492	180	2690	6
R3E1AC_L	185255	6521	15058	179	2909	0
R3E1CA	193652	6834	10300	197	2408	1
R3E1DB	193551	6832	10046	200	2354	1
R3E2AC	165738	5836	7945	128	1931	0
R3E3AC	226466	8256	11326	244	3145	14
R3STAC	307251	11478	9521	184	3269	12
R4E1AC	578951	22155	29808	918	9706	214
R4E1CF	3360314	133582	973865	41947	37731	1384
R4E1EC	469671	17914	24678	701	8097	160
R4E1FC	2359780	93751	423488	18189	33782	1263
R4E1FC_L	567813	21520	28521	737	9611	165
R4STAC	736102	28202	30179	1002	11996	302
R5E1AC	493971	19224	33402	1199	8453	203
`OttExtra` [85]						
m15b6	635	0	1940	0	6447	6
s11WW	2449	19	3475	0	12269	74
s25WW	2530	18	563253	17102	6577133	264683
`Yak` [132]						
s12_matter	104	0	1839	0	0	0
s15_matter	361	0	6380	0	0	0
s25_matter	76	0	2985	0	0	0

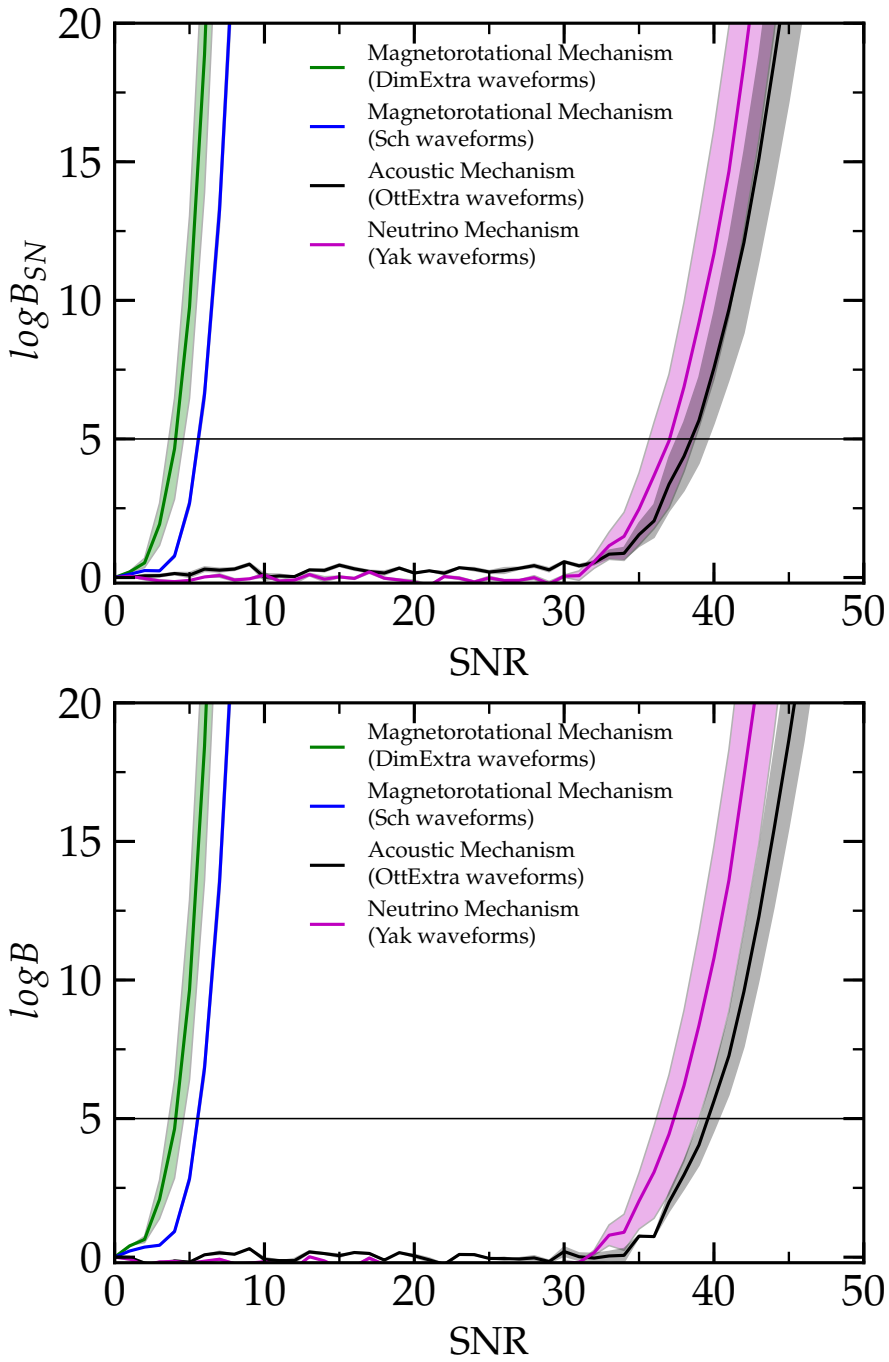

Figure 4.23: Mean and 1-σ range of $\log B_{SN}$ as a function of signal-to-noise ratio SNR comparing signal with noise evidence. The horizontal lines mark the threshold values of $\log B_{SN}$ above which it is considered an injected waveform to be distinct from Gaussian noise. **Top panel:** Results for the `Sch` and `DimExtra` in green and blue. These two were both reconstructed with 7 `Dim` PCs. Results for the `Yak` in mauve and `OttExtra` waveforms in black as reconstructed with 7 `Mur` for the first and 7 `Ott` PCs for the latter. The `Dim` PCs very efficiently reconstruct the `Sch` and `DimExtra` waveforms at moderate SNRs while the `Yak` and `OttExtra` require very high SNRs to be distinguished from noise by the `Mur` and `Ott` PCs, respectively. **Bottom panel:** This shows results for the same waveform catalogues when the results from the top panel are compared with the $\log B_{SN}$ found when attempting to reconstruct the injected waveform with the other two sets of PCs. The log Bayes Factor is then found i.e. in the case of the `Yak` catalogue $\log B$ is found for the `Mur` PCs versus the `Dim` and the `Ott` PCs. Out of the two results the minimum is plotted here to ensure that SMEE can distinguish between all sets of PCs. As in the results shown in the left panel the `Dim` PCs very efficiently reconstruct the `Sch` and `DimExtra` waveforms at moderate SNRs while the `Yak` and `OttExtra` require very high SNRs to be distinguished from both the noise and the other two sets of PCs.

4.5 Summary

The aim of this Chapter was to characterise a bayesian model selection pipeline known as the Supernova Model Evidence Extractor (SMEE). SMEE is designed to infer the physics behind a core collapse supernova by searching for features in the gravitational waveform indicative of one of three hypothesised supernova explosion mechanisms. This chapter has shown that SMEE is extremely successful at this in the simple case where only a single Advanced LIGO detector is used and the effect of the antenna response is ignored.

The time domain version of SMEE is very accurate and can correctly assign a waveform to the correct model (supernova mechanism) even in the case when comparing two models which employ the same supernova mechanism but differ in the type of source (Section 4.2.3). In the case where waveforms are tested which were not used to create the principal components (Section 4.2.4), time domain SMEE remains accurate when testing waveforms associated with the magnetorotational mechanism due to the large and varied parameter space provided for this mechanism. Time domain SMEE is less successful when testing waveforms associated with the neutrino and acoustic mechanisms and requires extremely large SNRs before model selection can be performed. This is due to the lack of accurately modelled waveforms meaning TD_SMEE does not have access to complete information about these mechanisms.

The power spectrum domain version of SMEE performs the poorest out of the 3 versions tested. This is due to the fact that higher SNRs are required to correctly perform model selection. The reason that a higher SNR is needed is because of the nature of the supernova waveforms in the power spectrum domain in that features that differ between mechanisms occur in a frequency band where the detector is less sensitive, see Figure 4.11. Despite this limitation, this version of SMEE is still able to correctly assign waveforms from the magnetorotational and acoustic mechanisms to a distance of at least 10kpc. It is also successful at separating the majority of waveforms from the `Abd` and `Dim` catalogues. PSD_SMEE fails to correctly determine the mechanism behind the `Yak` catalogue due to the fact that these waveforms contain features not seen in the `Mur` catalogue, see Figure 4.18.

The spectrogram domain version of SMEE is very successful over all the tests

performed in Section 4.4. By combining data from time and power spectrum domain, SMEE contains as much information as possible about each supernova mechanism. While it performs less well than TD_SMEE at smaller SNRs (Section 4.4.1) it has improved on the ability to correctly assign non-catalogue waveforms to their associated supernova mechanisms (Section 4.4.4).

The next test of SMEE is to characterise its ability in the more realistic scenario where data from multiple detectors is utilised and the effects of the antenna response is taken into account. This is done in Chapter 6. However, before this is done a series of steps are taken to attempt to improve model selection in SMEE, see Chapter 5.

Chapter 5

Improving Model Selection in SMEE

In this chapter techniques which can be employed to improve the Supernova Model Evidence Extractor (SMEE) are investigated. Firstly, how changing the inputs of the nested sampling algorithm improve the reconstruction of the injected waveform as well as the Bayes Factors will be tested. Next the effectiveness of shifting from global priors which encompass all supernova models to local priors which are dependent on the PC catalogue used to reconstruct the waveform is examined. The majority of this chapter will then focus on the different techniques used to determine the ideal number of PCs to use for each waveform model.

5.1 Refining Signal Reconstruction in the Nested Sampling Algorithm

It was stated in Section 2.2 that the number of live points in the nested sampling algorithm was chosen to be 50. These live points are, for every new iteration of the nested sampling algorithm, objects which are restricted to the parameter space defined by the priors [108, 106]. For each of these objects a likelihood is calculated and the object with the smallest likelihood is replaced. This number can be changed by the user and it is a useful exercise to investigate how using different values for the

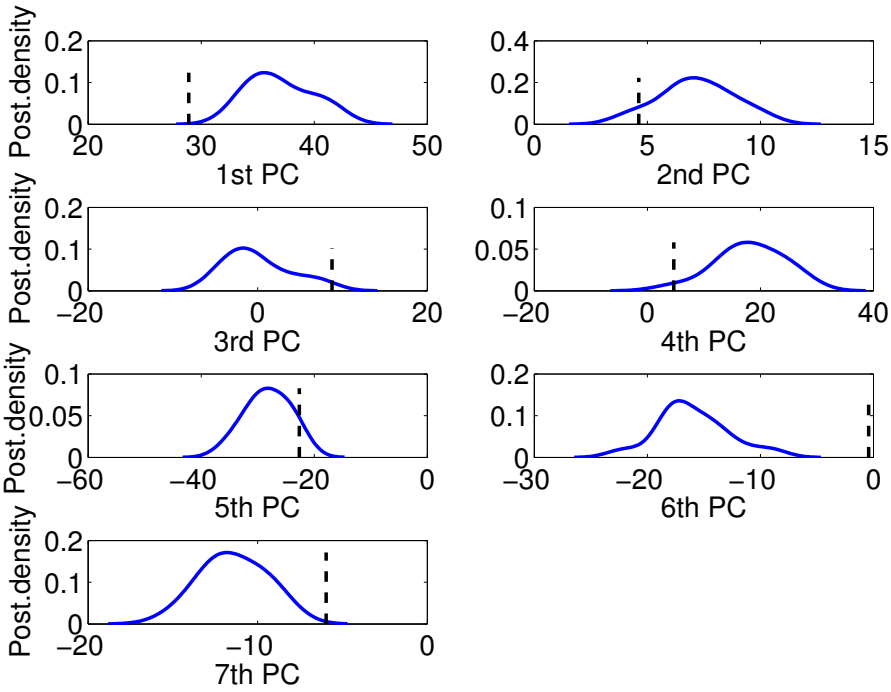

Figure 5.1: Posterior densities for reconstruction of the first 7 PC coefficients using time domain SMEE and 10 live points in the nested sampling algorithm. The dashed line represents the correct value and only appears at the very edges of the posterior distributions or not at all.

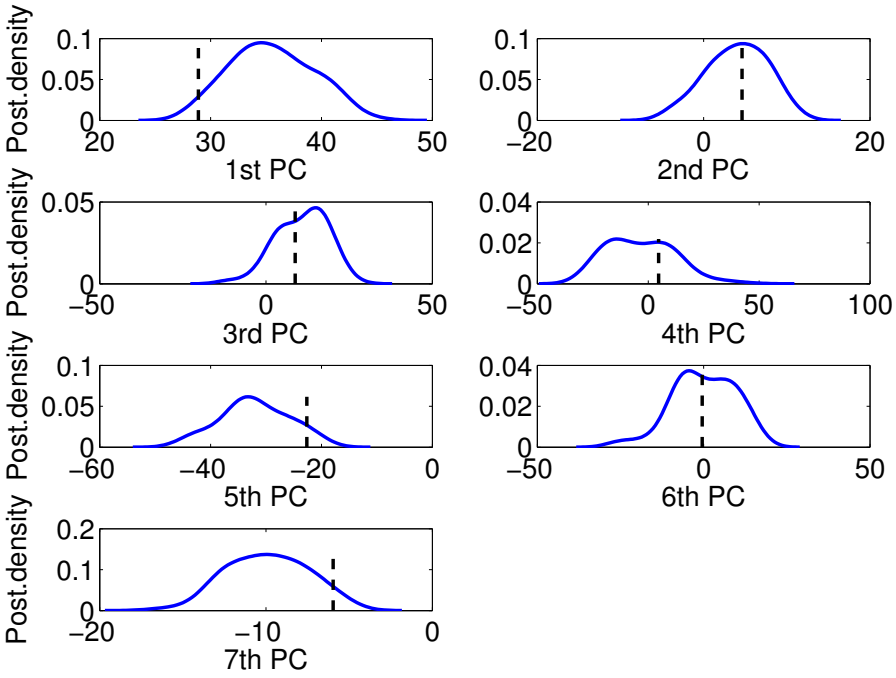

Figure 5.2: Same as Figure 5.1 but using 50 live points in the nested sampling algorithm. Note here that the dashed line which represents the correct answer always lies with the posterior distribution.

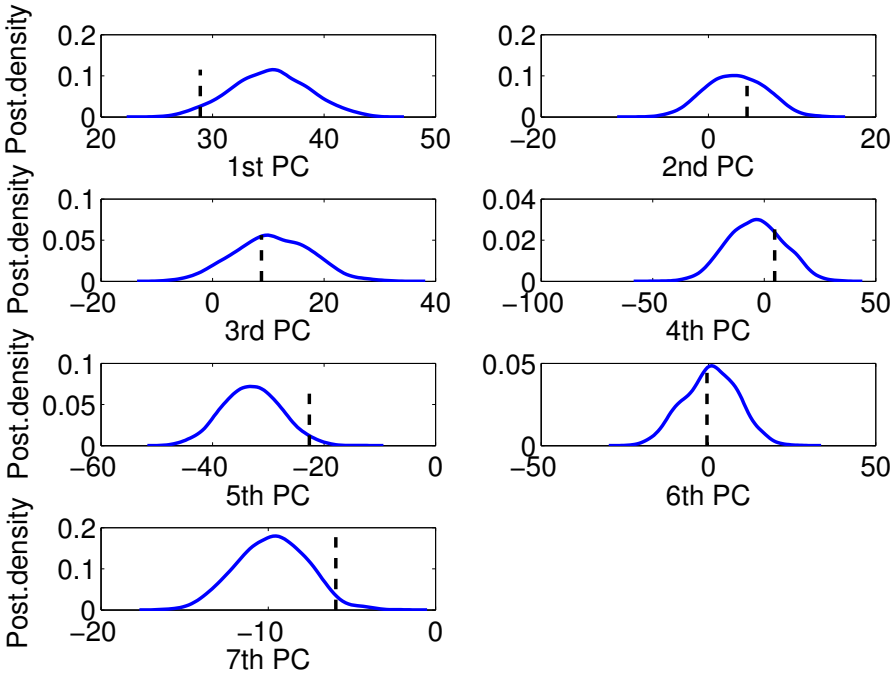

Figure 5.3: Same as Figure 5.1 but using 500 live points in the nested sampling algorithm. Note here that the dashed line which represents the correct answer always lies with the posterior distribution but there does not appear to be any significant improvement over Figure 5.2.

number of live points could potentially improve the accuracy of the reconstruction. Thus a qualitative investigation is performed where a `Dim` waveform is chosen and run using TD_SMEE with 7 PCs as before. The number of live points is increased in steps of 10 from 10 to 500. The Bayes Factor comparing the signal model to the noise model, $\log B_{SN}$, is calculated for each variation of the number of live points and a set of these Bayes factors is shown in Table 5.1. The posteriors for the 7 PC coefficients are plotted and compared with the expected values. The posterior distributions for a range of live points is plotted in Figures 5.1 to 5.3.

Over the range of live points used there is no significant change in $\log B_{SN}$, however there is an improvement in SMEE's ability to estimate the PC coefficients when the number of live points increases. This can be seen when Figures 5.1 and 5.2 are compared. While there is a significant improvement when the number of live points is increased from 10 to 50, there is less improvement when the number of live points is increased to 500 (Figure 5.3). This is reflected in Table 5.1 where $\log B_{SN}$ does slightly improve when the number of live points is increased from 10 to 50.

Due to the fact that using a higher number of live points increases the computing

Table 5.1: $\log B_{SN}$ for a single `Dim` waveform with an increasing number of live points utilised in the nested sampling algorithm. This shows that after 50 live points there is no significant improvement in $\log B_{SN}$ to the first decimal point.

No. live points	$\log B_{SN}$
10	248.6
50	251.2
100	251.4
200	251.8
300	251.6
400	251.3
500	251.2

cost as well as the fact there are no improvements in Bayes Factors or reconstructions the number of live points will remain at 50.

5.2 Refining Priors

In Section 3.1.4, priors for the PC coefficients were chosen so that they would encompass the parameter space for all of the different supernova models. This ensured that only using a single prior for each coefficient would be required. A potential drawback of this technique is that the nested sampling algorithm may search an area of the parameter space that is not necessary for a particular model.

Adjusting the priors such that each set of PCs would have an associated set of priors would ensure that only the parameter space associated with a particular set of PCs would be searched. This change is implemented in SMEE and a waveform from the `Dim`, `Mur` and `Ott` catalogues is tested using TD_SMEE using the global set of priors and the local priors for each set of PCs. 7 PCs are used at a distance of 10kpc with $F_+ = 1$. The posterior distributions for each waveform is shown in Figures 5.4 to 5.6 and show that there is a minimal improvement in SMEE's ability to estimate the PC coefficients. This is because whilst the parameter space has been reduced for each model the parameter space for each model is still large and SMEE still has to search over a large parameter space for each PC.

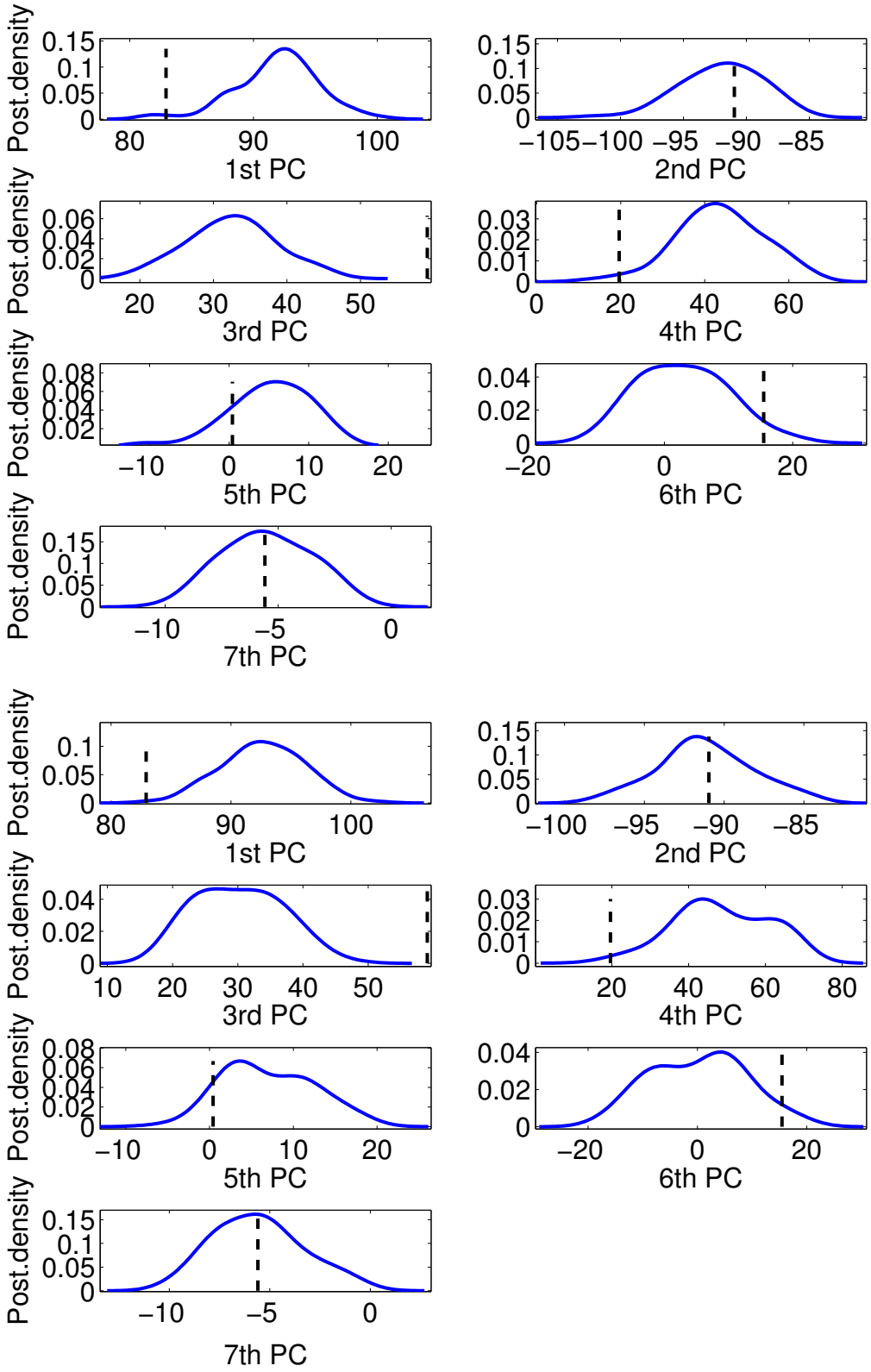

Figure 5.4: Posterior densities for reconstruction of the first 7 PC coefficients using time domain SMEE on a `Dim` waveform. The dashed line indicates the correct value. **Top Plot** shows posteriors using the global priors which encompass the parameter space for all of the different supernova models. **Bottom Plot** Same as the top plot utilising local priors which only cover the parameter space for the `Dim` PCs are used. There does not appear to any qualitative improvement between each set of priors.

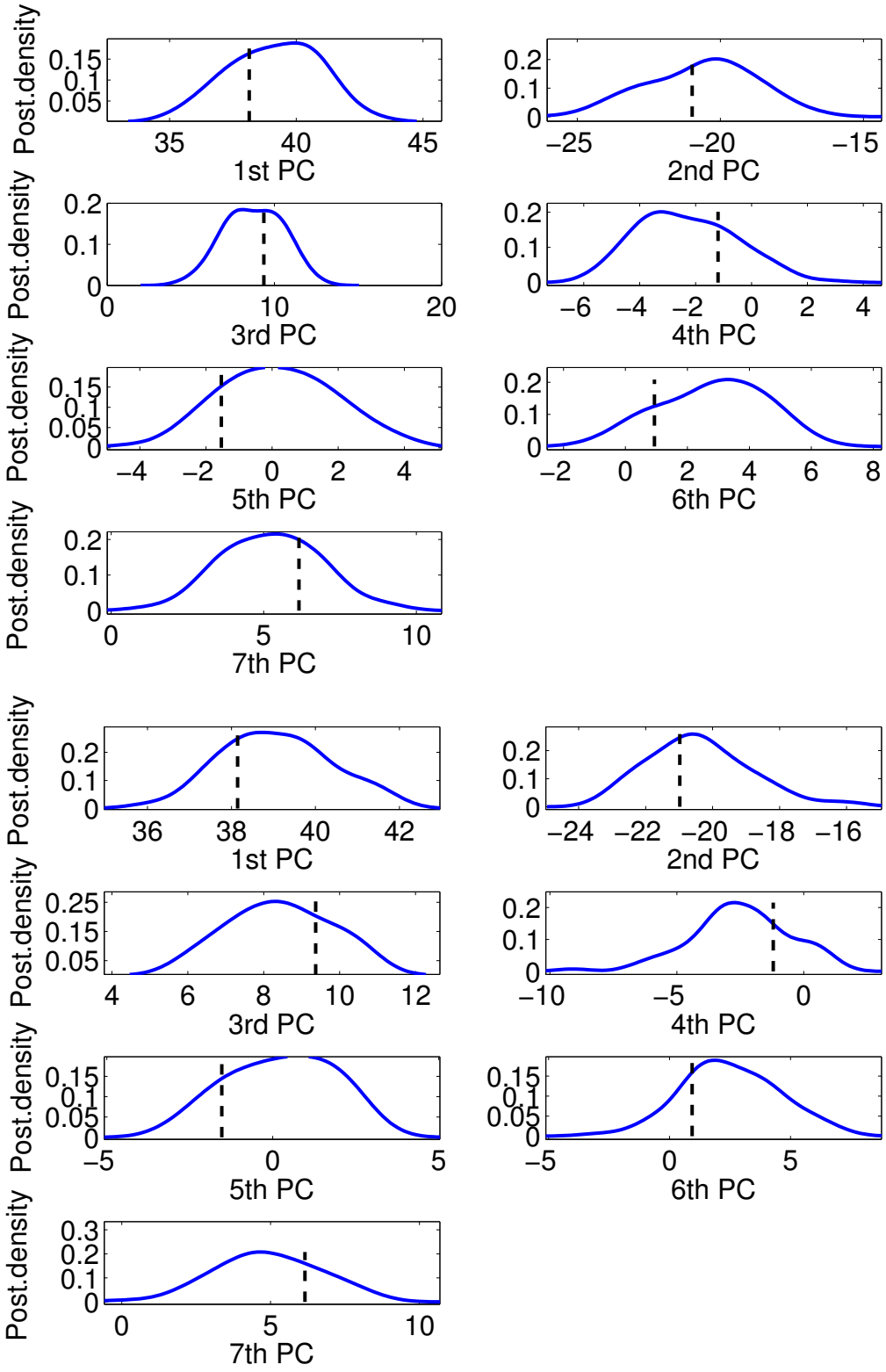

Figure 5.5: Same as Figure 5.4 but for a `Mur` waveform. As before, there is no significant improvement.

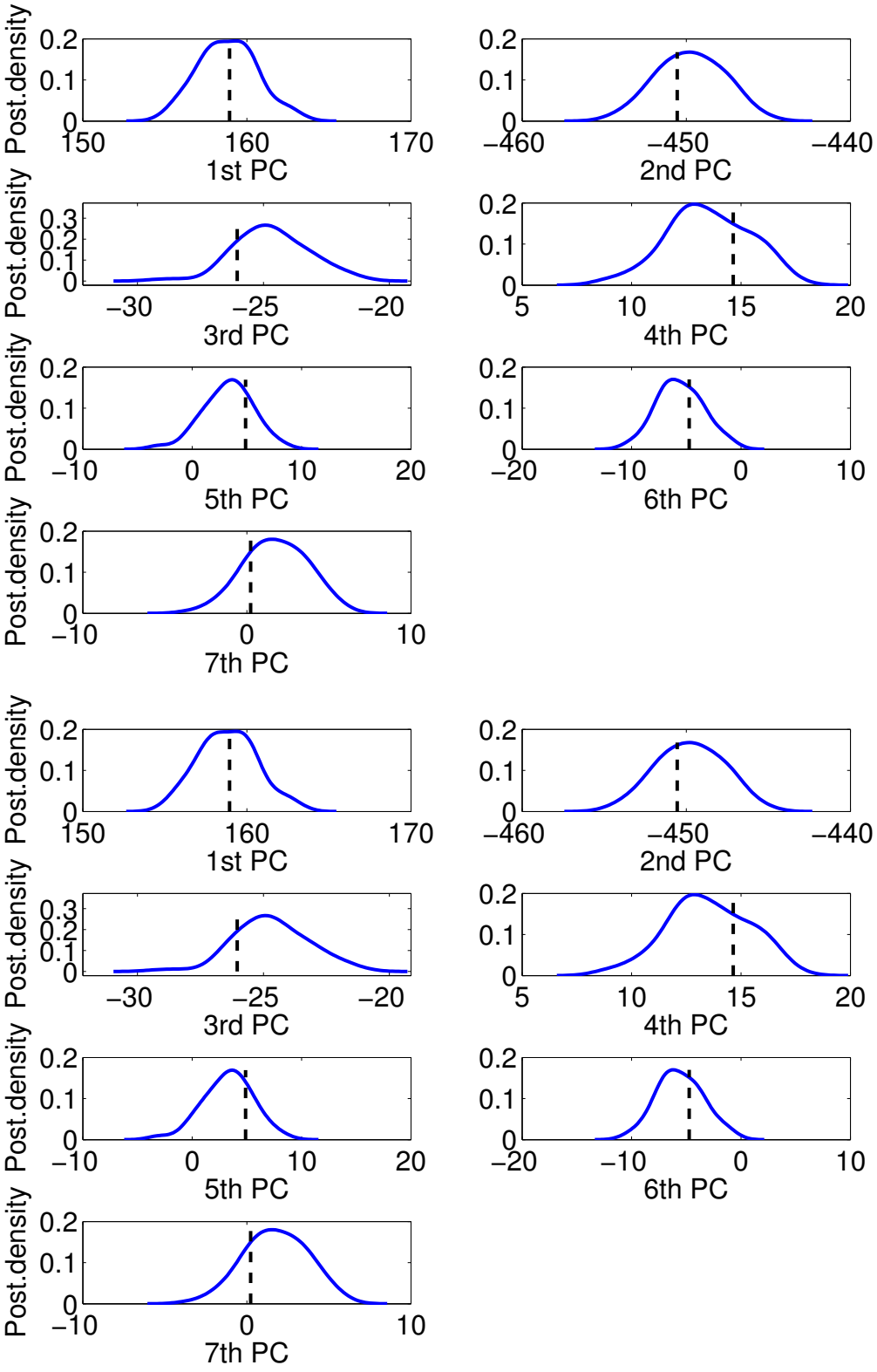

Figure 5.6: Same as Figure 5.4 but for a `Ott` waveform. Once again there is no significant improvement.

Table 5.2: Results for a waveform from `Dim`, `Mur` and `Ott` catalogue for the time taken to run SMEE and $\log B_{SN}$ using global priors and local priors. This shows that there is no improvement in $\log B_{SN}$ however the time taken to run SMEE has reduced.

Waveform	Global Priors		Local Priors	
	Time (seconds)	$\log B_{SN}$	Time (seconds)	$\log B_{SN}$
`Dim`	189	2223	163	2223
`Mur`	114	317	51	317
`Ott`	106	24511	85	24511

Table 5.2 shows how $\log B_{SN}$ changes when the priors are changed as well as the time taken for the nested sample to find the maximum likelihoods. Whilst $\log B_{SN}$ does not change, the time taken to run the nested sampling algorithm does reduce due to the fact that a smaller parameter space is being searched over. Having a version of SMEE that is faster but is still accurate is desirable thus the local priors are used for the results shown in the rest of this thesis.

5.3 Ideal number of PCs used in SMEE?

5.3.1 Match Method and Limitations of Small Catalogues

To find the number of PCs required to adequately reconstruct each waveform in a given catalogue a metric known as the match parameter, μ, is used [56]. This value is used to determine how well a set of principal components (PCs) reconstructs a waveform. The match parameter is calculated by the addition of the projections of the chosen number of PCs, k, onto the waveform such that

$$\mu_i = \left|\left| \sum_{j=1}^{k} (h_i, U_j) U_j \right|\right|. \tag{5.1}$$

h_i represents a chosen waveform and U_j are the PCs for a chosen supernova mechanism with the brackets denoting an inner product. If the catalogue of waveforms is normalised with no detector noise added to the waveform, then μ_i will be equal to 1 if the sum of the projection of the PCs match a particular waveform exactly.

The use of all PCs representing a particular supernova mechanism would clearly

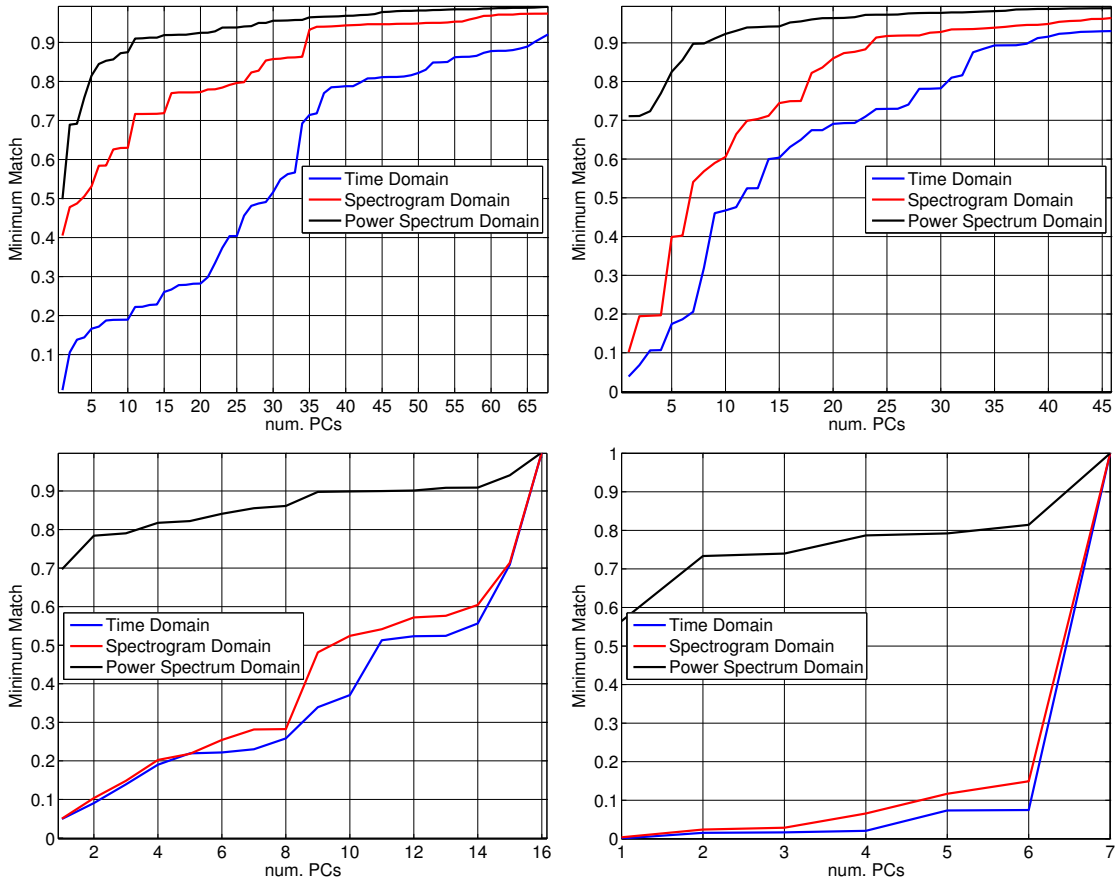

Figure 5.7: Minimum match parameter for each waveform catalogue with increasing number of PCs where no detector noise is added for each version of SMEE. `Abd` results are shown in the top left, `Dim` results are shown in the top right, `Mur` results are shown in the bottom plot and `Ott` results are shown in the bottom right. Note that for the `Mur` and `Ott` catalogues, every PC is required to ensure that the match for every waveform in the catalogue is greater than 0.9.

give a match of 1 for any waveform from the corresponding catalogue. However, using all PCs may not be feasible due to the increased computing costs. Therefore, a threshold is chosen such that the match need only equal 0.9. This value ensures that the reconstruction of a waveform is achieved to an acceptable level but computing costs are reduced. Thus for every catalogue of waveforms which are used to create PCs (the `Abd`, `Dim`, `Mur` and `Ott` catalogues) the match where no detector noise has been added to the waveform is found. For example, when the `Dim` catalogue is tested, for every PC, 128 matches are calculated. The minimum value out of these 128 values is chosen and is labelled as the minimum match. This is repeated for each waveform catalogue and the minimum match is plotted in Figure 5.7 for each version of SMEE.

For the case of the `Ott` catalogue, all 7 PCs are required to find a minimum match of 0.9 for each waveform in the catalogue. The reason for this is due to the

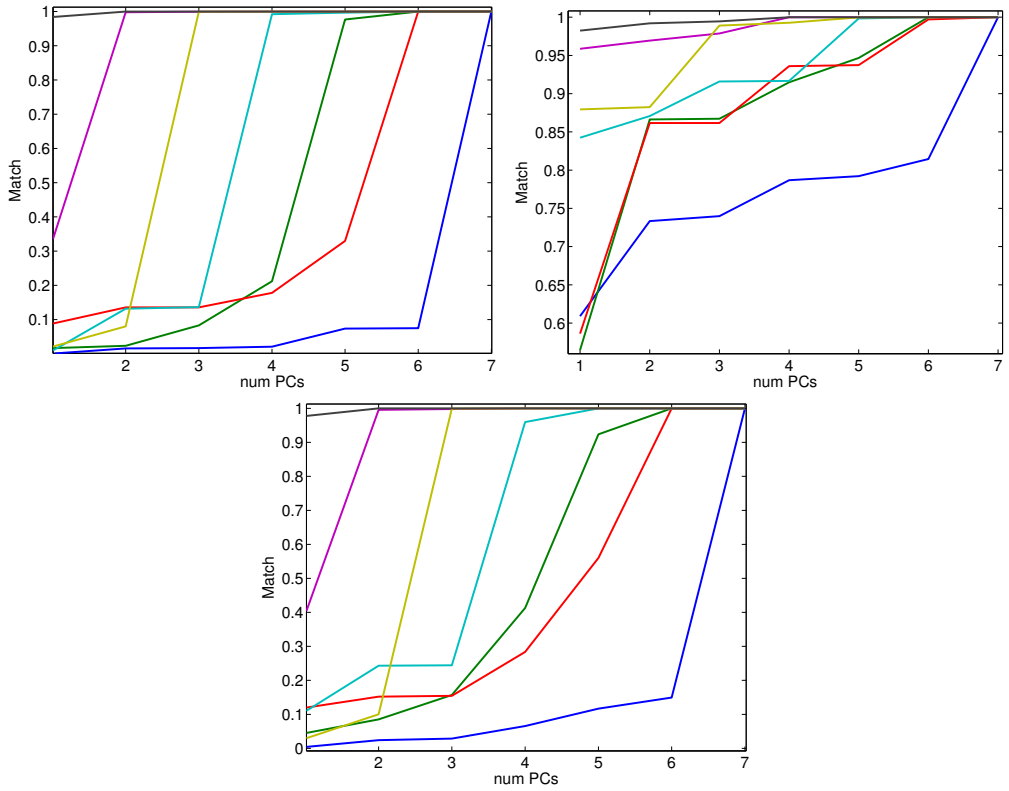

Figure 5.8: Match parameter for each `Ott` waveform with increasing number of PCs. Time domain results are shown in the top left, PSD results are shown in the top right and spectrogram results are shown in the bottom plot. Each coloured line represents a single waveform from the `Ott` catalogue. The match tends to increase only once a certain PC has been added implying that a single PC contains information about a specific waveform in the catalogue. This means that 7 PCs from the `Ott` catalogue will be used in all future results.

small size of the `Ott` catalogue meaning that a large and varied parameter space has not been provided. This is demonstrated in Figure 5.8 where, for each version of SMEE, the match for each waveform is shown. Each line represents a single waveform and shows that the match will increase rapidly once a corresponding PC has been added, i.e. the match for the 3rd waveform increases when the 3rd PC is added. This implies that the information for each waveform is embedded in a single PC and that a waveform will not reach a match of 0.9 until the corresponding PC is included. Because of this, to ensure that each waveform is satisfactorily reconstructed all 7 `Ott` PCs will continue to be used.

This same effect of the limitations of a small parameter set is evident in the `Mur` catalogue which requires all 16 PCs in the time and spectrogram domains to reach a minimum match of 0.9. The individual matches for each waveform is shown for each version of SMEE in Figure 5.9. The same scenario seen with the `Ott` catalogue is also seen here. Again, certain features only seen in individual waveforms are

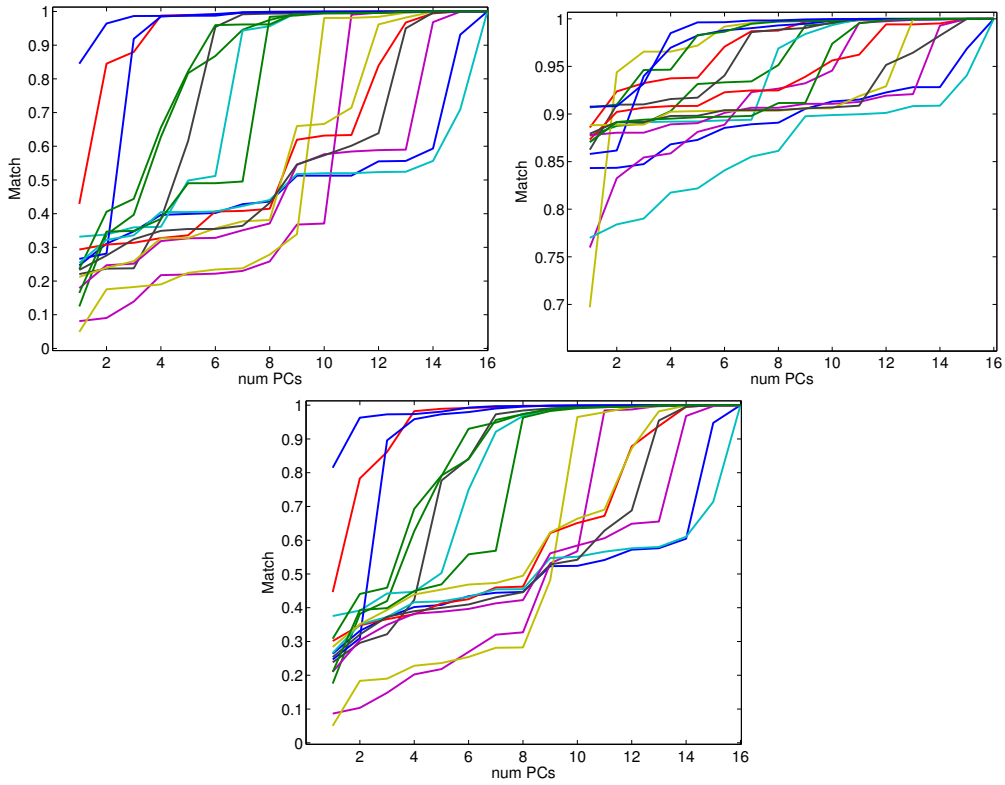

Figure 5.9: Same as Figure 5.8 but with the `Mur` catalogue. Time domain results are shown in the top left, PSD results are shown in the top right and spectrogram results are shown in the bottom plot.The match tends to increase only one a certain PC has been added implying that a single PC contains information about a specific waveform in the catalogue. This means that all 16 PCs from the `Mur` catalogue will be used in all future results.

encoded in a single PC meaning that to reach a minimum match of 0.9 all 16 PCs are required.

The limitations of a small catalogue with a small parameter space is overcome with the use of a larger catalogue with contains as much variation as possible. This is evident in the case of the `Abd` and `Dim` catalogues where a number significantly smaller than the total number of PCs is required to ensure a match of 0.9 for every waveform in each catalogue. For example, in the spectrogram domain, 23 PCs are required with the `Dim` catalogue and 35 PCs for the `Abd` catalogue. Whilst these numbers are small compared to the total number of waveforms in each catalogue, using these numbers in SMEE would greatly add to the computing cost. As SMEE is designed to run quickly, a smaller number of PCs is desirable. To find a smaller number, the number of PCs required to allow SMEE to run quickly but still provide Bayes Factors which are adequate for Bayesian model selection must be found.

5.3.2 How many PCs to use with Magnetorotational Mechanism?

To find the number of PCs to use with the `Dim` and `Abd` catalogues, SMEE's effectiveness at successfully using Bayes Factors to select which catalogue a chosen waveform belongs to with an increasing number of PCs is investigated. As was first shown in Chapter 4 in Section 4.2.3, SMEE's ability to tell apart 2 catalogues which share the same mechanism but have different sources is a useful metric for the success of SMEE.

Thus for an increasing number of PCs, each version of SMEE is tested for all of the `Dim` and `Abd` waveforms on both the `Dim` and `Abd` PCs and a value for $\log B_{AbdDim}$ is found. To ensure all waveforms have an SNR large enough to be detected over detector noise, each waveform is scaled to a distance of 2 kpc. In this case, the scale factor, s_f, is kept as a fixed parameter that is not marginalised in SMEE. The results of this are shown in Tables 5.3 to 5.5.

Time Domain

Results for the time domain are shown in Table 5.3. A maximum of 10 PCs to test is chosen as the computing costs above this value are deemed to be too high. For simplicity, it is decided to give the `Abd` and `Dim` catalogues equal weight therefore the same number of PCs will be used with each catalogue. As the number of PCs used increases, SMEE is better able to correctly assign the waveform to its corresponding catalogue. Using 10 PCs, time domain SMEE is successful for over 90% of both the `Dim` and `Abd` catalogues and thus this is chosen as the ideal number of PCs to use when using either of the PC sets made using catalogues created from the magnetorotational mechanism.

Power Spectrum Domain

Results for the power spectrum domain are shown in Table 5.4. As in the time domain, a maximum of 10 PCs to be tested is chosen as the computing costs above this value are deemed to be too high. As the number of PCs used increases, SMEE

is better able to correctly assign the waveform its corresponding catalogue. When increasing from 7 to 10 PCs, the number of `Dim` waveforms assigned correctly decreases from 124 to 120. The number of `Abd` waveforms assigned correctly does not significantly change when going from 7 to 10 PCs. As the aim is to have has many waveforms assigned correctly as possible while reducing computing costs, 7 PCs are chosen to be used in this case.

Spectrogram Domain

Results for the spectrogram domain are shown in Table 5.5. A maximum of 7 PCs to be tested is chosen as the computing costs above this value are deemed to be too high as this version of SMEE has increased computing cost from calculating the spectrogram of each iteration in the nested sampling algorithm. As the number of PCs used increases, SMEE is better able to correctly assign the waveform its corresponding catalogue. Using 7 PCs, spectrogram SMEE is successful for over 90% of both the `Dim` and `Abd` catalogues and thus this is chosen as the ideal number of PCs to use when using either of the PC sets made using catalogues created from the magnetorotational mechanism.

Thus, the number of PCs to be used for each supernova mechanism for all 3 versions of SMEE has been found and is summarised in Table 5.6. These changes along with the change of priors discussed in Section 5.2 will be applied to SMEE in all results shown in Chapter 6.

Table 5.3: Number of `Abd` and `Dim` waveforms (with percentage of the catalogue in brackets) which time domain SMEE correctly matches to the correct catalogue using increasing numbers of PCs at 2kpc. Results which agree with the wrong catalogue are labelled Incorrect, results where $\log B_{AbdDim}$ is between -5 and 5 are labelled as Inconclusive and results which agree with the correct catalogue are labelled Correct. Here, 10 PCs is chosen as the ideal number of PCs to be used in future results.

num. PCs	Catalogue	Incorrect	Inconclusive	Correct
3	`Abd`	10 (9.4%)	2 (1.9%)	94 (88.7%)
3	`Dim`	14 (10.9%)	0	114 (89.1%)
5	`Abd`	13 (12.3%)	1 (0.9%)	92 (86.8%)
5	`Dim`	9 (7%)	1 (0.8%)	118 (92.2%)
7	`Abd`	10 (9.4%)	2 (1.9%)	94 (88.7%)
7	`Dim`	7 (5.5%)	0	121 (94.5%)
10	`Abd`	7 (6.6%)	1 (0.9%)	98 (92.5%)
10	`Dim`	3 (2.3%)	0	125 (97.7%)

Table 5.4: Number of `Abd` and `Dim` waveforms (with percentage of the catalogue in brackets) which power spectrum domain SMEE correctly matches to the correct catalogue using increasing numbers of PCs at 2kpc. Results which agree with the wrong catalogue are labelled Incorrect, results where $\log B_{AbdDim}$ is between -5 and 5 are labelled as Inconclusive and results which agree with the correct catalogue are labelled Correct. Here, 7 PCs is chosen as the ideal number of PCs to be used in future results.

num. PCs	Catalogue	Incorrect	Inconclusive	Correct
3	`Abd`	24 (22.6%)	3 (2.8%)	79 (74.6%)
3	`Dim`	12 (9.4%)	0	116 (90.6%)
5	`Abd`	18 (17%)	3 (2.8%)	85 (80.2%)
5	`Dim`	6 (4.7%)	0	122 (95.3%)
7	`Abd`	15 (14.2%)	3 (2.8%)	88 (83%)
7	`Dim`	4 (3.1%)	0	124 (96.9%)
10	`Abd`	11 (10.4%)	6 (5.6%)	89 (84%)
10	`Dim`	8 (6.2%)	0	120 (93.8%)

Table 5.5: Number of `Abd` and `Dim` waveforms (with percentage of the catalogue in brackets) which spectrogram domain SMEE correctly matches to the correct catalogue using increasing numbers of PCs at 2kpc. Results which agree with the wrong catalogue are labelled Incorrect, results where $\log B_{AbdDim}$ is between -5 and 5 are labelled as Inconclusive and results which agree with the correct catalogue are labelled Correct. Here, 7 PCs is chosen as the ideal number of PCs to be used in future results.

num. PCs	Catalogue	Incorrect	Inconclusive	Correct
3	`Abd`	17 (16%)	0	89 (84%)
3	`Dim`	2 (1.9%)	0	126 (98.1%)
5	`Abd`	17 (16%)	0	89 (84%)
5	`Dim`	0	0	128 (100%)
7	`Abd`	7 (6.6%)	1 (0.9%)	98 (92.5%)
7	`Dim`	0	0	128 (100%)

Table 5.6: Number of PCs now implemented in each version of SMEE for results shown Chapter 6.

PC catalogue	Time Domain	Power Spectrum Domain	Spectrogram Domain
`Abd`	10	7	7
`Dim`	10	7	7
`Mur`	16	16	16
`Ott`	7	7	7

Chapter 6

SMEE with Multiple Detectors

In Chapter 4 the Supernova Model Evidence Extractor (SMEE) was shown to be effective at inferring the physics behind a detected gravitational waveform from a supernova through the use of Bayesian model selection. However, Chapter 4 dealt only with the overly simplified case where only one GW detector is used and the effect of the antenna response is not included.

In this Chapter, SMEE is tested using 3 detectors (the Advanced LIGO detectors, labelled as H and L and Advanced Virgo, labeled as V) and the full effect of the time delay between detectors and the antenna response on each detector is included. As well as this, detector noise from the Science runs from both LIGO and Virgo are utilised here. These noise files have been adjusted to better match the sensitivity of the Advanced detectors and are known as 'recoloured' noise files [114]. These noise files are used as they provide a closer resemblance to the total noise that will be seen in the Advanced detectors. The improvements to SMEE discussed in Chapter 5 are also employed in this case. Finally, only the linear polarisation is used.

6.1 Reconstruction of Additional Parameters

The full versions of equations 3.19 and 3.23 are used here with Earth centre time of arrival, the polarisation angle and distance kept as free parameters. Before

the success of SMEE using multiple detectors can be assessed, the effectiveness of SMEE's ability to adequately reconstruct these additional 3 parameters must be determined. Only then can SMEE with multiple detectors be fully tested.

To do this a polaristation angle of 0.3046 radians, an Earth centre GPS time of arrival of 981940624 and the distance of 10 kpc is selected. The right ascension used is 4.464 radians with a declination of -0.5063 which are the coordinates of the Galactic Centre. These values are chosen to reduce the effect of the antenna response in the Advanced LIGO detectors thus ensuring the Network SNR remains large enough so that the parameters can be reconstructed. With these coordinates $F_+ = -0.88$ for H, 0.99 for L and -0.26 for Virgo, V. As the value for V is small the SNR of the signal at this detector will be reduced however since this detector is only used alongside the 2 Advanced LIGO detectors it should still provide enough information to aid the reconstruction of the chosen waveform, see Figure 6.1. Descriptions for the priors for these paramters can be found in Sections 3.1.4 to 3.4.

To analyse SMEE's ability to reconstruct these parameters, each version of SMEE is employed on a single `Dim` waveform using a detector configuration of H, followed by HL and finally HLV. The results for each version of SMEE are shown in the following sections. As per the results from Chapter 5, 10 PCs are used when the TD_SMEE (time domain) is used and 7 PCs are used when PSD_SMEE (power spectrum domain) or Spec_SMEE (spectrogram domain) are employed.

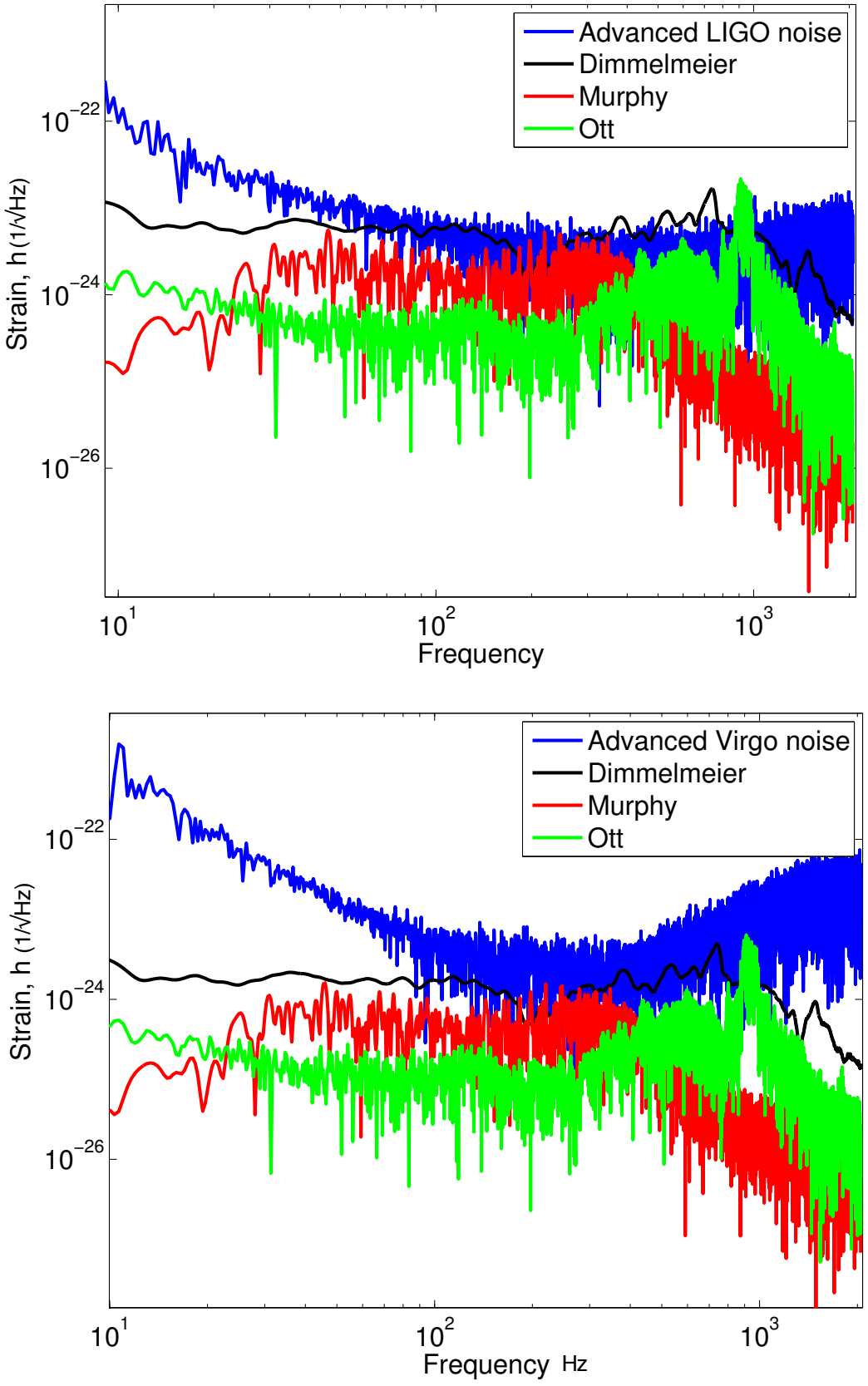

Figure 6.1: Plots of catalogue waveforms scaled by F_+ for Advanced LIGO (H) and Advanced Virgo (V). **Top** Waveform from `Dim`, `Mur` and `Ott` catalogue scaled by the antenna response $F_+ = 0.99$ in Advanced LIGO noise. **Bottom** Same waveforms are plotted scaled by the antenna response $F_+ = -0.26$ in Advanced Virgo noise.

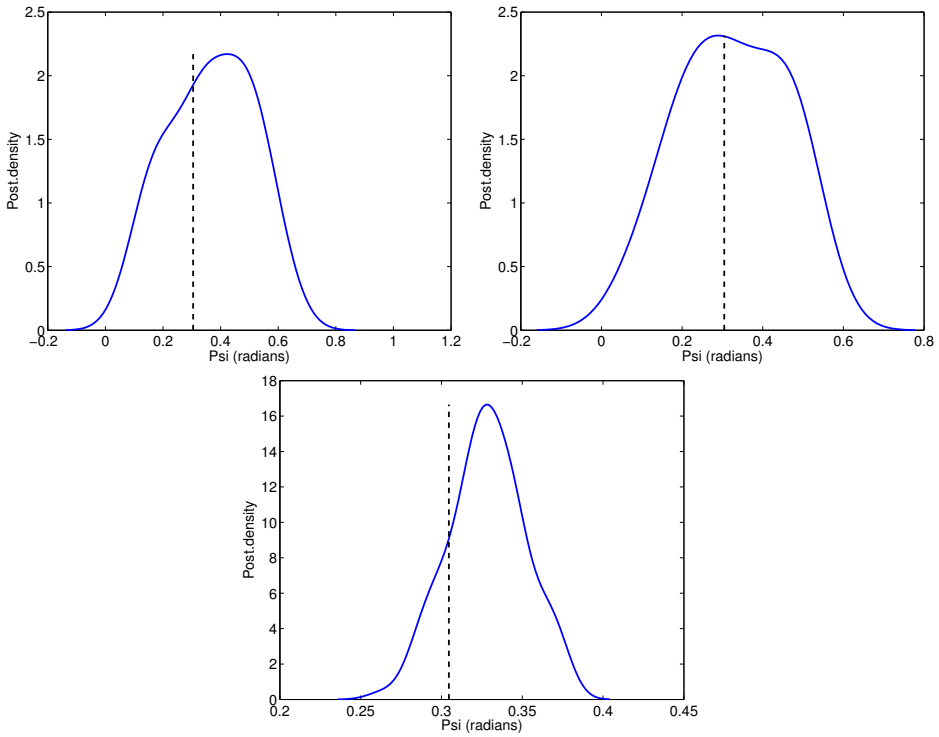

Figure 6.2: Posterior distribution of polarisation angle in the time domain. In each plot the dashed line indicates the value chosen by the user. **Top Left** Using 1 detector (H). **Top Right** Using 2 detectors (HL). **Bottom** Using 3 detector (HLV).

6.1.1 Time Domain

Plots of the posterior distributions for the polarisation angle, Earth centre arrival time (which has been shifted so that the correct time is at 0 seconds) and the distance when using TD_SMEE are shown in Figures 6.2 to 6.4. The dashed line indicates the value chosen by the user. These Figures demonstrate that TD_SMEE is satisfactorily able to determine the values chosen by the user. The addition of other detectors improves the ability to estimate these values. This can be seen by either the increased density (in the y-axis of each plot) as detectors are added as well as the narrowed range of values in the posterior distribution (in the x-axis).

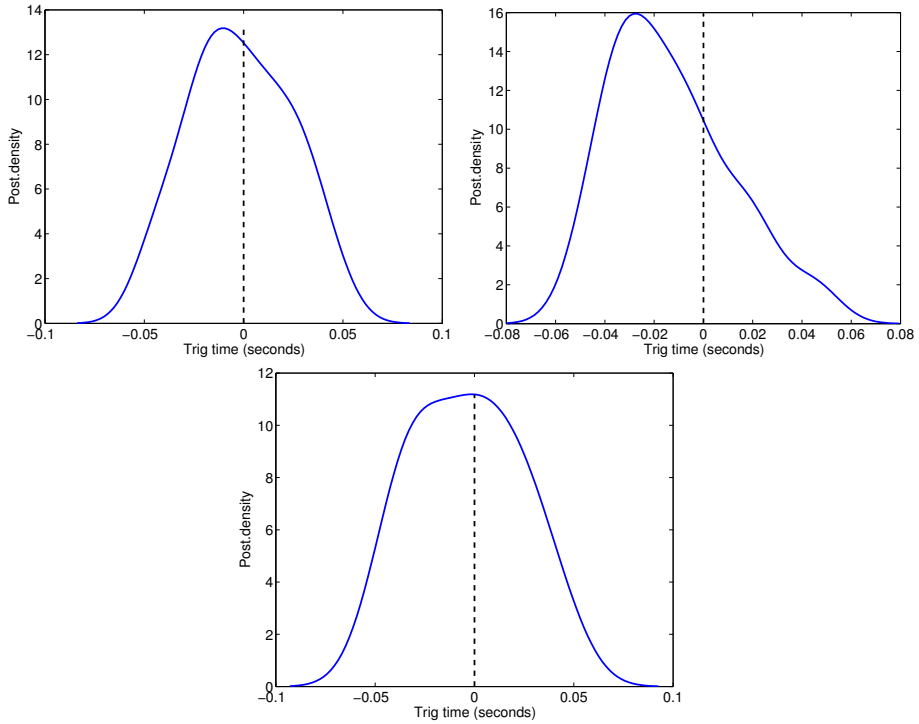

Figure 6.3: Posterior distribution of Earth Centre time used in TD_SMEE. In each plot the dashed line represents where the correct value chosen by the user is placed. **Top Left** Using 1 detector (H). **Top Right** Using 2 detectors (HL). **Bottom** Using 3 detector (HLV).

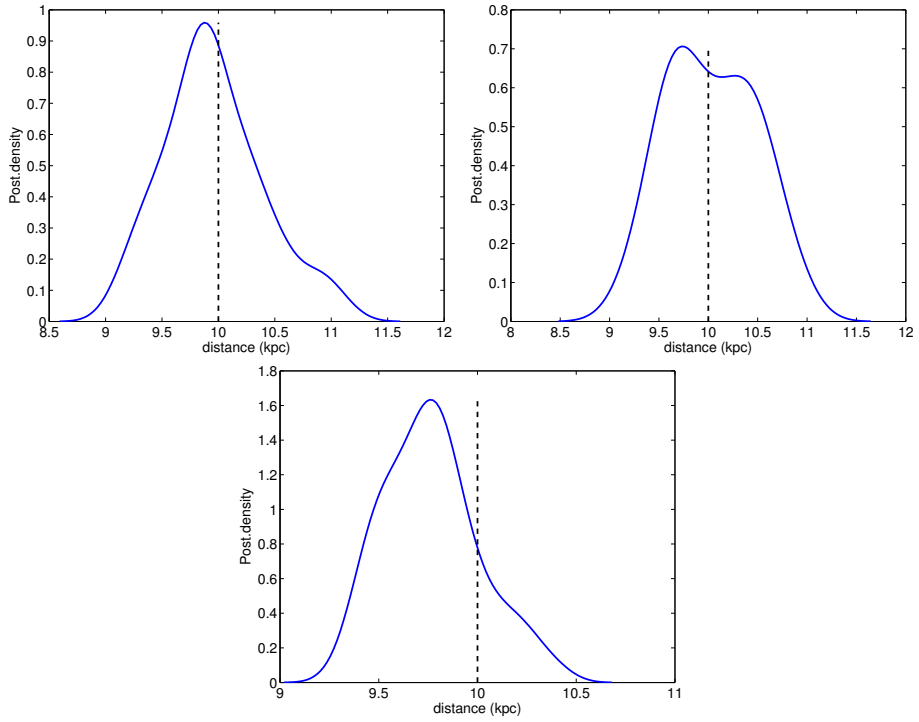

Figure 6.4: Posterior distribution of distance which is chosen as $10kpc$ used in TD_SMEE. In each plot the dashed line indicates the distance chosen by the user. **Top Left** Using 1 detector (H). **Top Right** Using 2 detectors (HL). **Bottom** Using 3 detector (HLV).

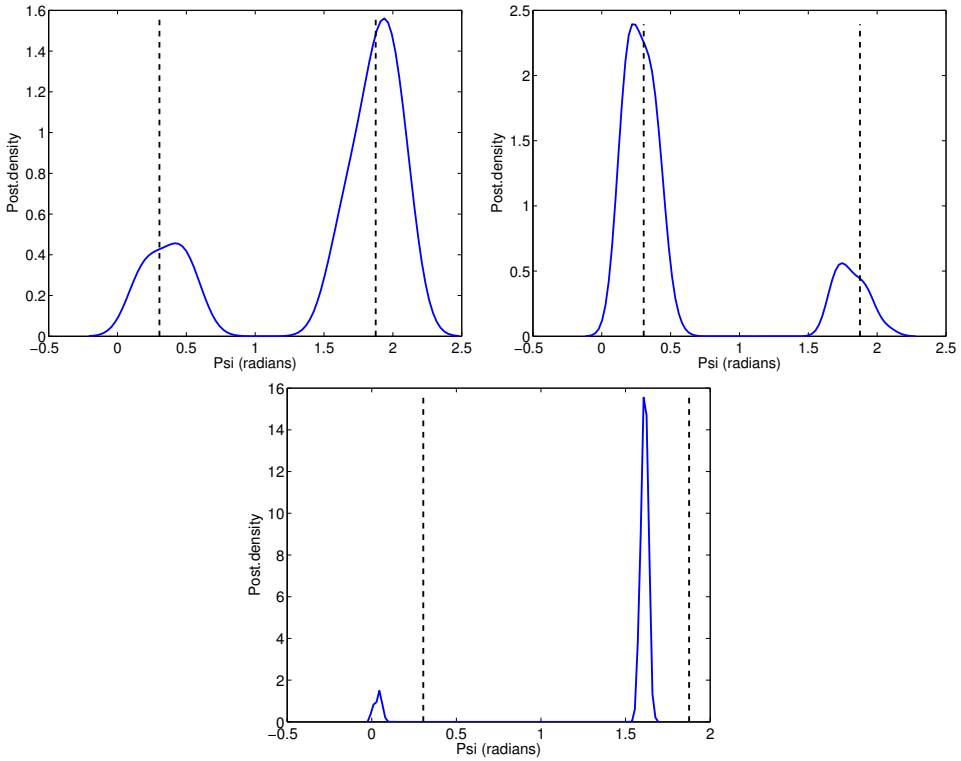

Figure 6.5: Posterior distribution of polarisation angle, same as Figure 6.2 but using PSD_SMEE. There are 2 dashed lines which indicate the two possible polarisation angles, the angle chosen by the user and this angle+$\pi/2$. Due to the fact that the data here is squared, both these values will yield equivalent values for F_+. Thus, PSD_SMEE is working as expected. **Top Left** Using 1 detector (H). **Top Right** Using 2 detectors (HL). **Bottom** Using 3 detector (HLV).

6.1.2 Power Spectrum Domain

Plots of the posterior distributions for the polarisation angle, Earth centre arrival time (which has been shifted so that the correct time is at 0 seconds) and the distance when using PSD_SMEE are shown in Figures 6.5 to 6.7. The dashed line indicates the value chosen by the user. As in the time domain Figures 6.6 and 6.7 demonstrate that PSD_SMEE is satisfactorily able to determine the values chosen by the user. The addition of other detectors improves the ability to estimate these values. This can be seen by either the increased density (in the y-axis of each plot) as detectors are added as well as the narrowed range of values in the posterior distribution (in the x-axis).

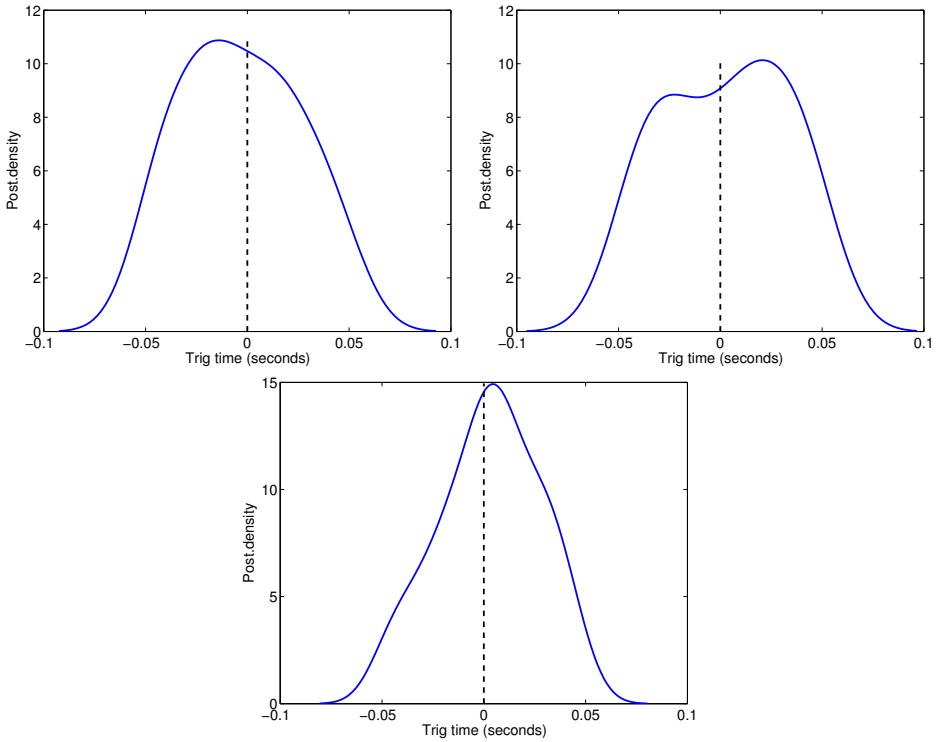

Figure 6.6: Posterior distribution of the Earth centre time, same as Figure 6.3 but using PSD_SMEE. In each plot the dashed line indicates the distance chosen by the user. **Top Left** Using 1 detector (H). **Top Right** Using 2 detectors (HL). **Bottom** Using 3 detector (HLV).

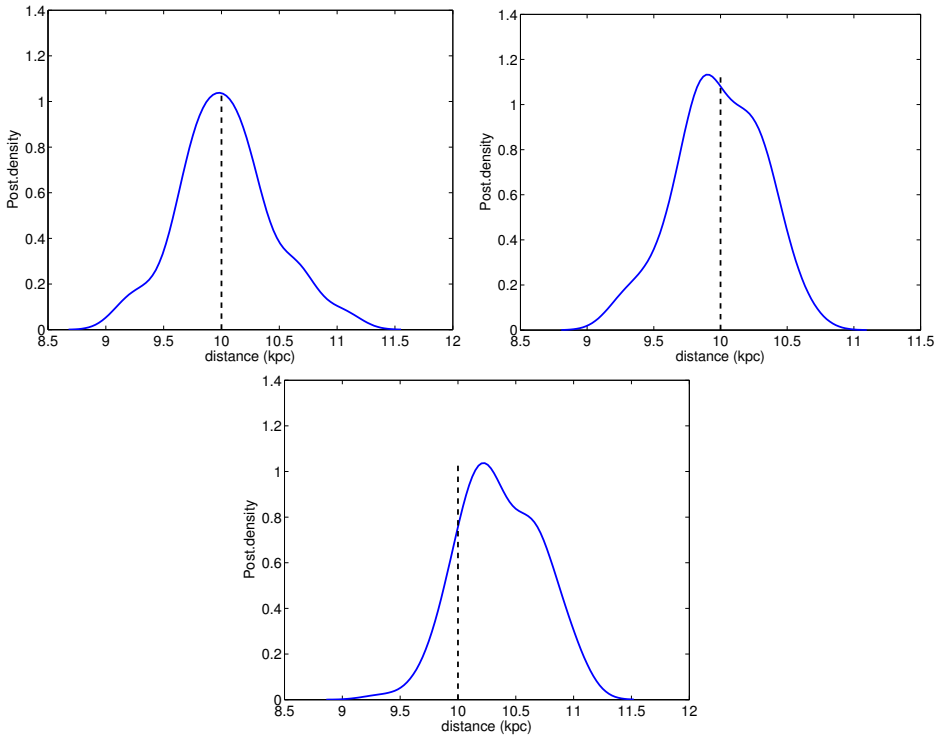

Figure 6.7: Posterior distribution of the distance chosen to be $10kpc$, same as Figure 6.4 but using the PSD_SMEE. In each plot the dashed line indicates the distance chosen by the user. **Top Left** Using 1 detector (H). **Top Right** Using 2 detectors (HL). **Bottom** Using 3 detector (HLV).

In Figure 6.5 two peaks can be seen. The reason for this is due to the nature of the data being used. In Equation 3.23 it is the square of the data and the reconstructed signal that is compared and every value becomes positive. This implies that the sign on F_+ is not important as the reconstructed signal will be made positive. Thus F_+ can be either positive or negative so that there are two values for the polaristion angle which can be used to successfully reconstruct the signal, the value chosen by the user and that value added by $\pi/2$. The two dotted lines in Figure 6.5 represent these two values. PSD_SMEE is able to focus on one of these values and a value for the polarisation angle which will adequately reconstruct the desired waveform.

6.1.3 Spectrogram Domain

Plots of the posterior distributions for the polarisation angle, Earth centre arrival time (which has been shifted so that the correct time is at 0 seconds) and the distance when using Spec_SMEE are shown in Figures 6.8 to 6.10. The dashed line indicates the value chosen by the user. As in the time domain Figures 6.9 and 6.10 demonstrate that Spec_SMEE is satisfactorily able to determine the values chosen by the user. The addition of other detectors improves the ability to estimate these values. This can be seen by either the increased density (in the y-axis of each plot) as detectors are added as well as the narrowed range of values in the posterior distribution (in the x-axis).

In Figure 6.8 two peaks can be seen for the same reason discussed in Section 6.1.2. The two dotted lines in Figure 6.8 represent the two possible values for F_+. Spec_SMEE is successfully able to focus on one of these values and a value for the polarisation angle which will adequately reconstruct the desired waveform.

It has been demonstrated that each version of SMEE is able to adequately infer the values for the polarisation angle, Earth centre arrival time and distance chosen by the user. The estimates on these values could be improved by narrowing the priors on these terms if more accurate information on the correct values from astrophysical measurements can be inferred. This is especially important when using either the power spectrum or spectrogram versions of SMEE where two values for the polarisation angle can be given equal weight. If the range could be reduced from 0 to π to one that has a range of less than $\pi/2$ the accuracy could be greatly

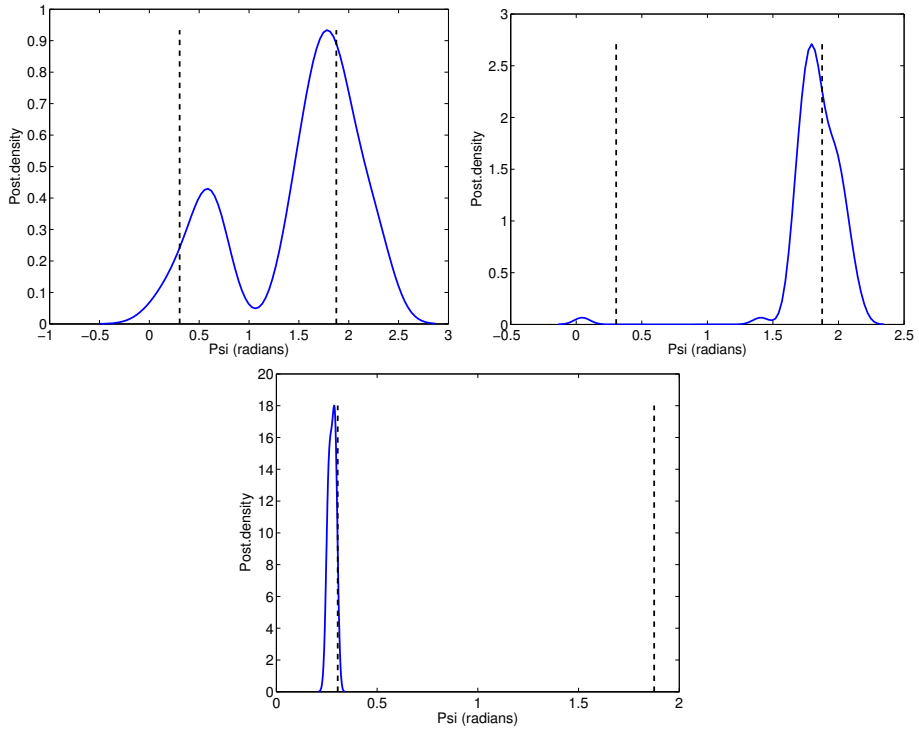

Figure 6.8: Posterior distribution of polarisation angle, same as Figure 6.2 but using Spec_SMEE. There are 2 dashed lines which indicate the two possible polarisation angles, the angle chosen by the user and this angle+$pi/2$. Due to the fact that the data here is squared, both these values will yield equivalent values for F_+. Spec_SMEE is successfully able to reconstruct one of these values when data for 3 detectors is added. Thus, Spec_SMEE is working as expected. **Top Left** Using 1 detector (H). **Top Right** Using 2 detectors (HL). **Bottom** Using 3 detector (HLV).

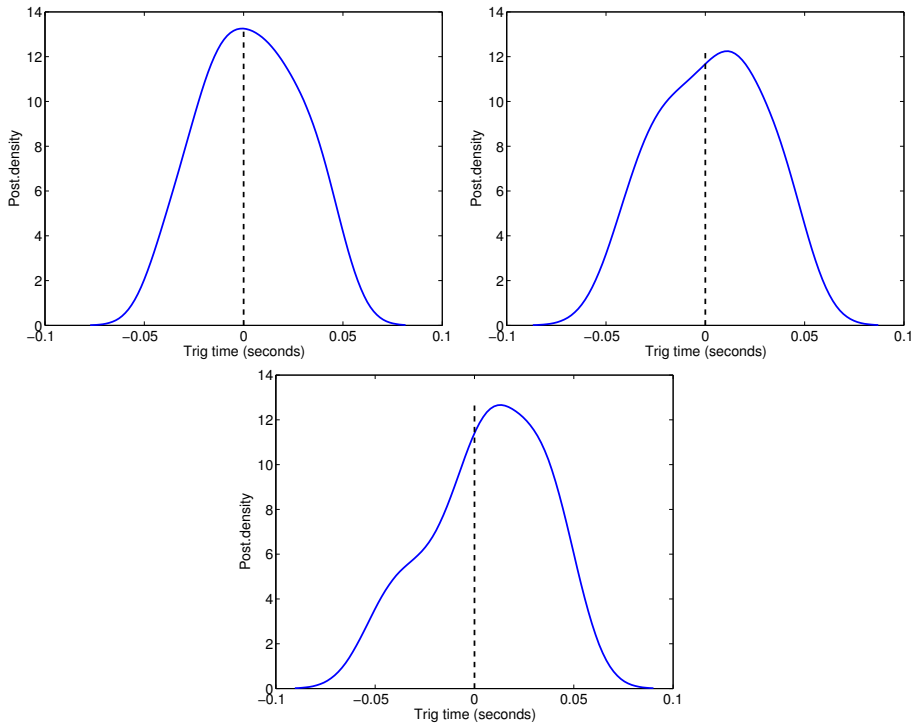

Figure 6.9: Posterior distribution of the Earth centre time, same as Figure 6.3 but using Spec_SMEE. In each plot the dashed line indicates the distance chosen by the user. **Top Left** Using 1 detector (H). **Top Right** Using 2 detectors (HL). **Bottom** Using 3 detector (HLV).

improved. The success of this test means that SMEE with multiple detectors is working as expected and will be able to calculate accurate Bayes Factors and thus allow Bayesian model selection to be performed. The rest of this Chapter will present results with SMEE run with multiple detectors at two different sky positions and distances. The distance at which each version of SMEE can still successfully separate the three different supernova mechanisms will also be determined.

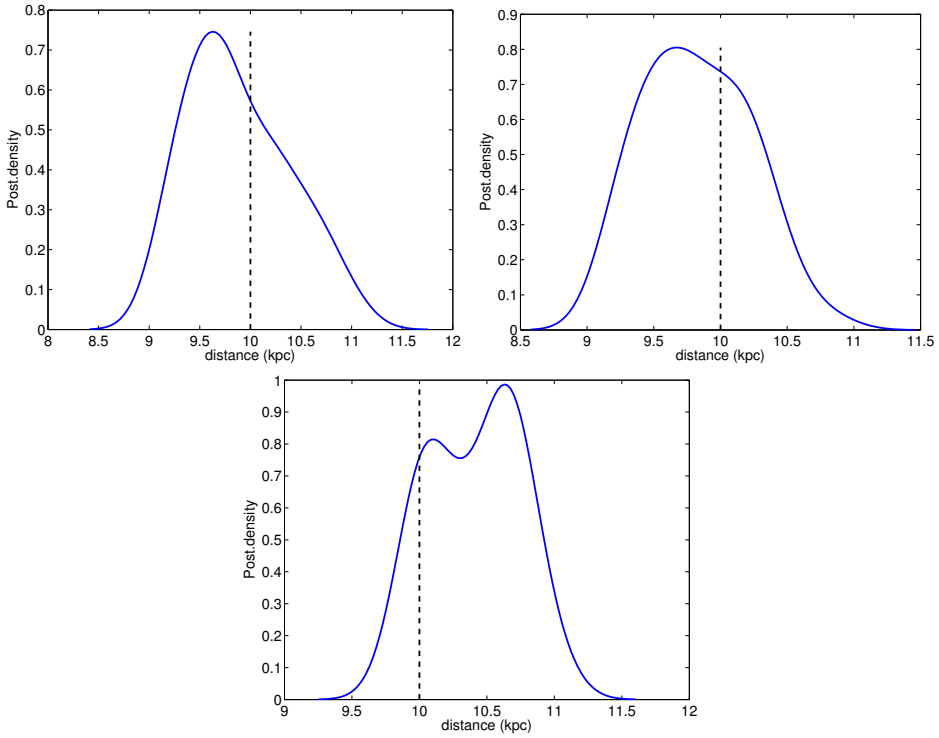

Figure 6.10: Posterior distribution of the distance chosen to be $10kpc$, same as Figure 6.4 but using Spec_SMEE. In each plot the dashed line indicates the distance chosen by the user. **Top Left** Using 1 detector (H). **Top Right** Using 2 detectors (HL). **Bottom** Using 3 detector (HLV).

6.2 Multiple Detector SMEE in the Time Domain

6.2.1 Distinguishing the Supernova Mechanism with Multiple Detectors

As discussed in Section 4.2.2 the assumption that each supernova mechanism has robustly distinct GW signatures can be tested by the addition of simulated waveforms into recoloured S5 detector noise and running SMEE on the data using PCs of waveform catalogues representative of the neutrino, magnetorotational, and acoustic mechanisms was proven to be true in the simple case used in Chapter 4.

Here, this assumption is tested in the more realistic scenario where multiple detectors (HLV) with different antenna responses are used. SMEE calculations are

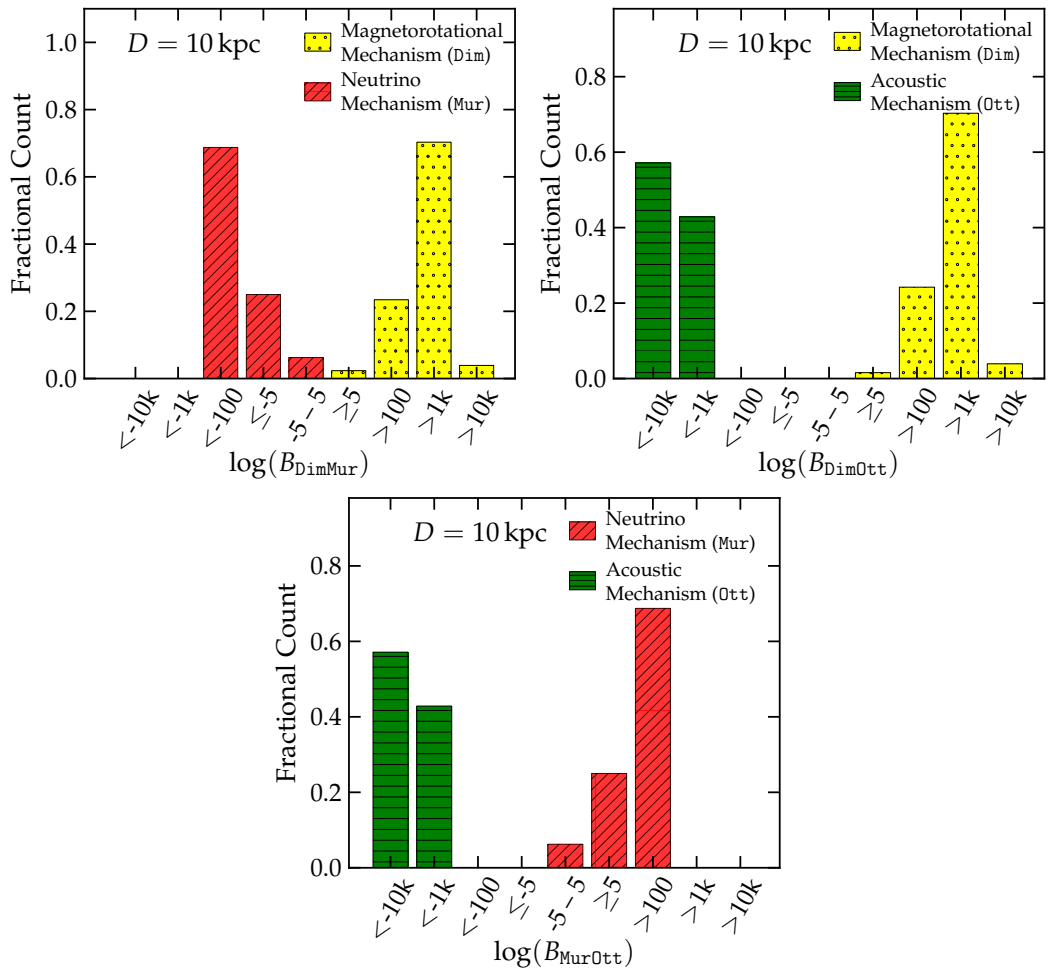

Figure 6.11: Histograms describing the outcome of signal model comparisons in the time domain by means of the Bayes Factors $\log B_{ij} = \log p(D|M_i) - \log p(D|M_j)$, where $i \neq j$ and M_i and M_j are signal models described by the `Dim` (magnetorotational mechanism), `Mur` (neutrino mechanism), and `Ott` (acoustic mechanism) waveform catalogues. This is done using 3 detectors (HLV) and the Bayes Factors are computed with 10 PCs for the `Dim` catalogue, 7 PCs for the `Ott` catalogues and 16 PCs for the `Mur` catalogue at a source distance of 10 kpc using the sky position of the Galactic Center. A positive value $\log B_{ij}$ indicates that the injected waveform most likely belongs to model M_i, while a negative value suggest that model M_j is the more probable explanation. The bars are colour-coded according to the type of injected waveform. The results are binned into ranges of varying size from < -10000 to > 10000 and the height of the bars indicates what fraction of the waveforms of a given catalogue falls into a given bin of $\log B_{ij}$. A range of $(-5, 5)$ of $\log B_{ij}$ is considered as inconclusive evidence (see §4.1).

carried out for events located at 10 kpc, and 50 kpc using 7 PCs when the PCs created from the `Ott` catalogue are used, 10 when PCs from the `Dim` PCs are used and 16 when the `Mur` PCs are used. The same values for polarisation angle, Earth centre arrival time, right ascension and declination used in Section 6.1 are used here when signals are located at a distance of 10 kpc. At 50 kpc the right ascension and declination of the Large Magallenic Cloud are selected, right ascension is 1.3158 and the declination is -1.2175 radians. A polarisation angle of 0.6446 radians and a Earth centre arrival time of 981990824 seconds are chosen. With these coordinates $F_+ = -0.919$ for H, 0.759 for L and -0.374 for Virgo, V.

As in Fig. 4.5, results are shown for injection studies of *all* waveforms from the `Dim`, `Mur`, and `Ott` catalogues run through TD_SMEE and analysed with the `Dim`, `Mur`, and `Ott` PCs at a source distance of 10 kpc. The results of this are shown in Figure 6.11. The top left panel depicts the $\log B_{\texttt{DimMur}}$ result for injected waveforms from the `Dim` and `Mur` catalogues, that are taken to be representative of the magnetorotational and neutrino mechanisms, respectively. Even at 10 kpc all waveforms characteristic for magnetorotational explosions are clearly identified as belonging to this mechanism. For the neutrino mechanism, the evidence is generally weaker and ∼70% of the `Mur` waveforms are identified with $\log B_{\texttt{DimMur}} < -100$, while only 1 waveform (∼6%) is in the inconclusive regime of $-5 < \log B_{\texttt{DimMur}} < 5$.

In the top right panel of Fig. 6.11, results are shown for $\log B_{\texttt{DimOtt}}$ for waveforms corresponding to the magnetorotational (`Dim`) and the acoustic (`Ott`) mechanisms. In this case, all waveforms are correctly identified as most likely belonging to their respective catalogue/mechanism. Finally, the bottom panel of Fig. 6.11 presents $\log B_{\texttt{MurOtt}}$ for waveforms representative of the neutrino (`Mur`) and acoustic (`Ott`) mechanisms. As in the previous panel, TD_SMEE associates the waveforms corresponding to the acoustic mechanism with high confidence to the `Ott` catalogue. The evidence suggesting correct association of the neutrino mechanism waveforms is once again less strong, but $\log B_{\texttt{MurOtt}}$ is still conclusive for ∼94% of the `Mur` waveforms. Only 1 waveform is in the inconclusive region as this waveform does not have the required Network SNR to be detected in any of the 3 detectors.

Figure 6.12 shows the results for $\log B_{\texttt{DimMur}}$, $\log B_{\texttt{DimOtt}}$, and $\log B_{\texttt{MurOtt}}$ obtained by TD_SMEE at a source distance of 50 kpc. Even at this increased distance all acoustic waveforms (`Ott`) are correctly separated from both the magnetorotational and neutrino mechanisms. The `Dim` waveforms also perform very well and only

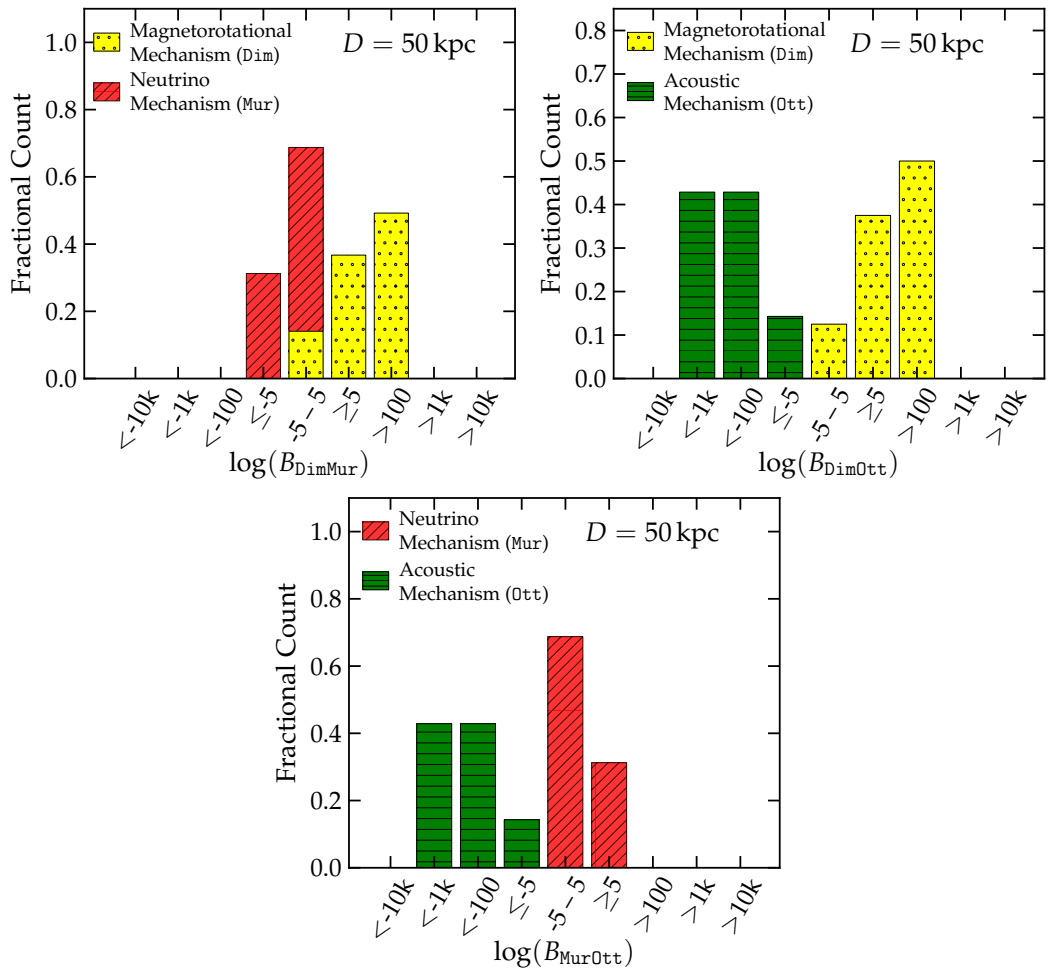

Figure 6.12: Same as Fig. 6.11, but computed for a source distance of 50 kpc using the sky position of the Large Magallenic Cloud (LMC).

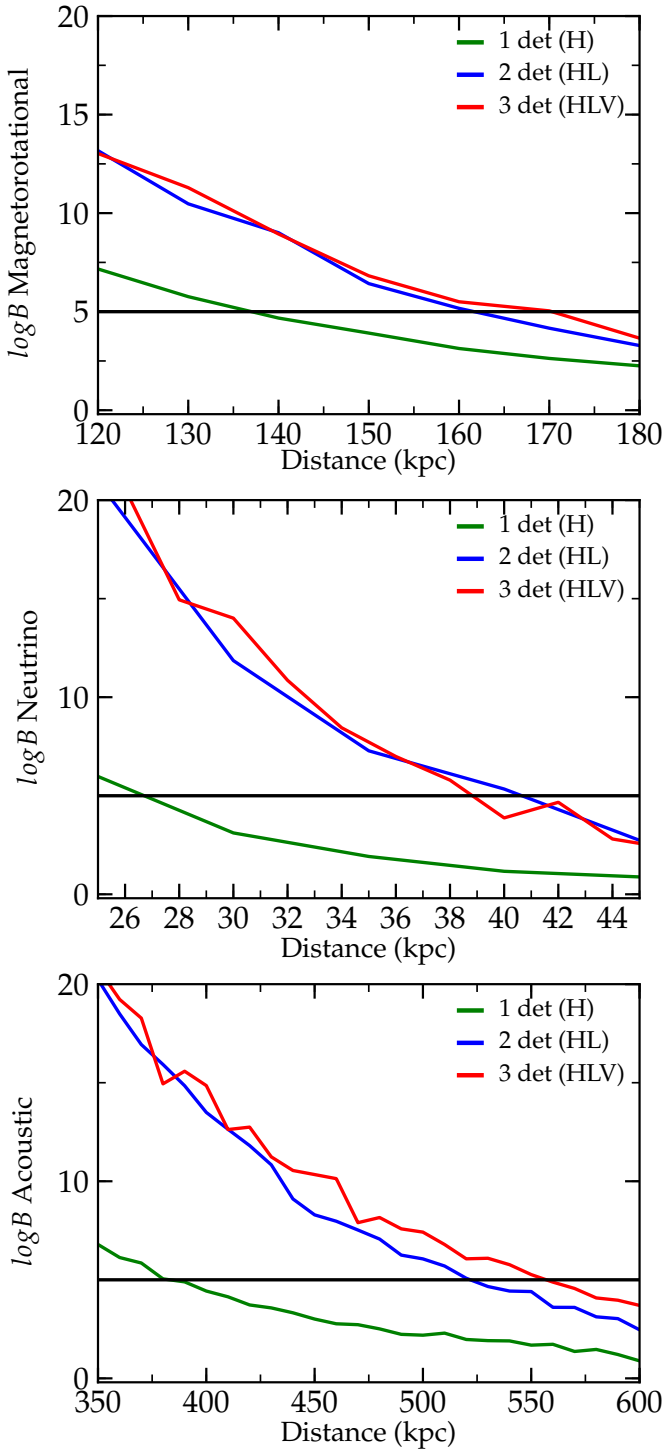

Figure 6.13: Distance to which SMEE using multiple detectors can successfully distinguish one catalogue from two others using the sky position for the Galactic Centre. This shows results for the waveform catalogues when the $\log B_{SN}$ for the expected correct mechanism is compared with the $\log B_{SN}$ found when attempting to reconstruct the injected waveform with the other two sets of PCs. The log Bayes Factor is then found i.e. in the case of the `Dim` catalogue $\log B_{Magnetorotational}$ is found for the `Dim` PCs versus the `Mur` and the `Ott` PCs. Out of the two results the minimum is plotted here to ensure that SMEE can distinguish between all sets of PCs. The mean log Bayes Factor for every waveform in the catalogue is shown here. **Top Plot** Results for the `Dim` catalogue. In the time domain using 3 detectors, the maximum mean distance that signal can be distinguished from both the `Mur` and `Ott` PCs is $\sim$ 170 kpc. **Middle Plot** Results for the `Mur` catalogue. In the time domain using 3 detectors, the maximum mean distance that signal can be distinguished from both the `Dim` and `Ott` PCs is $\sim$ 40 kpc. **Bottom Plot** Results for the `Ott` catalogue. In the time domain using 3 detectors, the maximum mean distance that signal can be distinguished from both the `Dim` and `Mur` PCs is $\sim$ 550 kpc.

∼12% of the waveforms in this catalogue do not have the required SNR to be distinguished from the noise. However, the `Mur` waveforms perform less well and only ∼31% are correctly matched to the correct mechanism.

It is scientifically interesting to determine to what distance SMEE is successfully able to not only detect a waveform within detector noise but also infer which mechanism it most resembles. To find this distance for each mechanism all waveforms are tested at an increasing distance using all 3 sets of PCs and the coordinates used for the Galactic Centre. For each distance tested a mean value from every waveform in the catalogue is calculated. Results for the `Dim`, `Mur` and `Ott` catalogues are shown in Figure 6.13. As expected both the `Dim` and `Ott` are successful at distances over 50kpc whereas `Mur` is effective to distances of ∼40 kpc. The maximum distance improves when more detectors are added however there is minimal improvement from adding Advanced Virgo. This is due to the fact that F_+ is a lot smaller here and so the waveforms have a smaller SNR. Therefore they do not contribute as much as the 2 Advanced LIGO detectors. If a different sky position was chosen where F_+ was larger then the contribution from Advanced Virgo would increase, see Figure 6.28 .

Thus it has been shown that TD_SMEE can successfully perform Bayesian model selection to distances throughout the Milky Way and to at least one of its satellite galaxies in the case where different mechanisms are compared. As in Section 4.2.3, TD_SMEE can be tested when two catalogues with similar dynamics are compared.

6.2.2 Rotating Accretion-Induced Collapse or Rotating Iron Core Collapse?

As in Section 4.2.3 all `Abd` and `Dim` waveforms are added to recoloured S5 noise, in this case noise from 2 Advanced LIGO detectors and Advanced Virgo. TD_SMEE is then run with 10 PCs to once again calculate $\log B_{\texttt{AbdDim}}$. The results are shown in Figure 6.14 for source distances of 10 kpc and 50 kpc.

SMEE correctly identifies the majority of injected waveforms as most likely being emitted by a rotating iron core collapse or by rotating accretion induced collapse (AIC) in TD_SMEE at both 10 and 50 kpc. At 10 kpc ∼5% of the `Dim` waveforms and ∼18% of the `Abd` waveforms are incorrectly identified as belonging to the wrong

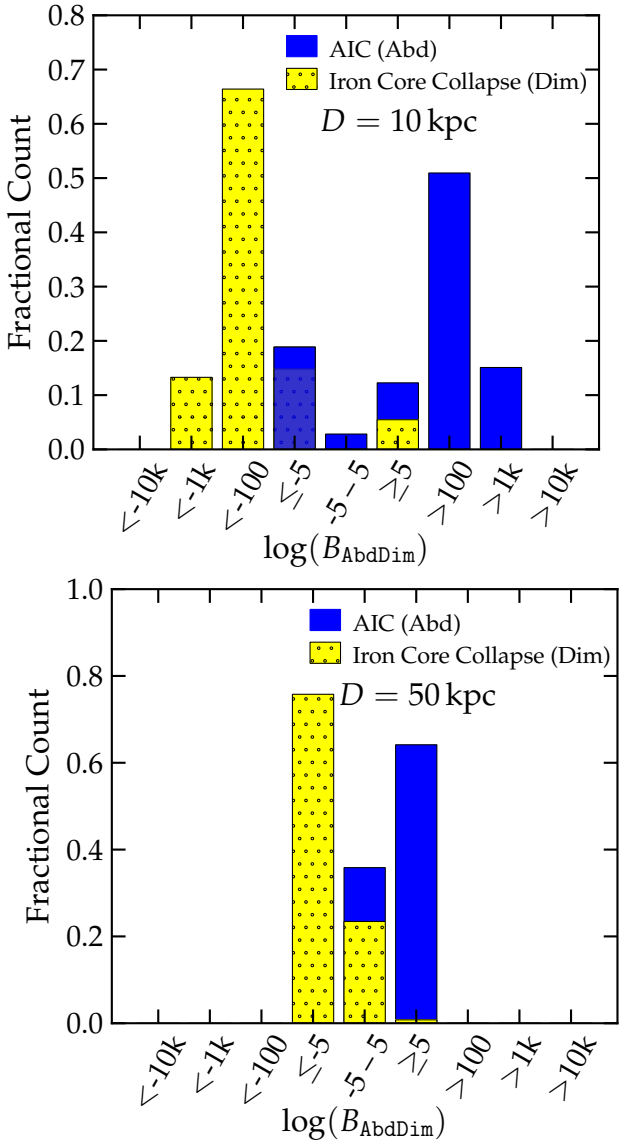

Figure 6.14: Outcome of the SMEE analysis in the time domain of injected rotating iron core collapse (`Dim` catalogue) and rotating accretion-induced collapse (AIC, `Abd` catalogue) waveforms using 3 detectors (HLV). The top panel shows results for a source distance of 10 kpc (at the Galactic Centre) and the right panel depicts the results for a distance of 50 kpc (at the Large Magallenic Cloud). The Bayes Factors $\log B_{\mathtt{AbdDim}}$ are computed on the basis of 10 PCs from the `Abd` and `Dim` catalogue. A positive value of $\log B_{\mathtt{AbdDim}}$ indicates that an injected waveform is most likely associated with rotating AIC and a negative value suggests it to be more consistent with rotating iron core collapse. The results are binned into ranges of varying size from < -10000 to > 10000 and the height of the colour-coded bars indicates what fraction of the waveforms of a given catalogue falls into a given bin of $\log B_{\mathtt{AbdDim}}$. A range of $(-5, 5)$ of $\log B_{ij}$ is considered as inconclusive evidence (see §4.1).

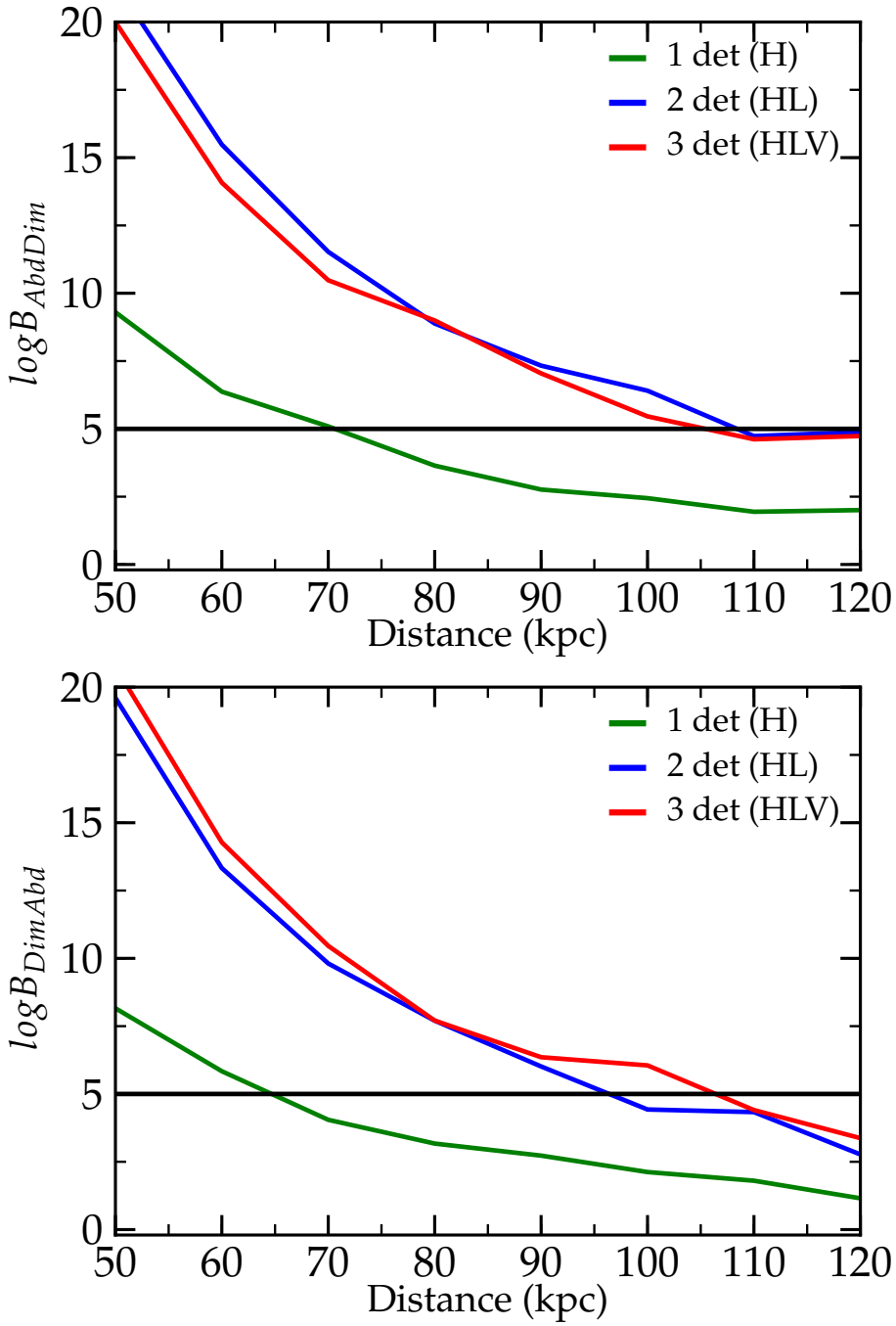

Figure 6.15: Distance to which SMEE using multiple detectors can successfully distinguish the `Abd` and `Dim` catalogues using the sky position for the Galactic Centre. **Top Plot** Results for the `Abd` catalogue. In the time domain using 3 detectors, the maximum mean distance that signal can be distinguished from the `Dim` PCs is $\sim$ 110 kpc. **Bottom Plot** Results for the `Dim` catalogue. In the time domain using 3 detectors, the maximum mean distance that signal can be distinguished from the `Abd` PCs is $\sim$ 105 kpc.

catalogue. In addition none of the `Dim` waveforms and ∼3% of the `Abd` are in the inconclusive region. At 50 kpc TD_SMEE is still very accurate and over 70% of the `Dim` and over 65% of the `Abd` waveforms are correctly identified.

In Figure 6.15, distance plots are shown to identify the mean distance TD_SMEE can still separate the 2 waveform catalogues. While less successful than in the case where the magnetorotational mechanism is compared to the neutrino and acoustic mechanisms the `Dim` and `Abd` catalogues can still be correctly identified to distances greater that 100 kpc.

6.2.3 Testing Robustness of SMEE using non-catalogue waveforms

As in Section 4.2.4, TD_SMEE can be tested using waveform catalogues that share the same supernova mechanism but were not used in the creation of the PCs. The same catalogues used in Section 4.2.4 are analysed using TD_SMEE with the improvements described in Chapter 5 and Section 6.1 using the same distances and coordinates used in previous sections. Results for $\log B_{SN}$ are shown in Table 6.1. Plots like those shown in Figure 6.13 are shown in Figure 6.16.

Magnetorotational Mechanism

For the magnetorotational mechanism, three additional `Dim` waveforms (`DimExtra`, Sec. 1.7) are employed that were not included in the calculation of the `Dim` PCs. Furthermore, waveforms from rotating models of the `Sch` catalogue of Scheidegger *et al.* [102, 23] are injected (see Sec. 1.7). The results of both the $\log B_{SN}$ calculation for the magnetorotational, neutrino, and acoustic mechanism signal models are summarized in Tab. 6.1. `DimExtra` waveforms are identified as being most consistent with the `Dim` catalogue and, hence, the magnetorotational mechanism for all `DimExtra` signals at both 10 kpc and 50 kpc. The Distance plot in Figure 6.16 shows that `DimExtra` waveforms can be correctly identified up to a mean distance of ~ 170 kpc.

The `Sch` waveforms were generated with a completely different numerical code

Table 6.1: Time domain:log B_{SN} for gravitational waveforms that were not included in the catalogues used for PC computation. The `DimExtra`, `Sch`, `OttExtra`, and `Yak` waveforms are discussed in §1.7. Results are shown for source distances of 10 kpc and 50 kpc and for evaluations using 7 PCs for the `Ott` PCs, 10 for the `Dim` PCs and 16 for the `Mur` PCs . Larger values indicate stronger evidence that the waveform is matched to the model catalogue from which the PCs were constructed. $\log B_{SN} < 5$ indicates that the injected signal is likely consistent with noise while larger values suggests that the signal belongs to the signal model whose PCs were used in the analysis.

Waveform	$\log B_{SN}$ Dim PCs		$\log B_{SN}$ Mur PCs		$\log B_{SN}$ Ott PCs	
	10 kpc	50 kpc	10 kpc	50 kpc	10 kpc	50 kpc
`DimExtra` [97]						
s20a1o05_shen	4315	155	102	35	71	32
s15a1o03_LS	9680	348	225	56	184	52
s40a1o10_LS	3105	107	383	1	103	0
`Sch` [102]						
R1E1CA	23	4	8	3	8	3
R1E1CA_L	10	1	7	2	9	0
R1E1DB	19	3	3	2	6	2
R1E3CA	34	0	3	0	5	0
R1STCA	8	0	5	0	7	0
R2E1AC	477	24	37	17	37	16
R2E3AC	512	17	41	13	44	11
R2STAC	966	38	45	18	46	18
R3E1AC	4819	170	121	51	127	51
R3E1AC_L	3394	86	372	0	343	0
R3E1CA	4064	146	141	51	139	51
R3E1DB	4008	147	141	53	141	53
R3E2AC	3551	132	106	44	100	43
R3E3AC	4590	158	114	40	94	38
R3STAC	6720	232	117	59	113	58
R4E1AC	11345	331	146	40	118	36
R4E1CF	21841	753	615	71	223	66
R4E1EC	9184	315	109	32	81	33
R4E1FC	23934	833	395	54	192	49
R4E1FC_L	10670	371	209	82	192	79
R4STAC	14793	467	294	33	259	30
R5E1AC	7629	276	178	19	143	17
`OttExtra` [85]						
m15b6	166	56	165	57	166	56
s11WW	171	43	177	43	188	43
s25WW	1489	1400	2165	2163	20235	2264
`Yak` [132]						
s12_matter	159	4	159	4	158	4
s15_matter	105	2	106	3	106	3
s25_matter	69	12	67	13	67	12

and thus allow for a truly independent test of SMEE. Also, unlike the `Dim` waveforms, the `Sch` waveforms are based on 3D simulations. Hence, they are not linearly polarized. For consistency with our current approach, $h_\times$ is neglected and only h_+ as seen by an equatorial observer is injected. Results of TD_SMEE $\log B_{SN}$ calculations for all injected `Sch` waveforms are summarized in Table 6.1. TD_SMEE correctly identifies the majority of the `Sch` waveforms as indicative of magnetorotational explosions at a source distance of 50 kpc. At 10 kpc, still 92% of the injected `Sch` waveforms are attributed to the magnetorotational mechanism, which is an indication of the robustness of the GW associated with rapid rotation and magnetorotational explosions. The very few `Sch` waveforms that TD_SMEE is not able to clearly associate with the magnetorotational mechanism have such weak SNRs that they are more consistent with noise than with any of the catalogues at 50 kpc. The distance plot in Figure 6.16 shows that `Sch` waveforms can be correctly identified up to a mean distance of ~ 220 kpc.

Acoustic Mechanism

TD_SMEE's ability to identify core-collapse supernovae exploding via the acoustic mechanism is tested by injecting the three `OttExtra` waveforms (see Sec. 1.7). The results of this test are again summarized in Tab. 6.1. They suggest that the a-priori unknown `OttExtra` waveforms can be identified as belonging to the acoustic mechanism out to 50 kpc for 1 of the waveforms with great confidence when 7 PCs are used in the analysis. At 10 kpc, the waveforms are still correctly attributed to the acoustic mechanism, but the evidence is much weaker. The `OttExtra` 3 waveform (labelled as s25WW), which is clearly identified at 10 kpc, has an extreme SNR of $\sim$2530 at this distance, while the two other waveforms have SNRs of ~ 50. TD_SMEE's difficulty in this was illustrated in Section 4.2.4 and can be seen in the distance plot in Figure 6.16 where the mean distance model selection is successful has decreased from $\sim 550kpc$ when `Ott` waveforms are tested to $\sim 180kpc$. As in Section 4.2.4, large-scale features such as the time between peaks are imprinted onto the PCs and make it difficult to identify waveforms whose two peaks are separated by significantly different intervals. As in the 1 detector case an alternative method that may work much better for waveforms of this kind is to compute PCs based on waveform power spectra, which would remove any potentially problematic phase information.

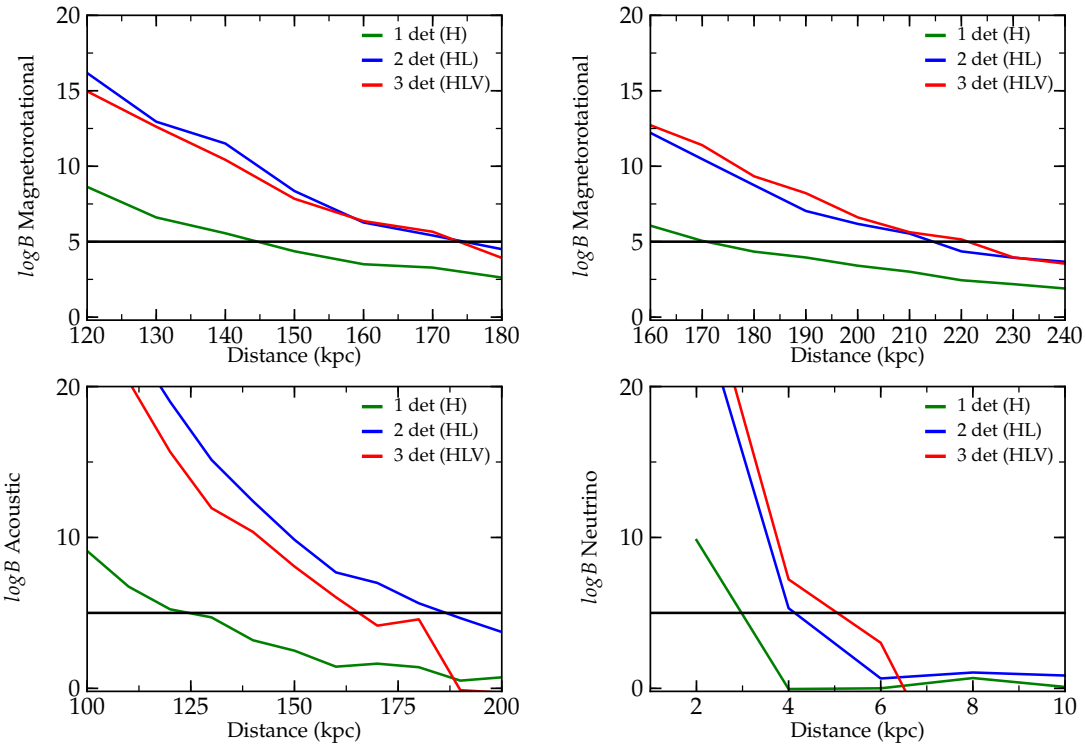

Figure 6.16: Distance to which SMEE using multiple detectors can successfully distinguish one catalogue from two others using the sky position for the Galactic Centre. This shows results for the waveform catalogues when the $\log B_{SN}$ for the expected correct mechanism is compared with the $\log B_{SN}$ found when attempting to reconstruct the injected waveform with the other two sets of PCs. The log Bayes Factor is then found i.e. in the case of the `DimExtra` catalogue $\log B_{Magnetorotational}$ is found for the `Dim` PCs versus the `Mur` and the `Ott` PCs. Out of the two results the minimum is plotted here to ensure that SMEE can distinguish between all sets of PCs. The mean log Bayes Factor for every waveform in the catalogue is shown here. **Top Left Plot** Results for the `DimExtra` catalogue. In the time domain using 3 detectors, the maximum mean distance that signal can be distinguished from both the `Mur` and `Ott` PCs is $\sim$ 170 kpc. **Top Right Plot** Results for the `Sch` catalogue. In the time domain using 3 detectors, the maximum mean distance that signal can be distinguished from both the `Mur` and `Ott` PCs is $\sim$ 220 kpc. **Bottom Left Plot** Results for the `OttExtra` catalogue. In the time domain using 3 detectors, the maximum mean distance that signal can be distinguished from both the `Dim` and `Mur` PCs is $\sim$ 180 kpc. **Bottom Right Plot** Results for the `Yak` catalogue. In the time domain using 3 detectors, the maximum mean distance that signal can be distinguished from both the `Dim` and `Ott` PCs is $\sim$ 5 kpc.

Neutrino Mechanism

TD_SMEE's ability to identify GWs emitted by core-collapse supernovae exploding via the neutrino mechanism is tested using the waveforms of the `Yak` catalogue (see Sec. 1.7) that were obtained with a completely different numerical code. The three available `Yak` waveforms are added to Advanced LIGO and Advanced Virgo noise and TD_SMEE computes $\log B_{SN}$. The results are listed in Tab. 6.1. Even at 10 kpc the `Yak` waveforms appear to give very similar results for $\log B_{SN}$ which implies that no one set of PCs can successfully reconstruct the waveform. The bottom right panel of Figure. 6.16 shows that the `Yak` waveforms require a distance of less than 5kpc to be clearly associated with the neutrino mechanism that is more than ~ 8 times less than for `Mur` waveforms. As discussed in Section 4.2.4, while the `Yak` waveforms are qualitatively very similar to the `Mur` waveforms, they differ significantly in quantitative aspects. The `Yak` waveforms are generally only half as long (~ 1 s for `Mur` and 0.5 s for `Yak`, whose models explode much earlier than the `Mur` models). This may be due to the more simplified treatment of gravity and neutrino microphysics and transport in the study of Murphy *et al.* [79] underlying the `Mur` catalogue compared to the work of Yakunin *et al.* [132] that led to the `Yak` catalogue.

Results in this Section have been made from TD_SMEE and limitations on the ability to correctly identify waveforms from the `OttExtra` and `Yak` waveforms have been found. In the next section PSD_SMEE will be tested and compared with the results using TD_SMEE.

6.3 Multiple Detector SMEE in the Power Spectrum Domain

6.3.1 Distinguishing the Supernova Mechanism with Multiple Detectors

Here results are shown using the same method utilised in Section 6.2.1 using power spectrum domain SMEE (PSD_SMEE). PSD_SMEE is run for all waveforms from

the Dim, Mur and Ott catalogues using 3 detectors (HLV) at 10 and 50 kpc using the same coordinates for each distance that were used in Section 6.2.1. In this case 7 PCs are used for both the Dim and Ott PCs and 16 for the Mur PCs.

Results for 10 kpc are shown in Figure 6.17. The top left panel depicts the $\log B_{\texttt{DimMur}}$ result for injected waveforms from the Dim and Mur catalogues. At 10 kpc all but ∼7% of waveforms characteristic for magnetorotational explosions are clearly identified as belonging to this mechanism. For the neutrino mechanism, the evidence is significantly weaker and all of the waveforms remain in the inconclusive regime of $-5 < \log B_{\texttt{DimMur}} < 5$. This is the same outcome that was seen in Figure 4.12 where ∼19% were in the inconclusive region. As in the 1 detector case, this is because of the low SNR of the signals at 10kpc, neither the Dim nor Mur PCs can distinguish the waveform from the noise.

In the top right panel of Fig. 6.17, results are shown for $\log B_{\texttt{DimOtt}}$ for waveforms corresponding to the magnetorotational (Dim) and the acoustic (Ott) mechanisms. In this case, all waveforms from the Ott catalogue are correctly identified as most likely belonging to the acoustic mechanism, albeit with a smaller certainty than what was seen with TD_SMEE. The same ∼7% of Dim waveforms remain in the inconclusive region and the rest have smaller Bayes Factors than those seen with TD_SMEE. The waveforms in the inconclusive region do not have the necessary SNR to be distinguished from the added noise.

Finally, the bottom panel of Fig. 6.17 presents $\log B_{\texttt{MurOtt}}$ for waveforms representative of the neutrino (Mur) and acoustic (Ott) mechanism. As in the previous panel, PSD_SMEE associates the waveforms corresponding to the acoustic mechanism with high confidence to the Ott catalogue. The evidence suggesting correct association of the neutrino mechanism waveforms is once again lacking with all waveforms in the inconclusive region.

When the PSD version of SMEE was tested at a distance of 50 kpc all but 2 Ott waveforms of the simulated waveforms tested from any of the 3 catalogues gave a Bayes Factor greater than 5. This is confirmed in the distance plots in Figure 6.18 where only the Ott waveforms can reach a mean distance greater than 50 kpc. The Dim waveforms reach a mean distance of ∼ 35 kpc where Bayesian model selection is still successful. The Mur catalogue, as expected, is significantly poorer and Bayesian model selection is successful only to a mean distance of ∼ 7.5 kpc. As was shown

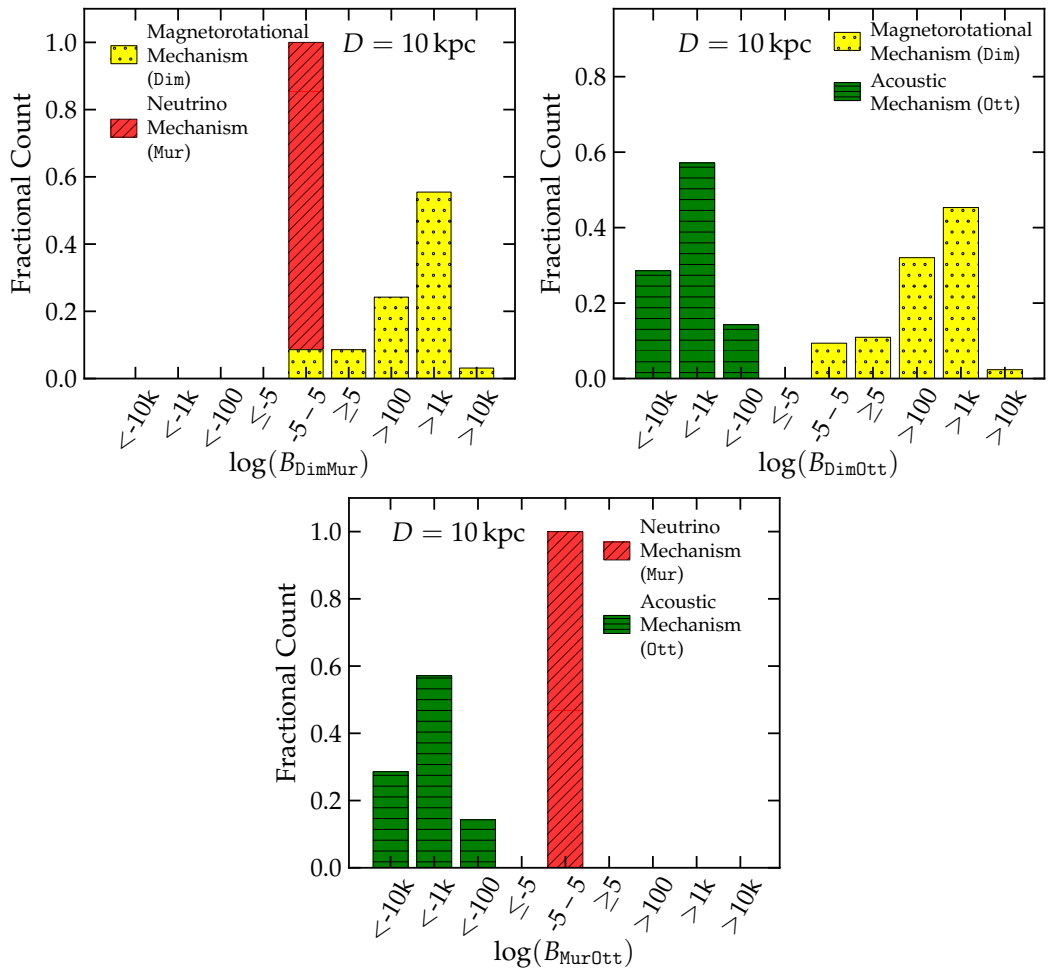

Figure 6.17: Histograms describing the outcome of signal model comparisons in the power spectrum domain by means of the Bayes Factors $\log B_{ij} = \log p(D|M_i) - \log p(D|M_j)$, see Figure 6.11. This is done using 3 detectors (HLV) and the Bayes Factors are computed with 7 PCs for the `Dim` and `Ott` catalogues and 16 PCs for the `Mur` catalogue at a source distance of 10 kpc using the sky position of the Galactic Center.

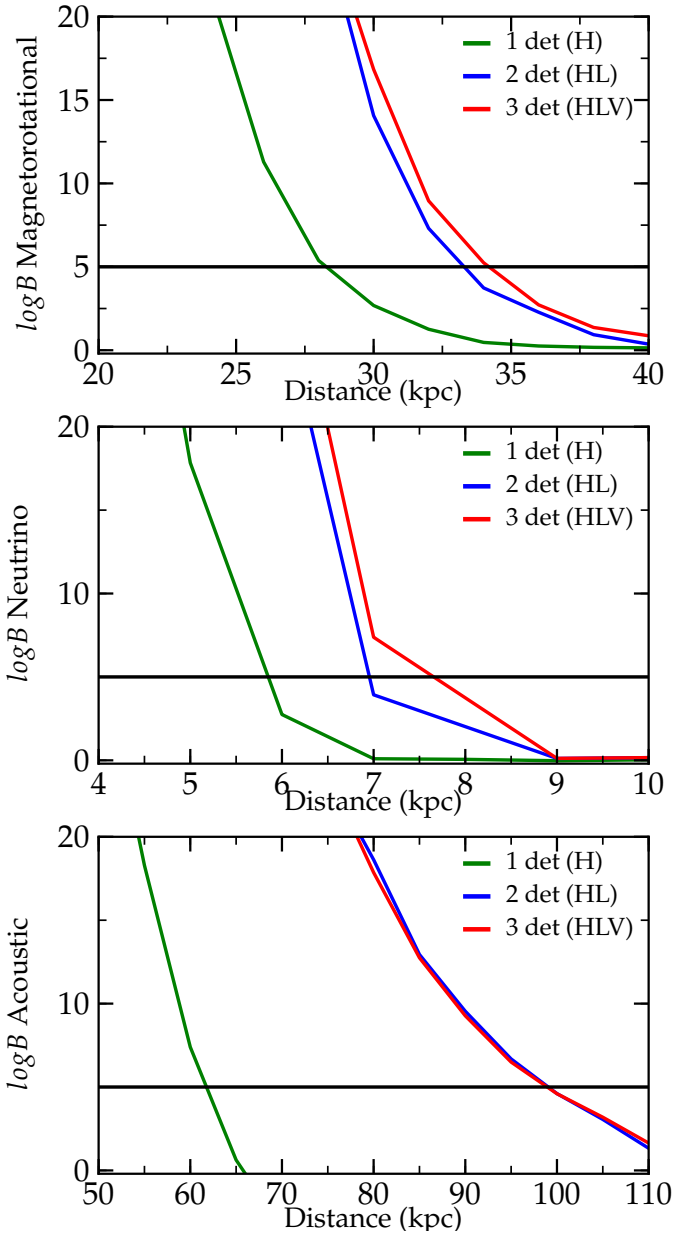

Figure 6.18: Same results shown as in 6.13 using the power spectrum version of SMEE. **Top Plot** Results for the `Dim` catalogue. In the power spectrum domain using 3 detectors, the maximum mean distance that signal can be distinguished from both the `Mur` and `Ott` PCs is $\sim$ 34 kpc. **Middle Plot** Results for the `Mur` catalogue. In the power spectrum domain using 3 detectors, the maximum mean distance that signal can be distinguished from both the `Dim` and `Ott` PCs is $\sim$ 7.5 kpc. **Bottom Plot** Results for the `Ott` catalogue. In the power spectrum domain using 3 detectors, the maximum mean distance that signal can be distinguished from both the `Dim` and `Mur` PCs is $\sim$ 100 kpc.

in Section 4.3.1, losing the phase data means the waveforms are less distinct from the noise so even with the improvements made in Chapter 5 PSD_SMEE is less successful than TD_SMEE.

6.3.2 Rotating Accretion-Induced Collapse and Rotating Iron Core Collapse?

As in Section 6.2.2 all `Abd` and `Dim` waveforms are then added to noise, in this case noise from 2 Advanced LIGO detectors and Advanced Virgo. PSD_SMEE is then run with 7 PCs to calculate $\log B_{\texttt{AbdDim}}$. The results are shown in Figure 6.19 for a source distances of 10 kpc, using the coordinates for the Galactic Centre.

PSD_SMEE correctly identifies the majority of injected waveforms as most likely being emitted by a rotating iron core collapse or by rotating AIC. However, these results are poorer than what was seen in TD_SMEE. At 10 kpc ∼5% of the `Dim` waveforms and ∼22% of the `Abd` waveforms are incorrectly identified as belonging to the wrong catalogue. In addition ∼14% of the `Dim` waveforms and ∼23% of the `Abd` are in the inconclusive region.

Figure 6.20 distance plots are shown to identify the mean distance PSD_SMEE can still separate the 2 waveform catalogues. As expected, PSD_SMEE is less successful than in the case where TD_SMEE was tested (Figure 6.15). The `Dim` catalogue is correctly identified to a maximum mean distance of $\sim$ 35 kpc and the `Abd` catalogues to $\sim$ 21kpc.

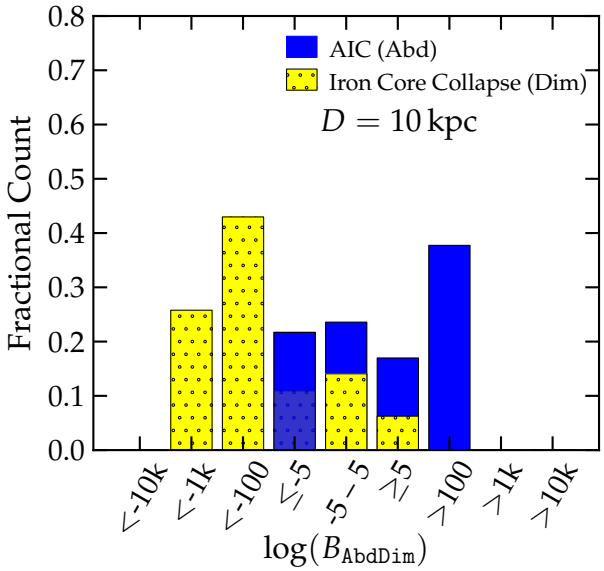

Figure 6.19: Outcome of the SMEE analysis in the power spectrum domain of injected rotating iron core collapse (`Dim` catalogue) and rotating accretion-induced collapse (AIC, `Abd` catalogue) waveforms using 3 detectors (HLV). Results shown here are for a source distance of 10 kpc (at the Galactic Centre). The Bayes Factors $\log B_{\mathtt{AbdDim}}$ are computed on the basis of 7 PCs from the `Abd` and `Dim` catalogue, see Figure 6.14.

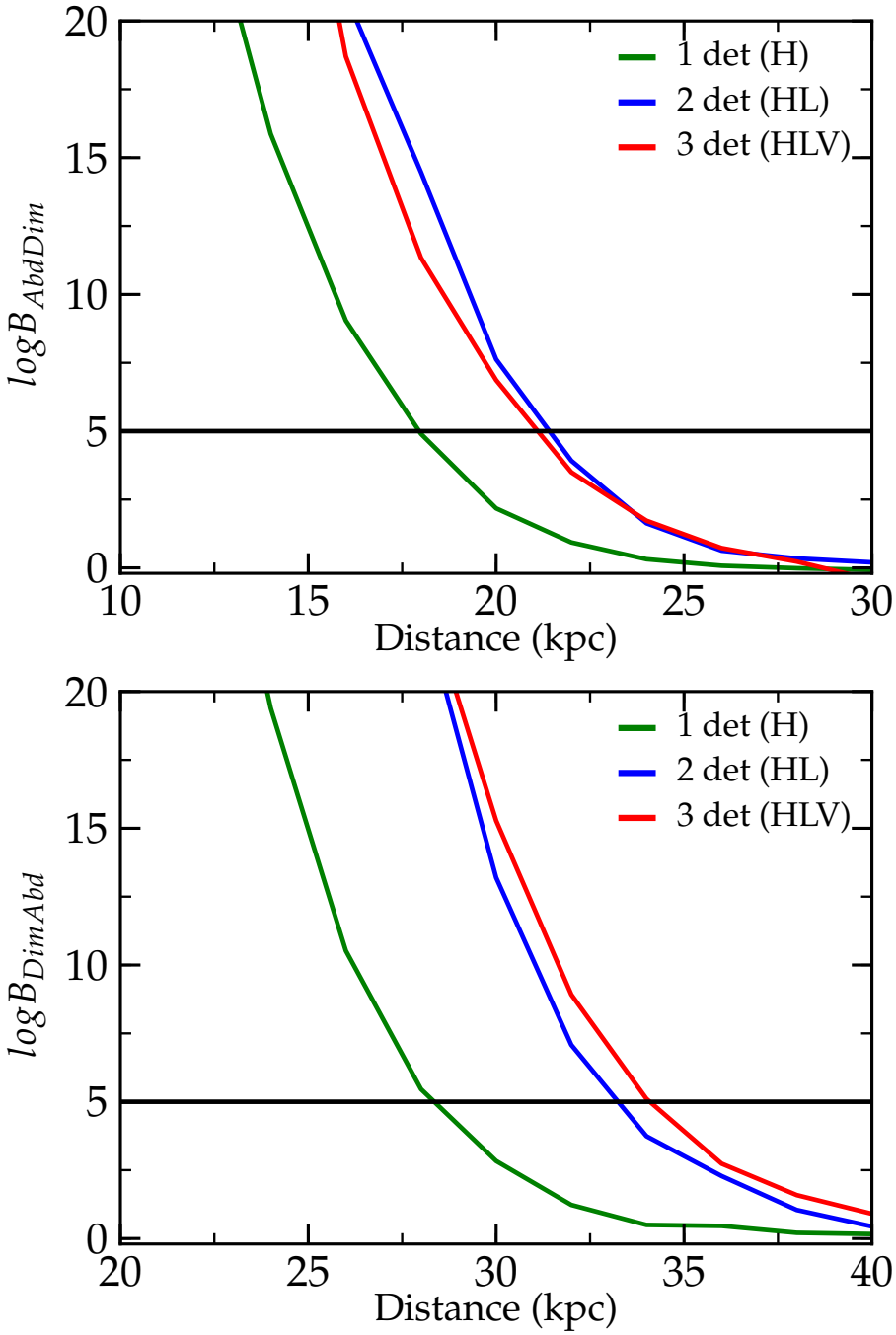

Figure 6.20: Same as Figure 6.15 using power spectrum version of SMEE. **Top Plot** Results for the `Abd` catalogue. In the power spectrum domain using 3 detectors, the maximum mean distance that signal can be distinguished from the `Dim` PCs is ~ 22 kpc. **Bottom Plot** Results for the `Dim` catalogue. In the power spectrum domain using 3 detectors, the maximum mean distance that signal can be distinguished from the `Abd` PCs is ~ 34 kpc.

6.3.3 Testing Robustness of SMEE using non-catalogue waveforms

As in Section 6.2.3, PSD_SMEE is now tested using waveform catalogues that share the same supernova mechanism but were not used in the creation of the principal components. Results for $\log B_{SN}$ are shown in Table 6.2. Distance plots like those shown in Figure 6.13 are shown in Figure 6.21.

Magnetorotational Mechanism

As in the time domain `Dim Extra` and `Sch` waveforms are employed here. The results of the $\log B_{SN}$ calculation for the magnetorotational, neutrino, and acoustic mechanism signal models are summarized in Tab. 6.2. `DimExtra` waveforms are identified as being most consistent with the `Dim` catalogue and, hence, the magnetorotational mechanism out to distances $\gtrsim$10 kpc. The distance plot in Figure 6.21 shows that `DimExtra` waveforms can be correctly identified up to a mean distance of ~ 30 kpc.

Results of PSD_SMEE $\log B_{SN}$ calculations for all injected `Sch` waveforms are summarized in Tab. 6.2. At 10 kpc, 82% of the injected `Sch` waveforms are attributed to the magnetorotational mechanism, which is an indication of the robustness of the GW associated with rapid rotation and magnetorotational explosions. At 50 kpc only 2 waveforms with large SNRs give a positive $\log B_{SN}$. The very few `Sch` waveforms that SMEE is not able to clearly associate with the magnetorotational mechanism have such weak SNRs that they are more consistent with noise than with any of the catalogues at 10 kpc. This is confirmed in the distance plot in Figure 6.21 which shows that `Sch` waveforms can be correctly identified up to a mean distance of ~ 62 kpc. This is due to the 2 waveforms which give positive Bayes Factors above 50 kpc.

Acoustic Mechanism

As in the time domain the three `OttExtra` waveforms are utilised here. The results of this test are again summarized in Tab. 6.2. They suggest that the a-priori

unknown `OttExtra` waveforms can be identified as belonging to the acoustic mechanism out to 10 kpc with great confidence when 7 PCs are used in the analysis. As in the 1 detector case, this is an improvement over the time domain results and shows that there is a strong indication that the range of possible waveform features associated with the acoustic mechanism is much more efficiently covered by the 7 PCs generated from the `Ott` catalogue in the power spectrum domain confirming that any problematic phase and time information has been removed. This is confirmed in the distance plot in Figure 6.21 which shows that `OttExtra` waveforms can be correctly identified up to a mean distance of ~ 475 kpc. This is due to the extreme SNR of the waveform labelled s25WW and in a more realistic scenario with a more conservative SNR the distance would be closer to that seen in Figure 6.18.

Neutrino Mechanism

As in the time domain case the waveforms of the `Yak` catalogue (see Sec. 1.7) that were obtained with a completely different numerical code are tested. The results are listed in Tab. 6.2. At 10 kpc and 50 kpc, the `Yak` waveforms appear to be most consistent with noise for PSD_SMEE. The bottom right panel of Figure 6.21 confirms this by showing that $\log B_{\mathrm{Neutrino}}$ decreases with increasing distance which shows that the $\log B_{SN}$ is higher for the other two sets of PCs. This is for the same reason as discussed in Figure 4.18 and is due to the more simplified treatment of gravity and neutrino microphysics and transport in the study of Murphy *et al.* [79] underlying the `Mur` catalogue compared to the work of Yakunin *et al.* [132] that led to the `Yak` catalogue.

Table 6.2: Power spectrum: $\log B_{SN}$ for gravitational waveforms that were not included in the catalogues used for PC computation. The `DimExtra`, `Sch`, `OttExtra`, and `Yak` waveforms are discussed in §1.7. Results are shown for source distances of 10 kpc and 50 kpc and for evaluations using 7 PCs for the `Ott` and `Dim` PCs and 16 for the `Mur` PCs. Larger values indicate stronger evidence that the waveform is matched to the model catalogue from which the PCs were constructed. $\log B_{SN} < 5$ indicates that the injected signal is likely consistent with noise while larger values suggests that the signal belongs to the signal model whose PCs were used in the analysis.

Waveform	$\log B_{SN}$ Dim PCs		$\log B_{SN}$ Mur PCs		$\log B_{SN}$ Ott PCs	
	10 kpc	50 kpc	10 kpc	50 kpc	10 kpc	50 kpc
`DimExtra` [97]						
s20a1o05_shen	1121	0	679	0	0	0
s15a1o03_LS	5624	0	1697	0	33	0
s40a1o10_LS	8749	0	2577	0	0	0
`Sch` [102]						
R1E1CA	0	0	0	0	0	0
R1E1CA_L	0	0	0	0	0	0
R1E1DB	0	0	0	0	0	0
R1E3CA	0	0	0	0	0	0
R1STCA	0	0	0	0	0	0
R2E1AC	0	0	0	0	0	0
R2E3AC	0	0	0	0	0	0
R2STAC	25	0	0	0	17	0
R3E1AC	1572	0	398	0	787	0
R3E1AC_L	7206	0	1287	0	3534	0
R3E1CA	1154	0	340	0	616	0
R3E1DB	1214	0	352	0	616	0
R3E2AC	711	0	195	0	443	0
R3E3AC	1912	0	563	0	774	0
R3STAC	19328	0	2238	0	12594	0
R4E1AC	8056	0	1811	0	2071	0
R4E1CF	86723	1117	13272	34	847	0
R4E1EC	5766	0	1462	0	1326	0
R4E1FC	59192	299	9064	4	583	0
R4E1FC_L	26912	6	2779	0	18788	4
R4STAC	16929	0	2930	0	5825	0
R5E1AC	7735	0	2385	0	3	0
`OttExtra` [85]						
m15b6	215	0	0	0	314	0
s11WW	156	0	0	0	267	0
s25WW	140270	2699	4138	0	324640	8405
`Yak` [132]						
s12_matter	0	0	0	0	0	0
s15_matter	1	0	0	0	0	0
s25_matter	0	0	0	0	1	0

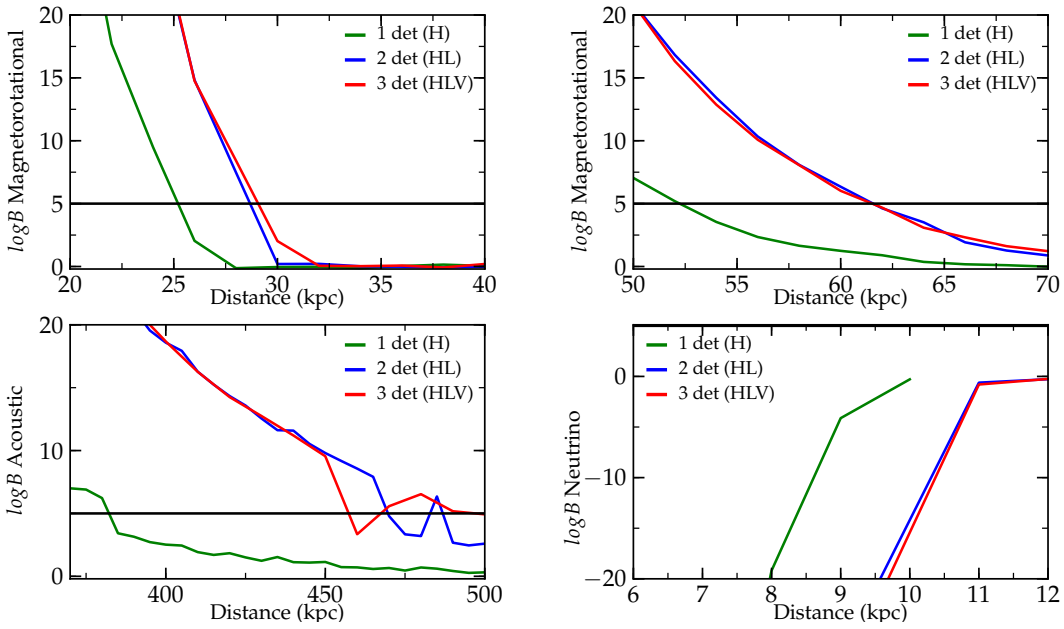

Figure 6.21: Same as Figure 6.16 using power spectrum version of SMEE. **Top Left Plot** Results for the `DimExtra` catalogue. In the power spectrum domain using 3 detectors, the maximum mean distance that signal can be distinguished from both the `Mur` and `Ott` PCs is $\sim$ 30 kpc. **Top Right Plot** Results for the `Sch` catalogue. In the power spectrum domain using 3 detectors, the maximum mean distance that signal can be distinguished from both the `Mur` and `Ott` PCs is $\sim$ 64 kpc. **Bottom Left Plot** Results for the `OttExtra` catalogue. In the power spectrum domain using 3 detectors, the maximum mean distance that signal can be distinguished from both the `Dim` and `Mur` PCs is $\sim$ 420 kpc. **Bottom Right Plot** Results for the `Yak` catalogue. In the power spectrum domain using 3 detectors as in the case of the 1 detector case, the `Yak` catalogue incorrectly favours the `Dim` and `Ott` PCs, see Figure 4.18

6.4 Multiple Detector SMEE in the Spectrogram Domain

6.4.1 Distinguishing the Supernova Mechanism with Multiple Detectors

Here results are shown using the same method utilised in Section 6.2.1 using spectrogram domain SMEE (Spec_SMEE). Spec_SMEE is run for all waveforms from the `Dim`, `Mur` and `Ott` catalogues using 3 detectors (HLV) at 10 and 50 kpc using the same coordinates for each distance that were used in Section 6.2.1. In this case 7 PCs are used for both the `Dim` and `Ott` PCs and 16 for the `Mur` PCs.

The results of this are shown in Figure 6.22. The top left panel depicts the $\log B_{\texttt{DimMur}}$ result for injected waveforms from the `Dim` and `Mur` catalogues, that

are taken to be representative of the magnetorotational and neutrino mechanism, respectively. Even at 10 kpc all waveforms characteristic for magnetorotational explosions are clearly identified as belonging to this mechanism. For the neutrino mechanism, the evidence is generally weaker and ∼50% of the `Mur` waveforms are identified with $\log B_{\texttt{DimMur}} < -5$, while ∼50% are either in the inconclusive regime of $-5 < \log B_{\texttt{DimMur}} < 5$ or incorrectly identified. as in the 1 detector case, this is due to the fact that at SNRs, typically less than 10, these waveforms favour the magnetorotational mechanism and only start agreeing with the neutrino waveforms at higher SNRs.

In the top right panel of Fig. 6.22, results are shown for $\log B_{\texttt{DimOtt}}$ for waveforms corresponding to the magnetorotational (`Dim`) and the acoustic (`Ott`) mechanisms. In this case, all waveforms are correctly identified as most likely belonging to their respective catalogue/mechanism. Finally, the bottom panel of Fig. 6.22 presents $\log B_{\texttt{MurOtt}}$ for waveforms representative of the neutrino (`Mur`) and acoustic (`Ott`) mechanism. As in the previous panel, Spec_SMEE associates the waveforms corresponding to the acoustic mechanism with high confidence to the `Ott` catalogue. The evidence suggesting correct association of the neutrino mechanism waveforms is once again less strong, but $\log B_{\texttt{MurOtt}}$ is still conclusive for ∼50% of the `Mur` waveforms. These waveforms in the inconclusive region do not have the required Network SNR to be detected in any of the 3 detectors.

Figure 6.23 shows the results for $\log B_{\texttt{DimMur}}$, $\log B_{\texttt{DimOtt}}$, and $\log B_{\texttt{MurOtt}}$ obtained by Spec_SMEE at a source distance of 50 kpc. Even at this increased distance all acoustic waveforms (`Ott`) are correctly separated from both the magnetorotational and neutrino mechanisms. The `Dim` waveforms also perform very well and only ∼20% of the waveforms in this catalogue do not have enough SNR to be distinguished from the noise. However, the `Mur` waveforms perform less well none are correctly identified as belonging to the correct mechanism.

Results for the `Dim`, `Mur` and `Ott` catalogues at varying distances is shown in Figure 6.24. As expected both the `Dim` and `Ott` are successful at distances over 50kpc whereas `Mur` is successful to distances of ∼21 kpc. The maximum distance improves when more detectors are added however there is minimal improvement from adding Advanced Virgo. This is due to the fact that F_+ is a lot smaller here and so the waveforms have a smaller SNR. Therefore they do not contribute as much as the 2 Advanced LIGO detectors. If a different sky position was chosen

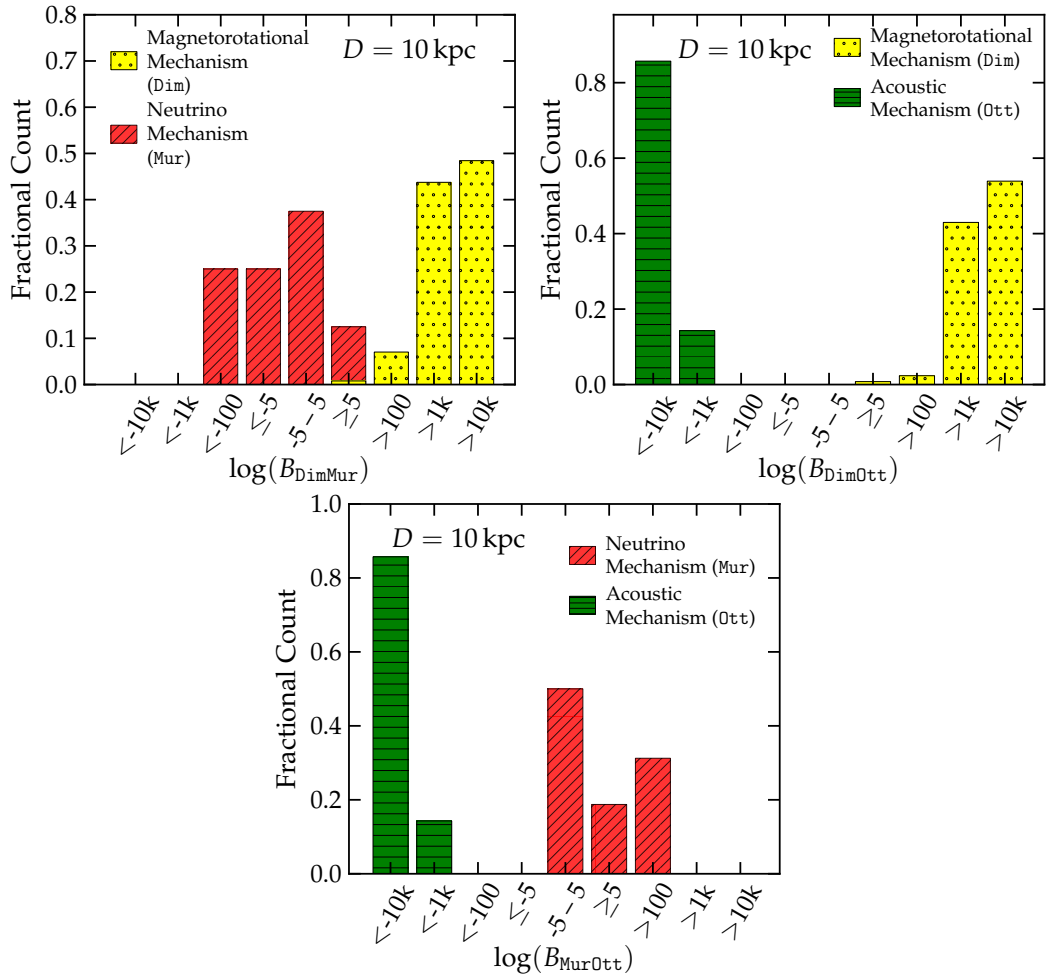

Figure 6.22: Histograms describing the outcome of signal model comparisons in the spectrogram domain by means of the Bayes Factors $\log B_{ij} = \log p(D|M_i) - \log p(D|M_j)$, see Figure 6.11. This is done using 3 detectors (HLV) and the Bayes Factors are computed with 7 PCs for the `Dim` and `Ott` catalogues and 16 PCs for the `Mur` catalogue at a source distance of 10 kpc using the sky position of the Galactic Center.

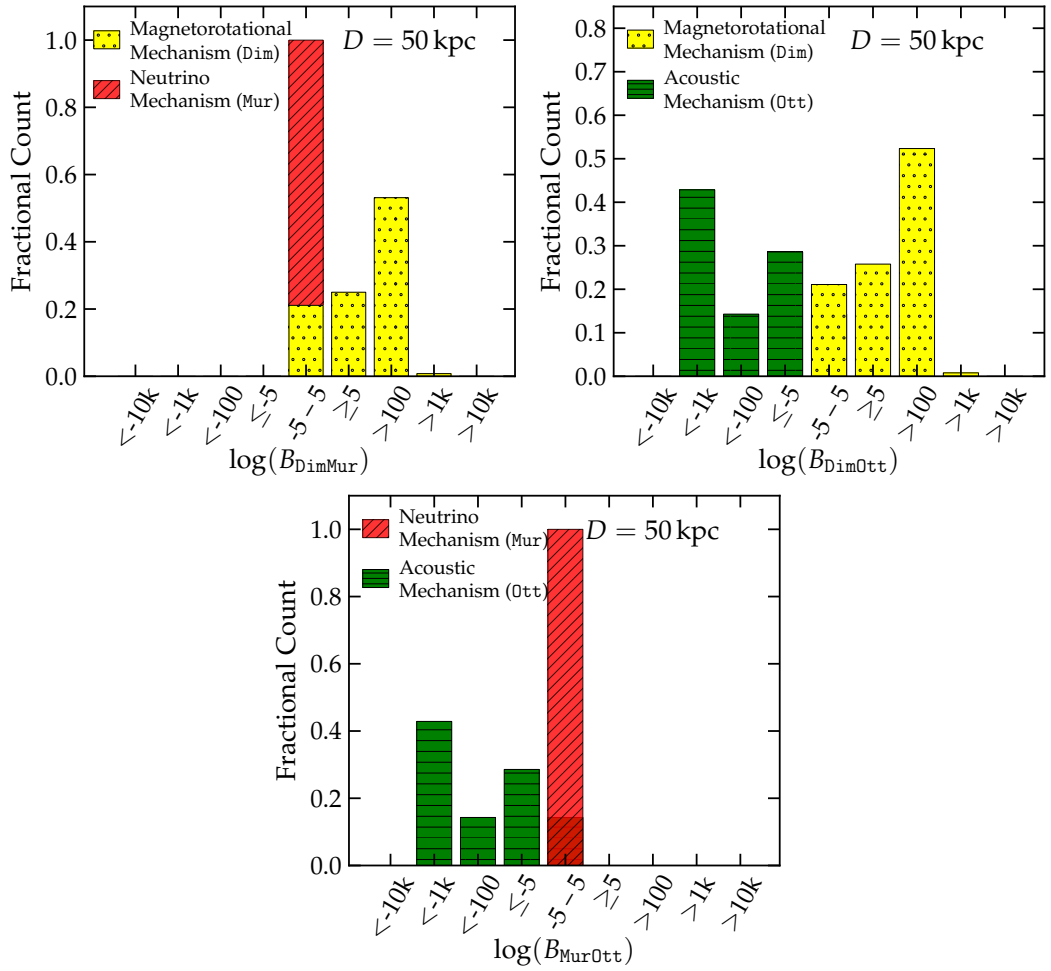

Figure 6.23: Same as Fig. 6.22, but computed for a source distance of 50 kpc using the sky position of the Large Magallenic Cloud (LMC).

where F_+ was larger then the contribution from Advanced Virgo was increase, see Figure 6.28.

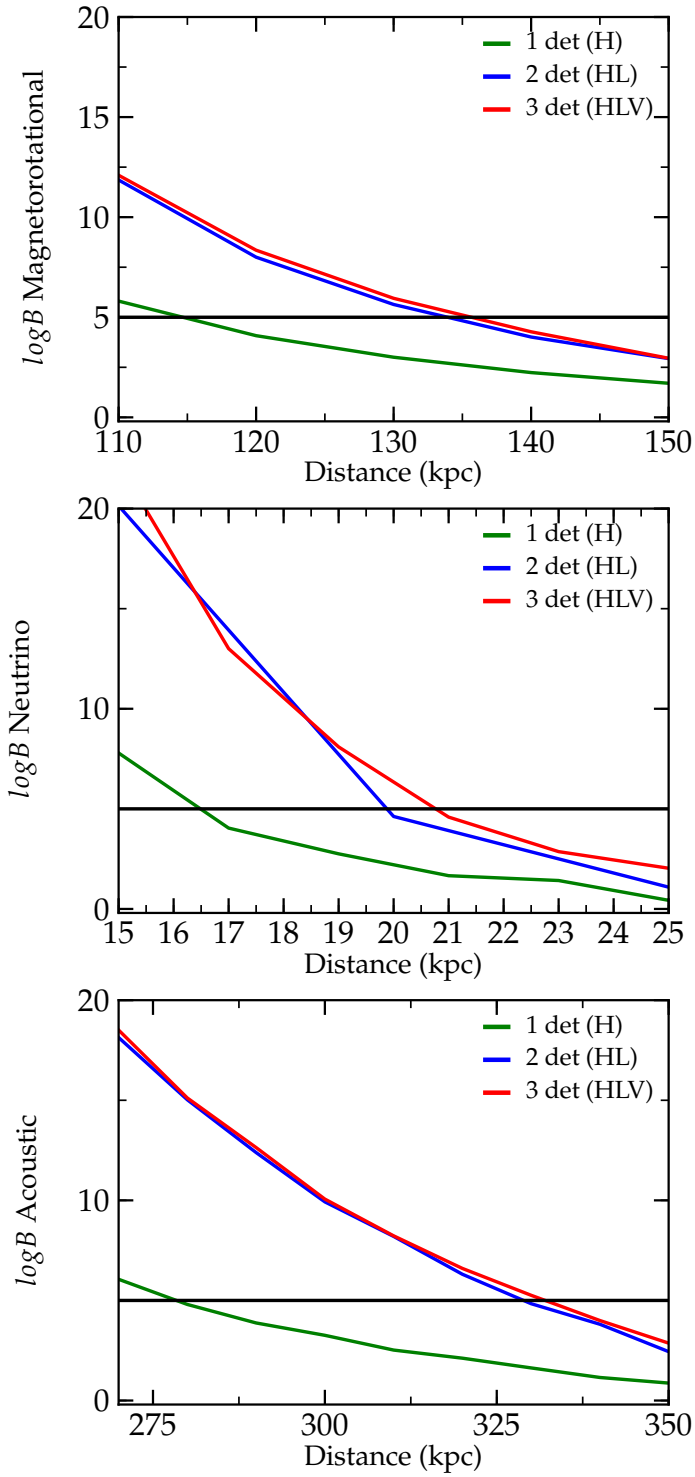

Figure 6.24: Same results shown as in 6.13 using the spectrogram version of SMEE. **Top Plot** Results for the `Dim` catalogue. In the spectrogram domain using 3 detectors, the maximum mean distance that signal can be distinguished from both the `Mur` and `Ott` PCs is $\sim$ 135 kpc. **Middle Plot** Results for the `Mur` catalogue. In the spectrogram domain using 3 detectors, the maximum mean distance that signal can be distinguished from both the `Dim` and `Ott` PCs is $\sim$ 21 kpc. **Bottom Plot** Results for the `Ott` catalogue. In the spectrogram domain using 3 detectors, the maximum mean distance that signal can be distinguished from both the `Dim` and `Mur` PCs is $\sim$ 330 kpc.

6.4.2 Rotating Accretion-Induced Collapse or Rotating Iron Core Collapse?

As in Section 6.2.2 all `Abd` and `Dim` waveforms are then added to noise, in this case noise from 2 Advanced LIGO detectors and Advanced Virgo. Spec_SMEE is then tested using 7 PCs to once again calculate $\log B_{\texttt{AbdDim}}$. The results are shown in Figure 6.25 for source distances of 10 kpc and 50 kpc.

Spec_SMEE correctly identifies the majority of injected waveforms as most likely being emitted by a rotating iron core collapse or by rotating AIC at both 10 kpc but is less successful at 50 kpc. At 10 kpc none of the `Dim` waveforms and ∼3% of the `Abd` waveforms are incorrectly identified as belonging to the wrong catalogue. In addition none of the `Dim` waveforms and ∼13% of the `Abd` are in the inconclusive region. At 50 kpc spectrogram domain SMEE is still very accurate and ∼70% of the `Dim` are correctly identified. However, `Abd` fairs less well and the majority do not have the SNR necessary to give a Bayes Factor greater than 5.

Figure 6.26 distance plots are shown to identify the mean distance Spec_SMEE can still separate the 2 waveform catalogues. While less successful than in the case where the magnetorotational mechanism is compared to the neutrino and acoustic mechanisms the `Dim` catalogue can still be correctly identified to distances greater that 100 kpc. As expected, the `Abd` catalogue can only be correctly identified to a mean distance of ∼48kpc. This disappointing result is due to the nature of Spec_SMEE. It was shown in Section 4.4.1 that this version of SMEE is less sensitive at smaller SNRs (or larger distances).

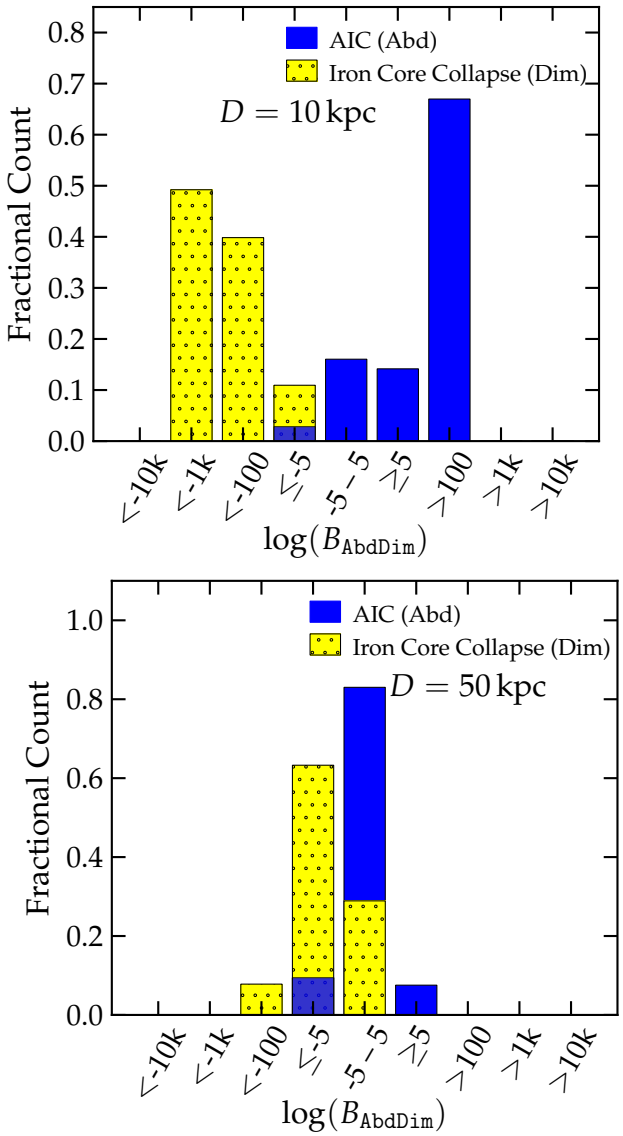

Figure 6.25: Outcome of the SMEE analysis in the spectrogram domain of injected rotating iron core collapse (`Dim` catalogue) and rotating accretion-induced collapse (AIC, `Abd` catalogue) waveforms using 3 detectors (HLV). The top panel shows results for a source distance of 10 kpc (at the Galactic Centre) and the right panel depicts the results for a distance of 50 kpc (at the Large Magallenic Cloud). The Bayes Factors $\log B_{\mathtt{AbdDim}}$ are computed on the basis of 7 PCs from the `Abd` and `Dim` catalogue, see Figure 6.14

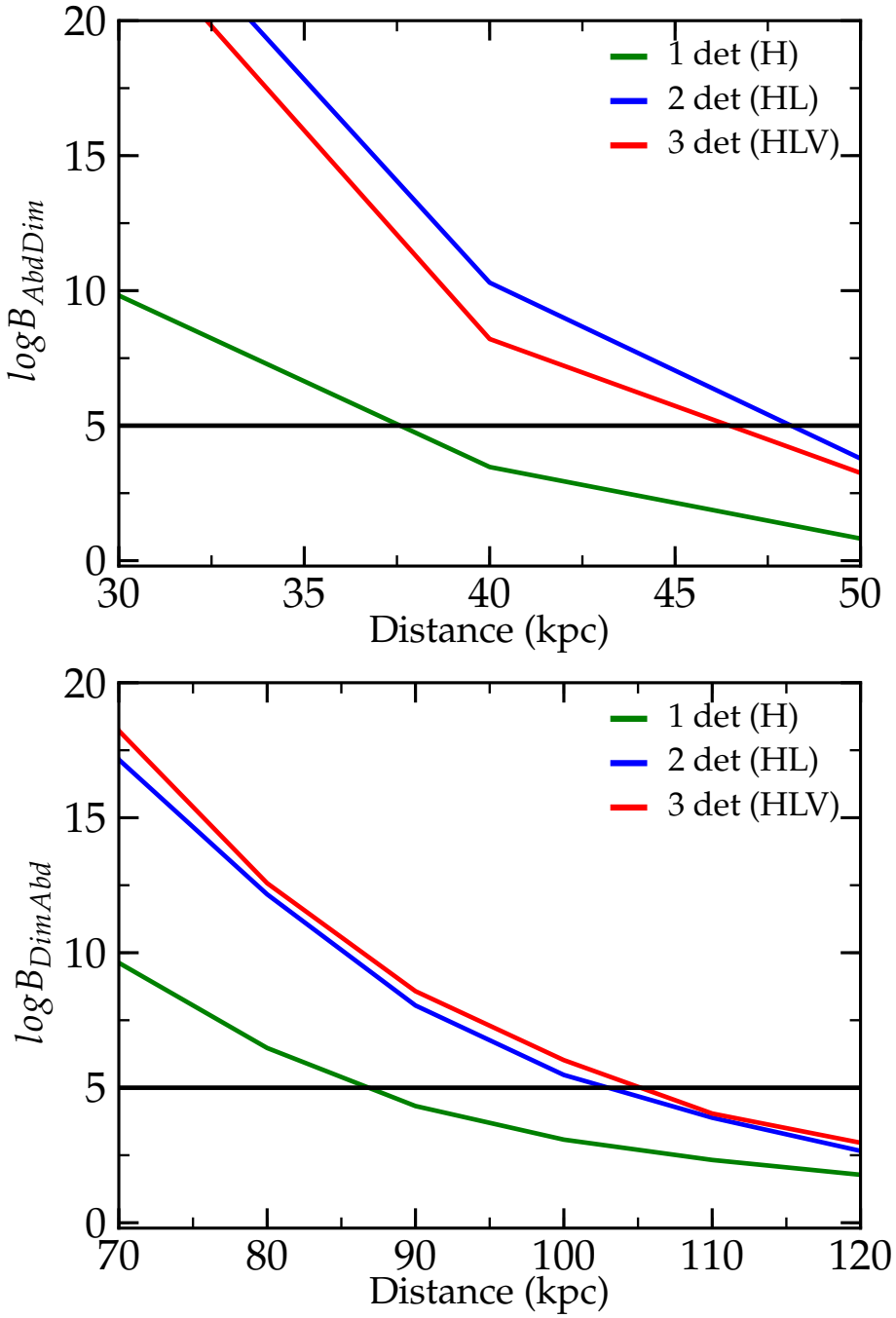

Figure 6.26: Distance to which SMEE using multiple detectors can successfully distinguish the `Abd` and `Dim` catalogues using the sky position for the Galactic Centre. **Top Plot** Results for the `Abd` catalogue. In the spectrogram domain using 3 detectors, the maximum mean distance that signal can be distinguished from the `Dim` PCs is $\sim$ 48 kpc. **Bottom Plot** Results for the `Dim` catalogue. In the spectrogram domain using 3 detectors, the maximum mean distance that signal can be distinguished from the `Abd` PCs is $\sim$ 105 kpc.

6.4.3 Testing Robustness of SMEE using non-catalogue waveforms

As in Section 6.2.3, Spec_SMEE is now tested using waveform catalogues that share the same supernova mechanism but were not used in the creation of the principal components. Results for $\log B_{SN}$ are shown in Table 6.3. Distance plots like those shown in Figure 6.13 are shown in Figure 6.27.

Magnetorotational Mechanism

For the magnetorotational mechanism, three additional `Dim` waveforms (`DimExtra`, Sec. 1.7) are employed that were not included in the calculation of the `Dim` PCs. Furthermore, waveforms from rotating models of the `Sch` catalogue of Scheidegger *et al.* [102, 23] are injected (see Sec. 1.7). The results of both the $\log B_{SN}$ calculation for the magnetorotational, neutrino, and acoustic mechanism signal models are summarized in Tab. 6.3. `DimExtra` waveforms are identified as being most consistent with the `Dim` catalogue and, hence, the magnetorotational mechanism for all `DimExtra` signals at both 10 kpc and 50 kpc. The distance plot in Figure 6.27 shows that `DimExtra` waveforms can be correctly identified up to a mean distance of ~ 170 kpc.

Results of Spec_SMEE $\log B_{SN}$ calculations for all injected `Sch` waveforms are summarized in Tab. 6.3. Spec_SMEE correctly identifies the 16 of the `Sch` waveforms as indicative of magnetorotational explosions at a source distance of 50 kpc. At 10 kpc, still 23 of the injected `Sch` waveforms are attributed to the magnetorotational mechanism, which is an indication of the robustness of the GW associated with rapid rotation and magnetorotational explosions. The very few `Sch` waveforms that Spec_SMEE is not able to clearly associated with the magnetorotational mechanism have such weak SNRs that they are more consistent with noise than with any of the catalogues at 50 kpc. The distance plot in Figure 6.27 shows that `Sch` waveforms can be correctly identified up to a mean distance of ~ 215 kpc.

Table 6.3: Spectrogram: $\log B_{SN}$ for gravitational waveforms that were not included in the catalogues used for PC computation. The `DimExtra`, `Sch`, `OttExtra`, and `Yak` waveforms are discussed in §1.7. Results are shown for source distances of 10 kpc and 50 kpc and for evaluations using 7 PCs for the `Ott` and `Dim` PCs and 16 for the `Mur` PCs. Larger values indicate stronger evidence that the waveform is matched to the model catalogue from which the PCs were constructed. $\log B_{SN} < 5$ indicates that the injected signal is likely consistent with noise while larger values suggests that the signal belongs to the signal model whose PCs were used in the analysis.

Waveform	$\log B_{SN}$ Dim PCs		$\log B_{SN}$ Mur PCs		$\log B_{SN}$ Ott PCs	
	10 kpc	50 kpc	10 kpc	50 kpc	10 kpc	50 kpc
`DimExtra` [97]						
s20a1o05_shen	1349	181	1186	0	19	0
s15a1o03_LS	30223	644	2362	0	156	0
s40a1o10_LS	21627	583	5618	80	19	0
`Sch` [102]						
R1E1CA	12	0	0	0	0	0
R1E1CA_L	0	0	0	0	0	0
R1E1DB	8	0	0	0	0	0
R1E3CA	59	0	0	0	0	0
R1STCA	0	0	0	0	1	0
R2E1AC	746	0	0	0	0	0
R2E3AC	862	0	0	0	0	0
R2STAC	1853	0	0	0	0	0
R3E1AC	12014	59	184	0	0	0
R3E1AC_L	9333	27	329	0	0	0
R3E1CA	10135	32	204	0	0	0
R3E1DB	10155	32	199	0	0	0
R3E2AC	8465	22	128	0	0	0
R3E3AC	17199	69	247	0	0	0
R3STAC	17125	123	234	0	0	0
R4E1AC	31307	447	1125	0	116	0
R4E1CF	102830	3008	13904	271	736	0
R4E1EC	25149	335	887	0	79	0
R4E1FC	95945	2728	10279	161	792	0
R4E1FC_L	31767	410	991	0	85	0
R4STAC	40801	649	1313	0	191	0
R5E1AC	22932	487	1454	0	97	0
`OttExtra` [85]						
m15b6	0	0	0	0	2	0
s11WW	15	0	2	0	99	0
s25WW	4	0	14260	36	479440	14118
`Yak` [132]						
s12_matter	0	0	0	0	0	0
s15_matter	0	0	0	0	0	0
s25_matter	0	0	0	0	0	0

Acoustic Mechanism

Spec_SMEE's ability to identify core-collapse supernovae exploding via the acoustic mechanism is tested by injecting the three `OttExtra` waveforms (see Sec. 1.7). The results of this test are again summarized in Tab. 6.3. They suggest that the a-priori unknown `OttExtra` waveforms can be identified as belonging to the acoustic mechanism out to 50 kpc for 1 of the waveforms with great confidence when 7 PCs are used in the analysis. At 10 kpc, 2 of the waveforms are still correctly attributed to the acoustic mechanism, but the evidence is much weaker than in the time domain case. The `OttExtra` 3 waveform (labelled as s25WW), which is clearly identified at 10 kpc, has an extreme SNR of ∼2530 at this distance, while the two other waveforms have SNRs of ∼50. From the Distance plot in Figure 6.27 the maximum mean distance that the `OttExtra` can be successfully matched to the acoustic mechanism is ∼380 kpc.

While this distance is not as large as in PSD_SMEE, it is an improvement over TD_SMEE. This is a strong indication that, as in the case of the time domain, the range of possible waveform features associated with the acoustic mechanism is not efficiently covered by the 7 PCs generated from the `Ott` catalogue and that since we retain the time domain information when computing the spectrogram PCs, such large-scale features are again imprinted onto the PCs. However, this limitation is partly overcome by including the frequency information which has been shown in the PSD to give a more accurate reconstruction of the `OttExtra` waveforms.

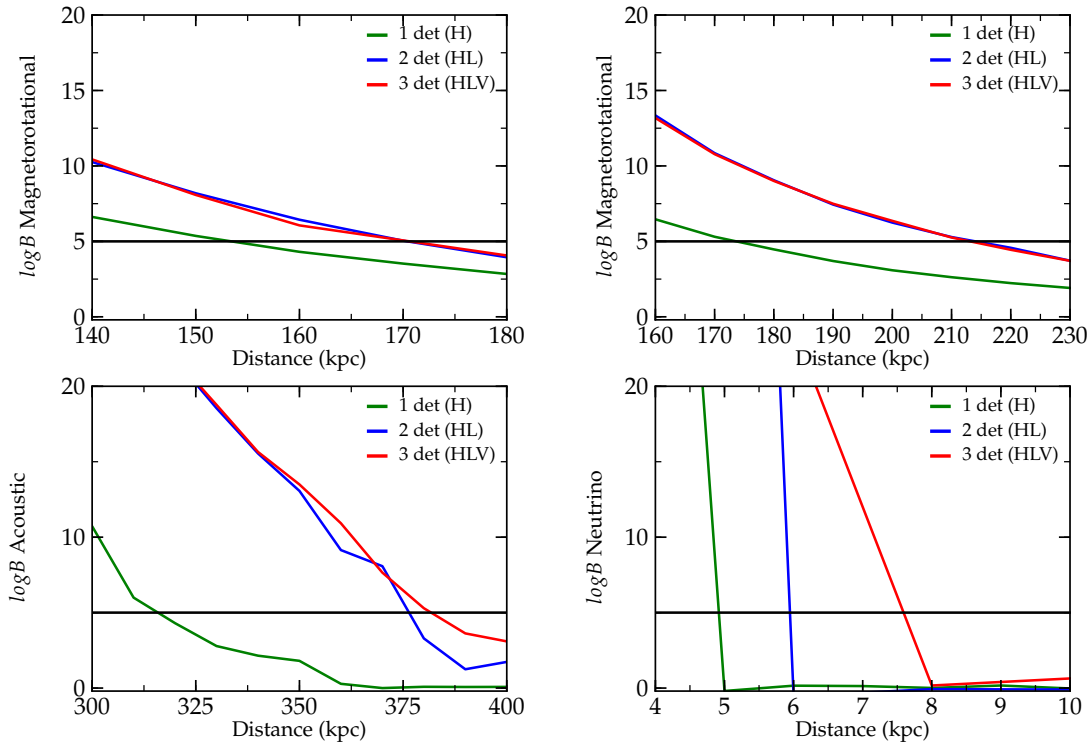

Figure 6.27: Same as Figure 6.16 using spectrogram version of SMEE. **Top Left Plot** Results for the `DimExtra` catalogue. In the spectrogram domain using 3 detectors, the maximum mean distance that signal can be distinguished from both the `Mur` and `Ott` PCs is $\sim$ 170 kpc. **Top Right Plot** Results for the `Sch` catalogue. In the spectrogram domain using 3 detectors, the maximum mean distance that signal can be distinguished from both the `Mur` and `Ott` PCs is $\sim$ 215 kpc. **Bottom Left Plot** Results for the `OttExtra` catalogue. In the spectrogram domain using 3 detectors, the maximum mean distance that signal can be distinguished from both the `Dim` and `Mur` PCs is $\sim$ 380 kpc. **Bottom Right Plot** Results for the `Yak` catalogue. In the spectrogram domain using 3 detectors,the maximum mean distance that signal can be distinguished from both the `Dim` and `Ott` PCs is $\sim$ 7.5 kpc.

Neutrino Mechanism

As in the case for the time and power spectrum domains, the three available `Yak` waveforms are added to Advanced LIGO and Advanced Virgo noise and Spec_SMEE computes $\log B_{SN}$. The results are listed in Tab. 6.3. Even at 10 kpc the `Yak` waveforms appear to be most consistent with noise for Spec_SMEE. The bottom right panel of Figure. 6.27 shows that the `Yak` waveforms require a distance of less than 7.5kpc to be clearly associated with the neutrino mechanism which is an improvement over the time and power spectrum domain versions of SMEE.

This indicates that including the frequency information improves the reconstruction but by also having the time domain information the errors seen in the power spectrum domain are reduced.

6.5 Conclusions

In Chapter 4 it was shown that SMEE can effectively be used to infer the physics behind core-collapse supernova in a simplified environment. The purpose of this Chapter was to investigate SMEE's reliability in a more realistic scenario closer to what will be seen in the Advanced detector era. This includes taking the antenna response and different times of arrival at each detector into account. It also means using noise from a working GW detector which has been altered to better represent the detector noise that will be seen in future detectors.

SMEE has been shown to be extremely successful in this scenario, especially in the spectrogram and time domain versions of SMEE. Both are able to perform model selection to large distances and a case could be made for either version being deemed the most successful. However, in the test where waveforms which were not used to create the principal components it is Spec_SMEE which is most successful. For both the neutrino and acoustic mechanisms it is able to correctly assign the `Ott Extra` and `Yak` catalogues to a higher distance. The results for the magnetorotational mechanism are equivalent to results seen using TD_SMEE. This test is the closest to the scenario which will be seen when a detection is made in the future i.e. where no prior knowledge is known about the detected waveform. Because of this, the spectrogram version of SMEE is chosen as the most successful version of SMEE. However, the time domain version of SMEE should still be pursued and run as an extra test, especially in the case where the SNR is less than 10, as TD_SMEE is more successful at smaller SNRs.

PSD_SMEE is significantly poorer, especially in the case where complete knowledge of the catalogues is known. In this case, the distance to which model selection can be performed is much smaller than in the other two versions of SMEE. While it does improve in the case of the `Ott Extra` waveforms the most damning evidence for PSD_SMEE is the inability to correctly assign waveforms of the `Yak` catalogue to the neutrino mechanism. Therefore, it is not recommended that this version of SMEE be used in future results.

The limitations discussed in Chapter 4 when dealing with waveforms that were not used to create the principal components are still evident here. This is not due to a fault in SMEE but a lack of reliable Supernova models with a large and varied

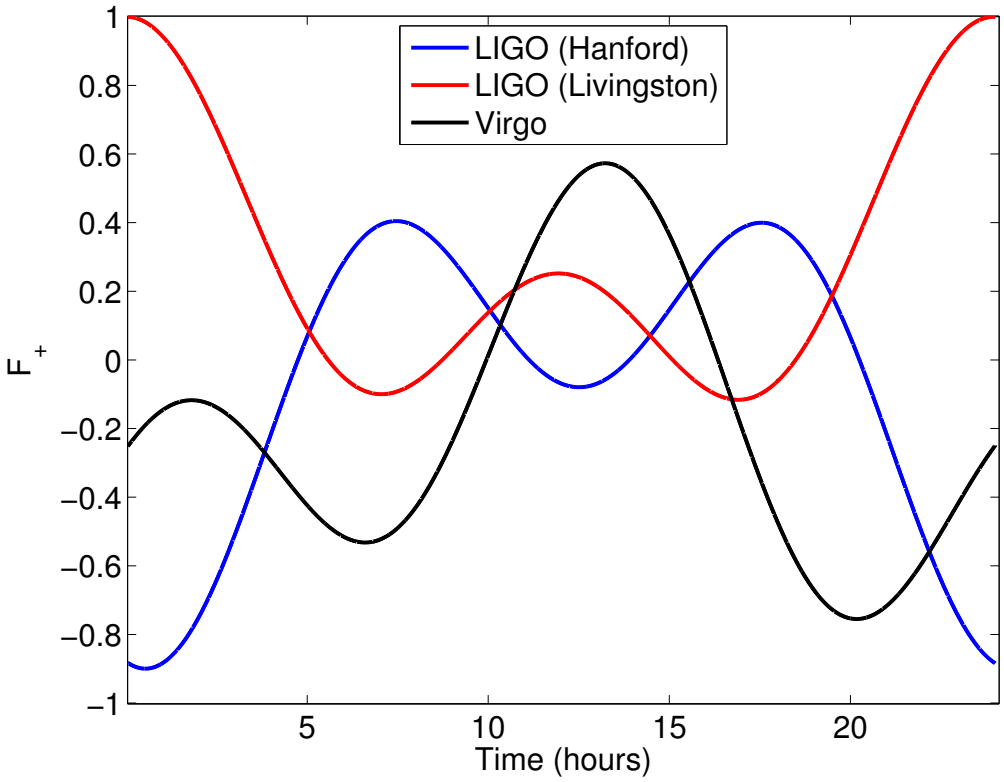

Figure 6.28: Here, F_+ is plotted using the coordinates of the Galactic Centre over a period of 24 hours. There are times where F_+ is higher for Advanced Virgo than in Advanced LIGO e.g. after 12 hours or where it is more equal such as after 17 hours. If one of these times was chosen SMEE would improve when being tested with Advanced Virgo noise albeit at the expense of the Advanced LIGO result.

parameter space. As more models are explored and simulated waveforms created SMEE will be adapted and improved upon.

Throughout the results shown in this Chapter, the contribution from Advanced Virgo has been minimal due to the fact that F_+ is small at the coordinates chosen. If a different Earth centre time of arrival was chosen where F_+ was more equal over the 3 detectors the addition of Advanced Virgo would have had more of an impact. This can be seen in Figure 6.28 where F_+ is plotted using the coordinates of the Galactic Centre over a period of 24 hours. As can be seen in the plot there are times where F_+ is higher for Advanced Virgo than in Advanced LIGO or where it is more equal. If one of these times was chosen SMEE would improve when being tested with Advanced Virgo noise.

Chapter 7

Conclusions

The second generation of GW detectors, Advanced LIGO [121] and Virgo [30], are due to come online in 2015 and they promise to bring the first direct detection of GWs. One possible source is from a core collapse supernova which are rare events within the Galaxy but could potentially occur during the next decade. Thus, it is important to have algorithms set up that can analyse a GW emitted by a supernova and provide information on the physics occurring during the core collapse. To this end, the focus of this thesis has been a Bayesian model selection algorithm known as the Supernova Model Evidence Extractor (SMEE). The necessity of such an algorithm is due to the fact that there is no agreed upon mechanism which drives a supernova and there are many theories of the physical processes behind the supernova mechanism. GWs provide an opportunity to see through to the core of a collapsing star. Thus if a gravitational wave from a core collapse supernova is detected it could provide information as to which supernova mechanism is reenergising the supernova. Acheiving this goal would immediately provide inference on the physics behind a core collapse supernova, which would be a great advancement in the understanding of one the most important processes in the universe.

Three different versions of SMEE are tested in this thesis. Firstly a version where principal component analysis is performed in time domain. Next a version that uses principal components created in the power spectrum domain and finally a version in the spectrogram domain. It has been shown in this thesis that all versions of SMEE are successful and are able to infer the supernova mechanism for a galactic supernova. The background and information for the implementation of SMEE is

shown in Chapters 2 and 3 and results are first shown in Chapter 4 for a simplified scenario. This Chapter demonstrated SMEE's success in the simple case where only a single Advanced LIGO detector is used and the effect of the antenna response is ignored. Chapter 6 provides results for the more realistic scenario where data from multiple detectors is utilised and the effects of the antenna response is taken into account. It also utilises a series of steps that were taken to improve model selection in SMEE, see Chapter 5.

In Chapter 6, SMEE proved to be extremely successful and is able to perform model selection to large distances. Out of the 3 versions of SMEE tested, the spectrogram version of SMEE is chosen as the most successful. However, the time domain version of SMEE should still be pursued and run as an extra test, especially in the case where the SNR is less than 10, as the time domain version of SMEE is more successful at smaller SNRs. The power spectrum version of SMEE is significantly poorer than the other two versions. Therefore, it is not recommended that this version of SMEE be used in the future.

The dominant limitation of SMEE is due to a lack of reliable supernova models with a large and varied parameter space. In future work, as more models are explored and simulated waveforms created, SMEE and the ability to infer the physics behind a supernova will only improve. Another improvement will be the addition of more detectors, mainly KAGRA [11] and LIGO India [118]. Initially SMEE will only have access to Advanced LIGO and Advanced Virgo but both these two additional detectors will both come online in the next decade. With two extra detectors SMEE will be able to successfully perform model selection and infer the mechanism behind a detected gravitational wave signal to ever increasing distances.

SMEE has been adapted by others to solve other problems such as inferring the angular momentum distribution of a core collapse supernova reenergised through the magnetorotational mechanism [2]. The techniques employed in SMEE have been applied to GWs from other sources such as the merging of Binary Black Holes [27]. Currently, work is being done to apply SMEE to classifying glitches in future detectors. Glitches are features in the detector noise which have a terrestrial origin but could be mistaken for a gravitational wave. It is important to classify the source of a glitch so that it can be removed in future analysis and this can be done by comparing a detected glitch with catalogues of previously seen features. A process similar to SMEE can be applied to this problem and at this time has proven

successful [91].

Bibliography

[1] E. B. Abdikamalov, C. D. Ott, L. Rezzolla, L. Dessart, H. Dimmelmeier, A. Marek, and H.-T. Janka. Axisymmetric general relativistic simulations of the accretion-induced collapse of white dwarfs. *Phys. Rev. D*, 81:044012, February 2010.

[2] Ernazar Abdikamalov, Sarah Gossan, Alexandra M. DeMaio, and Christian D. Ott. Measuring the angular momentum distribution in core-collapse supernova progenitors with gravitational waves. *Phys. Rev. D*, 90:044001, Aug 2014.

[3] Matthew R. Adams and Neil J. Cornish. Detecting a stochastic gravitational wave background in the presence of a galactic foreground and instrument noise. *Phys. Rev. D*, 89:022001, Jan 2014.

[4] Rana X. Adhikari. Gravitational radiation detection with laser interferometry. *Rev. Mod. Phys.*, 86:121–151, Feb 2014.

[5] O. D. Aguiar. Past, present and future of the Resonant-Mass gravitational wave detectors. *Research in Astronomy and Astrophysics*, 11:1–42, January 2011.

[6] P. et al. Amaro-Seoane. eLISA: Astrophysics and cosmology in the millihertz regime. *GW Notes, Vol. 6, p. 4-110*, 6:4–110, May 2013.

[7] Christophe Andrieu. An introduction to mcmc for machine learning, 2003.

[8] Szilrd Andrs and rpd Baricz. Properties of the probability density function of the non-central chi-squared distribution. *Journal of Mathematical Analysis and Applications*, 346(2):395 – 402, 2008.

[9] Muzammil A. Arain and Guido Mueller. Design of the advanced ligo recycling cavities. *Opt. Express*, 16(14):10018–10032, Jul 2008.

[10] W. D. Arnett. Gravitational collapse and weak interactions. *Canadian Journal of Physics*, 44:2553, 1966.

[11] Yoichi Aso et al. Interferometer design of the KAGRA gravitational wave detector. *Phys.Rev.*, D88(4):043007, 2013.

[12] P. Astone et al. The next science run of the gravitational wave detector nautilus. *Classical and Quantum Gravity*, 19, 2002.

[13] S. A. Balbus and J. F. Hawley. A powerful local shear instability in weakly magnetized disks. I - Linear analysis. II - Nonlinear evolution. *Astrophys. J.*, 376:214, July 1991.

[14] M.G. Beker, G. Cella, R. DeSalvo, M. Doets, H. Grote, J. Harms, E. Hennes, V. Mandic, D.S. Rabeling, J.F.J. van den Brand, and C.M. van Leeuwen. Improving the sensitivity of future gw observatories in the 110hz band: Newtonian and seismic noise. *General Relativity and Gravitation*, 43(2):623–656, 2011.

[15] H. A. Bethe. Supernova mechanisms. *Rev. Mod. Phys.*, 62:801, 1990.

[16] H. A. Bethe and J. R. Wilson. Revival of a stalled supernova shock by neutrino heating. *Astrophys. J.*, 295:14, August 1985.

[17] G. S. Bisnovatyi-Kogan. The Explosion of a Rotating Star As a Supernova Mechanism. *Astron. Zh.*, 47:813, August 1970.

[18] J. M. Blondin, A. Mezzacappa, and C. DeMarino. Stability of Standing Accretion Shocks, with an Eye toward Core-Collapse Supernovae. *Astrophys. J.*, 584:971, February 2003.

[19] R. Buras, H.-T. Janka, M. Rampp, and K. Kifonidis. Two-dimensional hydrodynamic core-collapse supernova simulations with spectral neutrino transport. II. Models for different progenitor stars. *Astron. Astrophys.*, 457:281, October 2006.

[20] A. Burrows, L. Dessart, E. Livne, C. D. Ott, and J. Murphy. Simulations of Magnetically Driven Supernova and Hypernova Explosions in the Context of Rapid Rotation. *Astrophys. J.*, 664:416, July 2007.

[21] A. Burrows, E. Livne, L. Dessart, C. D. Ott, and J. Murphy. A New Mechanism for Core-Collapse Supernova Explosions. *Astrophys. J.*, 640:878, April 2006.

[22] A. Burrows, E. Livne, L. Dessart, C. D. Ott, and J. Murphy. Features of the Acoustic Mechanism of Core-Collapse Supernova Explosions. *Astrophys. J.*, 655:416, January 2007.

[23] Basel GW Signal Catalog. http://phys-merger.physik.unibas.ch/ simon/gw_data.

[24] MPA Garching Gravitational Wave Signal Catalog. http://www.mpa-garching.mpg.de/rel_hydro/wave_catalogue.shtml.

[25] ORNL/FAU Gravitational Wave Signal Catalog. http://astrodev.phys.utk.edu/chimera/.

[26] P. Cerdá-Durán, J. A. Font, L. Antón, and E. Müller. A new general relativistic magnetohydrodynamics code for dynamical spacetimes. *Astron. Astrophys.*, 492:937, December 2008.

[27] J. Clark, L. Cadonati, J. Healy, I. S. Heng, J. Logue, N. Mangini, L. London, L. Pekowsky, and D. Shoemaker. Investigating Binary Black Hole Mergers with Principal Component Analysis. *ArXiv e-prints*, June 2014.

[28] S. A. Colgate and R. H. White. The Hydrodynamic Behavior of Supernovae Explosions. *Astrophys. J.*, 143:626, March 1966.

[29] K. Danzmann, H. Lück, A. Rüdiger, R. Schilling, M. Schrempel, W. Winkler, J. Hough, G. P. Newton, N. A. Robertson, H. Ward, A. M. Campbell, J. E. Logan, D. I. Robertson, K. A. Strain, J. R. J. Bennett, V. Kose, M. Kühne, B. F. Schutz, D. Nicholson, J. Shuttleworth, H. Welling, P. Aufmuth, R. Rinkleff, A. Tünnermann, and B. Willke. Geo 600 - a 600-m laser interferometric gravitational wave antenna. In E. Coccia, G. Pizzella, and F. Ronga, editors, *Gravitational Wave Experiments*, pages 100–111, Singapore; River Edge, NJ, 1995. World Scientific.

[30] J Degallaix et al. Advanced Virgo Status. In G. Auger, P. Binétruy, and E. Plagnol, editors, *9th LISA Symposium*, volume 467 of *Astronomical Society of the Pacific Conference Series*, page 151, January 2013.

[31] L. Dessart, A. Burrows, E. Livne, and C. D. Ott. Magnetically Driven Explosions of Rapidly Rotating White Dwarfs Following Accretion-Induced Collapse. *Astrophys. J.*, 669:585, November 2007.

[32] L. Dessart, A. Burrows, E. Livne, and C. D. Ott. The Proto-Neutron Star Phase of the Collapsar Model and the Route to Long-Soft Gamma-Ray Bursts and Hypernovae. *Astrophys. J. Lett.*, 673:L43, January 2008.

[33] H. Dimmelmeier, C. D. Ott, H.-T. Janka, A. Marek, and E. Müller. Generic Gravitational-Wave Signals from the Collapse of Rotating Stellar Cores. *Phys. Rev. Lett.*, 98:251101, June 2007.

[34] H. Dimmelmeier, C. D. Ott, A. Marek, and H.-T. Janka. Gravitational wave burst signal from core collapse of rotating stars. *Phys. Rev. D*, 78:064056, 2008.

[35] F. W. Dyson, A. S. Eddington, and C. Davidson. A Determination of the Deflection of Light by the Sun's Gravitational Field, from Observations Made at the Total Eclipse of May 29, 1919. *Royal Society of London Philosophical Transactions Series A*, 220:291–333, 1920.

[36] A Einstein and A Engel. *The Collected Papers of Albert Einstein: The Berlin Years: Writings*. Princeton University Press, Princeton, NJ, 1997.

[37] Abadie et al. Search for gravitational waves from binary black hole inspiral, merger, and ringdown. *Phys. Rev. D*, 83:122005, Jun 2011.

[38] Abadie et al. Search for gravitational waves from intermediate mass binary black holes. *Phys. Rev. D*, 85:102004, May 2012.

[39] B. Abbot et al. Searches for periodic gravitational waves from unknown isolated sources and scorpius x-1: Results from the second ligo science run. *Phys. Rev. D*, 76:082001, Oct 2007.

[40] J. Aasi et al. Gravitational waves from known pulsars: Results from the initial detector era. *The Astrophysical Journal*, 785(2):119, 2014.

[41] J. Abadie et al. Predictions for the rates of compact binary coalescences observable by ground-based gravitational-wave detectors. *Classical and Quantum Gravity*, 27, 2010.

[42] M Punturo et al. The einstein telescope: a third-generation gravitational wave observatory. *Classical and Quantum Gravity*, 27(19):194002, 2010.

[43] Pau Amaro-Seoane et al. Low-frequency gravitational-wave science with elisa/ngo. *Classical and Quantum Gravity*, 29(12):124016, 2012.

[44] M. Evans, L. Barsotti, P. Kwee, J. Harms, and H. Miao. Realistic filter cavities for advanced gravitational wave detectors. *Phys. Rev. D*, 88:022002, Jul 2013.

[45] X. Fan, C. Messenger, and I. S. Heng. A Bayesian approach to multi-messenger astronomy: Identification of gravitational-wave host galaxies. *ArXiv e-prints*, June 2014.

[46] T. Foglizzo, P. Galletti, L. Scheck, and H.-T. Janka. Instability of a Stalled Accretion Shock: Evidence for the Advective-Acoustic Cycle. *Astrophys. J.*, 654:1006, January 2007.

[47] T. Foglizzo, L. Scheck, and H.-T. Janka. Neutrino-driven Convection versus Advection in Core-Collapse Supernovae. *Astrophys. J.*, 652:1436, December 2006.

[48] C. L. Fryer and A. Heger. Core-Collapse Simulations of Rotating Stars. *Astrophys. J.*, 541:1033, October 2000.

[49] C. L. Fryer, D. E. Holz, and S. A. Hughes. Gravitational Waves from Stellar Collapse: Correlations to Explosion Asymmetries. *Astrophys. J.*, 609:288, July 2004.

[50] C. L. Fryer and M. S. Warren. The Collapse of Rotating Massive Stars in Three Dimensions. *Astrophys. J.*, 601:391, January 2004.

[51] GEO600. `http://www.geo600.org/1032083/GEO600_Sensitivity_Curves`.

[52] A. et al. Giazotto. The virgo experiment: Status of the art. In E. Coccia, G. Pizzella, and F. Ronga, editors, *Gravitational Wave Experiments*, pages 86–99, Singapore; River Edge, NJ, 1995. World Scientific.

[53] M. Hamuy. Observed and Physical Properties of Core-Collapse Supernovae. *Astrophys. J.*, 582:905, January 2003.

[54] F. Hanke, A. Marek, B. Müller, and H.-T. Janka. Is Strong SASI Activity the Key to Successful Neutrino-Driven Supernova Explosions? *Submitted to the Astrophys. J., arXiv:1108.4355*, August 2011.

[55] A. Heger, S. E. Woosley, and H. C. Spruit. Presupernova Evolution of Differentially Rotating Massive Stars Including Magnetic Fields. *Astrophys. J.*, 626:350, June 2005.

[56] I. S. Heng. Rotating stellar core-collapse waveform decomposition: a principal component analysis approach. *Class. Quantum Grav.*, 26:105005, May 2009.

[57] S. Hild. Beyond the Second Generation of Laser-Interferometric Gravitational Wave Observatories. *Class.Quant.Grav.*, 29:124006, 2012.

[58] M. M. Hohle, R. Neuhäuser, and B. F. Schutz. Masses and luminosities of O- and B-type stars and red supergiants. *Astron. Nachr.*, 331:349, April 2010.

[59] D. E. Holz and S. A. Hughes. Using Gravitational-Wave Standard Sirens. *Astrophys. J.*, 629:15–22, August 2005.

[60] W. Iwakami, K. Kotake, N. Ohnishi, S. Yamada, and K. Sawada. Effects of Rotation on Standing Accretion Shock Instability in Nonlinear Phase for Core-Collapse Supernovae. *Astrophys. J.*, 700:232, July 2009.

[61] F. S. Kitaura, H.-T. Janka, and W. Hillebrandt. Explosions of O-Ne-Mg cores, the Crab supernova, and subluminous type II-P supernovae. *Astron. Astrophys.*, 450:345, April 2006.

[62] K. Kotake, W. Iwakami, N. Ohnishi, and S. Yamada. Stochastic Nature of Gravitational Waves from Supernova Explosions with Standing Accretion Shock Instability. *Astrophys. J. Lett.*, 697:L133, June 2009.

[63] K. Kotake, W. Iwakami Nakano, and N. Ohnishi. Effects of Rotation on Stochasticity of Gravitational Waves in Nonlinear Phase of Core-Collapse Supernovae. *Astrophys. J. in press; arXiv:1106.0544*, 736:124, August 2011.

[64] K. Kotake, N. Ohnishi, and S. Yamada. Gravitational Radiation from Standing Accretion Shock Instability in Core-Collapse Supernovae. *Astrophys. J.*, 655:406, January 2007.

[65] K. Kotake, S. Yamada, K. Sato, K. Sumiyoshi, H. Ono, and H. Suzuki. Gravitational radiation from rotational core collapse: Effects of magnetic fields and realistic equations of state. *Phys. Rev. D*, 69:124004, June 2004.

[66] T. Kuroda, K. Kotake, and T. Takiwaki. Fully General Relativistic Simulations of Core-Collapse Supernovae with An Approximate Neutrino Transport. *Submitted to the Astrophys. J.; arXiv:1202.2487*, 2012.

[67] learner.org. http://www.learner.org/courses/physics/unit/text.html?unit=3&secNum=7

[68] M. Liebendörfer. A Simple Parameterization of the Consequences of Deleptonization for Simulations of Stellar Core Collapse. *Astrophys. J.*, 633:1042, November 2005.

[69] M. Liebendörfer, M. Rampp, H.-T. Janka, and A. Mezzacappa. Supernova Simulations with Boltzmann Neutrino Transport: A Comparison of Methods. *Astrophys. J.*, 620:840, February 2005.

[70] J. Logue et al. Inferring the core-collapse supernova mechanism with gravitational waves. *arXiv:1202.3256v2*, 2012.

[71] E. Müller, M. Rampp, R. Buras, H.-T. Janka, and D. H. Shoemaker. Toward Gravitational Wave Signals from Realistic Core-Collapse Supernova Models. *Astrophys. J.*, 603:221, March 2004.

[72] K. V. Mardia, J. T. Kent, and J. M. Bibby. *Multivariate analysis*. Academic Press, London, UK, 1979.

[73] A. Marek, H. Dimmelmeier, H.-T. Janka, E. Müller, and R. Buras. Exploring the relativistic regime with Newtonian hydrodynamics: an improved effective gravitational potential for supernova simulations. *Astron. Astrophys.*, 445:273, January 2006.

[74] A. Marek and H.-T. Janka. Delayed Neutrino-Driven Supernova Explosions Aided by the Standing Accretion-Shock Instability. *Astrophys. J.*, 694:664, March 2009.

[75] A. Marek, H.-T. Janka, and E. Müller. Equation-of-state dependent features in shock-oscillation modulated neutrino and gravitational-wave signals from supernovae. *Astron. Astrophys.*, 496:475, March 2009.

[76] B. Müller, H.-T. Janka, and A. Marek. A New Multi-Dimensional General Relativistic Neutrino Hydrodynamics Code for Core-Collapse Supernovae II. Relativistic Explosion Models of Core-Collapse Supernovae. *Submitted to the Astrophys. J. ArXiv:1202.0815*, February 2012.

[77] E. Müller, H.-T. Janka, and A. Wongwathanarat. Parametrized 3D models of neutrino-driven supernova explosions. Neutrino emission asymmetries and gravitational-wave signals. *Astron. Astrophys.*, 537:A63, January 2012.

[78] J. W. Murphy and A. Burrows. Criteria for Core-Collapse Supernova Explosions by the Neutrino Mechanism. *Astrophys. J.*, 688:1159, December 2008.

[79] J. W. Murphy, C. D. Ott, and A. Burrows. A Model for Gravitational Wave Emission from Neutrino-Driven Core-Collapse Supernovae. *Astrophys. J.*, 707:1173, December 2009.

[80] J. Nordhaus, A. Burrows, A. Almgren, and J. Bell. Dimension as a Key to the Neutrino Mechanism of Core-Collapse Supernova Explosions. *Astrophys. J.*, 720:694, September 2010.

[81] M. Obergaulinger, M. A. Aloy, H. Dimmelmeier, and E. Müller. Axisymmetric simulations of magnetorotational core collapse: approximate inclusion of general relativistic effects. *Astron. Astrophys.*, 457:209, October 2006.

[82] M. Obergaulinger, P. Cerdá-Durán, E. Müller, and M. A. Aloy. Semi-global simulations of the magneto-rotational instability in core collapse supernovae. *Astron. Astrophys.*, 498:241, April 2009.

[83] C. D. Ott. Probing the core-collapse supernova mechanism with gravitational waves. *Class. Quantum Grav.*, 26:204015, October 2009.

[84] C. D. Ott. TOPICAL REVIEW: The gravitational-wave signature of core-collapse supernovae. *Class. Quantum Grav.*, 26:063001, March 2009.

[85] C. D. Ott, A. Burrows, L. Dessart, and E. Livne. A New Mechanism for Gravitational-Wave Emission in Core-Collapse Supernovae. *Phys. Rev. Lett.*, 96:201102, May 2006.

[86] C. D. Ott, A. Burrows, L. Dessart, and E. Livne. Two-Dimensional Multiangle, Multigroup Neutrino Radiation-Hydrodynamic Simulations of Post-bounce Supernova Cores. *Astrophys. J.*, 685:1069, 2008.

[87] C. D. Ott, A. Burrows, T. A. Thompson, E. Livne, and R. Walder. The Spin Periods and Rotational Profiles of Neutron Stars at Birth. *Astrophys. J. Suppl. Ser.*, 164:130, May 2006.

[88] C. D. Ott, H. Dimmelmeier, A. Marek, H.-T. Janka, I. Hawke, B. Zink, and E. Schnetter. 3D Collapse of Rotating Stellar Iron Cores in General Relativity Including Deleptonization and a Nuclear Equation of State. *Phys. Rev. Lett.*, 98:261101, June 2007.

[89] M. Pitkin, S. Reid, S. Rowan, and J. Hough. Gravitational Wave Detection by Interferometry (Ground and Space). *Living Reviews in Relativity*, 14:5, July 2011.

[90] M. V. Plissi, K. A. Strain, C. I. Torrie, N. A. Robertson, S. Killbourn, S. Rowan, S. M. Twyford, H. Ward, K. D. Skeldon, and J. Hough. Aspects of the suspension system for geo 600. *Review of Scientific Instruments*, 69(8):3055–3061, 1998.

[91] J. Powell and I. S. Heng. Classifying glitch types with lalinference burst and principal component analysis. LVC Meeting, September 2014, 2014.

[92] F. J. (for the LIGO Scientific Collaboration) Raab. The status of laser interferometer gravitational-wave detectors. *J. Phys.: Conf. Ser.*, 39:25–31, 2006.

[93] M. Rampp and H.-T. Janka. Radiation hydrodynamics with neutrinos. Variable Eddington factor method for core-collapse supernova simulations. *Astron. Astrophys.*, 396:361, December 2002.

[94] T. Regimbau. The astrophysical gravitational wave stochastic background. *Research in Astronomy and Astrophysics*, 11:369–390, April 2011.

[95] N.A. Robertson et al. Seismic isolation and suspension systems for advanced ligo. In James Hough and Gary H. Sanders, editors, *Gravitational Wave and Particle Astrophysics Detectors*. SPIE, 2004.

[96] C. Roever. Bayesian inference on astrophysical binary inspirals based on gravitational-wave measurements, 2007.

[97] C. Röver, M.-A. Bizouard, N. Christensen, H. Dimmelmeier, I. S. Heng, and R. Meyer. Bayesian reconstruction of gravitational wave burst signals from simulations of rotating stellar core collapse and bounce. *Phys. Rev. D*, 80:102004, November 2009.

[98] B. Sathyaprakash, M. Abernathy, F. Acernese, P. Ajith, B. Allen, P. Amaro-Seoane, N. Andersson, S. Aoudia, K. Arun, P. Astone, and et al. Scientific objectives of Einstein Telescope. *Classical and Quantum Gravity*, 29(12):124013, June 2012.

[99] B.S Sathyaprakash and Bernard F. Schutz. Physics, astrophysics and cosmology with gravitational waves. *Living Reviews in Relativity*, 12(2), 2009.

[100] L. Scheck, H.-T. Janka, T. Foglizzo, and K. Kifonidis. Multidimensional supernova simulations with approximative neutrino transport. II. Convection

and the advective-acoustic cycle in the supernova core. *Astron. Astrophys.*, 477:931, January 2008.

[101] S. Scheidegger, T. Fischer, S. C. Whitehouse, and M. Liebendörfer. Gravitational waves from 3D MHD core collapse simulations. *Astron. Astrophys.*, 490:231, 2008.

[102] S. Scheidegger, R. Käppeli, S. C. Whitehouse, T. Fischer, and M. Liebendörfer. The influence of model parameters on the prediction of gravitational wave signals from stellar core collapse. *Astron. Astrophys.*, 514:A51, May 2010.

[103] A Sesana. Gravitational wave emission from binary supermassive black holes. *Classical and Quantum Gravity*, 30(24):244009, 2013.

[104] M. Shibata, Y. T. Liu, S. L. Shapiro, and B. C. Stephens. Magnetorotational collapse of massive stellar cores to neutron stars: Simulations in full general relativity. *Phys. Rev. D*, 74:104026, November 2006.

[105] D. Shoemaker. Advanced ligo anticipated sensitivity curves. Technical Report LIGO-T0900288-v3, LIGO Scientific Collaboration, 2010.

[106] D. S. Sivia and J. Skilling. *Data Analysis: A Bayesian Tutorial*. Oxford University Press, Oxford, UK, second edition, 2006.

[107] Skilling. `http://www.inference.phy.cam.ac.uk/bayesys/`.

[108] J. Skilling. Nested Sampling. In R. Fischer, R. Preuss, & U. V. Toussaint, editor, *AIP Conference Proceedings: 24th International Workshop on Bayesian Inference and Maximum Entropy Methods in Science and Engineering,*, volume 735, page 395, November 2004.

[109] S. J. Smartt. Review of core-collapse progenitors. *Annual Review of Astronomy and Astrophysics*, 47:63–106, 2009.

[110] Kentaro Somiya. Detector configuration of kagra the japanese cryogenic gravitational-wave detector. *Classical and Quantum Gravity*, 29(12):124007, 2012.

[111] Y. Suwa, K. Kotake, T. Takiwaki, S. C. Whitehouse, M. Liebendörfer, and K. Sato. Explosion Geometry of a Rotating 13 $M_\odot$ Star Driven by the SASI-Aided Neutrino-Heating Supernova Mechanism. *Pub. Astr. Soc. Jap.*, 62:L49, December 2010.

[112] T. Takiwaki and K. Kotake. Gravitational Wave Signatures of Magnetohydrodynamically Driven Core-collapse Supernova Explosions. *Astrophys. J.*, 743:30, 2011.

[113] T. Takiwaki, K. Kotake, and Y. Suwa. Three-dimensional Hydrodynamic Core-Collapse Supernova Simulations for an $11.2 M_{\odot}$ Star with Spectral Neutrino Transport. *Submitted to the Astrophys. J., arXiv:1108.3989*, August 2011.

[114] The LIGO Scientific Collaboration, the Virgo Collaboration, the NINJA-2 Collaboration, :, J. Aasi, B. P. Abbott, R. Abbott, T. Abbott, M. R. Abernathy, T. Accadia, and et al. The NINJA-2 project: Detecting and characterizing gravitational waveforms modelled using numerical binary black hole simulations. *ArXiv e-prints*, January 2014.

[115] T. A. Thompson, A. Burrows, and P. A. Pinto. Shock Breakout in Core-Collapse Supernovae and Its Neutrino Signature. *Astrophys. J.*, 592:434, July 2003.

[116] K. S. Thorne. 300 years of gravitation. In S. W. Hawking and W. Israel, editors, *300 Years of Gravitation*, Cambridge, UK, 1987. Cambridge University Press.

[117] K.S Thorne. A new window onto the universe. *ArXiv General Relativity and Quantum Cosmology e-prints*, 1997.

[118] C. S. UNNIKRISHNAN. Indigo and ligo-india: Scope and plans for gravitational wave research and precision metrology in india. *International Journal of Modern Physics D*, 22(01):1341010, 2013.

[119] J. Veitch and A. Vecchio. Bayesian coherent analysis of in-spiral gravitational wave signals with a detector network. *Phys. Rev. D*, 81:062003, March 2010.

[120] R. Walder, A. Burrows, C. D. Ott, E. Livne, I. Lichtenstadt, and M. Jarrah. Anisotropies in the Neutrino Fluxes and Heating Profiles in Two-dimensional, Time-dependent, Multigroup Radiation Hydrodynamics Simulations of Rotating Core-Collapse Supernovae. *Astrophys. J.*, 626:317, June 2005.

[121] S. J. Waldman. The Advanced LIGO Gravitational Wave Detector. *ArXiv e-prints*, March 2011.

[122] J. Weber. Gravitational radiation. *Phys. Rev. Lett.*, 18:498–501, 1967.

[123] N. N. Weinberg and E. Quataert. Non-linear saturation of g-modes in proto-neutron stars: quieting the acoustic engine. *Mon. Not. Roy. Astron. Soc.*, 387:L64, June 2008.

[124] G. Weinstein. Einstein, Schwarzschild, the Perihelion Motion of Mercury and the Rotating Disk Story. *ArXiv e-prints*, November 2014.

[125] J. M. Weisberg and J. H. Taylor. The Relativistic Binary Pulsar B1913+16: Thirty Years of Observations and Analysis. In F. A. Rasio and I. H. Stairs, editors, *Binary Radio Pulsars*, volume 328 of *Astronomical Society of the Pacific Conference Series*, page 25, July 2005.

[126] J.M. Weisberg and J.H. Taylor. Relativistic binary pulsar b1913+16: Thirty years of observations and analysis. *Binary Radio Pulsars, ASP Conference Series*, 328, 2005.

[127] N. Wex. Testing Relativistic Gravity with Radio Pulsars. *ArXiv e-prints*, February 2014.

[128] J. C. Wheeler, I. Yi, P. Höflich, and L. Wang. Asymmetric Supernovae, Pulsars, Magnetars, and Gamma-Ray Bursts. *Astrophys. J.*, 537:810, July 2000.

[129] John Archibald Wheeler. *A Journey into Gravity and Spacetime.* Scientific American Library, 1990.

[130] Wikipedia. `http://en.wikipedia.org/wiki/Gravitational_waves/`.

[131] S. E. Woosley and A. Heger. The Progenitor Stars of Gamma-Ray Bursts. *Astrophys. J.*, 637:914, February 2006.

[132] K. N. Yakunin, P. Marronetti, A. Mezzacappa, S. W. Bruenn, C.-T. Lee, M. A. Chertkow, W. R. Hix, J. M. Blondin, E. J. Lentz, O. E. Bronson Messer, and S. Yoshida. Gravitational waves from core collapse supernovae. *Class. Quantum Grav.*, 27:194005, October 2010.